Table of contents

NEGF26-684788

A Conforming Interface Approach for Phase Transitions in Rarefied Gas Dynamics Based on the R13 Equations

Manuel Torrilhon[1], Donat Weniger[1]
[1]Applied and Computational Mathematics, RWTH Aachen University, Germany
mt@acom.rwth-aachen.de

KEY WORDS

Non-equilibrium gas flow, moment equations, kinetic gas theory, phase transition, level-set interface tracking, finite element method

ABSTRACT

In rarefied gas dynamics, classical models like Fourier's law cannot be used due to insufficient collisions and the lack of equilibrium, typically represented by a larger Knudsen number. Extended gas dynamics models, such as moment approximations in kinetic theory, augment traditional continuum mechanics and include more variables and equations to describe the state of the gas, resulting in increased complexity of the equations. One of the most successfull such approximations are the regularized 13-moment-equations. Originally derived in [1] to overcome the subshock problem of moment equations [2] they exhibit superior accuracy and stability properties, see also the review [3]. Boundary conditions for R13 have been established in [4, 5] which allowed analytical solutions for fluid dynamic model problems with comparison to experiments in [6, 7]. Over time regularized moment equations have been derived for different molecule models, mixtures as well as polyatomic and granular gases, see [8, 9, 10, 11, 12]. For increased accuracy higher order moment models are possible [13, 14].
Linearized around a constant ground state and in dimensionless and steady state form the equations are given by

$$\begin{aligned}
\nabla\cdot\mathbf{v} &= f_{\text{mass}} && \text{mass balance}\\
\nabla\rho+\nabla\theta+\nabla\cdot\boldsymbol{\sigma} &= f_{\text{force}} && \text{momentum balance}\\
\nabla\cdot\mathbf{v}+\nabla\cdot\mathbf{q} &= f_{\text{heat}} && \text{energy balance}\\
-\tfrac{4}{5}(\nabla\cdot\mathbf{q})_{\text{stf}}+2(\nabla\cdot\mathbf{v})_{\text{stf}} &= -\tfrac{1}{\text{Kn}}\boldsymbol{\sigma}-\tfrac{4}{3}\text{Kn}\Delta\boldsymbol{\sigma}+\tfrac{8}{5}\text{Kn}\nabla\cdot(\nabla\cdot\boldsymbol{\sigma})_{\text{stf}} && \text{stress balance}\\
\nabla\cdot\boldsymbol{\sigma}+\tfrac{5}{2}\nabla\theta &= -\tfrac{2}{3\text{Kn}}\mathbf{q}-\tfrac{12}{5}\text{Kn}\Delta\mathbf{q}+\tfrac{12}{5}\text{Kn}\nabla\cdot(\nabla\cdot\mathbf{q}) && \text{heat flux balance}
\end{aligned} \tag{1}$$

where the first three equations are for desnity ρ, velocity v and temperature θ, while the last two equations are constitutive laws or closures for the fields of stress tensor σ and heat flux q.
A variety of numerical methods for moment equations have been developed in [15, 16, 17, 18]. In this work we will on a mixed finite element solver for the steady, linearized, regularized 13-moment equations [16]. The Python implementation builds upon the software tools provided by the FEniCS computing

platform. We use a new tensorial approach utilizing the extension capabilities of FEniCS' Unified Form Language to define required differential operators for tensors above second degree. Using the software abstraction levels provided by the Unified Form Language allows an almost one-to-one correspondence between the underlying mathematical equation (1) and the resulting source code. Test cases support the validity of the proposed implementation using validation with analytical solutions. The documented and validated solver is provided publicly under the name *fenicsR13*.
In rarefied or non-equilibrium environments a phase interface is subject to jump conditions that couple interface velocity, local equilibrium, and non-equilibrium variables in a possibly discontinuous way, triggering boundary layer effects that shape the bulk solution [19]. Together with the nonlinear coupling of the evolving domain and the physical field equations, phase transitions in rarefied gas dynamics pose a significant challenge to numerical discretizations. In [20], we present a mesh-conforming interface method using the finite element framework FEniCS and the level-set method with remeshing. At each time step, the domain is remeshed such that the computational mesh is conforming to the interface. This yields highly accurate and robust representations of the phase interface, allowing the non-equilibrium interface conditions to be imposed directly and thus avoiding interpolation errors. The finite element solver and the meshing tool in our framework are exchangeable and adaptable. We provide an example implementation that is freely available and reusable in the reproducibility repository accompanying this paper. The framework is validated with simulations of the classical Stefan problem, and its flexibility is demonstrated on a model problem for the R13 equations for rarefied gas heat conduction using *fenicsR13*.

References

[1] H. Struchtrup and M. Torrilhon. *Regularization of Grad's 13 moment equations: derivation and linear analysis*. Phys. Fluids, **15**(9):p. 2668–2680 (2003)
[2] M. Torrilhon and H. Struchtrup. *Regularized 13-moment equations: shock structure calculations and comparison to Burnett models*. J. Fluid Mech., **513**:p. 171–198 (2004)
[3] M. Torrilhon. *Modeling nonequilibrium gas flow based on moment equations*. Ann. Rev. Fluid Mech., **48**:pp. 429–458 (2016)
[4] H. Struchtrup and M. Torrilhon. *H theorem, regularization, and boundary conditions for linearized 13 moment equations*. Phys. Rev. Let., **99**(1):p. 014502 (2007)
[5] M. Torrilhon and H. Struchtrup. *Boundary conditions for regularized 13-moment-equations for micro-channel-flows*. J. Comput. Phys., **227**(3):pp. 1982–2011 (2008)
[6] P. Taheri, M. Torrilhon, and H. Struchtrup. *Couette and Poiseuille microflows: analytical solutions for regularized 13-moment equations*. Phys. Fluids, **21**(1):p. 017102 (2009)
[7] M. Torrilhon. *Slow gas microflow past a sphere: Analytical solution based on moment equations*. Phys. Fluids, **22**(7):p. 072001 (2010)
[8] H. Struchtrup and M. Torrilhon. *Regularized 13 moment equations for hard sphere molecules: Linear bulk equations*. Phys. Fluids, **25**(5):p. 052001 (2013)
[9] B. Rahimi and H. Struchtrup. *Capturing non-equilibrium phenomena in rarefied polyatomic gases: A high-order macroscopic model*. Phys. Fluids, **26**(5):p. 052001 (2014)
[10] V. K. Gupta, P. Shukla, and M. Torrilhon. *Higher-order moment theories for dilute granular gases of smooth hard spheres*. J. Fluid Mech., **836**:pp. 451–501 (2018)
[11] V. K. Gupta, H. Struchtrup, and M. Torrilhon. *Regularized moment equations for binary gas mixtures: Derivation and linear analysis*. Phys. Fluids, **28**(4):p. 042003 (2016)
[12] Z. Cai, M. Torrilhon, and S. Yang. *Linear regularized 13-moment equations with Onsager boundary conditions for general gas molecules*. SIAM Journal on Applied Mathematics, **84**(1):pp. 215–245 (2024)
[13] A. S. Rana, V. K. Gupta, J. E. Sprittles, and M. Torrilhon. *H-theorem and boundary conditions for the linear R26 equations: application to flow past an evaporating droplet*. Journal of

Fluid Mechanics, **924** (2021)

[14] J. BÜNGER, E. CHRISTHURAJ, A. HANKE, and M. TORRILHON. *Structured derivation of moment equations and stable boundary conditions with an introduction to symmetric, trace-free tensors*. Kinetic and Related Models, **16**(3):pp. 458–494 (2023)

[15] M. TORRILHON and N. SARNA. *Hierarchical Boltzmann Simulations and Model Error Estimation*. J. Comput. Phys., **342**:pp. 66–84 (2017)

[16] L. THEISEN and M. TORRILHON. *FenicsR13: A Tensorial Mixed Finite Element Solver for the Linear R13 Equations Using the FEniCS Computing Platform*. ACM Trans. Math. Softw., **47**(2) (2021)

[17] S. SINGH, H. SONG, and M. TORRILHON. *Modal discontinuous Galerkin simulations for Grad's 13 moment equations: Application to Riemann problem in continuum-rarefied flow regime*. Journal of Computational and Theoretical Transport, pp. 1–25 (2024)

[18] L. THEISEN, A. S. RANA, M. TORRILHON, V. K. GUPTA, ET AL. *A generalized fundamental solution technique for the regularized 13-moment system in rarefied gas flows*. arXiv preprint arXiv:2504.18261 (2025)

[19] D. WENIGER, P. L. VARGHESE, J. KOWALSKI, and M. TORRILHON. *Unsteady Stefan problem with kinetic interface conditions for rarefied gas deposition*. International Journal of Heat and Mass Transfer, **217**:p. 124696 (2023)

[20] D. WENIGER and M. TORRILHON. *A conforming interface approach for phase transitions in rarefied gas dynamics*. Journal of Computational Physics, **542**:p. 114376 (2025)

NEGF26-678700

A DENOISING MULTISCALE PARTICLE METHOD FOR SIMULATING NONEQUILIBRIUM GAS FLOWS

Hao Yang[1], Jun Zhang*[1]

[1] School of Aeronautic Science and Engineering, Beihang University, Beijing 100191, PR China.
yang_hao@buaa.edu.cn, jun.zhang@buaa.edu.cn

KEY WORDS

Rarefied gas dynamics, Kinetic theory, DSMC, Multiscale modelling, Denoising technique

ABSTRACT

The direct simulation Monte Carlo (DSMC) method is promising for simulating rarefied nonequilibrium flows, but its inherent statistical noise and spatiotemporal resolution limitation hinder its applications for low-signal and near-continuum regimes. This work presents a denoising multiscale particle (DMP) method for efficient particle simulation of non-equilibrium gas flows. By extending particle attributes, each simulated particle in the DMP method carries both microscopic velocity and macroscopic flow information. Its low-noise property, where the signal-to-noise ratio is independent of signal magnitude, is achieved by statistically averaging the macroscopic information carried by particles. Additionally, anti-dissipation terms and spatial interpolation of macroscopic quantities are introduced to effectively compensate for numerical dissipation under large spatiotemporal steps, enabling multiscale computational capability. The method maintains high accuracy at coarse resolutions and significantly reduces the number of sampling particles required.

Specifically, from the perspective of denoising, inspired by the information preservation (IP) method, we generalize the velocity distribution function (VDF) to a velocity-information joint distribution function (VIJDF),

$$F(t, \boldsymbol{x}, \boldsymbol{c}, \boldsymbol{u}, \mathcal{T}) \tag{1}$$

where (t, x) denote the spatiotemporal coordinates, $\boldsymbol{c}$ is the molecular velocity, and $(\boldsymbol{u}, \mathcal{T})$ represent the low-noise information velocity and temperature preserved additionally by simulated particles. The evolution of the VIJDF is governed by an information-augmented Boltzmann equation,

$$\frac{\partial F}{\partial t} + c_i \frac{\partial F}{\partial x_i} + G_{u_i} \frac{\partial F}{\partial u_i} + G_{\mathcal{T}} \frac{\partial F}{\partial \mathcal{T}} = C(F, F) \tag{2}$$

Based on this formulation, both transport properties and denoising properties are theoretically analyzed [1].

Furthermore, to overcome the spatiotemporal resolution limitation of DSMC, we analyze the spatiotemporal discretization errors, and derive modified formulations for transport coefficients under finite time step Δt and cell size Δx:

$$\frac{\mu(\Delta t)}{\mu} = \frac{\Delta t}{2\tau} \coth\left(\frac{\Delta t}{2\tau}\right), \quad \frac{\kappa(\Delta t)}{\kappa} = \frac{\Delta t \mathrm{Pr}}{2\tau} \coth\left(\frac{\Delta t \mathrm{Pr}}{2\tau}\right) \tag{3}$$

* Corresponding author

$$\frac{\mu(\Delta x)}{\mu} = \xi\frac{\Delta x}{2\lambda}\coth\left(\xi\frac{\Delta x}{2\lambda}\right), \quad \frac{\kappa(\Delta t)}{\kappa} = \xi\frac{\Delta x\mathrm{Pr}}{2\lambda}\coth\left(\xi\frac{\Delta x\mathrm{Pr}}{2\lambda}\right) \tag{4}$$

where μ and κ are the viscosity and heat conductivity, τ and λ are the mean collision time (MCT) and mean free path (MFP), Pr is the Prandtl number. To mitigate these errors, an anti-dissipation distribution is incorporated into a second-order exponential Runge-Kutta scheme to reduce temporal errors, while a local sampling collision approach is proposed to alleviate spatial errors. These techniques enable the use of coarser spatiotemporal resolutions without compromising accuracy [3].

The DMP method integrates the above designs, and can achieves high accuracy at coarse resolutions while substantially reducing the number of sampling particles required [2]. A schematic diagram of the DMP method is shown in Fig. 1.

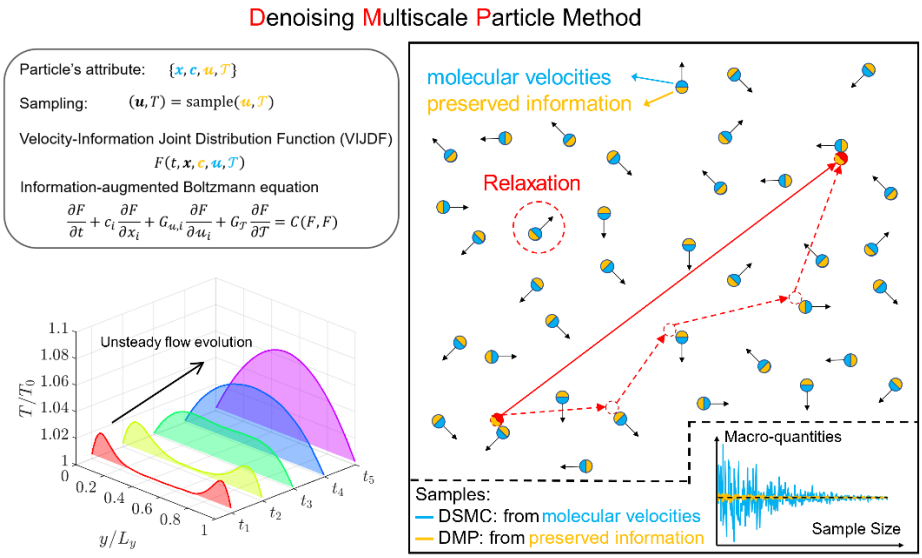

Figure 1: Schematic diagram of the DMP method.

Acknowledgments

This work was supported by the National Natural Science Foundation of China (Grant Nos. 92371102 and 12272028).

References and Citations

[1] H. Yang, J. Zhang, "A Theoretical Framework of Information Preservation Method and Its Application to Low-speed Nonequilibrium Gas Flows", Physics of Fluids, 35(7) (2023).
[2] H. Yang, K. Feng, Z. Cui, J. Zhang, "A Denoising Multiscale Particle Method for Nonequilibrium Flow Simulations", Journal of Computational Physics, 114096 (2025).
[3] H. Yang, J. Zhang, "Multiscale Simulation Monte Carlo Method: Linking Spatiotemporal Discretization Error Analysis to Algorithmic Development", Available at SSRN 5388713.

NEGF26-679350

A NOVEL SPLITTING SCHEME AND ITS APPLICATION TO STOCHASTIC PARTICLE SIMULATION OF DIATOMIC GAS FLOWS

Ziqi Cui[1], Jun Zhang*[1]
[1]School of Aeronautic Science and Engineering, Beihang University, Beijing, China
ziqicui@buaa.edu.cn, jun.zhang@buaa.edu.cn

KEY WORDS

Stochastic particle method, operator splitting, slow manifold analysis, Fokker–Planck model

ABSTRACT

Stochastic particle methods, exemplified by the Direct Simulation Monte Carlo (DSMC) approach, are widely used for nonequilibrium gas flows. However, they impose strict constraints on the time step (resolving the mean collision time) and cell size, which are fundamentally consequences of operator-splitting errors. Specifically, while standard Strang splitting is formally second-order accurate, its accuracy degrades to first order in the stiff regime. This "order reduction" implies that the scheme is not asymptotic-preserving with respect to the Navier-Stokes limit in under-resolved scenarios. In this work, we revisit this issue through a manifold-based analysis. We demonstrate that when the time step under-resolves the relaxation process, conventional splitting acting on the collision substep erroneously projects the distribution function directly onto the Euler limit (a perfect Maxwellian). This intermediate state of complete equilibrium directly leads to a final state after the subsequent half-step transport where the non-equilibrium components scale linearly with time step. Physically, this manifests as a spurious time-step dependent viscosity. To address this, we propose a structure-preserving splitting scheme that modifies the collision substep using an implicit midpoint method, thereby maintaining both symmetry and asymptotic consistency. The scheme is implemented within a Fokker-Planck model covering both monatomic and diatomic gases, where particle evolution is governed by Langevin equations coupled with implicit moment-level updates. The resulting Multiscale Stochastic Particle (MSP) method is validated against the SR3 low-density wind-tunnel condition. Results demonstrate that, compared to standard DSMC, the MSP method exhibits uniform second-order accuracy and significantly improved robustness in the coarse-resolution regime.

INTRODUCTION

Stochastic particle methods, exemplified by the Direct Simulation Monte Carlo (DSMC) approach, have become the standard for simulating nonequilibrium gas flows in the rarefied regime. These methods are commonly implemented using operator-splitting schemes, where the transport (convection) and collision (relaxation) operators are decoupled and advanced sequentially in time. While this splitting ensures algorithmic simplicity and high parallel efficiency, it introduces splitting errors that become significant in the near-continuum or stiff regimes.

* Corresponding author

It is well documented that standard DSMC imposes strict constraints on the numerical parameters: the time step Δt must be smaller than the mean collision time τ [1], and the cell size Δx must resolve the mean free path λ [2]. These constraints are largely consequences of the splitting error. Specifically, although the symmetric Strang splitting [3] is formally second-order accurate ($O(\Delta t^2)$), its accuracy has been observed to degrade to first order ($O(\Delta t)$) when the time step under-resolves the collision scale ($\Delta t \gg \tau$) [4, 5]. This phenomenon, often referred to as "order reduction," indicates that the traditional splitting procedure is not Asymptotic-Preserving (AP) with respect to the Navier-Stokes limits. In this work, we aim to address this limitation by analyzing the geometric properties of the splitting error relative to the hydrodynamic manifold.

METHOD

To understand the root cause of the accuracy degradation, we revisit the operator splitting technique through a manifold-based analysis of the relaxation dynamics.

2.1. Slow Manifold Analysis

We consider the kinetic equation in the stiff limit, where the collision operator drives the distribution function towards a local equilibrium (Maxwellian). Geometrically, this equilibrium defines a "slow manifold" within the state space. Our analysis examines how the transport and collision substeps act on the system state relative to this manifold.

(i) Resolved Regime: When the time step resolves the relaxation process ($\Delta t < \tau$), standard Strang splitting accurately captures the relaxation dynamics. Crucially, it preserves the asymptotic structure associated with the Navier-Stokes manifold, allowing the distribution function to retain the correct non-equilibrium perturbations required for transport phenomena.

(ii) Under-resolved Regime: When the time step is large compared to the relaxation time ($\Delta t \gg \tau$), the stiff collision substep acts as a stiff projection that forces the distribution function directly onto the Euler limit (a perfect Maxwellian). This rapid projection eliminates the exponentially small non-equilibrium components essential for viscous stress and heat flux, effectively decoupling the solution from the Navier-Stokes slow manifold. This loss of physical structure is the direct cause of the order reduction observed in stiff simulations.

2.2. A Structure-Preserving Splitting Scheme

Building on this geometric insight, we propose a new splitting scheme designed to be uniformly accurate across all regimes. The core idea is to modify the splitting sequence to ensure the solution state is correctly projected onto (or remains close to) the slow manifold after the complete time step, even when $\Delta t \gg \tau$.

The proposed scheme preserves the modularity of classical operator splitting and retains the ease of implementation in existing DSMC codes. Specifically, we modify only the collision substep by adopting an implicit midpoint scheme, which allows the method to maintain symmetry even in stiff scenarios. This new approach maintains second-order accuracy in the coarse-resolution regime where standard Strang splitting typically degrades. The schematic of the proposed algorithm is illustrated in Figure 1.

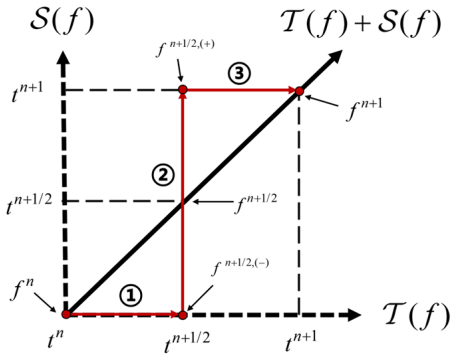

Figure 1: Schematic of the proposed splitting scheme. Adapted from our previous work [4].

2.3. Implementation in a Fokker-Planck Solver

The MSP method adopts a symmetric Strang operator-splitting framework, advancing the particle system through a sequence of half-step transport, collision relaxation, and a final half-step transport. The core innovation lies in the collision substep, which replaces the binary scattering integral with a continuous drift-diffusion process governed by the Langevin equation. To address numerical stiffness, this stochastic process is discretized using an implicit midpoint scheme at the moment level, ensuring exact conservation and asymptotic consistency without iterative overhead. For detailed numerical implementation and specific parameters for monatomic and diatomic gases, we refer the reader to [6, 7].

RESULTS AND DISCUSSION

We evaluated the performance of the MSP method using the 70-degree blunted cone geometry derived from the SR3 low-density wind tunnel experiments [8] (see Fig. 2), simulated at a 30-degree angle of attack. Focusing on a comparative analysis between numerical schemes, we benchmarked the MSP method against the standard DSMC method (utilizing classical Strang splitting) across a wide range of time-step sizes.

The results demonstrate a critical improvement: the standard DSMC solution exhibits significant sensitivity to the time step, with surface heat flux deviating rapidly as time step increases beyond the mean collision time. In contrast, the MSP method maintains consistent accuracy even with large time steps. As shown in Figure 3, the error norm for the MSP method remains bounded and significantly lower than that of the standard splitting scheme in the stiff regime. These results confirm that the new splitting strategy effectively suppresses the numerical stiffness associated with the collision term, allowing for larger time steps without compromising the physical fidelity.

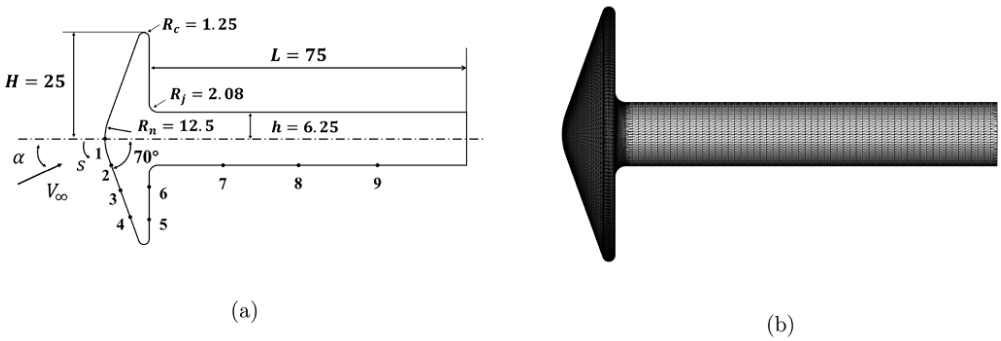

(a) (b)

Figure 2: Experimental (a) and computational (a) geometries for the SR3 blunted cone test case. Adapted from our previous work [6].

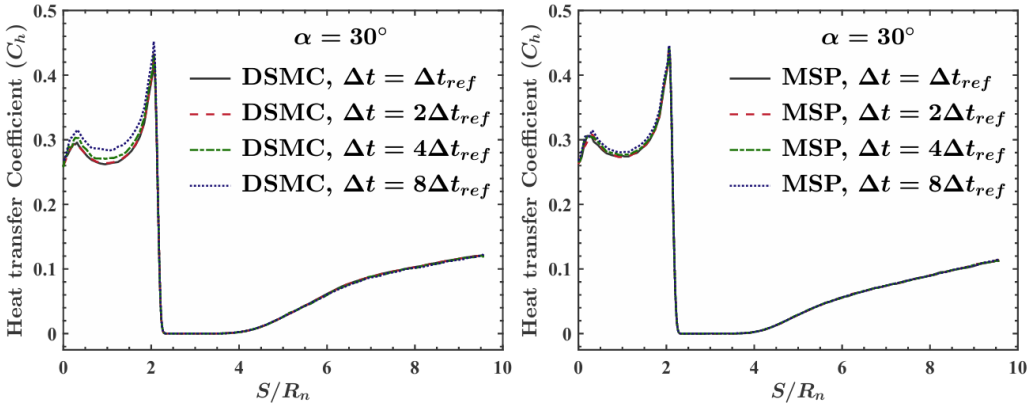

Figure 3: Sensitivity of the surface heat transfer coefficient to the global time step in the SR3 low-density wind-tunnel condition at $\alpha = 30°$. Left: DSMC. Right: MSP. Adapted from our previous work [6].

CONCLUSION

This work presents a novel operator-splitting framework for stochastic particle methods, grounded in the analysis of slow manifolds in kinetic theory. By correcting the splitting error that drives the solution off the hydrodynamic manifold, our proposed scheme achieves uniform second-order accuracy from the kinetic to the hydrodynamic regimes. The successful application to the Fokker-Planck model for diatomic gases in the SR3 benchmark highlights the potential of the MSP method as a robust tool for multiscale simulations of high-speed nonequilibrium flows.

References and Citations

[1] Hadjiconstantinou, N.G. (2000). Analysis of discretization in the direct simulation Monte Carlo. *Physics of Fluids*, **12**(10).
[2] Alexander, F.J., A.L. Garcia, and B.J. Alder. (1998). Cell size dependence of transport coefficients in stochastic particle algorithms. *Physics of Fluids*, **10**(6): p. 1540-1542.
[3] Strang, G. (1968). On the construction and comparison of difference schemes. *SIAM Journal on Numerical Analysis*, 1968. **5**(3): p. 506-517.
[4] Jin, S. (1995). Runge-Kutta methods for hyperbolic conservation laws with stiff relaxation terms. *Journal of Computational Physics*, **122**(1): p. 51-67.
[5] Sportisse, B. (2000). An Analysis of Operator Splitting Techniques in the Stiff Case. *Journal of Computational Physics*, **161**(1): p. 140-168.
[6] Cui, Z., et al. (2026). A multiscale stochastic particle method based on the Fokker-Planck model for diatomic gas flows. *Computer Physics Communications*, **319**.
[7] Cui, Z., et al. (2025). A multiscale stochastic particle method based on the Fokker-Planck model for nonequilibrium gas flows. *Journal of Computational Physics*, **520**.
[8] Allegre, J., D. Bisch, and J.C. Lengrand. (1997). Experimental Rarefied Heat Transfer at Hypersonic Conditions over 70-Degree Blunted Cone. *Journal of Spacecraft and Rockets*, **34**(6): p. 724-728.

NEGF26-677751

A semi-Lagrangian method for the polyatomic ESBGK model and its comparison to DSMC

Klaas Willems*[1,2], Erik Arlemark[3], Giovanni Samaey[1], Axel Klar[2],
[1]Department of Computer Science Celestijnenlaan 200 A box 2402 3001 Leuven, Belgium
klaas.willems@kuleuven.be, giovanni.samaey@kuleuven.be
[2]RPTU Kaiserslautern-Landau Gottlieb-Daimler-Straße 48 67663 Kaiserslautern
klar@rptu.de
[3]ASML
erik.arlemark@asml.com

KEY WORDS

BGK model, deterministic method, discrete velocity method

ABSTRACT

We present a new semi-Lagrangian scheme for the polyatomic Ellipsoidal Statistical BGK (ESBGK) model of the Boltzmann equation. The polyatomic ESBGK model [1] describes molecular collisions as a relaxation towards a generalized Gaussian distribution with an anisotropic covariance matrix and an exponentially decaying internal energy distribution. The semi-Lagrangian framework [2], being deterministic and grid-based, removes the time-step restriction associated with the linear transport term by following the method of characteristics. The potentially stiff relaxation term is treated using an implicit A-stable linear multistep method which, owing to the structure of the BGK operator, can be reformulated into a fully explicit time-stepping scheme. This yields a highly efficient and numerically stable method. In addition, we propose inflow and outflow boundary conditions suitable for BGK-type kinetic equations. Several numerical experiments are presented to verify the accuracy and efficiency of the scheme, and to compare its performance with results obtained from the Direct Simulation Monte Carlo (DSMC) method.

Introduction and the model

Non-equilibrium gases are encountered in many applications such as hypersonic flows, spacecraft re-entry problems, micro-electromechanical (MEMS) systems and vacuum technology. In these regimes, the usual macroscopic constitutive laws break down and a kinetic description of the gas is required. The fundamental equation describing a rarefied gas is the Boltzmann equation, which governs the evolution of the distribution of monoatomic particles $f(t, x, v)$ with $x, v \in \mathbb{R}^3$. Since the Boltzmann equation has

* Corresponding author

a relatively complex form, simplified models such as the BGK equation have been introduced,

$$\frac{\partial f}{\partial t} + v \cdot \nabla_x f = Q(f) \tag{1}$$

In the BGK equation, collisions ($Q(f)$ in (1)) are modeled by a relaxation towards the local thermodynamic equilibrium

$$Q_{BGK} = \frac{p}{\mu}\left[\frac{\rho}{(2\pi T)^{3/2}} \exp\left(-\frac{|U-v|^2}{2R_s T}\right) - f\right], \tag{2}$$

with ρ, U and T the density, mean velocity and temperature of the gas, and R_s the gas constant. It is well known that this model cannot recover realistic Prandtl numbers. As a solution, the Maxwellian distribution in (2) can be replaced by a Gaussian, which yields the so-called Ellipsoidal Symmetric BGK model (ESBGK) [5]. In [1], the ESBGK model was extended to polyatomic gases. Now, the internal energy is an additional independent parameter $I \in R^+$, such that $f(t, x, v, I)$. In this case, BGK relaxation operator looks like

$$\mathcal{Q}_{pESBGK} = \frac{p}{\mu(1-\nu+\theta\nu)}\left[\frac{\rho\Lambda_s}{det(2\pi\mathbb{T})^{\frac{1}{2}} R_s T_{rel}^{\delta/2}} \exp\left(-\frac{1}{2}(v-U)^T\mathbb{T}^{-1}(v-U) - \frac{I^{\delta/2}}{R_s T_{rel}}\right) - f\right], \tag{3}$$

with p the pressure, Λ_s a normalization constant, μ the dynamic viscosity, T_{rel} the relaxation temperature, δ the additional degrees of freedom of a polyatomic gas and the corrected tensor

$$\mathbb{T} = (1-\theta)\left((1-\nu)R_s T_{tr} I_d + \nu\Theta\right) + \theta R_s T_{eq} I_d. \tag{4}$$

The quantities T_{tr}, T_{eq} and Θ are the translational temperature, equilibrium temperature and the pressure tensor. The parameters θ and ν are used to set the Prandtl number and second-viscosity coefficient.
Although DSMC-type methods for the polyatomic ESBGK model exist, they can suffer from excessive noise, especially in low-Mach flows, and can be computationally unfeasible for transient flows. Alternatively, grid-based deterministic methods can be used. These methods do not suffer from statistical noise, and trivially allow for transient simulations. In this manuscript, we will introduce a deterministic method, known as a semi-Lagrangian method, for polyatomic ESBGK model.

A semi-Lagrangian method for the polyatomic ESBGK model

In the semi-Lagrangian framework[2], the kinetic equation is written in Lagrangian form,

$$\frac{\mathrm{d}f}{\mathrm{d}t} = \mathcal{Q}_{pESBGK} \tag{5}$$

$$\dot{x} = v. \tag{6}$$

We discretise space on a uniform grid with spacing Δx. Velocity space is truncated to $[-v_{max}, v_{max}]^3$ and uniformly discretised using grid spacing Δv. Due to the stiff nature of $\mathcal{Q}_{pESBGK}$ for low Knudsen numbers, we use an implicit first-order time integration routine for (5). Equation (6) is solved using the method of characteristics. If we denote $f_{i,j}^n$ as an approximation for $f(t^n, x_i, v_j)$, the full first-order scheme looks like

$$\tilde{f}_{ij}^n = f(t^n, x_i - v_j\Delta t, v_j) \tag{7}$$

$$f_{ij}^{n+1} = \tilde{f}_{ij}^n + \Delta t Q_{pESBGK}(f_{ij}^{n+1}). \tag{8}$$

Equation (7), requires interpolation of the function at the previous time step. This is performed using a bilinear or a bicubic interpolation routine. Equation (8), implies a nonlinear system solve since Q_{pESBGK}

nonlinearly depends on the temperature T_{rel}^{n+1}, mean velocity U^{n+1} and corrected tensor $\mathbb{T}^{n+1}$ (4). We extend the mathematical trick from [2, 4] for the ESBGK model to make the computation explicit. First, by multiplying (8) with $(1, v, \frac{|v|^2}{2})$ and then integrating with respect to v, we obtain that

$$\rho_i^{n+1} = \tilde{\rho}_i, \quad U_i^{n+1} = \tilde{U}_i, \quad T_{eq,i}^{n+1} = \tilde{T}_{eq,i}, \tag{9}$$

where the values with a tilde are the macroscopic quantities of $\tilde{f}_{ij}^n$. In a similar manner, by multiplying (8) by $v \otimes v$ and $I^{2/\delta}$, the corrected tensor and relative temperature can be obtained explicitly,

$$T_{int,i}^{n+1} = \left(\tilde{T}_{int,i} + \theta\, \tau_i^{n+1} \Delta t T_{eq,i}^{n+1}\right) / \left(1.0 + \theta\, \tau_i^{n+1} \Delta t\right) \tag{10}$$

$$\begin{aligned}\mathbb{T}^{n+1} = I_3 \Bigg[(1-\theta) \left((1-\nu) R_s\, T_{tr,i}^{n+1} + \nu_i^{n+1} R_s \tau_i^{n+1} \Delta t \Big((1-\nu) T_{tr,i}^{n+1} + \theta\, T_{eq,i}^{n+1} \Big) \right) + \theta R_s T_{eq,i}^{n+1} \Bigg] \\ + (1-\theta) \nu_i^{n+1} \left(\frac{\tilde{\Sigma}_i}{\rho_i^{n+1}} - U_i^{n+1} \otimes U_i^{n+1} \right),\end{aligned} \tag{11}$$

with

$$\tau_i^{n+1} = \frac{p^{n+1}}{\mu\,(1 - \nu + \theta\nu)}, \quad \nu_i^{n+1} = \frac{\nu}{1 + \Delta t \tau_i^{n+1}\,(1 - (1-\theta)\nu)}. \tag{12}$$

Now, the Gaussian inside (8) can be computed explicitly, and the equation can be trivially solved for f_{ij}^{n+1}. We thus have a scheme that is explicit in time, but has the stability properties of an implicit scheme. This first-order method presented here was extended to a second-order. We restrict ourselves to 2D simulations. To this end, we use a Chu-reduction[3][1] on the I variable and the third component of the microscopic velocity vector to drastically reduce the dimension of the equation.

Inflow boundary conditions

For the simulations below we require inflow and outflow boundary conditions. We assume we have a pressure and temperature known at the inlet, and only a pressure known at the outlet. We define a normal vector n pointing from the boundary inside the domain. Then, we impose a boundary condition only on the characteristics that enter the domain like so

$$\tilde{f}_{ij}^n = \begin{cases} f(t^n, x_i - v_j \Delta t, v_j), & v_j \cdot n < 0 \\ \mathcal{M}(\rho_w, U_w, T_w), & \text{else.} \end{cases} \tag{13}$$

We assume the flow entering the domain is in thermodynamic equilibrium where $\mathcal{M}(\rho_w, U_w, T_w)$ is a Maxwellian distribution with density, mean velocity and temperature determined by a boundary routine for the Euler equations[6].

Poiseuille flow test case

We test the numerical method and model on a Poiseuille flow between two infinitely long parallel plates[6]. We choose a channel length of 1mm and a channel width of 0.1mm. The gas is Hydrogen. We discretise the domain using a 400 by 40 Cartesian grid. The ambient temperature is set to 300K. We choose the pressure at the inlet and outlet to obtain a flow in continuum regime, slip flow regime and transition regime. We plot the velocity along the centreline of the channel using a second-order semi-Lagrangian scheme for the polyatomic ESBGK equation, an analytical result with first-order slip

boundary conditions for the Navier-Stokes equation, polyatomic DSMC and a numerical solution to the Navier-Stokes equation obtained with starccm software. The results are plotted in figure 1. As expected, the result for the polyatomic BGK equation is very close to the result for Navier-Stokes for the flow in continuum regime. As we increase the Knudsen number, we observe a discrepancy with the DSMC simulation, which remains reasonable given the model approximation.

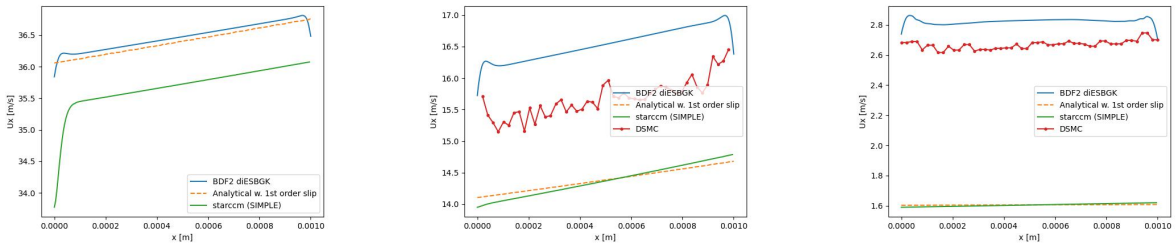

(a) $Kn = 6 \times 10^{-3}$ (b) $Kn = 6 \times 10^{-2}$ (c) $Kn = 6 \times 10^{-1}$

Figure 1: Velocity along the centreline of the channel.

Outlook

In the upcoming months, we intend to carry out additional Poiseuille flow simulations with faster flows, Fourier (heat transfer) simulations, and simulations with moving boundaries. Our intent is to both compare the polyatomic ESBGK model with polyatomic DSMC simulations, and to show the strengths and weaknesses of the semi-Lagrangian method.

Acknowledgments

The first author receives funding from the European Union's Framework Program for Research and Innovation HORIZON-MSCA-2021-DN-01 under the Marie Sklodowska-Curie Grant Agreement Project 101072546 – DATAHYKING.

References and citations

[1] Andries, P., Le Tallec, P., Perlat, J.-P., and Perthame, B. The Gaussian-BGK model of Boltzmann equation with small Prandtl number. *European Journal of Mechanics - B/Fluids 19*, 6 (Nov. 2000), 813–830.

[2] Boscarino, S., Cho, S. Y., Russo, G., and Yun, S.-B. A conservative semi-Lagrangian scheme for the ellipsoidal BGK model of the Boltzmann equation. *Journal of Scientific Computing 105*, 1 (Oct. 2025), 9.

[3] Chu, C. K. Kinetic-Theoretic Description of the Formation of a Shock Wave. *The Physics of Fluids 8*, 1 (Jan. 1965), 12–22.

[4] Filbet, F., and Jin, S. An Asymptotic Preserving Scheme for the ES-BGK Model of the Boltzmann Equation. *Journal of Scientific Computing 46*, 2 (Feb. 2011), 204–224.

[5] Holway, Jr., L. H. Kinetic Theory of Shock Structure Using an Ellipsoidal Distribution Function. In *Proceedings of the fourth international symposium on rarefied gas dynamics* (Toronto, Jan. 1965), vol. 1, p. 193. Conference Name: Rarefied Gas Dynamics, Volume 1 ADS Bibcode: 1965rgd1.conf..193H.

[6] Wang, M., and Li, Z. Simulations for gas flows in microgeometries using the direct simulation Monte Carlo method. *International Journal of Heat and Fluid Flow 25*, 6 (Dec. 2004), 975–985.

NEGF26-700556

ACTUATION OF ARTIFICIAL MICRO-MUSCLES USING A KNUDSEN MICROPUMP

Dingdong Zhang[1], Paul Oumaziz[2], Guillermo Lopez-Quesada[3], Marcos Rojas-Cárdenas[2], Stéphane Colin[2*]

[1] School of Mechanical and Electrical Engineering, Lanzhou University of Technology, Lanzhou, China
dingdongzhang@lut.edu.cn
[2] Univ Toulouse, IMT Mines Albi, INSA Toulouse, ISAE-SUPAERO, CNRS, ICA, Toulouse, France
paul.oumaziz@insa-toulouse.fr, marcos.rojas@insa-toulouse.fr, stephane.colin@insa-toulouse.fr
[3] Department of Thermal and Fluid Engineering, University Carlos III of Madrid, Spain
gulopezq@pa.uc3m.es

KEYWORDS

Microfluidics, rarefied gas, soft micro-actuation, thermally induced flow, transient response

ABSTRACT

Pneumatic artificial micro-muscles (PAμMs) offer large strain, low weight, and compliant actuation, making them attractive for microscale devices [1,2]. Emerging work has focused on negative-pressure actuation, which allows PAμMs to operate efficiently at small pressure differentials while enabling compact, safe, and lightweight designs [3–5]. This approach supports the development of fully integrated microsystems, in which compact pressure generation replaces external hardware, enabling autonomous soft actuators to be embedded in multifunctional platforms for mobility, manipulation, and adaptive structures.

Knudsen micropumps (KμPs) generate gas flow by thermal transpiration in rarefied regimes, without moving parts, and are compatible with microfabrication techniques [6,7]. Their performance depends strongly on microchannel geometry and architecture [8–10]. A configuration consisting of multiple parallel microchannels connected to a macrochannel enables scalable mass flowrate while maintaining structural simplicity [11]. Thus, integrating a KμP with a PAμM has the potential to create a compact, self-contained microsystem where thermal energy is converted into mechanical motion.

This work presents a preliminary theoretical investigation of a coupled microsystem in which a single-stage Knudsen pump, composed of n parallel microchannels connected to a macrochannel, actuates an artificial micro-muscle. Emphasis is placed on understanding how the number of parallel microchannels influences the system response, particularly the contraction dynamics. The system is operated with atmospheric outlet conditions; therefore, the inlet pressure of the KμP is approximately 100 kPa. Thermal-transpiration-driven flow creates a pressure drop inside the PAμM, resulting in its contraction. For the selected geometry, both the microchannel flow and the counterflow within the macrochannel are assumed to experience negligible viscous losses. Microchannels are cylindrical (radius r, length L); the macrochannel has radius R and length L. Air is used as the working gas. This architecture supports both rarefaction-induced pressure generation and sufficient volumetric flow to enable soft actuation.

Geometry Configuration of the Microsystem

The microsystem consists of *n* parallel microchannels connected to a single macrochannel, all having equal length. The pump inlet is connected to a deformable PAμM cavity with variable internal volume V_{in}, while a fixed dead volume V_s accounts for non-collapsible regions (Fig. 1).

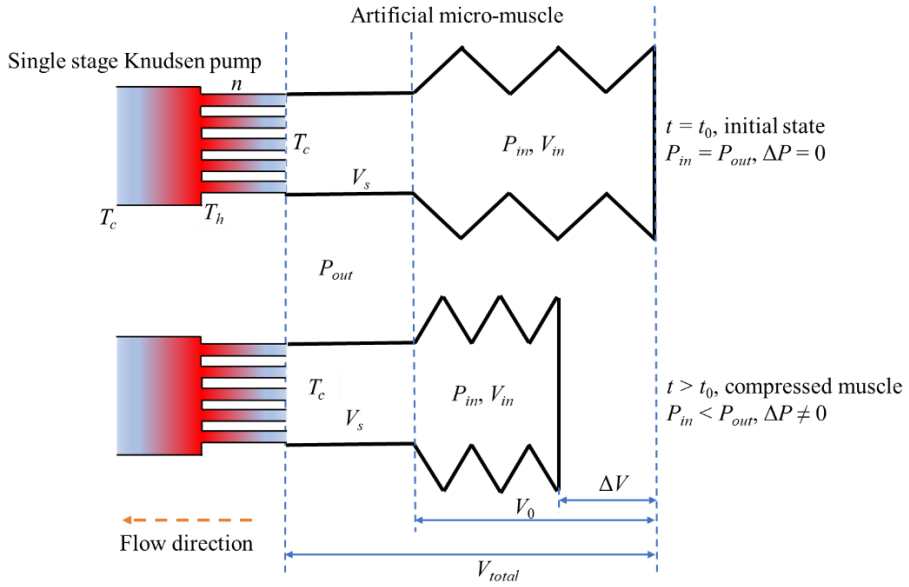

Figure 1 Schematic of the coupled microsystem showing parallel microchannels connected to a macrochannel, driving pressure reduction in a PAμM with dead volume.

Analytical Model

The system dynamics is governed by mass conservation and the ideal gas law:

$$\frac{dP}{dt} = -\frac{R_g T}{V(t)}\dot{m} \quad (1)$$

where $\dot{m}$ is the mass flowrate delivered by the Knudsen pump, and $V(t) = V_{in}(t) + V_s$.

The deformation of the PAμM is linked to the internal volume reduction, assuming axisymmetric contraction. The contraction ratio is defined as:

$$e(t) = \frac{\Delta V(t)}{V_0} \quad (2)$$

The coupled system—gas flow, pressure evolution, and cavity deformation—is solved numerically until steady state is reached.

Simulation Results

Characteristic Curves of the Knudsen Pump

Built on the kinetic model reported in [6,9], the characteristic curves are obtained by prescribing the inlet pressure P_i and sweeping the mass flowrate $\dot{m}$ between two limiting cases. The maximum mass flow rate, $\dot{m}_{\max}$, is computed under open-system conditions ($P_o = P_i$), while the maximum pressure difference, $\Delta P_{\max}$, is obtained under closed-system conditions ($\dot{m} = 0$). Accordingly, a set of mass flowrates $\dot{m} \in [0, \dot{m}_{\max}]$ is sampled. For each prescribed value of $\dot{m}$, the unified kinetic pressure-evolution equation is integrated once along the axial coordinate *z*, without nested iterations.

This yields the outlet pressure P_o and, consequently, the pressure difference $\Delta P = P_o - P_i$. The resulting pairs $(\dot{m}, \Delta P)$ define the characteristic curve of the Knudsen pump.

Figure 2 shows mass flowrate versus pressure difference for several values of n for a Knudsen pump characterized by $r = 5$ μm, $R = 100$ μm and $L = 50$ μm. The curves are linear with identical intercepts, demonstrating that (1) increasing n increases the mass flowrate (slope), and (2) the maximum pressure difference, $\Delta P_{\max}$, is independent of n.

This trend reflects thermal transpiration physics and macrochannel back-pressure constraints.

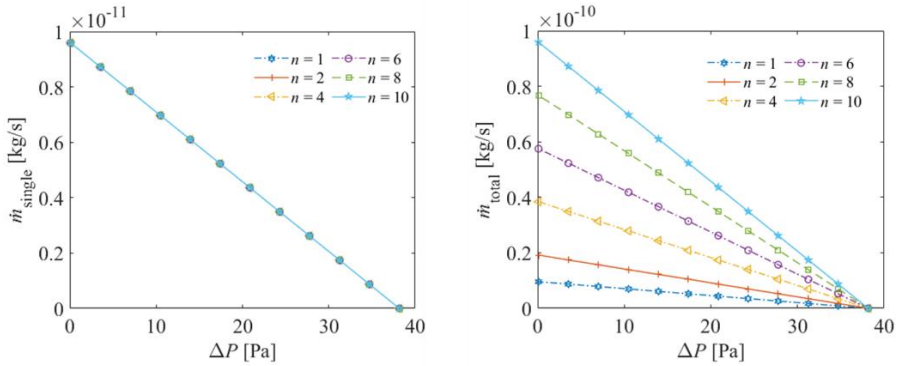

Figure 2 Simulated characteristic curves of Knudsen pump: mass flowrate versus pressure difference for different numbers of microchannels n. Left: flowrate through one of the parallel microtubes; right: total mass flow rate through all microtubes.

Transient Contraction of the Artificial Muscle

Experimental characterization of three-bellows mini-muscles (bellows length $L_{\text{mini}} = 3$ mm, bellows radius $r_{mini} = 4.44$ mm, membrane thickness $d = 0.57$ mm) revealed an approximately linear relationship between contraction ratio and pressure difference (Fig. 3). These mini-muscles share the same geometric configuration as the simulated micro-muscles (bellows length $L_{micro} = 254.56$ μm, bellows radius $r_{micro} = 360$ μm). This linear relationship is therefore adopted to model the response of the coupled system.

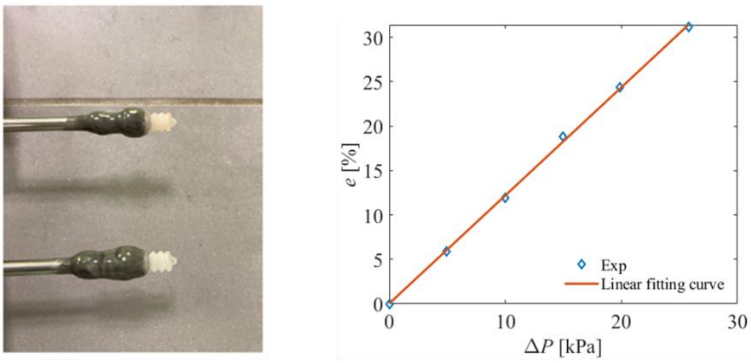

(a) (b)

Figure 3 (a) Test on mini-muscles actuated by negative pressure. (b) Relationship between contraction ratio and applied pressure difference, where blue diamonds denote experimental data and the red line represents the linear fitting curve.

Figure 4 shows the time evolution of contraction ratio e for different values of n. The final contraction ratio $e_{\max}$ is identical for all configurations, determined exclusively by $\Delta P_{\max}$ and initial cavity volume. Response time decreases significantly with increasing n, due to higher outflow rates.

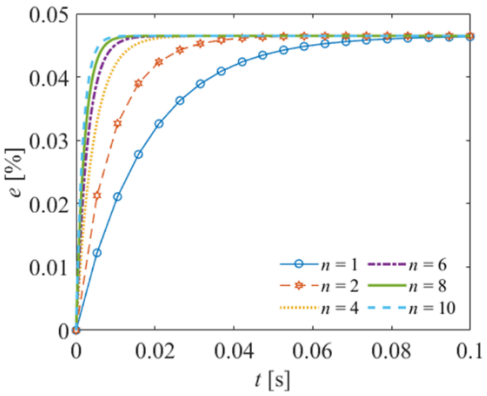

Figure 4 Transient contraction ratio versus time for various *n* values, showing identical saturation but reduced response times with increasing *n*.

Discussion

Channel parallelization in the Knudsen pump provides a straightforward means to increase mass flowrate without altering the maximum pressure difference. As a result, the final contraction amplitude of the artificial micro-muscle remains unchanged, but the time required to reach steady-state decreases significantly with increasing channel number. This highlights a useful design strategy: actuation speed could be tuned by actuating the appropriate number of microchannels with an independent local heating.

The coupled pneumatic–mechanical system behaves predictably due to the near-linear relation between pressure and contraction, enabling simplified modeling and design. However, performance remains sensitive to system parameters such as internal volume and geometric configuration.

Conclusions and Perspectives

This work demonstrates that coupling a Knudsen micropump with a soft artificial micro-muscle enables compact actuation driven by thermal energy. The key insight is that channel parallelization increases actuation speed while maintaining identical final contraction, offering an efficient route to improve dynamic performance.

Future efforts should focus on experimental validation, refinement of mechanical models, and evaluation of thermal management strategies. Exploring multi-stage architectures and system-level integration could further expand capability and support autonomous microscale robotic applications.

References and Citations

[1] Coutinho A, Park J H, Jamil B, Choi H R and Rodrigue H 2023 Hyperbaric Vacuum-Based Artificial Muscles for High-Performance Actuation *Advanced Intelligent Systems* **5** 2200090

[2] Joe S, Totaro M, Wang H and Beccai L 2021 Development of the Ultralight Hybrid Pneumatic Artificial Muscle: Modelling and optimization ed T Ranzani *PLoS ONE* **16** e0250325

[3] Zhang Z, Fan W, Chen G, Luo J, Lu Q and Wang H 2021 A 3D Printable Origami Vacuum Pneumatic Artificial Muscle with Fast and Powerful Motion *2021 IEEE 4th International Conference on Soft Robotics (RoboSoft)* 2021 IEEE 4th International Conference on Soft Robotics (RoboSoft) (New Haven, CT, USA: IEEE) pp 551–4

[4] Li S, Vogt D M, Rus D and Wood R J 2017 Fluid-driven origami-inspired artificial muscles *Proc. Natl. Acad. Sci. U.S.A.* **114** 13132–7

[5] Mendoza M J, Gollob S D, Lavado D, Koo B H B, Cruz S, Roche E T and Vela E A 2021 A Vacuum-Powered Artificial Muscle Designed for Infant Rehabilitation *Micromachines* **12** 971

[6] López Quesada G, Tatsios G, Valougeorgis D, Rojas-Cárdenas M, Baldas L, Barrot C and Colin S 2019 Design Guidelines for Thermally Driven Micropumps of Different Architectures Based on Target Applications via Kinetic Modeling and Simulations *Micromachines* **10** 249

[7] Wang X, Su T, Zhang W, Zhang Z and Zhang S 2020 Knudsen pumps: a review *Microsyst Nanoeng* **6** 26

[8] Ye J, Jiao X, Tang S, Shao J and Zhao Z 2021 Three dimensional channel effect on the flow characteristics and the performance of hydrogen Knudsen compressors *International Journal of Hydrogen Energy* **46** 18128–36

[9] López Quesada G, Tatsios G, Valougeorgis D, Rojas-Cárdenas M, Baldas L, Barrot C and Colin S 2020 Thermally driven pumps and diodes in multistage assemblies consisting of microchannels with converging, diverging and uniform rectangular cross sections *Microfluid Nanofluid* **24** 54

[10] Wang X, Zhang Z, Liu X, Hu P and Han D 2024 Effects of geometrical parameters on rarefied gas flows and Knudsen force in the system of triangular-rectangular beams with different temperatures *International Communications in Heat and Mass Transfer* **156** 107722

[11] Ajuda A, Silva G and Semiao V 2025 Performance Analysis of Multi-Capillary Knudsen Heat Pumps *Fluids* **10** 236

NEGF26-686557

ANOMALOUS NONEQUILIBRIUM EFFECTS IN SUPERSONIC RAREFIED FLOWS

Vladimir Aristov*[1], Timur Mordukhay[2]
[1] Federal Research Center "Computer Science and Control" of Russian Academy of Sciences
Vavilova str., 44, bld.2, Moscow, 119333, Russia
aristovvl@yandex.ru,
[2]Khristianovich Institute of Theoretical and Applied Mechanics of the Siberian Branch of Russian Academy of Sciences
Institutskaya Street 4/1, Novosibirsk, 630090, Russia
mordukhay@itam.nsc.ru

KEY WORDS

Kinetic theory, rarefied gas dynamics, Boltzmann equation, direct simulation Monte Carlo method, flow through a grid, transport processes.

ABSTRACT

This study of nonequilibrium flows featuring novel and diverse nonclassical effects continues our previous research [1] on a monatomic gas. Specifically, it was demonstrated that in these flows, the heat flux vector can oppose the direction predicted by Fourier's law, enabling anomalous heat transfer from cold to hot regions. Currently, we have performed a series of direct Monte Carlo simulations for a diatomic gas using the SMILE++ software system [2].

This problem models a supersonic flow passing through a grid composed of infinite cylindrical bars with a square cross-section. The centerlines of the bars are equidistant and coplanar. The analysis employs a two-dimensional plane formulation**.** The flow, directed from left to right with its velocity vector normal to the grid plane, is aligned such that one side of the square cross-section is perpendicular to the flow direction. The solution is assumed to be periodic over the grid's spatial period. To reduce computational cost, the solution domain is restricted to a half-period, with symmetry conditions applied at the upper and lower boundaries.

According to previous calculations for monatomic gases, nonequilibrium distributions behind high-permeability grids (with a permeability of 0.9 or higher) should exhibit anomalous heat transfer, characterized by the heat flux and the downstream temperature gradient sharing the same sign**.** In the present study, a supersonic equilibrium flow at Mach number M = 4 encounters a grid at a Knudsen number of Kn = 2 (defined based on the wire diameter of the grid). This interaction generates a nonequilibrium flow downstream of the high-permeability grid. Calculations for a diatomic gas confirm the presence of anomalous heat transfer within this supersonic nonequilibrium region. A field representing the parameter characterizing this effect is presented in Figure 1. Positive values of this parameter indicate a deviation from Fourier's law. The anomalous heat transfer is particularly pronounced near the symmetry plane at $y = 5$, as evidenced by the extensive red region corresponding to high positive parameter values.

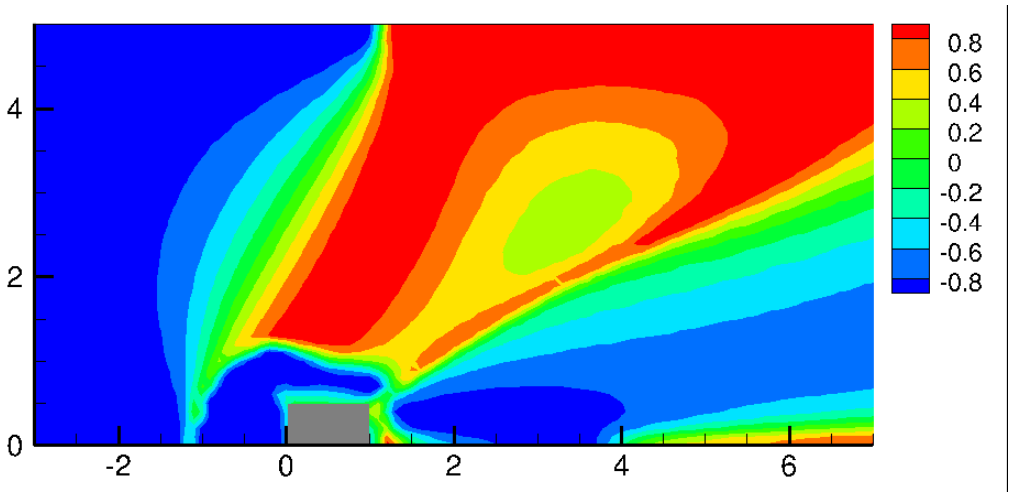

Figure 1: Field of cos(q, grad(T_{ov})), where T_{ov} and q are total (translational-rotational) temperature and heat flux respectively.

The main points of comparison is related to presentation of the temperature profiles in Figure 2, the heat flux profiles in Figure 3 and the density profile in Figure 4 behind the membrane (grid) and further downstream.

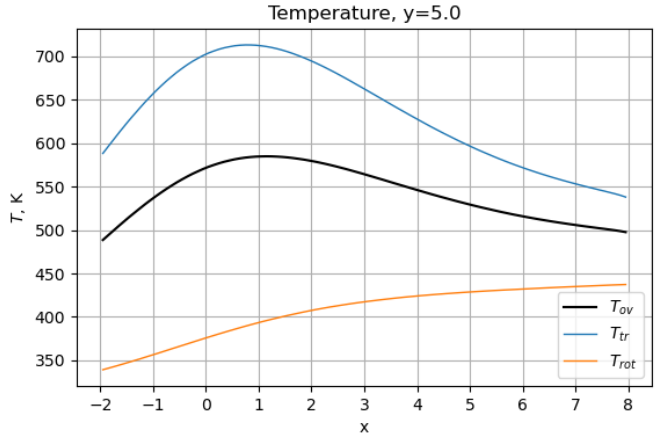

Figure 2: Profiles of the translational (*tr*), rotational (*rot*) and overall (*ov*) temperatures.

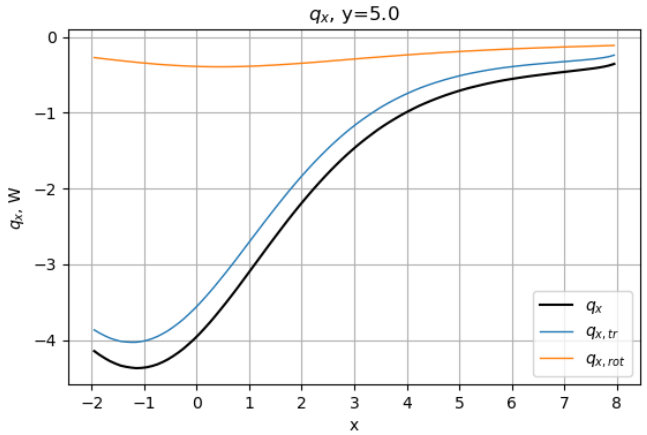

Figure 3: Profiles of the translational (*x*, *tr*), rotational (*x*, *rot*) and overall (*x*) *x*-component of the heat flux.

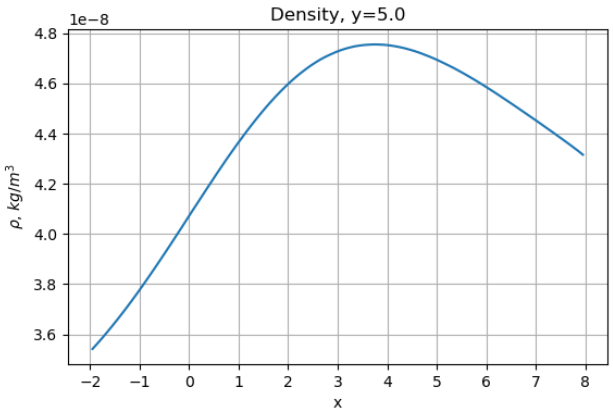

Figure 4: Profile of the gas density.

Several key properties can be observed in Figures 2-4. The profiles of macroscopic quantities along the *x*-coordinate are presented for the line $y = 5$. This line corresponds to the axis of symmetry between the grid rods in the cross-sectional plane. Notably, the overall temperature gradient and the total heat flux share the same sign. The membrane (grid) is positioned at $x = 0$. Downstream of the grid, the temperature initially rises due to the interaction between gas molecules and the grid molecules, and subsequently decreases further along the flow. The heat flux remains negative until it reaches zero at the equilibrium region downstream. The rotational temperature (T_{rot}) gradient and the heat flux ($q_{x,\,rot}$) exhibit classical spatial behavior, characterized by their identical signs.

Current theoretical and numerical research is being supplemented by experimental investigations of anomalous transport phenomena at Novosibirsk State University. Initial experimental results confirm, at minimum, the predicted behavior of nonequilibrium rotational states downstream of the grid.

Potential applications of the effects observed in numerical simulations are also discussed.

References and Citations

[1] Aristov V.V., Zabelok S.A., Frolova A.A. (2025). Nonclassical transport in nonequilibrium rarefied gas flows. *Uspekhi Fizicheskikh Nauk*, **195,** 276-293.

[2] Kashkovsky, A.V., Vashchenkov, P.V., Shevyrin, A.A. *et al.* Smile Family of Software Systems for the Direct Monte Carlo Simulations of Rarefied Gas Flows. *J Eng Phys Thermophy* (2026). https://doi.org/10.1007/s10891-026-03266-8

NEGF26-679210

COLD PLASMA-INDUCED LIQUID FLOW: WHAT IS THE ROLE OF ELECTROHYDRODYNAMIC PHENOMENA?

Eric Moreau, Lara Alomari, Fredric Dyson
eric.moreau@univ-poitiers.fr

KEY WORDS

Liquid flow, non-thermal plasma, electrical discharge, plasma jet, PIV measurements

ABSTRACT

The goal of this experimental study is to characterize the water flow induced by a DC discharge ignited between the water surface and a needle located a few millimeters above it. Firstly, we highlighted that two discharge regimes can be observed: a corona-like discharge with current from a few µA to a few dozen of µA, and a glow discharge with current of several mA. Secondly, particle image velocimetry (PIV) measurements allowed us to precisely characterize the liquid flow, that results in the formation of two symmetric and counter-rotating vortices. In the case of a normal-glow discharge, it seems that the water flow is due to two electrohydrodynamic (EHD) forces: a surface force due to the repulsion of charges at the surface, and an upward force in the liquid due to the migration of opposite charges from the bulk of the liquid. Moreover, we highlighted that the velocity (of a few cm/s) and the topology of the flow depend on the voltage polarity, the water conductivity and on its surface tension. In the case of a corona-like discharge, there is still a significant water flow, even for current of a few µA. In this case, a third phenomenon can be at the origin of the liquid flow: the shear stress due to the ionic wind induced in the air, between the needle tip and the water surface.

INTRODUCTION

The interactions between a cold plasma and a liquid are very complex but very important to study due to various applications in agriculture, biology, nanomaterial synthesis, and water treatment. However, because of the slow diffusion of reactive species in the liquid phase, the flow induced by the discharge in the liquid can play a key role in transporting species into the solution [1]. Therefore, it is imperative to analyse the flow in detail to control the plasma-liquid processes effectively. In this context, for a few years, we have been investigating the liquid flow induced by three different types of cold plasmas in contact with water. The first investigated cold plasma is a helium plasma jet [2]. The second one is a dielectric barrier discharge ignited between a needle placed a few millimetres above the liquid and a grounded electrode below the vessel containing the water [3]. The third type of discharge we have been investigating for a few years is ignited by applying a DC voltage between a needle placed a few millimetres above the surface of the liquid to be treated and a grounded electrode immersed inside the liquid [4]. In this presentation, we will focus on the flow induced by DC discharges, but we will also present a few results with AC discharges and with an helium plasma jet. In the case of a DC discharge, two main different discharge regimes can be observed when the voltage is increased: a corona regime (maximum currents of a few dozen µA) and a glow one (current up to 10 mA).

During the oral presentation, we will firstly present the flow induced in the water in the case of a glow discharge (current set at 3.8 mA). We will highlight that the high voltage polarity plays a key role in the flow topology. Moreover, we will see that the flow velocity decreases when the water conductivity and the superficial tension increase. Secondly, we will discuss the liquid flow in the case of a corona-like discharge (mean current between 7 µA and 30 µA). We will show that the flow is faster when the voltage is positive and when the gap between the needle tip and the water surface is increased because the surface forces are stronger.

LIQUID FLOW INDUCED BY A GLOW DISCHARGE

As indicated above, the discharge current was fixed at 3.8 mA for all the PIV measurements, and we investigated the effect of the voltage polarity, the water conductivity and the superficial tension of the water (the electrical power equals a few W). The water conductivity has been increased in adding KCl in water, and the superficial tension has been decreased in adding ethanol. Figure 1 presents the time-averaged velocity fields for the two polarities and three different values of water conductivity. The background color indicates the velocity modulus and the black arrows the flow direction (they are not the velocity vectors as their lengths are constant). The discharge impact is at x = 0, and the water surface around y = 21 mm. Several remarks can be made. First, two main phenomena take place: an upward flow, located directly beneath the point of discharge impact on the liquid surface, and a tangential flow along the water surface, originating from the point of discharge impact on the liquid surface and propagating towards the edges of the vessel. Consequently, this results in the formation of two counter-rotating vortices in the upper half of the liquid, which in fact correspond to a cross-sectional view of a single three-dimensional structure: a toroidal vortex ring. Secondly, we can see that the flow intensity decreases as the liquid conductivity increases. For instance, for the positive polarity, the liquid velocity reaches 60 mm/s for $\sigma = 3.4$ µS/cm when it is limited to about 35 mm/s for $\sigma = 800$ µS/cm. Third, the water flow velocity is slightly higher with the positive discharge than with the negative one.

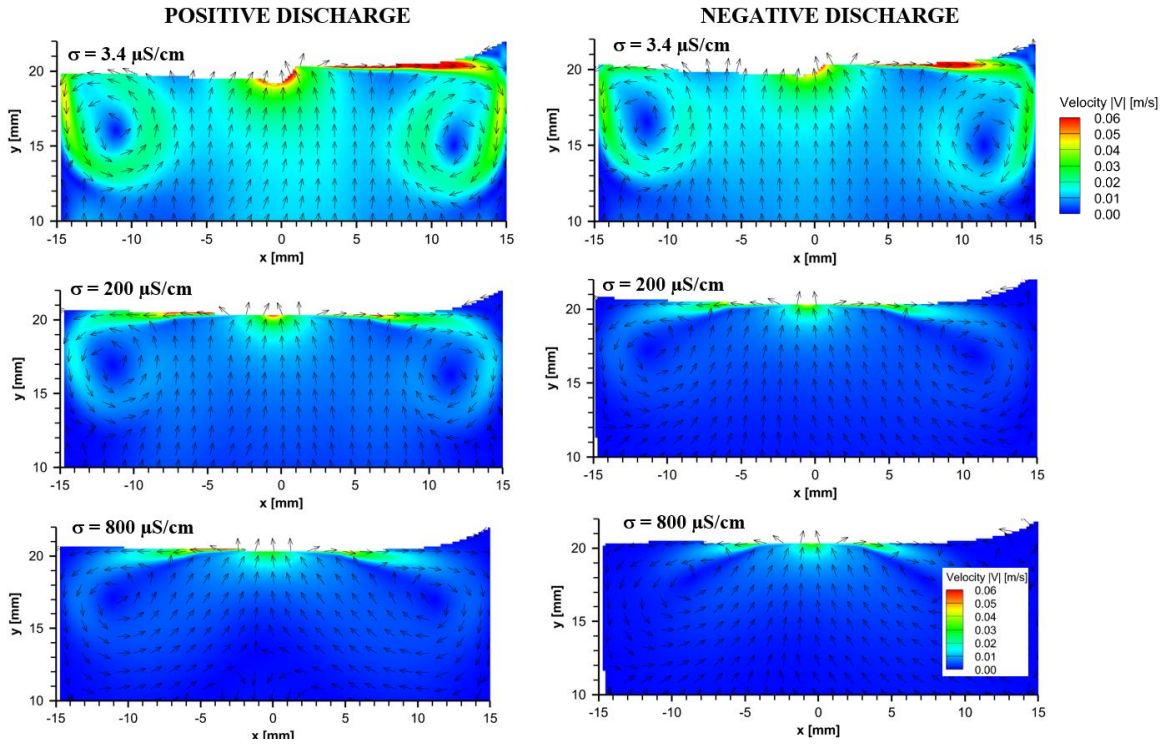

Figure 1: Time-averaged velocity fields of the discharge-induced water flow for the two polarities and three different values of water conductivity.

Figure 3 shows some instantaneous velocity fields at different times, the discharge being switched on at t = 0. A few tens of milliseconds after the discharge is applied, the onset of a flow can be observed at the water surface. At t = 109 ms, this flow is visible from x = 0 to x = 10 mm. At t = 376 ms, it reaches the walls of the 300-mm-wide glass container. Two counter-rotating vortices then appear. From about 1.5 second, the flow becomes rather steady.

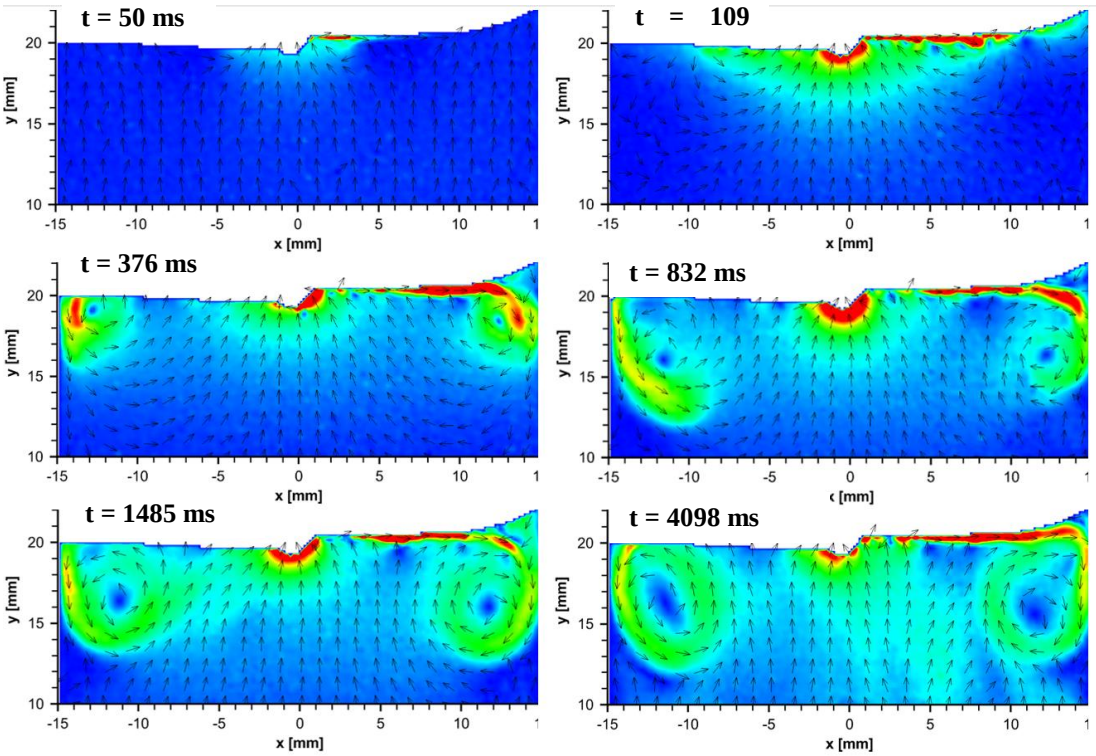

Figure 2: Instantaneous velocity fields at different times (t = 50 ms, 109 ms, 376 ms, 832 ms, 1485 ms and 4098 ms), the discharge is switched on at t = 0. The discharge is a positive glow.

LIQUID FLOW INDUCED BY A CORONA DISCHARGE

A second campaign of PIV measurements has been carried out with corona discharges. In this case, the electrical power is on the order of 100 mW. The liquid is deionized water with an electrical conductivity of about 3 µS/cm. Figure 3 shows the velocity fields of the water flow for the two polarities, when the gap equals 4 mm and the current 30 µA. First, we can see that the flow induced by the positive corona discharge is more intense than the one produced by the negative one. Furthermore, in the case of the positive corona discharge, the flow velocity is significant as it reaches 60 mm/s at the water surface and 30 mm/s in the vortices.

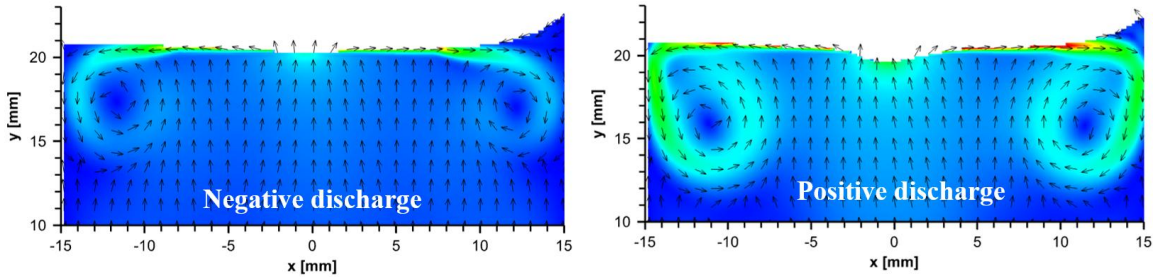

Figure 3: Time-averaged velocity fields of the discharge-induced water flow for the two polarities (corona discharge, current equal to 30 µA).

CONCLUSION

This study aimed to characterize the water flow induced by a DC discharge ignited between the water surface and a needle located a few millimeters above it. Particle image velocimetry (PIV) measurements allowed us to characterize the flow induced in water due to the DC electrical discharge. These measurements have revealed a flow characterized by the formation of two counter-rotating vortices, resulting from two electrohydrodynamic forces: a surface force due to the repulsion of charges at the surface, and an upward force in the liquid due to the migration of opposite charges from the bulk of the liquid. Moreover, in the case of a corona-like discharge, a third phenomenon can be at the origin of the liquid flow: the shear stress due to the ionic wind induced between the needle tip and the water surface. Fortunately, all these phenomena will be precisely explained and discussed during the oral presentation.

Acknowledgments

This project has received financial support from the CNRS through the MITI interdisciplinary programs through its exploratory research program. This work was supported by ANR-11-LABX-0017-01 and ANR-18-EUR-0010.

References and Citations

[1] Alomari L et al. Needle-to-liquid DC discharge in atmospheric air: electrical characteristics and impact on potassium halide solutions", *Plasma Chemistry and Plasma Processing*, 45, 677–705, 2025.
[2] Dyson F et al. Plasma jet impacting the surface of a liquid: electrical analysis and EHD flows, *Proc. ISEHD 2025, June 2025, Sevilla, Spain.*
[3] Alomari L et al. Time evolution of the EHD water flow produced by an AC dielectric barrier discharge ignited above its surface, *Proc. ISEHD 2025, June 2025, Sevilla, Spain.*
[4] Moreau E et al. Water flow induced by a DC corona discharge above the water surface, J. Phys D: Applied Physics, to be published.

NEGF26-701929

Consistent lattice Boltzmann modeling of low-speed isothermal flows in the slip flow regime: A unified slip velocity boundary scheme

Goncalo Silva[1]
[1] gnsilva@uevora.pt

KEY WORDS

Lattice Boltzmann Methods, Two-Relaxation-Time Collision, Wall Slip Velocity, Rarefied Gas Flows

Introduction

In microgeometries, gaseous flows frequently enter rarefied regimes, with the first stage corresponding to the *slip-flow regime* [1]. Under typical microfluidic operating conditions, low Mach and Reynolds numbers justify linearization and the bulk flow is described by the incompressible Stokes equations,

$$\nabla \cdot \mathbf{u} = 0, \qquad \nabla p - \mathbf{F} = \mu \nabla^2 \mathbf{u}, \tag{1}$$

where $\mathbf{u}$ denotes the velocity, p the pressure, $\mathbf{F}$ an external force, and μ the dynamic viscosity. At a solid wall with unit normal and tangential vectors $(\mathbf{n}, \mathbf{t})$ and prescribed wall velocity $\mathbf{U}_w$, the boundary conditions consist of impermeability,

$$(\mathbf{u} - \mathbf{U}_w) \cdot \mathbf{n} = 0, \tag{2}$$

and a second-order tangential slip condition,

$$(\mathbf{u} - \mathbf{U}_w) \cdot \mathbf{t} = -\mathcal{C}_1 \frac{\lambda}{\mu} \mathbf{n} \cdot \boldsymbol{\tau} \cdot \mathbf{t} - \mathcal{C}_2 \frac{\lambda^2}{\mu} \mathbf{n} \cdot \partial_n \boldsymbol{\tau} \cdot \mathbf{t}, \tag{3}$$

where λ is the mean free path, $\boldsymbol{\tau}$ is the viscous stress tensor with $\tau_{ij} = \mu(\partial_j u_i + \partial_i u_j)$, $\partial_n = \mathbf{n} \cdot \nabla$, and $\mathcal{C}_1, \mathcal{C}_2$ are the first- and second-order slip coefficients.
The present contribution investigates the *lattice Boltzmann method* (LBM) modeling [2] of the Stokes problem (1) subject to the slip boundary conditions (2)–(3). Although the LBM has long been regarded as a natural computational fluid dynamics (CFD) framework for modeling wall-slip phenomena, it is now well established that numerical artefacts may severely contaminate the solution if the slip boundary scheme is not properly designed [3, 4]. Existing approaches often rely on ad hoc calibration procedures, whose validity is restricted to very specific configurations and which do not provide a general or robust modeling framework. The objective of this work is therefore twofold: first, to identify the main difficulties underlying the LBM transcription of slip velocity boundary conditions, and second, to propose a consistent unified boundary scheme capable of accurately enforcing the physical slip model on arbitrarily discretized walls.

Lattice Boltzmann formulation

The lattice Boltzmann method [2] describes the space–time evolution of discrete distribution functions ("populations") $f_q(\boldsymbol{x}, t)$ associated with a discrete velocity set $\{\boldsymbol{c}_q\}$. Their evolution proceeds through successive streaming and collision steps on a uniform Cartesian lattice. Here, a two–relaxation–time (TRT) collision model is adopted, in which the symmetric and anti–symmetric components of the populations relax independently at rates τ^+ and τ^-. In lattice units, the LBM-TRT evolution equation reads:

$$\underbrace{f_q(\boldsymbol{x}+\boldsymbol{c}_q, t+1)}_{\text{streaming}} = \underbrace{f_q(\boldsymbol{x}, t) - \frac{1}{\tau^+}\left(f_q^+ - e_q^+\right) - \frac{1}{\tau^-}\left(f_q^- - e_q^-\right) + S_q}_{\text{collision}}. \tag{4}$$

Above, $f_q^\pm = (f_q \pm f_{\bar{q}})/2$ with $\boldsymbol{c}_{\bar{q}} = -\boldsymbol{c}_q$, $e_q^\pm$ denote the corresponding equilibrium components, and S_q accounts for the forcing term $\mathbf{F}$. The macroscopic fields are recovered from velocity moments as

$$c_s^{-2} p = \sum_q f_q, \qquad \boldsymbol{j} = \sum_q \boldsymbol{c}_q f_q + \tfrac{1}{2}\mathbf{F}, \tag{5}$$

where $\boldsymbol{j} = \rho_0 \mathbf{u}$ and $\rho_0 \in \mathbb{R}^+$ is an arbitrary reference density. The lattice sound speed c_s is a free parameter constrained by stability requirements. The kinematic viscosity $\nu = \mu/\rho_0$ is set by τ^+ as $\nu = \frac{1}{3}(\tau^+ - \frac{1}{2})$, while τ^- controls numerical characteristics without affecting the hydrodynamic limit.

Boundary condition closure relation and operation principles

A central difficulty in LBM concerns the prescription of *boundary conditions* [2]: the unknown incoming populations $f_q(\boldsymbol{x}_b)$ at boundary nodes must be reconstructed so that the intended macroscopic boundary behavior is recovered. This task is complicated by the fact that lattice nodes generally do not coincide with the physical wall location, so that the boundary condition must be enforced in a Taylor-series sense around the boundary node. Considering a lattice node at $\boldsymbol{x}_b$ and a wall at $\boldsymbol{x}_w$, a second-order Taylor expansion of the slip boundary condition projected onto lattice space reads [3]:

$$\begin{aligned} & j_q(\boldsymbol{x}_b) + \alpha_q^+ \partial_q j_q(\boldsymbol{x}_b) + \alpha_q^- \partial_q^2 j_q(\boldsymbol{x}_b) = j_q^{\text{wall}}(\boldsymbol{x}_w), \\ & \alpha_q^+ = \delta_q + \mathcal{C}_1 \lambda_q, \qquad \alpha_q^- = \tfrac{\delta_q^2}{2} + \mathcal{C}_1 \lambda_q \delta_q + \mathcal{C}_2 \lambda_q^2, \\ & \delta_q = \frac{(\boldsymbol{x}_w - \boldsymbol{x}_b)\cdot \boldsymbol{c}_q}{\|\boldsymbol{c}_q\|^2}, \qquad \lambda_q = \frac{\lambda}{\boldsymbol{c}_q \cdot \mathbf{n}}. \end{aligned} \tag{6}$$

Equation (6) provides the fundamental consistency condition to recover the second-order slip model with parabolic accuracy and may be implemented through either a *link-wise* or a *wet-node* strategy (Fig. 1).

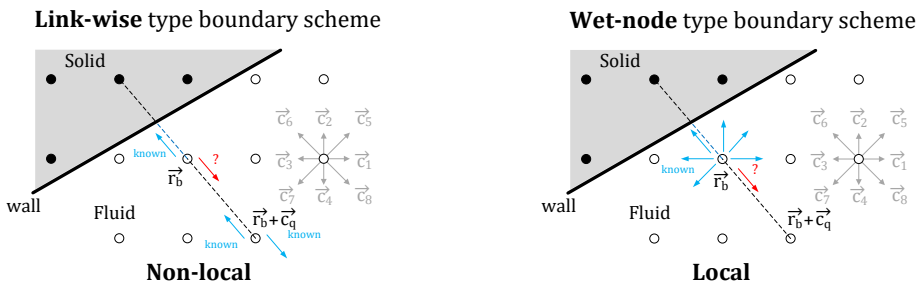

Figure 1: LBM modeling of solid walls in a D2Q9 lattice: link-wise vs. wet-node operation principles.

In the link-wise approach, the unknown incoming population associated with a given lattice direction is reconstructed independently along each boundary link, using only known populations belonging to the same link, possibly involving neighboring nodes. This directional construction leads to simple and robust formulations, exemplified by the bounce-back (BB) and multireflection (MR) schemes [3], but offers limited flexibility to prescribe boundary conditions with different mathematical character in the normal and tangential directions, as required by Eqs. (2)–(3).
In contrast, the wet-node approach reconstructs all unknown boundary populations simultaneously at the boundary node from local equilibrium and non-equilibrium moments associated with different lattice directions. This node-based reconstruction naturally accommodates directional information and derivative constraints, allowing an independent enforcement of impermeability and tangential slip conditions. Representative examples of this philosophy include the local second-order boundary (LSOB) scheme [4] and the non-equilibrium bounce-back (NEBB) method. This advantage comes at the price of a more elaborate formulation and implementation, and of a delicate consistency requirement to ensure that the reconstructed boundary solution remains fully compatible with the discrete bulk dynamics.
The present work proposes a unified boundary strategy based on the observation that the slip velocity condition is of Robin type and may be decomposed into Dirichlet and Neumann contributions as follows:

$$j_n - j_n^{\text{wall}} = 0, \tag{7a}$$

$$\underbrace{j_t - j_t^{\text{wall}} = 0}_{\text{Dirichlet-type condition}} + \underbrace{\left(-\mathcal{C}_1\,\lambda\left(\frac{\partial j_t}{\partial n} + \frac{\partial j_n}{\partial t}\right) - \mathcal{C}_2\,\lambda^2\,\frac{\partial}{\partial n}\left(\frac{\partial j_t}{\partial n} + \frac{\partial j_n}{\partial t}\right)\right)}_{\text{Neumann-type condition}}. \tag{7b}$$

Translated into the LBM algorithm, Eqs. (7) are implemented by combining a multireflection [3] link-wise scheme for the Dirichlet contribution with a wet-node LSOB [4] correction for the Neumann contribution. This hybrid strategy exploits the complementary strengths of both approaches, yielding a Robin type boundary scheme that is consistent with the second-order slip model and parabolically accurate.

Numerical validation

The performance of the proposed unified slip boundary strategy was assessed in several channel-like configurations, from which two classical benchmark cases are reported here.
First, a second–order slip Poiseuille flow in an inclined two–dimensional channel, not aligned with the underlying lattice, is considered, as shown in Fig. 2. This configuration provides a stringent test of boundary consistency in the presence of geometric non-alignment. The proposed parabolically accurate slip boundary conditions enable the LBM to recover the analytical parabolic velocity profile with machine precision over all mesh refinements.

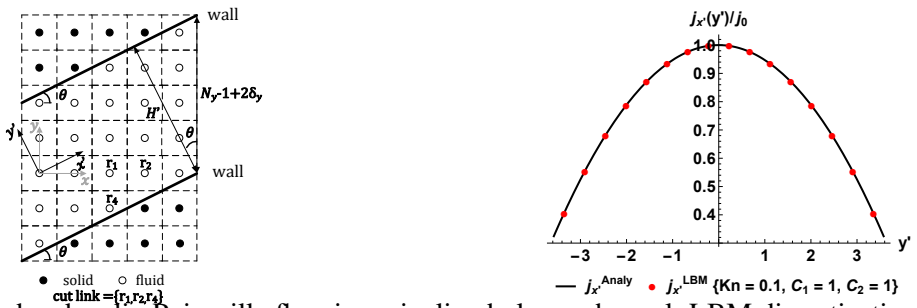

Figure 2: Second-order slip Poiseuille flow in an inclined planar channel: LBM discretization (left) and velocity profiles (right), illustrating machine-precision agreement with the analytical solution.

Second, a second-order slip circular Couette flow in a curved two–dimensional channel is considered, as shown in Fig. 3. For a very coarse grid resolution of only 10 lattice nodes across the gap, the proposed scheme reproduces the analytical solution with mean relative errors below 10^{-4} over the full range of parameters considered, demonstrating its ability to accurately resolve curved boundaries and strong geometric non-alignment within a parabolically consistent slip formulation.

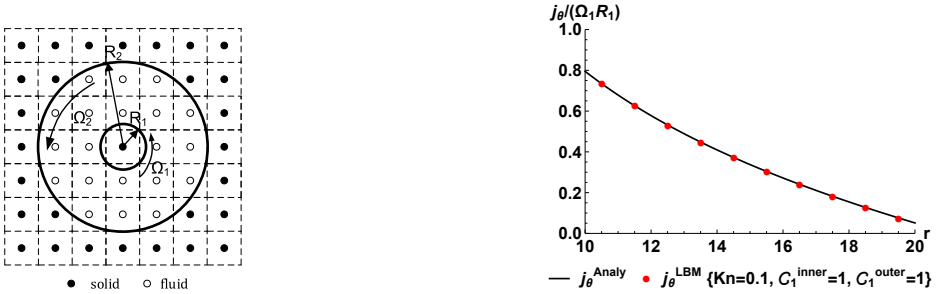

Figure 3: Second-order slip Couette flow in a curved channel: LBM discretization (left) and velocity profiles (right), obtained with only 10 lattice nodes across the annular gap, with average relative error below 10^{-4}.

Conclusions

In this work, a unified boundary scheme is proposed to address the long-standing consistency issues arising in lattice Boltzmann modeling of slip flows on non–mesh-aligned and curved boundaries. By combining link-wise and wet-node operation principles within a single closure framework, the method enables an accurate enforcement of impermeability and second-order tangential slip with parabolic accuracy on arbitrarily discretized walls.

Numerical tests in inclined planar and curved channel configurations confirm the performance of the proposed formulation. The inclined Poiseuille benchmark is recovered with machine precision despite the non–mesh-aligned geometry, while the circular Couette case achieves errors below 10^{-4} even with only 10 lattice nodes across the gap, providing a clear validation of the feasibility and high accuracy of the proposed scheme for lattice Boltzmann simulations of slip flows in complex geometries.

Acknowledgements

This work was supported by national funds through FCT – Fundação para a Ciência e a Tecnologia, I.P., under project 2023.13693.PEX, entitled “Novel unified multiscale predictive tool for gaseous microfluidic flows in Knudsen Pumps”.

References and citations

[1] Karniadakis, G. E., Beskok, A., & Aluru, N. (2005). *Microflows and Nanoflows: Fundamentals and Simulation*. Springer, New York. https://doi.org/10.1007/978-0-387-28676-1

[2] Krüger, T., Kusumaatmaja, H., Kuzmin, A., Shardt, O., Silva, G., & Viggen, E. M. (2017). *The Lattice Boltzmann Method: Principles and Practice*. Springer International Publishing, Cham. https://doi.org/10.1007/978-3-319-44649-3

[3] Silva, G., & Semiao, V. (2017). Consistent lattice Boltzmann modeling of low-speed isothermal flows at finite Knudsen numbers in slip-flow regime: Application to plane boundaries. *Physical Review E*, 96(1), 013311. https://doi.org/10.1103/PhysRevE.96.013311

[4] Silva, G., & Ginzburg, I. (2022). Slip velocity boundary conditions for the lattice Boltzmann modeling of microchannel flows. *International Journal for Numerical Methods in Fluids*, 94(12), 2104–2136. https://doi.org/10.1002/fld.5138

NEGF26-679624

CORRECTING NAVIER-STOKES-FOURIER SYSTEM FOR RAREFIED FLOWS WITH NON-LINEAR SUPER-STENCIL

Yijun Wang*[1], Patrick Jenny[1]
[1]Institute of Fluid Dynamics, ETH Zurich, Sonneggstrasse 3, CH-8092, Zurich
yijwang@student.ethz.ch, jenny@ifd.mavt.ethz.ch

KEY WORDS

Navier-Stokes-Fourier, model correction, closure problem, non-linear super-stencil

ABSTRACT

Conventional particle-based methods for simulating rarefied gas flows, such as Direct Simulation Monte Carlo (DSMC), become prohibitively expensive in the near-continuum regime due to high collision rates. Despite their accuracy across a broad range of Knudsen numbers, generalizing continuum models such as the Navier-Stokes-Fourier (NSF) system become an appealing alternative given the much less computational cost and the deterministic nature, especially in transitional flows where the Knudsen number drastically varies.

Considerable efforts have been made to extend continuum models to broader flow regimes. There exist two approaches. First, the NSF system is directly extended by adding higher order derivatives and tensors. But no new variables and equations are introduced. For instance, the super-/Burnett equations keep higher order terms in the Chapman-Enskog expansion. The other approach is moment equations, of which the most famous example is the Grad's 13-moment equations. However, both approaches require truncations to close their equations and have achieved limited practical success. This is also known as the closure problem in generalizing continuum models.

In the era of data, we address the closure problem with the aid of machine learning. Following the Chapman–Enskog expansion, the conservation laws are decomposed into the NSF component

* Corresponding author

and a residual term encompassing all higher order terms as

$$\frac{\partial \rho}{\partial t} + \frac{\partial \rho u_j}{\partial x_j} = 0, \tag{1}$$

$$\frac{\partial \rho u_i}{\partial t} + \frac{\partial \rho u_i u_j}{\partial x_j} + \frac{\partial p}{\partial x_i} + \frac{\partial \sigma_{ij}^{(1)}}{\partial x_j} = \left\{ -\frac{\partial \sigma_{ij}^{(2)}}{\partial x_j} + \cdots \right\} = \mathcal{F}_i, \tag{2}$$

$$\frac{\partial \rho E}{\partial t} + \frac{\partial \rho E u_j}{\partial x_j} + \frac{\partial \left(p u_j\right)}{\partial x_j} + \frac{\partial \left(u_i \sigma_{ij}^{(1)} + q_j^{(1)}\right)}{\partial x_j} = \left\{ -\frac{\partial \left(u_i \sigma_{ij}^{(2)} + q_j^{(2)}\right)}{\partial x_j} + \cdots \right\} = \mathcal{G}, \tag{3}$$

or more concisely,

$$\mathcal{M}(\boldsymbol{U}) = \boldsymbol{S}_{\text{res}} \tag{4}$$

with $\boldsymbol{U} = (\rho, \rho u_i, \rho E)^T$ the vector of conserved variable and $\boldsymbol{S}_{\text{res}} = (0, \mathcal{F}_i, \mathcal{G})$ the model residuals. For a given point $\boldsymbol{x}^*$ in space, we assume there exists an unambiguous mapping from the local flow pattern around that point to the model residuals and thus the model can be closed. To quantify the local flow pattern, we propose the non-linear super-stencil (NLSS) [1] as shown in Fig. 1, which is a compact stencil aligned with the velocity $\boldsymbol{u}^*$. The width of the stencil is proportional to the local mean free path length λ^*. The local flow quantities are transformed and normalized in order to exploit the Galilean invariance of the NSF equations. These quantities are

$$\hat{\rho} = \frac{\rho}{\rho^*},\ \hat{T} = \frac{T}{T^*},\ \hat{\boldsymbol{u}} = \frac{\boldsymbol{R}^T(\boldsymbol{u} - \boldsymbol{u}^*)}{c^*},\ \hat{\boldsymbol{\sigma}}^{(1)} = \frac{\boldsymbol{R}^T \boldsymbol{\sigma}^{(1)} \boldsymbol{R}}{\rho^* c^{*2}} \text{ and } \hat{\boldsymbol{q}}^{(1)} = \frac{\boldsymbol{R}^T \boldsymbol{q}^{(1)}}{\rho^* c^{*3}}, \tag{5}$$

where $\boldsymbol{R}$ is the rotational matrix to align the local stencil coordinates with $\boldsymbol{u}^*$ and c^* is the speed of sound.

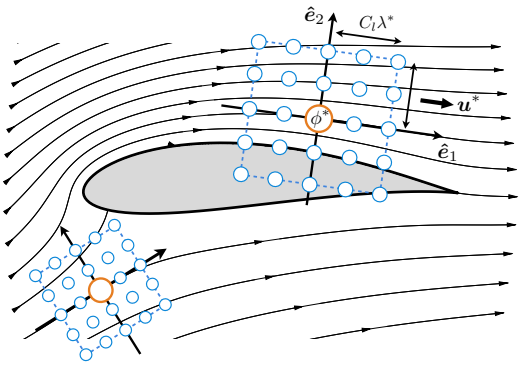

$$\hat{\boldsymbol{x}}\,(I, J) = C_l\lambda^* \left(\frac{I}{n_1}\hat{\boldsymbol{e}}_1 + \frac{J}{n_2}\hat{\boldsymbol{e}}_2 \right)$$

for $I, J \in \{-n_1, \ldots, n_1\} \times \{-n_2, \ldots, n_2\}$

Figure 1: Illustration of the non-linear super-stencil. The orange circles are stencil centers where the flow quantities are denoted with superscript *. The local coordinates of the stencil points are given the equations on the right.

RESULTS

We demonstrate the NLSS framework on planar channel flow shown in Fig.2. For the wall boundary conditions, a second neural network is trained to predict velocity and temperature

slips. After training on a limited dataset spanning a range of only Mach and Knudsen numbers with fixed wall temperatures $T_w = 273$ K, the NSF+NLSS system accurately predicts macroscopic flow behavior and wall slips in unseen conditions. Fig. presents two flow conditions that are outside the training dataset and compares the results against DSMC.

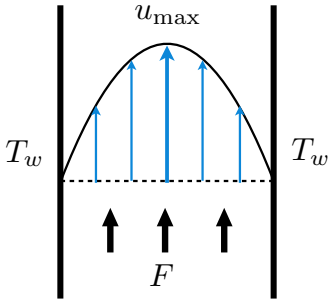

$$\mathrm{Ma} = \frac{u_{\max}}{\bar{c}_w}$$

$$\mathrm{Kn} = \frac{\lambda_0}{h}$$

$$\lambda_0 = \frac{k}{\sqrt{2}\pi d^2 R \rho_0}$$

$$F = \frac{8\mu u_{\max}}{\rho_0 h^2}$$

Figure 2: Planar channel flow: the flow is driven by a constant external force F. ρ_0 denotes the constant initial density.

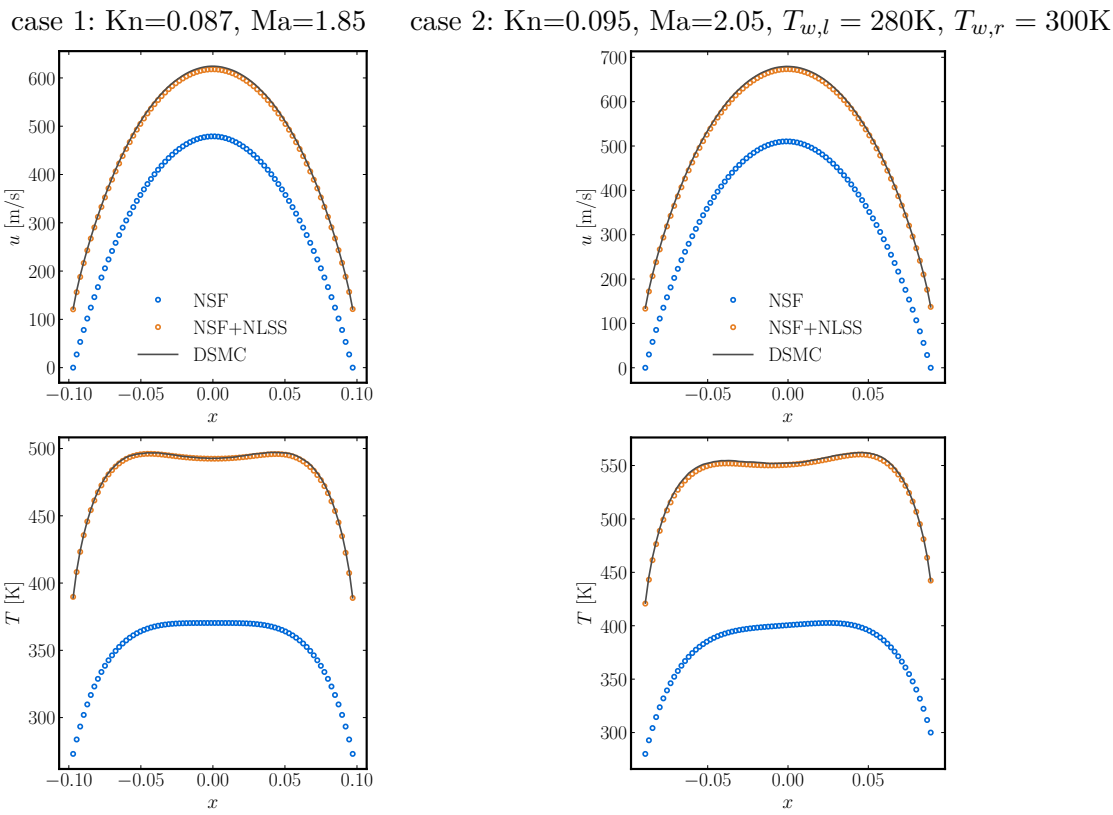

Figure 3: Results are drastically improved with NSF+NLSS compared agains DSMC.

REFERENCES

[1] Luther, J., & Jenny, P. (2025). Non-Linear Super-Stencils for turbulence model corrections. Communication Physics 8 (1), 233.

NEGF26-685492

DSMC evaluation of the thermophoretic force on micron-sized particles in rarefied gas conditions with Hermite boundary domain truncation.

R.R.L. Reinartz[1,2*], G. Di Staso[1,2], R.P.J. Kunnen[1], F. Toschi[1] and H.J.H. Clercx[1]
[1]*Fluids and Flows, Department of Applied Physics and Science Education, Eindhoven University of Technology, P.O. Box 513, 5600MB Eindhoven, The Netherlands*
[2]*Flow Matters Consultancy BV, Groene Loper 5, 5612 AE, Eindhoven, The Netherlands*
r.r.l.reinartz@tue.nl, gds@flow-matters.com, r.p.j.kunnen@tue.nl, f.toschi@tue.nl, h.j.h.clercx@tue.nl

KEY WORDS

Thermophoresis, Direct Simulation Monte Carlo, Hermite polynomial expansion, surrogate boundaries.

INTRODUCTION

The thermophoretic force may be an effective mechanism to control the dynamics of micron-sized particles in high-tech mechanical systems under low pressure conditions [1]. This force occurs when a particle is placed within a temperature gradient, typically opposite to this temperature gradient. Theoretical expressions for the thermophoretic force for spherical particles in the continuum and free molecular limit have been obtained by Epstein [2] and Waldmann et al. [3], respectively. For the transition regime interpolation functions were introduced by Talbot et al. [4]. These functions, based on limited experimental data, recover the correct continuum and free molecular limits for the thermophoretic force. Beresnev et al. [5] proposed numerical solutions based on more reliable kinetic model equations. Young [6] performed a review of existing methods to solve the Boltzmann equation to obtain the thermophoretic force, including one based on the Grad's 13 moment equations (G13). To improve the G13 results, a Millikan-type interpolation factor was included to give an approximate analytical expression for the thermophoretic force for all Knudsen numbers [6]. More recently, advances have been made by regularizing the G13 moment equations, known as the R13 equations [7], which are more accurate in the transition regime. Padrino et al. [8] applied R13 equations to study the thermophoretic force on spherical particles. Most of these methods are only valid for a limited rarefaction range and/or for small temperature gradients. In this research, we want to create a complete picture of the thermophoretic force in the transition regime and free molecular regime, including a large variety of gas and particle properties, that goes beyond the limitations of the literature results.

METHODOLOGY

We measure the thermophoretic force on a micron-sized particle using an in-house developed Direct Simulation Monte Carlo (DSMC) code based on the work of Bird [9]. A particle is placed in a Fourier setup, with two plates at a distance L from each other, at a temperature of T_1 and T_2, respectively, creating a temperature gradient. The two plates are separated by argon gas which is modeled with the variable hard-sphere (VHS) model. Changing the particle size, gas pressure, and temperature gradient, we evaluated the force in the transition regime. The Knudsen number $Kn_R = \lambda/R$, with λ the mean free

* Corresponding author

path of the gas and R the radius of the particle is in the range $0.1 < Kn_R < 20$. The thermophoretic force is obtained by particle-surface interaction using a raytracing collision method [11]. The force exerted by the gas on the particle surface, evaluated through momentum exchange between the gas molecules and the particle, is compared with analytical expressions [4, 6] and numerical results [5]. Fig.1 shows the results obtained for spherical particles with different accommodation coefficients: fully diffuse, specular or adiabatic. We consider two cases, one with $\nabla T = 100K/m$ and $Kn_L = 0.01$, and one with $\nabla T = 300K/m$ and $Kn_L = 0.05$, with $Kn_L = \lambda/L$.

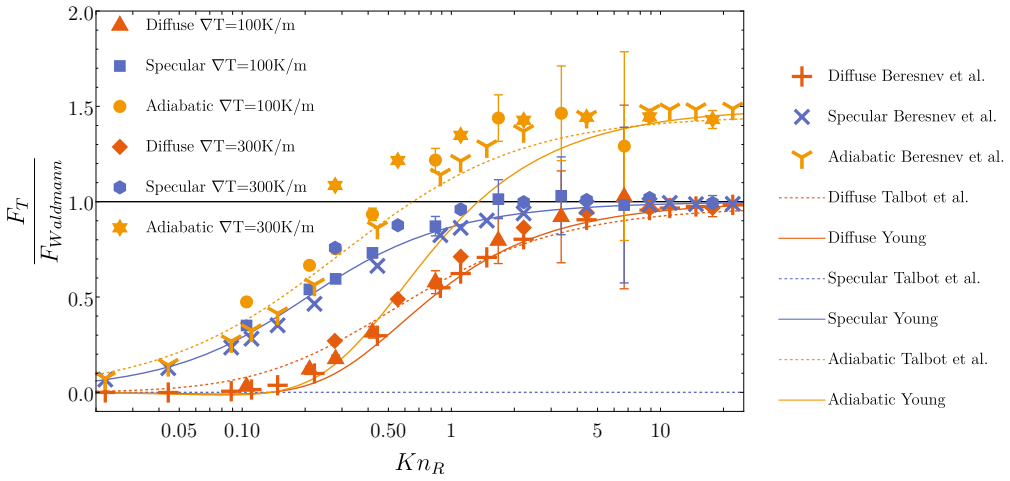

Figure 1: Thermophoretic force F_T normalized by the free molecular thermophoretic force as found by Waldmann [3], as function of the Knudsen number Kn_R for a diffuse (red), specular (blue) and adiabatic (yellow) spherical particle for two different temperature gradients, $\nabla T = 100K/m$ (upward triangle, square and circle) and $\nabla T = 300K/m$ (circle, hexagon and star). The error bars represent twice the standard deviation of the mean (around 5.4×10^5 samples are used). For a part of the data, these error bars fall within the symbols. Beresnev's results [5] for a diffuse, specular and adiabatic particle are shown by the cross shaped symbols. The analytical expressions for the thermophoretic force as obtained by Talbot [4] and Young [6] are shown in dashed and solid lines.

RESULTS AND ALTERNATIVE APPROACH

The results for the diffuse interaction show the best agreement with Beresnev for $\nabla T = 100K/m$, although the DSMC results give slightly higher forces in the transition regime, and are in satisfactory agreement with Talbot and Young. For specular interaction, we see similar agreement between our results and those of Beresnev and Young, while Talbot predicts zero force for this case. For the adiabatic interaction, our results agree with Beresnev, although the difference in the force obtained in the range $0.1 < Kn_R < 1$ is slightly larger than for diffuse and specular interaction. Talbot's equation is in line with our DSMC results, while Young's expression deviates considerably. For $\nabla T = 300K/m$ we see a deviation for $0.25 < Kn_R < 2$ for all three surface interactions, which is probably caused by non-linear rarefaction effects. The DSMC results for all three surface interactions have a large standard deviation in the force for $Kn_R \gtrsim 2$. This is caused by the particle size becoming very small and hence a large reduction in gas-surface collisions, decreasing the amount of cumulated statistics. Given this uncertainty we want to reduce the standard deviation of the obtained force without significantly increasing the calculation time. When this is achieved, large parameter sweeps over shape, gas-surface interaction models, and particle conductivity become possible.
A possible strategy to reduce the standard deviation is by reducing the computational time spent on the fluid region far away from the particle. Our proposal is illustrated in Figure 2. A particle only influences

the flow and temperature field in its vicinity, which we call the inner region. Outside this region, the outer region, these fields are almost undisturbed. At the boundary between the inner and outer region - the surrogate boundary - DSMC molecules are injected by sampling from the local velocity distribution that represents the local undisturbed field of the Fourier problem. For rarefied conditions, a simple Maxwellian boundary conditions will not suffice as this is not representative for the local velocity distribution. Therefore, we implement special boundary conditions based on Grad's Hermite polynomial expansion of the molecular velocity distribution function $f(\boldsymbol{x}, \boldsymbol{\xi}, t)$, which is a function of position $\boldsymbol{x}$, molecular velocity $\boldsymbol{\xi}$ and time t. The use of the Hermite polynomial expansion as introduced by Grad [12] allows writing the distribution function as an infinite series of orthogonal Hermite polynomials $H_i^{(n)}(\boldsymbol{\xi})$, where n is the order of the Hermite polynomial, in terms of the molecular velocity $\boldsymbol{\xi}$ as:

$$f(\boldsymbol{x}, \boldsymbol{\xi}, t) = f^{(0)}(\boldsymbol{x}, \boldsymbol{\xi}, t) \sum_{n=0}^{\infty} \sum_{i=1}^{3} \frac{1}{n!} \mathrm{a}_i^{(n)}(\boldsymbol{x}, t) H_i^{(n)}(\boldsymbol{\xi}), \tag{1}$$

where $f^{(0)}$ is the local Maxwellian distribution, $\mathrm{a}_i^{(n)}(\boldsymbol{x}, t)$ are the expansion coefficients and where the notation introduced by Grad [13] is used. The coefficients are calculated as:

$$\mathrm{a}_i^{(n)}(\boldsymbol{x}, t) = \int f(\boldsymbol{x}, \boldsymbol{\xi}, t) H_i^{(n)}(\boldsymbol{\xi}) d\boldsymbol{\xi}. \tag{2}$$

The polynomial expansion is truncated at order N to obtain an approximation $f^{(N)}(\boldsymbol{x}, \boldsymbol{\xi}, t)$. The coefficients are obtained by sampling the n^{th}-order moments of a 1D version of the Fourier problem in DSMC. At the surrogate boundary, DSMC molecules are injected with their velocity sampled from $f^{(N)}(\boldsymbol{x}, \boldsymbol{\xi}, t)$ using a modified version of the acceptance-rejection method introduced by Garcia et al. [14].

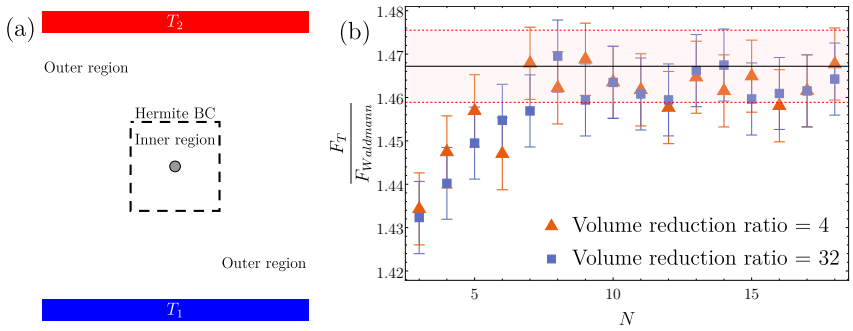

Figure 2: (a) A 2D sketch of the setup with the reduced domain extent where we will apply the Hermite based boundary condition. (b) Thermophoretic force on a particle as function of the order N of the Hermite expansion used as a boundary condition for a volume reduction ratio of four and 32, indicated by the red triangle and blue square, respectively. The black line with red shaded area is the results of the full size simulation reference case.

This method is applied to the thermophoretic force simulation of a particle. A typical result is shown in Figure 2b. This particular case entails an adiabatic particle with $Kn_R = 8.8$, placed in a Fourier problem setup with $Kn_L = 0.05$ and $\nabla T = 300K/m$. Two domain reductions have been applied: one with a factor four in the gradient direction and one with a factor eight in the gradient direction and a factor two in the other two directions, contributing to a total factor 32 in simulation volume reduction. The simulation time for these configurations decreases by a factor 5.8 and 51, respectively. This reduction is more than the volume reduction, which is a result of the negligible overhead that these boundary conditions create and the non-linear scaling for large simulation size. We show the normalized force and its standard deviation as function of the order N of the expansion, with $3 \leq N \leq 18$. The force originally obtained by the full Fourier setup is indicated by the black line and its standard deviation by the red shaded area.

Satisfactory results are obtained for $N \geq 7$, as the forces obtained are within the error margin of the reference case. This shows that we can effectively use these Hermite expanded boundary conditions to obtain the thermophoretic force at reduced computational cost.

CONCLUSION

In conclusion, we have shown that we can accurately obtain the thermophoretic force on a spherical particle in the transition and free-molecular regime with particle-resolved DSMC simulations. We have also shown that we can effectively speed-up the simulation time by up-to a factor 51 with the usage of Hermite expanded boundary conditions. This allows for simulating the thermophoretic force for a large variety of gas and particle properties that are relevant to the high-tech manufacturing community.

Acknowledgements

This research is co-financed by Holland High Tech with PPP allowance for research and development in the Dutch top sector of High-Tech Systems and Materials. We are grateful for our collaboration with and financial support of VDL Enabling Technologies Group. We especially wish to express deep gratitude to the late Dr. Dmitri Shestakov, who played an important role in the conceptualization and methodology of this research, and a crucial role in funding acquisition.

References and citations

[1] Shestakov, D., Cooijmans, W., Kalra, A., Reinartz, R.R.L., & Clercx, H.J.H. (2021). Modelling sub-micron particle trajectories. *Mikroniek*, **6**, pp. 12-14.
[2] Epstein, P. S. (1929). Zur theorie des radiometers. *Zeitschrift für Physik*, **54(7)**, pp. 537-563.
[3] Waldmann, L., & Schmitt, K. H. (1966). Thermophoresis and diffusiophoresis of aerosols. *Aerosol science*, **137**, pp. 137-162.
[4] Talbot, L., Cheng, R., Schefer, R., & Willis, D. (1980). Thermophoresis of particles in a heated boundary layer. *Journal of Fluid Mechanics*, **101(4)**, pp. 737-758.
[5] Beresnev, S., & Chernyak, V. (1995). Thermophoresis of a spherical in a rarefied gas: Numberical analysis based on the model kinetic equations. *Physics of Fluids*, **7(7)**, pp. 1743-1756.
[6] Young, J. B. (2011). Thermophoresis of a spherical particle: reassessment, clarification, and new analysis. *Aerosol Science and Technology*, **45(8)**, pp. 927-948.
[7] Struchtrup, H., & Torrilhon, M. (2003). Regularization of Grad's 13 moment equations: Derivation and linear analysis. *Physics of Fluids*, **15(9)**, pp. 2668-2680.
[8] Padrino, J. C., Sprittles, J. E., & Lockerby, D. A. (2019). Thermophoresis of a spherical particle: modelling through moment-based, macroscopic transport equations. *Journal of Fluid Mechanics*, **862**, 312-347.
[9] Bird, G. A. (1994). Molecular gas dynamics and the direct simulation of gas flows. *Molecular gas dynamics and the direct simulation of gas flows*.
[10] Gallis, M. A., Torczynski, J. R., & Rader, D. J. (2001). An approach for simulating the transport of spherical particles in a rarefied gas flow via the direct simulation Monte Carlo method. *Physics of Fluids*, **13(11)**, pp. 3482-3492.
[11] Livi, C., Di Staso, G., Clercx, H. J., & Toschi, F. (2022). Drag and lift coefficients of ellipsoidal particles under rarefied flow conditions. *Physical Review E*, **105(1)**, 015306.
[12] Grad, H. (1949). On the kinetic theory of rarefied gases. *Communications on Pure and Applied mathematics*, **2(4)**, pp. 331-407.
[13] Grad, H. (1949). Note on N-dimensional hermite polynomials. *Communications on Pure and Applied Mathematics*, **2(4)**, pp. 325-330.
[14] Garcia, A. L., & Alder, B. J. (1998). Generation of the Chapman–Enskog distribution. *Journal of Computational Physics*, **140(1)**, pp. 66-70.

NEGF26-679627

DESIGN AND MODELLING OF KNUDSEN MICROPUMPS FABRICATED VIA ADVANCED LASER MANUFACTURING

Thanasis Basdanis*[1], Phassawat Leelaburanathanakul[1], Thierry Camps[2], Marcos Rojas Cardenas[1], Christine Barrot[1], Lucien Baldas[1], Jürgen J. Brandner [3], Stéphane Colin[1]

[1] Univ Toulouse, CNRS, IMT Mines Albi, INSA Toulouse, ISAE-SUPAERO, ICA, 3 rue Caroline Aigle, Toulouse
basdanis@insa-toulouse.fr, leelabur@insa-toulouse.fr, marcos.rojas@insa-toulouse.fr, christine.barrot@insa-toulouse.fr, lucien.baldas@insa-toulouse.fr, stephane.colin@insa-toulouse.fr
[2]CNRS, LAAS, 7 Avenue du Colonel Roche, Toulouse, F-31400, France, France
camps@laas.fr
[3]Institute of Microstructure Technology (IMT), Karlsruhe Institute of Technology, 76344 Eggenstein-Leopoldshafen, Germany
juergen.brandner@kit.edu

KEY WORDS

Microfluidics, Knudsen pump, Heat transfer, Rarefied gas flows, Thermal transpiration

ABSTRACT

Knudsen pumps are promising candidates for gas pumping in a variety of scientific and industrial applications involving MEMS devices for hydrogen transfer, gas chromatography, aerosol sampling, heat pumps, biomedical systems and sensors etc. These pumps exploit the phenomenon of thermal transpiration, where gas under rarefied conditions flows along a channel due to temperature gradient. This enables gas transport without moving parts, resulting in vibration-free operation, an important feature for miniaturized applications [1].

For applications operating at atmospheric pressure, creating optimal rarefied conditions requires submicron-diameter channels, which is technically challenging. Only a few Knudsen pump prototypes have been reported in the literature, most of which are fabricated using Deep Reactive Ion Etching (DRIE) [2], wet etching [3], or porous materials [4]. DRIE enables the fabrication of channels with dimensions down to 1 μm, but with low aspect ratios (length/diameter ≈ 20) which impose constraints on thermal management. Porous materials contain natural defects that can restrict gas flow and reduce efficiency.

In this work, two Knudsen pumps for over- and sub-atmospheric applications were modeled and designed, taking into consideration the manufacturing capabilities of advanced laser fabrication techniques based on Bessel beams [5] and Selective Laser-Induced Etching (SLE) [6]. Bessel beams enables fabrication of high length-to-radius ratio (>100) nanochannels with diameters down to few nanometers and high writing speeds up to 1000 channels per second. SLE enables the fabrication of precise 3D structures and channels with length-to-radius ratios greater than 50 and diameters down to 3 μm.

* Corresponding author

Design

The proposed Knudsen pumps were designed within a 2×2 cm² footprint, ensuring effective thermal management and structural stability. Figure 1 shows a 3D CAD model of the Knudsen pump, illustrating the glass plate (500 µm thick for Bessel beam fabrication and 100 µm thick for SLE fabrication) with through-wafer micro- or nano-channels and integrated heaters on top, as well as the 500 µm thick silicon-based heat sink with micro-pillars on top and 80 µm diameter through-wafer openings. The 1×1 cm² central region is covered by channels, while the surrounding area is reserved for heater and heat sink connections. In the active 1 × 1 cm² region, 600 nm diameter nanochannels (for Bessel beam fabrication) and 3 µm diameter microchannels (for SLE fabrication), etched through the glass thickness, are arranged in a hexagonal pattern with a 20 µm spacing. This configuration results in approximately 300,000 channels.

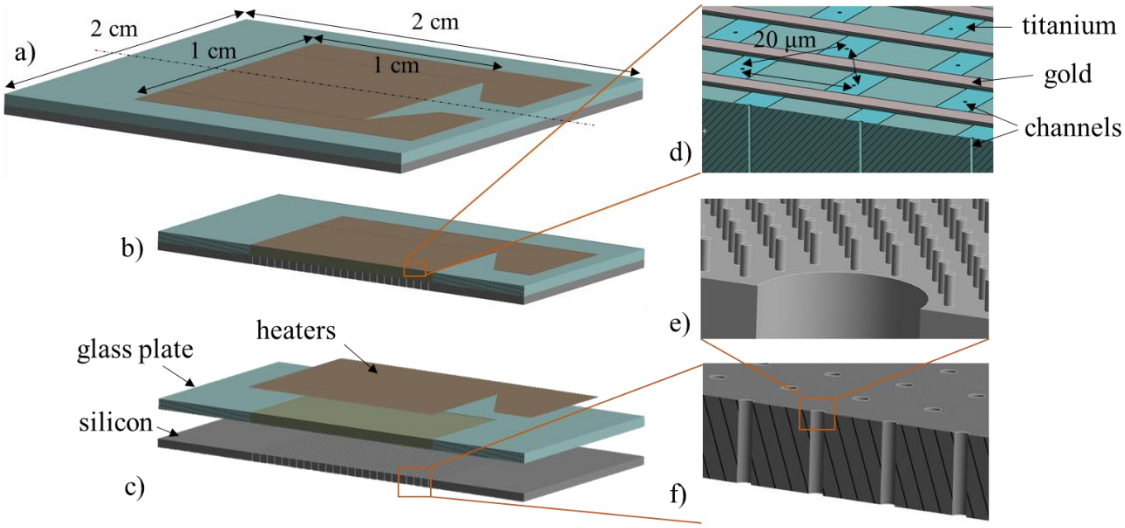

Figure 1: Knudsen pump design: a) complete design, b) half-section view, c) heaters, glass plate and silicon heat sink layers, d) magnified view of the heaters and channels, e) magnified view of the silicon pillars and f) magnified view of the silicon wafer with 80 µm diameter openings.

Gas flow modelling

To optimize the Knudsen pump architecture in terms of channel dimensions and operating pressures, the thermal transpiration flow through a single circular channel was modeled using kinetic theory. Assuming a large length-to-radius ratio (>50), the mass flow rate $\dot{m}$ and pressure distribution $P(z)$ along the channel $z \in [0, L]$ were computed based on the infinite capillary theory. The governing eq. (1)

$$\frac{dP(z)}{dz} = -\frac{v_0(z)}{\pi R^3 G_P(\delta)}\dot{m} + \frac{P(z)G_T(\delta)}{T(z)G_P(\delta)}\frac{dT(z)}{dz}, \quad (1)$$

where $v_0(z)$, R and $T(z)$ are the most probable speed, radius and temperature distribution, respectively, incorporates the Poiseuille G_P and thermal creep G_T flow coefficients, obtained from the linearized Shakhov kinetic model under diffuse boundary conditions [7]. The gas rarefaction parameter, defined as

$$\delta(z) = \frac{P(z)R}{\mu(z)v_0(z)} \quad (2)$$

characterizes the flow regime, where the dynamic viscosity $\mu(z)$ depends on temperature. Numerical solutions of eq. (1) allow computation of either mass flow or outlet pressure for given inlet conditions and temperature gradients. Parametric studies with nitrogen gas identified $R = 0.3$ µm as the optimal channel radius at atmospheric pressure, and 21 kPa as the optimal operating pressure for $R = 0.15$ µm, to get the maximum pressure difference. For practical applications, the flow characteristics of a single channel are often insufficient. Therefore, pump designs incorporate multiple parallel channels and stages to increase the total mass flow rate and pressure difference, respectively.

Heat transfer modelling

To optimize the temperature gradient across the glass thickness, corresponding to the channel length, heat transfer simulations were performed in ANSYS Mechanical, considering the placement, dimensions, and materials of heaters and heat sinks. Larger temperature differences enhance mass flow rate and pressure difference in thermal transpiration. Materials with lower thermal conductivity produce larger temperature gradients, supporting the choice of glass for channel fabrication. Heaters are applied to one side of the glass, while heat sinks efficiently dissipate heat from the opposite side. Thin gold-titanium layers enable Joule heating, and silicon heat sinks provide high thermal conductivity, mechanical stability, and compatibility with glass for bonding. Silicon pillars around each channel maximize temperature gradients while allowing gas flow, refining the thermal design of the pump.

Fig. 2 shows the results of heat transfer simulations of the designs presented in Fig. 1. They demonstrate that integrating heaters and heat sinks around each of the 300,000 channels produces: a) an average ΔT close to 47 °C for the Bessel beam design when 10 W of heating power is applied, and b) an average ΔT of about 20 °C for the SLE design when 20 W of heating power is applied, while maintaining a maximum temperature on the top side of the glass below 110 °C. The smaller ΔT in the case of SLE is due to the significantly thinner glass compared to the case of Bessel beams. However, the simulations indicate that increasing the channel density, i.e., packing the channels closer together, can enhance ΔT. These results confirm the effectiveness of the proposed thermal management strategy, enabling high-performance and compact Knudsen pump operation.

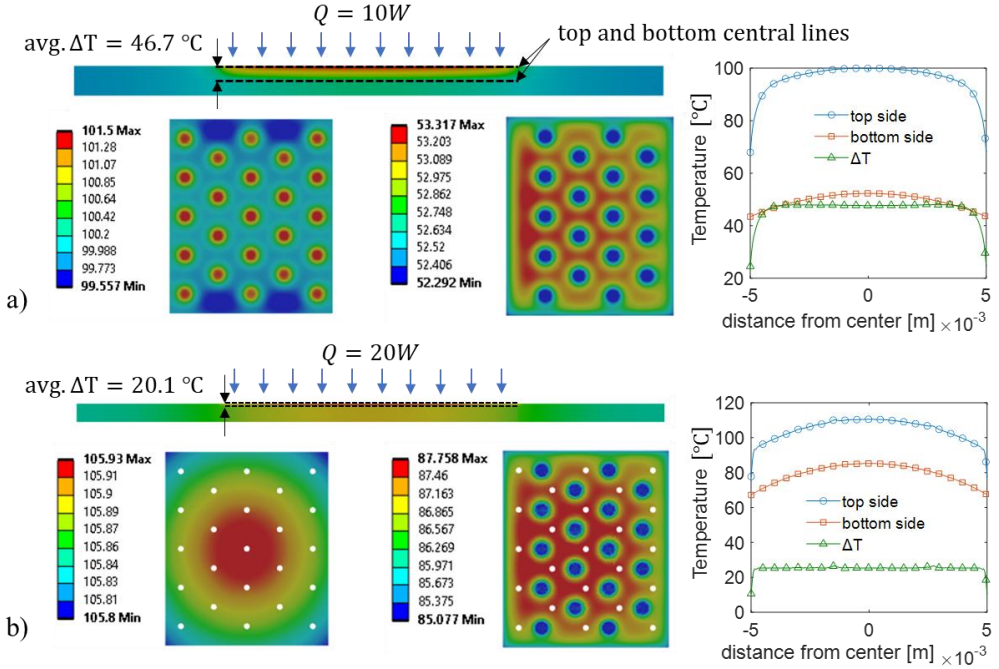

Figure 2: Thermal simulations results of the a) Bessel beams pump and b) SLE pump, showing the cross-sectional view, detailed views of the glass top beneath the heaters (on the left) and the glass bottom above the pillars (on the right), as well as the temperatures along the central line on the top and bottom glass surfaces and the corresponding ΔT graph on the right).

Performance study

In both Knudsen pump designs, the temperature gradients vary across channel positions, even under uniform heat flux on the top surface. Channels experiencing higher ΔT generate larger mass flow rates and pressure differences, while channels with lower ΔT can induce reverse flow. To model this behavior, an iterative scheme was developed for single-stage pumps, calculating the total mass flow and pressure difference by accounting for the individual temperature differences of each channel. A key finding is that using the average ΔT across all channels provides results in excellent agreement with simulations that apply different ΔT values for each channel. For the Bessel beam design with 300,000 channels, an average ΔT close to 47 °C yields a maximum mass flow of 3.5×10^{-10} kg/s and a pressure difference

of 1575 Pa. For the SLE design, the average ΔT of about 20 °C produces 2.46×10^{-8} kg/s and 72 Pa. For both pumps, atmospheric conditions were applied as initial conditions. Using upstream and downstream volumes of 86 mL, the maximum ΔP is reached within 3 hours with the Bessel beam pump and within 5 seconds with the SLE pump. The algorithm has also been extended to multi-stage pumps, enabling realistic simulation of gas flow through parallel channels and multiple stages. Fig. 3 presents the characteristic curves of the single-stage pumps for their optimal conditions (100 kPa for Bessel beams and 21 kPa for SLE) and at higher pressures, as well as the results of the multistage configuration of these two pumps at atmospheric inlet conditions. With 150 stages in the Bessel beams pump and 1800 stages in the SLE pump, pressure differences of 2 bar and 1 bar were achieved, respectively. It is observed that the Bessel beams pump can provide much higher pressure differences while the SLE pump much higher mass flows. Therefore, the most suitable pump can be selected based on the intended application.

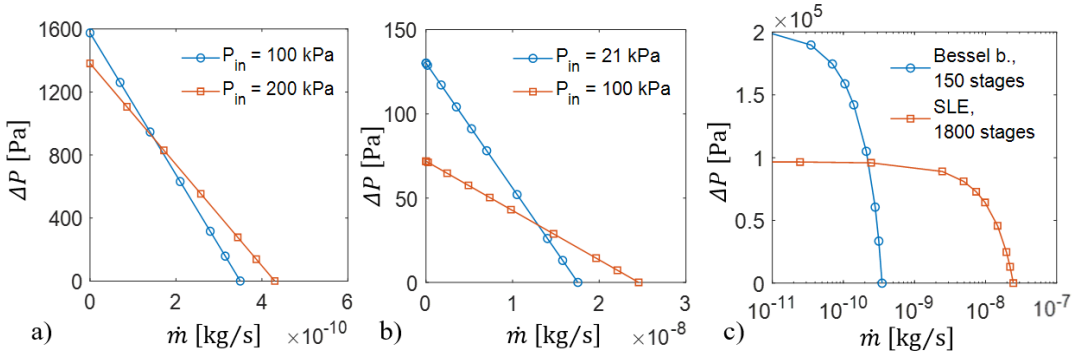

Figure 3: Characteristic curves of the single-stage pumps: a) the Bessel beam case, b) the SLE case, and c) the multistage operation of both pumps.

Acknowledgments

This work was funded by the French National Research Agency (ANR) and the German Research Agency (DFG) under the project "ANR-2022-CE92-0017-01" and “DFG BR 4175/8-1”.
This work was supported by LAAS-CNRs micro and nanotechnologies platform, a member of the Renatech French national network, under the project *Micro-actionneurs thermiques pour pompe Knudsen*, P-24-04914.

References

[1] Wang, X., Su, T., Zhang, W., Zhang, Z., & Zhang, S. (2020). Knudsen pumps: A review. Microsystems & Nanoengineering, 6(1), 26.
[2] Byambadorj, T., Zhao, X., Qin, Y., & Gianchandani, Y. B. (2024). Monolithic SOI through-wafer Knudsen pumps with mechanically robust Si channels. Sensors and Actuators A: Physical, 365, 114825.
[3] McNamara, S., & Gianchandani, Y. B. (2005). On-chip vacuum generated by a micromachined Knudsen pump. Journal of Microelectromechanical Systems, 14(4), 741-746.
[4] Kosyanchuk, V., Petrov, A., Kik, M., Yagodina, M., & Seredenko, R. (2025). Theoretical and experimental study of 3D-printed Knudsen pump with liquid cooling. International Journal of Heat and Mass Transfer, 249, 127178.
[5] Meyer, R., Froehly, L., Giust, R., Del Hoyo, J., Furfaro, L., Billet, C., & Courvoisier, F. (2019). Extremely high-aspect-ratio ultrafast Bessel beam generation and stealth dicing of multi-millimeter thick glass. Applied Physics Letters, 114(20).
[6] Gottmann, J., Hermans, M., Repiev, N., & Ortmann, J. (2017). Selective laser-induced etching of 3D precision quartz glass components for microfluidic applications—up-scaling of complexity and speed. Micromachines, 8(4), 110.
[7] López Quesada, G., Tatsios, G., Valougeorgis, D., Rojas-Cárdenas, M., Baldas, L., Barrot, C., & Colin, S. (2019). Design guidelines for thermally driven micropumps of different architectures based on target applications via kinetic modeling and simulations. Micromachines, 10(4), 249.

NEGF26 - 678653

DOMAIN DECOMPOSITION FOR THE BOLTZMANN EQUATION

R.K. Sharma[1], T. Keßler[2], M.R.A. Abdelmalik[3], A.J.H. Frijns[4], E.H. van Brummelen[5]
*r.k.sharma@tue.nl[1], t.kessler@tue.nl[2], M.Abdel.Malik@tue.nl[3], A.J.H.Frijns@tue.nl[4],
E.H.v.Brummelen@tue.nl[5]
TU Eindhoven[1,2,3,4,5]

KEY WORDS

Domain decomposition, Boltzmann equation, rarefied gas dynamics, method of moments, high performance computing.

ABSTRACT

The non-equilibrium kinetics of a rarefied monatomic gas can be described using the Boltzmann equation (BE)[4]. The BE itself captures several macroscopic phenomena through its structure, including the conservation of physical quantities (like mass, momentum and energy), and Galilean invariance[4]. The BE is an equation that shows the evolution of the probability density function under the given constraints, thus being a model in phase space. A general formulation is given by

$$\frac{\partial f}{\partial t} + v_i \frac{\partial f}{\partial x_i} = \mathcal{C}\left(f, f\right), \tag{1}$$

subjected to the initial and boundary conditions,

$$f(0, \boldsymbol{x}, \boldsymbol{v}) - f_0(\boldsymbol{x}, \boldsymbol{v}) = 0, \quad \boldsymbol{x} \in \Omega,\ \boldsymbol{v} \in \mathbb{R}^3; \tag{2a}$$

$$\boldsymbol{v} \cdot \boldsymbol{n}(\boldsymbol{x})(f(t, \boldsymbol{x}, \boldsymbol{v}) - f_{\text{in}}(t, \boldsymbol{x}, \boldsymbol{v})) = 0, \quad t \geq 0,\ \boldsymbol{x} \in \partial\Omega,\ \boldsymbol{v} \in \mathbb{R}^3 :\ (\boldsymbol{v} \cdot \boldsymbol{n}(\boldsymbol{x})) < 0 \tag{2b}$$

where Ω denotes the spatial domain considered, while the velocity domain will be the entire $\mathbb{R}^3$. $f(t, \boldsymbol{x}, \boldsymbol{v})$ is the distribution function of the gas, which contains the full information of the distribution of particles in space and velocity. v_i indicates the components of velocity, $\mathcal{C}\left(f, f\right)(v)$ is the bilinear collision operator.
For N_D spatial dimensions, BE will be a problem in $2N_D$ dimensions, making it computationally more expensive than the equivalent Navier-Stokes simulation. Furthermore, the dimensional expansion imposes substantial demands on memory resources.
One way to manage memory and computational load with the BE is to distribute the memory and computational load over a HPC infrastructure. One way to do this is through domain

* Corresponding author

decomposition, where the computational (spatial) domain for the problem is divided into several different subdomains such that each subdomain simulates a (smaller) part of the problem. The additional step when dealing with several subdomains (when compared to the monolithic solve) is the exchange of data at the interfaces at every timestep.
Here, we consider a finite element formulation for BE, where the test functions in the spatial ($\boldsymbol{\psi}(\boldsymbol{x})$) and velocity ($\boldsymbol{m}(\boldsymbol{v})$) domains are independent of each other. The weak form, considering test functions $\boldsymbol{m}(\boldsymbol{v})$ and $\boldsymbol{\psi}(\boldsymbol{x})$, are written as

$$A_t(f;\boldsymbol{m}\cdot\boldsymbol{\psi}) + A_x^{\Omega}(\boldsymbol{f};\boldsymbol{m}\cdot\boldsymbol{\psi}) + A_x^{\partial\Omega}(\boldsymbol{f}_{\text{out}};\boldsymbol{m}\cdot\boldsymbol{\psi}) - S(\boldsymbol{f};\boldsymbol{m}\cdot\boldsymbol{\psi}) = -A_x^{\partial\Omega}(\boldsymbol{f}_{\text{in}};\boldsymbol{m}\cdot\boldsymbol{\psi}) \tag{3a}$$

where

$$A_t(f;\boldsymbol{m}\cdot\boldsymbol{\psi}) = \frac{\partial}{\partial t}\int_{\Omega}\boldsymbol{\psi}(\boldsymbol{x})\left(\int_{\mathbb{R}^3}\boldsymbol{m}(\boldsymbol{v})f\ \mathrm{d}\boldsymbol{v}\right)\mathrm{d}\boldsymbol{x} \tag{3b}$$

$$A_x^{\Omega}(f;\boldsymbol{m}\cdot\boldsymbol{\psi}) = -\int_{\Omega}\frac{\partial\boldsymbol{\psi}(\boldsymbol{x})}{\partial x_i}\left(\int_{\mathbb{R}^3}v_i\boldsymbol{m}(\boldsymbol{v})f\ \mathrm{d}\boldsymbol{v}\right)\mathrm{d}\boldsymbol{x} \tag{3c}$$

$$A_x^{\partial\Omega}(f_{\text{out}};\boldsymbol{m}\cdot\boldsymbol{\psi}) = \int_{\partial\Omega}\int_{\mathbb{R}^3_{\text{out}}}(\boldsymbol{v}\cdot\boldsymbol{n}(\boldsymbol{x}))\ \boldsymbol{m}(\boldsymbol{v})\boldsymbol{\psi}(\boldsymbol{x})f\ \mathrm{d}\boldsymbol{v}\,\mathrm{d}\boldsymbol{s} \tag{3d}$$

$$A_x^{\partial\Omega}(f_{\text{in}};\boldsymbol{m}\cdot\boldsymbol{\psi}) = \int_{\partial\Omega}\int_{\mathbb{R}^3_{\text{in}}}(\boldsymbol{v}\cdot\boldsymbol{n}(\boldsymbol{x}))\ \boldsymbol{m}(\boldsymbol{v})\boldsymbol{\psi}(\boldsymbol{x})f_{\text{in}}\ \mathrm{d}\boldsymbol{v}\,\mathrm{d}\boldsymbol{s} \tag{3e}$$

$$S(f;\boldsymbol{m}\cdot\boldsymbol{\psi}) = \int_{\Omega}\boldsymbol{\psi}(\boldsymbol{x})\left(\int_{\mathbb{R}^3}\boldsymbol{m}(\boldsymbol{v})\mathcal{C}\left(f,f\right)\ \mathrm{d}\boldsymbol{v}\right)\mathrm{d}\boldsymbol{x} \tag{3f}$$

and

$$\mathbb{R}^3_{\text{in}} = \{\boldsymbol{v}\in\mathbb{R}^3 : \boldsymbol{v}\cdot\boldsymbol{n}(\boldsymbol{x}) < 0\}, \quad \mathbb{R}^3_{\text{out}} = \{\boldsymbol{v}\in\mathbb{R}^3 : \boldsymbol{v}\cdot\boldsymbol{n}(\boldsymbol{x}) \geq 0\}.$$

The right hand side in Eq.(3a) only consists of the boundary term Eq.(3e) which imposes the boundary conditions, determining the part of the probability distribution function that models the velocities concerning flow *into* the domain (which is the "inflow"). The left hand side consists of all terms within the spatial domain Ω, as well as the boundary term Eq.(3d), which models the part of the probability distribution function concerning flow *moving out* from the domain (which is the "outflow").

The outflow from a domain can only be calculated if the probability distribution function is known within the domain itself, and therefore can be seen as an "output" of the simulation. Conversely, the inflow, defined by the prescribed probability distribution at the domain boundaries, serves as the input. At the interface between two subdomains, the inflow to one subdomain corresponds to the outflow to the other, and vice versa, as shown in Fig.(1).

As an example, the fluid dynamics within a channel connected to two reservoirs at different pressures is considered. By changing the pressures of the reservoirs, the degree of rarefaction can be systematically altered. Within this experimental framework, the results from the decomposed domain studies are compared to the results from their equivalent monolithic simulations. The algorithm for such a decomposed domain simulation is shown in Fig.(2).

The discontinuous Galerkin (dG) discretization is used for the spatial domain. For the velocity discretization, the method of moments [5] is used, and as a consequence the structure of the BE is preserved. In addition, for the collisional operator $\mathcal{C}(f,f)$, the hard-sphere collisional

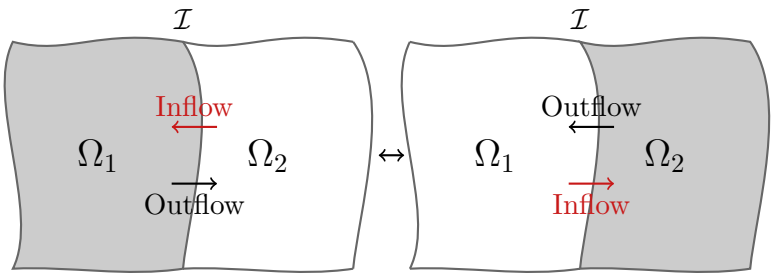

Figure 1: Depiction of how the inflow to one domain, will be the outflow to another domain and vice versa

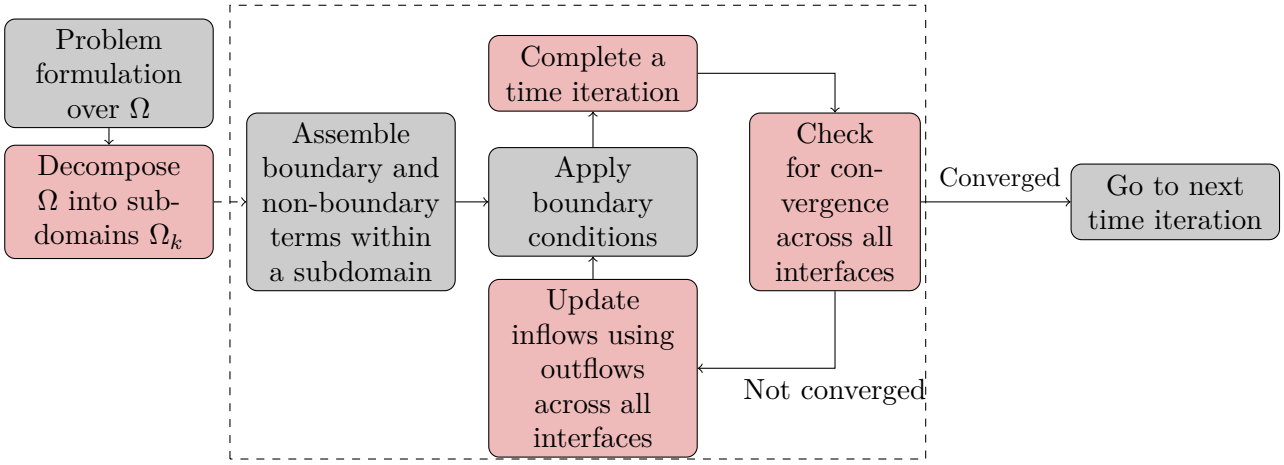

Figure 2: Flowchart indicating the algorithm followed for each implicit timestep

model is used. When using the method of moments, an appropriate closure is used, such that an accurate entropy dissipation that is similar to natural entropy dissipation is followed[1,2,3]. This formulation assumes a prior equilibrium (Maxwellian) distribution, given by a background density, velocity and temperature. The probability distribution function is approximated as a polynomial expansion around this equilibrium distribution.

However, as part of the initial setup of the simulation, it is necessary to provide an initial guess of not only the prior equilibrium distribution within each subdomain, but also across all interfaces. The worse the initial guess, the more the subiterations for each timestep (and thus, the longer it takes) for the decomposed domain simulation. In a decomposed domain framework, it is possible to assign distinct prior distributions and velocity-space resolutions to each subdomain. This flexibility allows for targeted refinement: only subdomains requiring detailed resolution of highly rarefied flows need to employ finer discretization. The reduced size of individual subdomains leads to smaller system matrices, which lowers computational cost and improves memory efficiency. Additionally, the use of Anderson acceleration [7] for the fixed-point subiterations within every timestep, thus further reducing the computational overhead. Our simulations are also compared to a monolithic model and show excellent agreement for a range of Knudsen numbers.

Since the limiting behavior of the Boltzmann Equation (BE) recovers continuum models such as the Euler and Navier–Stokes equations (NSE), it provides a natural framework for multiscale coupling. A domain decomposition approach enables the use of appropriate physical models in different subdomains, for instance, solving the BE in regions with rarefied flow and the NSE in continuum regimes, with flux exchange at the interfaces. This hybrid strategy captures rarefaction effects more accurately than NSE models with precomputed slip boundary conditions.

Acknowledgements

This project has received funding from the **European Union's Horizon programme under grant agreement No.101111948 (14AMI)**.

References and citations

[1] Abdelmalik, M.R.A., van Brummelen, E.H., (2016). Moment Closure Approximations of the Boltzmann Equation Based on φ-Divergences. J Stat Phys 164, 77–104.
[2] Abdelmalik, M.R.A., Van Der Woude, D.A.M., Van Brummelen, E.H., (2022). Entropy bounds for the space–time discontinuous Galerkin finite element moment method applied to the BGK–Boltzmann equation. Computer Methods in Applied Mechanics and Engineering 398, 115162.
[3] Abdelmalik, M.R.A., Gamba, I.M., Keßler, T., Rjasanow, S., (2026). Entropy-Based Ansatz for Galerkin Approximations of the Boltzmann Equation. tbp
[4] Cercignani, C., (1988). The Boltzmann Equation and Its Applications, Applied Mathematical Sciences. Springer New York, New York, NY.
[5] Levermore, C.D., (1996). Moment closure hierarchies for kinetic theories. J Stat Phys 83, 1021–1065.
[6] Saint-Raymond, L., (2009). Hydrodynamic Limits of the Boltzmann Equation, Lecture Notes in Mathematics. Springer, Berlin, Heidelberg.
[7] Anderson, D.G., (1965). Iterative Procedures for Nonlinear Integral Equations. J. ACM 12, 547–560.

NEGF26-701282

DYNAMICS OF MHD FLOWS IN LOW-DENSITY ARGON PLASMAS AT A STAGNATION-POINT DISK

Matteo Comito*[1,2], Viviana Lago[2], Benjamin Khiar[1]
[1]DPHY, ONERA, Université Paris-Saclay, 91120, Palaiseau, France
matteo.comito@onera.fr , benjamin.khiar@onera.fr
[2]FAST team, ICARE-CNRS, 45100, Orléans, France
viviana.lago@cnrs-orleans.fr

KEY WORDS

Hypersonics, Magnetohydrodynamics, Aerothermodynamics, Shock waves, Non-equilibrium plasma flows.

ABSTRACT

Atmospheric re-entry and hypersonic flight expose vehicles to extreme heat fluxes, aerodynamic loads, and communication blackouts, key issues for space missions and hypersonic systems. Magnetohydrodynamics (MHD) enables active control of ionized flows via Lorentz forces, with applications in heat-flux reduction, flow control, energy conversion, and blackout mitigation [1]. This experimental and numerical study focuses on ionized argon flows to isolate fundamental plasma–magnetic interactions, aiming to characterize MHD-induced flow structures and compare experiments with PIC-DSMC/MHD simulations. Simulations provide access to quantities difficult to measure experimentally, enabling interpretation of the observed structures and validation of the models.

Experimental setup

The PHEDRA wind tunnel [2] produces low-pressure supersonic and hypersonic ionized flows to reproduce high-enthalpy atmospheric re-entry conditions. It consists of a vacuum chamber of length $4.3\,\mathrm{m}$ and diameter $1.1\,\mathrm{m}$, equipped with a three-stage pumping system maintaining pressures in the range 2–8 Pa. The plasma is generated by a DC arc-jet, where argon is ionized between a cathode and the anode nozzle throat. Operating currents range from 50 to 250 A with mass flow rates of 0.1–$0.5\,\mathrm{g\,s^{-1}}$, providing specific enthalpies of 5–50 $\mathrm{MJ\,kg^{-1}}$. The generator is mounted on a two-axis support for accurate alignment. In this study, an argon plasma was used with operating conditions of $\dot{m} = 0.32\,\mathrm{g\,s^{-1}}$, $I_{\mathrm{arc}} = 100\,\mathrm{A}$, $V_{\mathrm{arc}} = 25\,\mathrm{V}$, and a chamber pressure of $7.6\,\mathrm{Pa}$. Diagnostics rely on Langmuir probes for the measurement of electron density, electron temperature, and floating potential, VUV imaging using a Kuro CMOS camera, and emission spectroscopy performed with an IsoPlane spectrometer. All optical measurements are focused at a distance of $3\,\mathrm{mm}$ above the disk center.

* Corresponding author

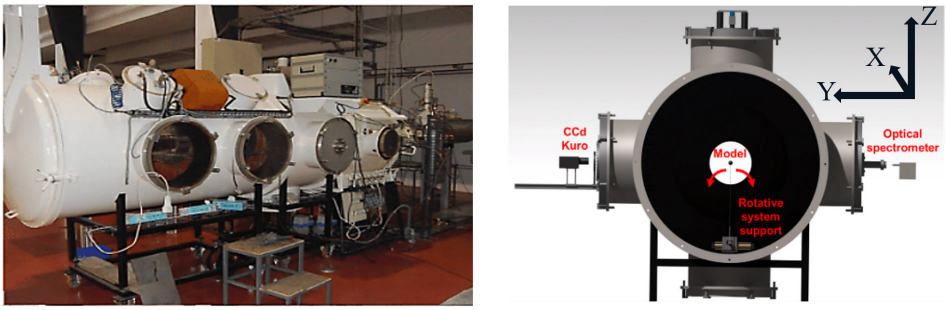

Figure 1: a) PHEDRA wind tunnel; b) set-up configuration.

The model consists of a coin-shaped stainless-steel disk with a diameter of 35 mm and a thickness of 3 mm, selected for its geometric simplicity and compatibility with numerical simulations. Localized magnetic fields are generated using neodymium magnets of two different sizes: $15 \times 15 \times 3$ mm^3 ($B_r \simeq 1.32$ T) and $20 \times 20 \times 10$ mm^3 ($B_r \simeq 1.3$ T) (Fig.2). The smaller magnet, shown in red in the figure below, is also used to position and secure the overall magnet assembly to prevent any movement, while the larger magnet is shown in blue. Two magnetic configurations are investigated: radial and axial orientations of the magnetic field vector with respect to the flow direction (x-axis).

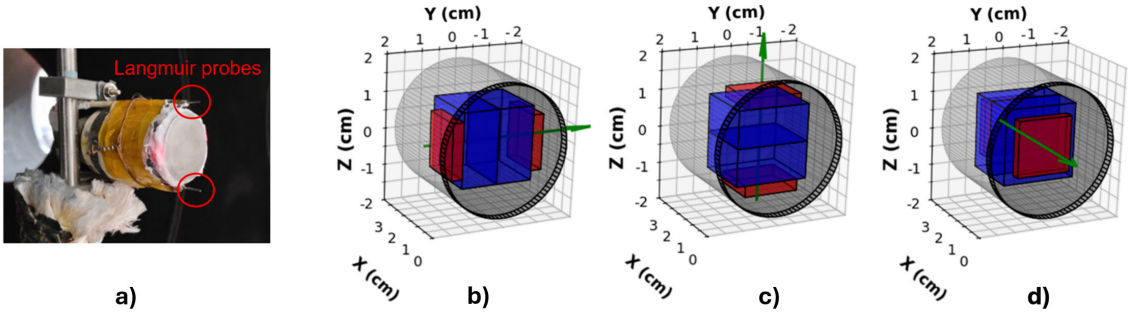

Figure 2: a) photograph of the mounted coin-shaped model equipped with localized Langmuir probes; b) radial magnetic field configuration along the $-Y$ direction; c) radial magnetic field configuration along the Z direction; d) axial magnetic field configuration along the $-X$ direction.

Results

Figure 3 displays Kuro camera images in the x–z plane, where the intensity is normalized by the nozzle-exit luminance corresponding to each operating condition, allowing meaningful comparison between different exposure times. The magnetic field lines, calculated using `Magpylib`, correspond to the same magnet configurations as those shown in Figure 2 and are overlaid on these images. Differences in plasma shock behavior are observed for the $-Y$ (Fig.2b), Z (Fig.2c) and $-X$ (Fig.2d) magnetic field configurations when compared with the no-field reference case.

In the presence of a radial magnetic field, the shock response is anisotropic, motivating the investigation of two orientations: along $-Y$ (Fig.3a) and along Z (Fig.3b). For the $-Y$ orientation, the shock exhibits a pronounced asymmetry, with increased brightness in the lower region, indicating an effect in the local $-\mathbf{v} \times \mathbf{B}$ direction. By contrast, the Z configuration results in a more symmetric and diffuse shock structure, characterized by a larger stand-off distance and the presence of a reduced-luminance region relative to the reference case.

With an axial magnetic field along $-X$ (Fig.3c), the shock exhibits a compressed, high-intensity region above the disk and a detached bright structure upstream. The shape of this structure follows the magnetic

field lines, in agreement with the funnel-like behavior in air reported by Oswald *et al.* [3]. Overall, the correlation between magnetic field lines and plasma luminosity highlights the strong coupling between field geometry and shock morphology.

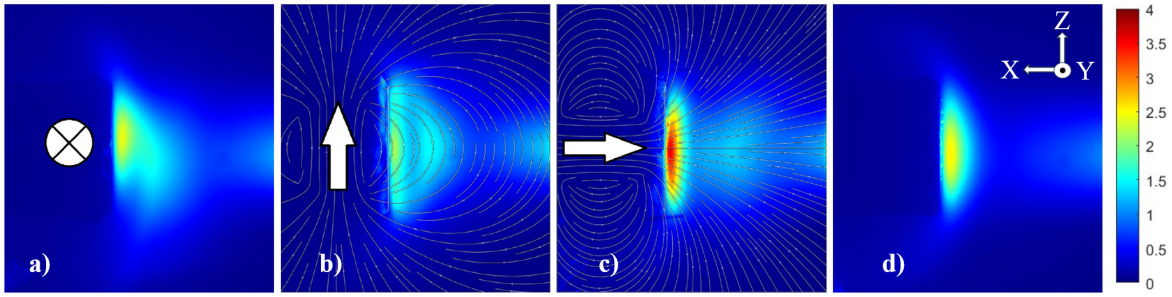

Figure 3: Plasma self-emission for the magnetic field configurations shown in Figure 2: (a) radial magnetic field along the $-Y$ direction, (b) radial magnetic field along the Z direction, (c) axial magnetic field along the $-X$ direction, and (d) no-field reference case.

Figure 4 presents a comparison between images acquired with a standard camera and those obtained using the Kuro camera. Figures 4a and 4c correspond to standard camera images, in which a distinct region is clearly visible and indicated by the dashed outline. Figures 4b and 4d show post-processed Kuro images obtained from the ratio between acquisitions with and without magnetic field, highlighting the regions where the magnetic field impact is strongest. These regions coincide spatially with the dashed area observed in the standard camera images, indicating that the zone most affected by the magnetic field is also associated with distinct emission features corresponding to different excited states of argon and suggesting localized magnetic-field-driven physical mechanisms.

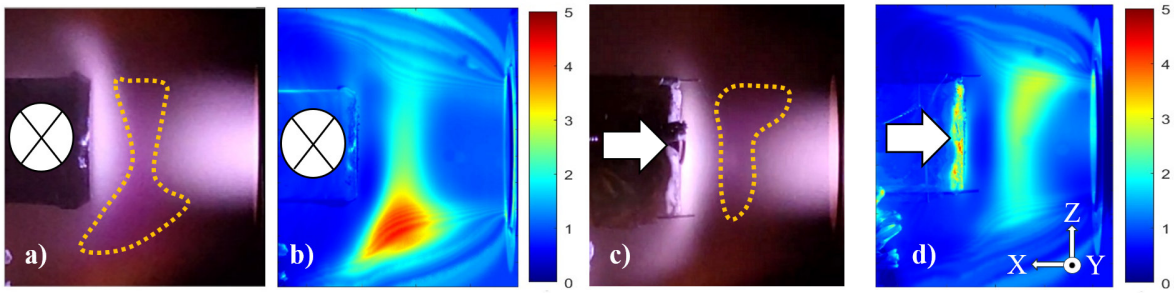

Figure 4: Visualization of excited argon states and magnetic field effects: standard camera images (a, c) compared to Kuro-processed images (b, d) using with/without field ratio.

Magnetic field influence on local measurements

The local argon excitation temperature was obtained from spectroscopic measurements using the Boltzmann method, based on emission lines in the 600–930 nm wavelength range. Figure 5a shows the results measured at the disk center, 3 mm from the surface. In the case without a magnetic field, the shock region shows an excitation temperature about 50% higher than in the freestream. Concerning magnetic field effects, the radial configuration increases the excitation temperature by 24%, while the axial configuration leads to a 36% rise, both relative to the no-field case, as the magnetic field allows only the highest-energy argon species to pass through. In the axial configuration, these high-energy argon atoms and electrons are concentrated at the disk center, resulting in a higher central excitation temperature than in the radial case.
Electron density and temperature (Fig.5b and 5c) were further determined using both upper and single Langmuir probes (Fig.2a). With an axial magnetic field, electrons are confined toward the flow center,

resulting in reduced electron density near the disk periphery. However, the most energetic electrons can still reach this region, leading to an increase in the measured electron temperature.

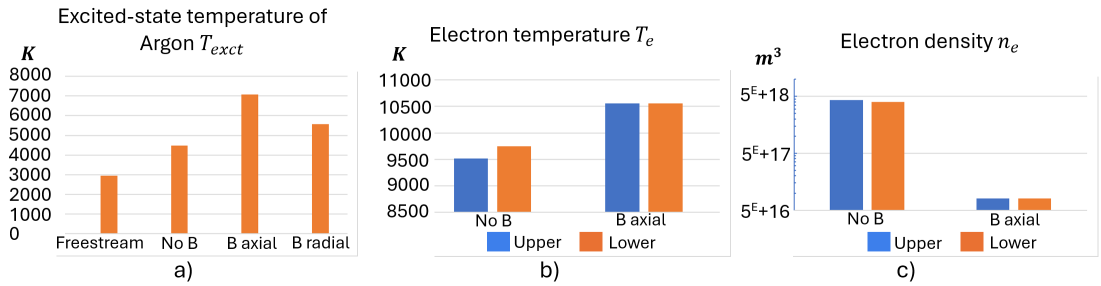

Figure 5: a) excited argon temperature determined 3mm in front of the disk; b and c) : electron temperature and density determined by the upper and lower Langmuir probes (Figure 2a)

To characterize the interaction between a PHEDRA-type plasma flow and the model, with particular emphasis on the influence of an applied magnetic field, two-dimensional axisymmetric (r–x) DSMC simulations were carried out using the SPARTA code. The plasma was modeled as a three-species mixture (Ar, Ar^+, e^-), with interparticle collisions described by a collision-averaged VSS model using parameters reported by Khiar *et al.* [4]. The freestream conditions correspond to a temperature of $2500\,\mathrm{K}$ and a bulk velocity of $3500\,\mathrm{m\,s^{-1}}$ aligned with the x-axis.
In the absence of a magnetic field, the simulated electron distribution (Figure 6) agrees well with measurements obtained using electrostatic probes positioned along the cylinder edge (Figure 5c).

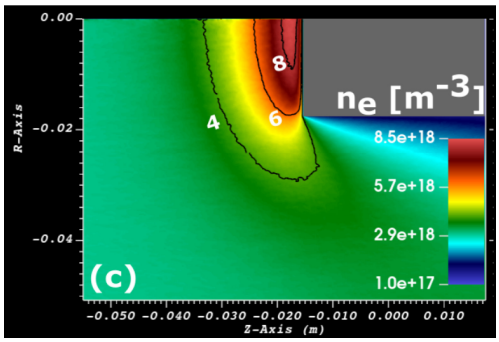

Figure 6: 2D maps of electron density calculated without magnetic field.

Acknowledgements

This research was funded in part by the Agence Nationale de la Recherche (ANR) under ASTRID project AMHYRA, grant number ANR-24-ASTR-0002.

References and citations

[1] Resler E.L., Sears W.R. (1958). Journal of the Aeronautical Sciences, 25, 235-258
[2] Lago V., Joussot R., Parisse J.-D. (2014). PHEDRA : a high enthalpy wind tunnel for atmospheric entry simulations, Space Access International Conference.
[3] Oswald J.W., Lani A., Herdrich G. (2025). Vacuum, 25, Article 114565
[4] Khiar B., Lago V., Boni F., (2025). Experimental and Numerical Investigations of Magnetohydrodynamic Hypersonic Interactions for High-Altitude Flight. The 4th International Conference on High-Speed Vehicle Science Technology.

NEGF26-677857

EFFICIENT ADJOINT OPTIMIZATION OF RAREFIED GAS FLOWS

Lei Wu[1]
[1]Department of Mechanics and Aerospace Engineering, Southern University of Science and Technology, Shenzhen 518055, PR China
wul@sustech.edu.cn

KEY WORDS

Shape optimization, topology optimization, multiscale simulation, Boltzmann model equation

ABSTRACT

Traditional aerodynamic optimization methods have primarily focused on continuum flows, with limited attention to rarefied flows—despite their significance in applications such as ultra-low Earth orbit vehicles, EUV lithography systems, and vacuum pumping equipment. To address this gap, we have developed two sets of adjoint-based optimization methods emphasizing efficiency and innovation, respectively: a shape optimization method using body-fitted grids, and a topology optimization method based on material density. The shape optimization method targets extreme efficiency, seeking to achieve most optimization effects within approximately ten iterations, thereby alleviating the high computational cost of rarefied flow simulations [1], see Fig.1 for an example. The topology optimization method broadens the design space, allowing the independent evolution of shape, size, and topology to explore more innovative configurations without relying on prior knowledge or experience [2], see Fig.2 and Fig.3 for examples. Both methods are built upon the General Synthetic Iterative Scheme [3], which deterministically and efficiently solves the Boltzmann model equation. This report will present the core concepts of these methods and their preliminary applications to aerofoils, pipelines, jets, and other systems.

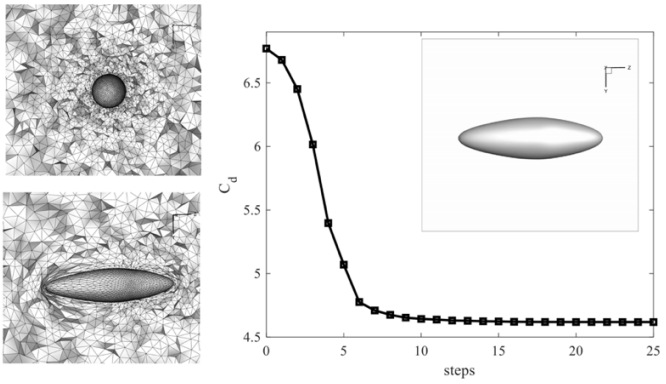

Figure 1: Shape optimization method to minimize drag configuration, based on the Boltzmann model equation. The incoming Mach number is 2, the Knudsen number based on the sphere radius is 0.1. A 34.5% reduction of drag is achieved after about 7 optimization steps.

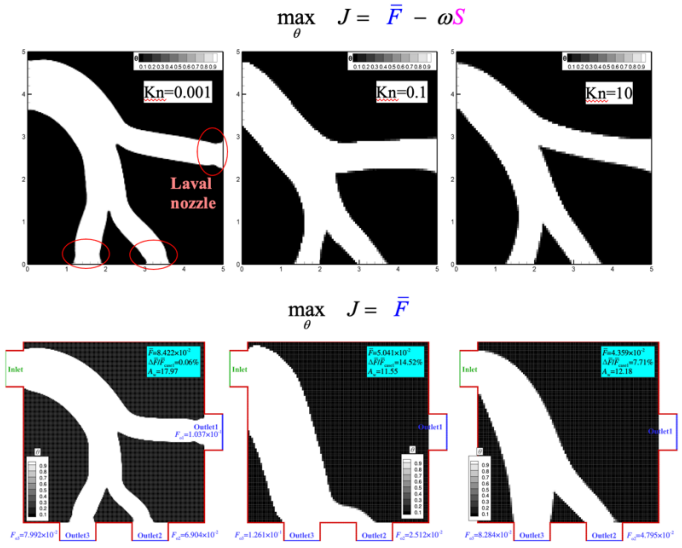

Figure 2: Topology optimization method to maximize flow rate under different constraints, based on the Boltzmann model equation, from the continuum to free-molecular flow regimes. First row: maximizing the overall flow rate while minimizing the flow variance at the three outlets. Second row: maximum the overall flow rate only.

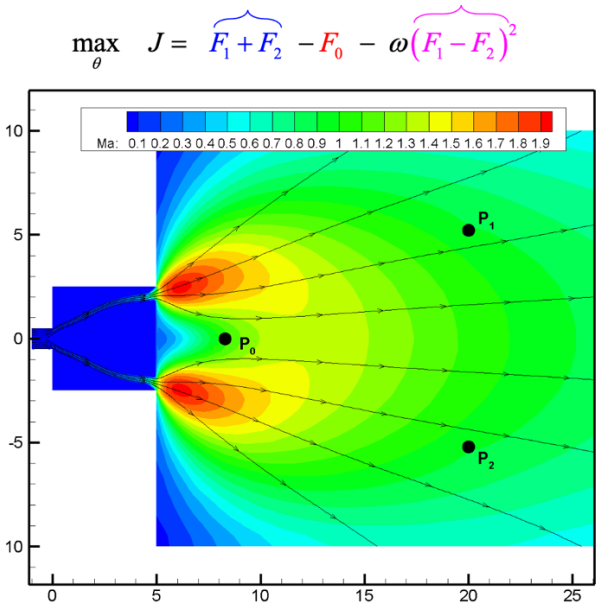

Figure 3: Topology optimization (of the two inlet channels) is used to maximize the forces acting on contaminant particles 1 and 2, while minimizing the force on the Sn droplet 0, mimicking the scenario in EUV light generation.

References and Citations

[1] Yuan, R. F. & Wu, L. (2025) Adjoint shape optimization from the continuum to free-molecular gas flows. *Journal of Computational Physics*, 537, 114102.

[2] Yuan, R. F. & Wu, L. (2024) *A design optimization method for rarefied and continuum gas flows. Journal of Computational Physics*, 517, 113366.

[3] Su, W., Zhu, L. H., Wang, P., Zhang, Y. H., & Wu, L. (2020) *Can we find steady-state solutions to multiscale rarefied gas flows within dozens of iterations? Journal of Computational Physics*, 407, 109245.

NEGF26-679102

ENHANCING DSMC SIMULATIONS OF RAREFIED GAS MIXTURES USING A FAST-CONVERGING AND ASYMPTOTIC-PRESERVING SCHEME

Liyan Luo[1], Lei Wu[1,a)]

[1] *Department of Mechanics and Aerospace Engineering, Southern University of Science and Technology, Shenzhen 518055, China*

[a)] Corresponding author: wul@sustech.edu.cn

KEY WORDS

Direct simulation Monte Carlo, fast convergence, gas mixtures, general synthetic iterative scheme

ABSTRACT

The numerical simulation of rarefied gas mixture dynamics with disparate masses using the direct simulation Monte Carlo (DSMC) method is slow, primarily because the time step is constrained by that of the lighter species, necessitating an enormous number of evolution steps to reach a steady state. Here, we address this issue by developing a general synthetic iterative scheme (GSIS)[1-2], in which the traditional DSMC simulation is intermittently enhanced using a macroscopic synthetic equation[3]. Specifically, after running the DSMC for a certain number of time steps, the high-order constitutive relations for stress and heat flux, as well as the momentum and energy exchange terms from inter-species collisions, are extracted from the DSMC and incorporated into the macroscopic synthetic equations. These equations are solved to obtain the steady state, and the solution is then used to update the particle distribution in DSMC, thereby skipping unnecessary intermediate evolutions. This two-way coupling not only accelerates convergence to the steady state but also asymptotically preserves the Navier-Stokes limit in the continuum flow regime, allowing the spatial cell size to be much larger than the molecular mean free path. The accuracy of our method is validated for one-dimensional force-driven Poiseuille flow and two-dimensional hypersonic flow past cylinders, considering Maxwell and hard-sphere gases with mass ratios of 10 and 100. Moreover, the one-dimensional shock wave structure and thermal driven low-speed flow have been investigated using a more realistic intermolecular potential. Although our in-house DSMC method is approximately an order of magnitude slower than the open-source DSMC code SPARTA, intermittently augmenting it with the synthetic equation makes it roughly 30 times faster at a Knudsen number of 0.01, with even greater computational gains anticipated at smaller Knudsen numbers. This work represents a critical step toward developing fast-converging and asymptotic-preserving schemes for hypersonic chemical reactions.

METHODOLOGY

The Direct Intermittent GSIS-DSMC coupling (DIG) method for gas mixtures boosts the convergence of DSMC method to steady state by iteratively coupling with a macroscopic synthetic equation. The general flowchart of DIG is shown in Figure 1. Within each unit cycle, the traditional DSMC is first executed for a prescribed number of time steps N_d, during which the time-averaged source terms $\Delta \boldsymbol{Q}_s^*$, macroscopic properties $\boldsymbol{M}_s^{k+1/2}$, and higher-order terms $\mathbf{HoT}^{k+1/2}$ are sampled. These quantities are then used to solve the macroscopic synthetic via a time-implicit finite-volume scheme, with boundary conditions imposed following the Grad 13-moment method[4]. The updated macroscopic properties $\boldsymbol{M}_s^{k+1}$ are subsequently employed to adjust the particle information for each species by a linear

transformation of particle velocities, thereby driving the particle distribution in the flow field closer to the steady state.

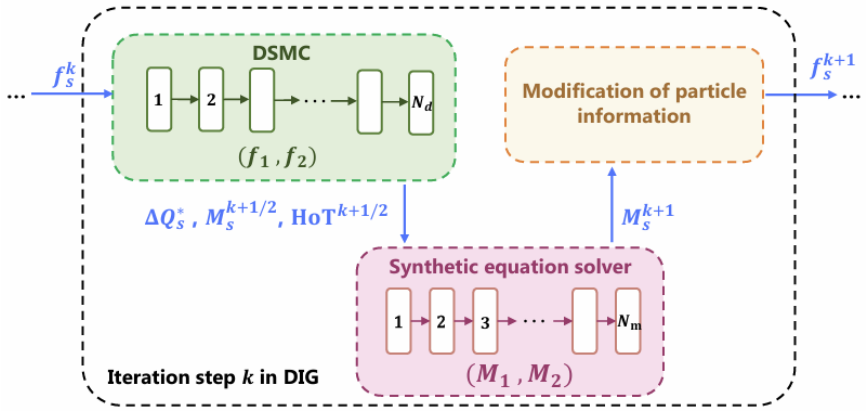

Figure 1: Flowchart of the DIG algorithm for two-species monatomic gas mixture. In each iteration step, the DSMC is run for $N_d = 100$ steps and the synthetic equations are solved for $N_m = 200{\sim}1000$ iterations, or until the maximum relative error of the conservative variables among the two species between two successive steps drops below 10^{-5}.

NUMERICAL RESULTS

Figure 2 compares the computational grid applied in DSMC and DIG method, when the global Knudsen number is 0.1 and 0.01. The computations are performed for a gas mixture of two Maxwellian species with a mass ratio of 10 at a Mach number of 5. The DSMC results are provided by the open-source SPARTA code. In DSMC, cartesian grids are adaptively refined to be less than one-third of the mean free path. As a result, DSMC requires approximately 250,000 cells for $\mathrm{Kn} = 0.1$ and 1.9 million cells for $\mathrm{Kn} = 0.01$. In contrast, the spatial cell sizes in DIG are significantly larger than the mean free path, particularly in the near-continuum regime. For example, at $\mathrm{Kn} = 0.01$, the cell size near the cylinder surface in DIG can be nearly 15 times larger than that required by standard DSMC. However, as shown in Figure 3, despite the substantial difference in the number of computational cells, the macroscopic results obtained from the DSMC and DIG exhibit excellent agreement.

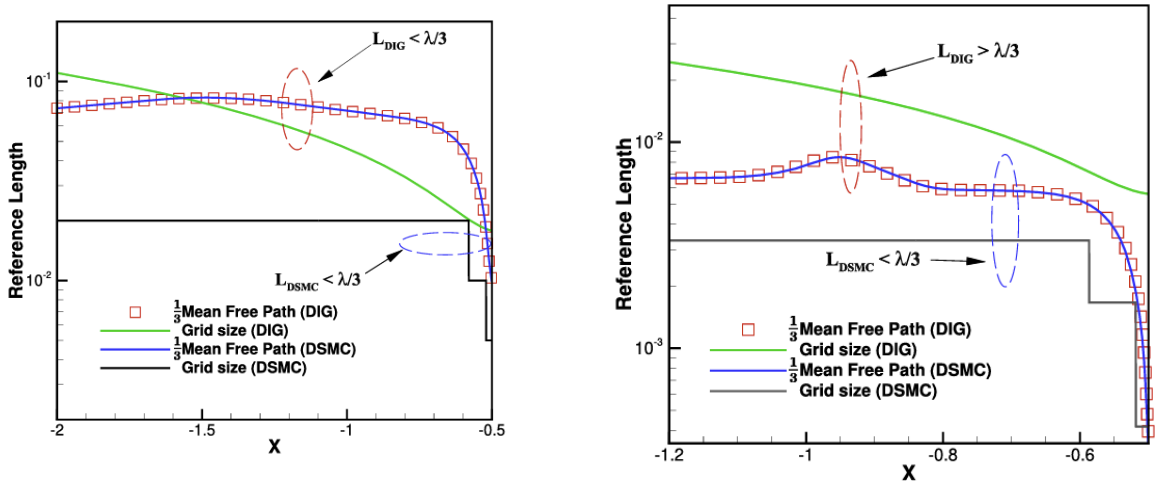

Figure 2: The computational grid size employed in the hypersonic gas flow passing over a cylinder for DSMC and DIG method when the global Knudsen number is 0.1 (left) and 0.01 (right). The grid size in DSMC is adaptively refined and strictly lower than one-third of the local mean free path for the heavy species. The time step Δt, multiplied by the most probable speed, is carefully constrained to remain smaller than the length of the smallest grid.

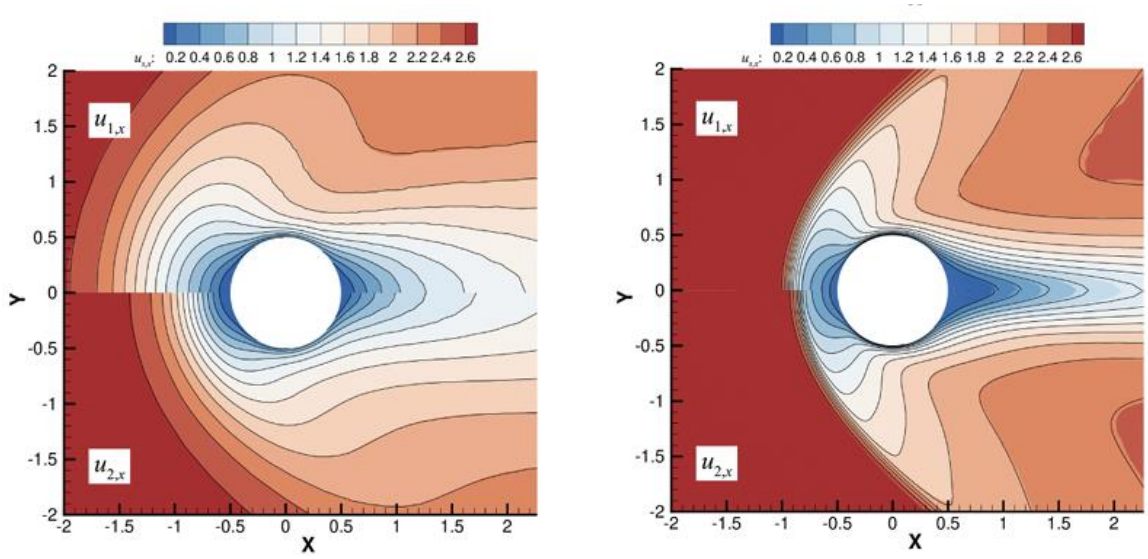

Figure 3: Comparisons of velocity fields predicted by DIG (lines) and DSMC (contours) for the Maxwellian gas mixture with a mass ratio of 10 at the incoming Mach number of 5.

As a result, although the parallel efficiency of our in-house DSMC code is roughly an order of magnitude lower than that of SPARTA, primarily due to its Cartesian grid structure and the more advanced parallelization strategy implemented in SPARTA. Nevertheless, for a mass ratio of 10, the total computational time (including both transitional and steady-state phases) of DIG is reduced by approximately a factor of 3 for $\mathrm{Kn} = 0.1$ and a factor of 15 for $\mathrm{Kn} = 0.01$. And this advantage becomes even more pronounced at a mass ratio of 100, where the DIG achieves a CPU time reduction of more than a factor of 30 for $\mathrm{Kn} = 0.01$ compared with SPARTA.

REFERENCES

[1] W. Su, L. Zhu, P. Wang, Y. Zhang, L. Wu (2020). Can we find steady-state solutions to multiscale rarefied gas flows within dozens of iterations? *J. Comput. Phys*, **407**, 109245.
[2] J. Zeng, Q. Li, L. Wu (2024). General synthetic iterative scheme for rarefied gas mixture flows. *J. Comput. Phys*, **519**, 113420.
[3] L. Luo, L. Wu (2024). Multiscale simulation of rarefied gas dynamics via direct intermittent GSIS-DSMC coupling. *Adv. Aerodyn*, **6**, 22
[4] W. Liu, Y. Zhang, J. Zeng, L. Wu (2024). Further acceleration of multiscale simulation of rarefied gas flow via a generalized boundary treatment. *J. Comput. Phys*, **503**, 112830.

NEGF26-686009

Estimation of N_2 volume viscosity by Classical Trajectories simulations

Domenico Bruno*[1], Aldo Frezzotti[2]
[1]domenico.bruno@cnr.it, [2]aldo.frezzotti@polimi.it

KEY WORDS

Nitrogen transport coefficients, Rayleigh-Brillouin scattering, Direct Simulation Monte Carlo, Nitrogen Potential Energy Surfaces

ABSTRACT

The knowledge of nitrogen transport coefficients is of fundamental importance. However, not all of them have been determined with the same accuracy. In particular, volume viscosity experimental measurements and theoretical estimations exhibit considerable uncertainties. Figure 1 shows experimental volume viscosity data, in the temperature range $[180 : 500]$ K, obtained by sound absorption [1, 2, 3] and by the more recent Rayleigh-Brillouin scattering (RBS) technique [4, 5]. On the theoretical side, a number of potential energy surfaces (PES) have been proposed to describe the pairwise interaction of N_2 molecules and predict nitrogen transport properties in the low density limit. The rigid rotor approximation, neglecting vibrational degrees of freedom, has been used in Refs. [6, 7, 8, 9] for low temperature estimations, of primary interest for the present work. More general PESs, in which vibrational levels are taken into account are described in Ref. [10] and Ref. [11], the latter being also capable of describing N_2 dissociation.
Once the PES is known, transport properties can be obtained by a variety of techniques. Nitrogen shear and volume viscosity have been obtained in Ref. [12] by nonequilibrium CT-DSMC simulations [13] based on the PES proposed in Ref. [6]. Although shear viscosity predictions were in good agreement with reference experimental data [14], volume viscosity estimations inherited large uncertainty from the original uncertainties associated with the anisotropic PES contributions. Excellent agreement with shear viscosity and thermal conductivity experimental data has been obtained in Ref. [7] by Monte Carlo evaluation of collision integrals, based on a PES accurately derived from quantum *ab initio* methods. The same strategy has been adopted in Ref. [9] where shear viscosity, thermal conductivity and volume viscosity have been estimated by equilibrium simulations and Green-Kubo expressions for transport properties. The PES has been obtained from a suitable interpolation of DFT data. Good agreement has been obtained with reference experimental data [14] of shear viscosity and thermal conductivity. The predicted volume viscosity lies below most of experimental data but it is close to the RBS measurement by Meijer [5] and to the lowest temperature point of Gu's RBS measurements [4].
The work described here originates from the observation that volume viscosity has not been estimated

* Corresponding author

from the PES proposed in Ref. [7], which appears to be quite accurate, although computationally expensive. Volume viscosity estimations have been obtained by nonequilibrium CT-DSMC simulations [13]. The latter are, in general, computationally more expensive than Monte Carlo estimations [7, 13] but directly provide values of transport coefficients that do not require higher order corrections [15]. Furthermore, they provide a better understanding of the physical processes determining a specific transport coefficient. Two different CT-DSMC configurations have been used. In the first one, volume viscosity $\eta_v(T_{eq})$ is obtained from the expression [16]:

$$\eta_v = \frac{4}{15} p\tau \tag{1}$$

where p is the pressure and τ is the relaxation time to the equilibrium temperature T_{eq} of rotational temperature T_{rot} and translation temperature T_{tr}, in an isochoric and adiabatic space homogeneous simulation. Relaxation times τ are obtained by exponential fits of $\Delta T(t) = T_{rot}(t) - T_{tr}(t)$, with $|\Delta T(t)|/T_{eq} << 1$ (see Fig. 1b). As show in Fig. (1)a, the estimated η_v, in the range $[250 : 400]$ K, lie between the numerical results from Refs. [10, 8] and they are close experimental data from Ref. [1]. The second one consists in an expansion with uniform and constant divergence. In this case, the flow

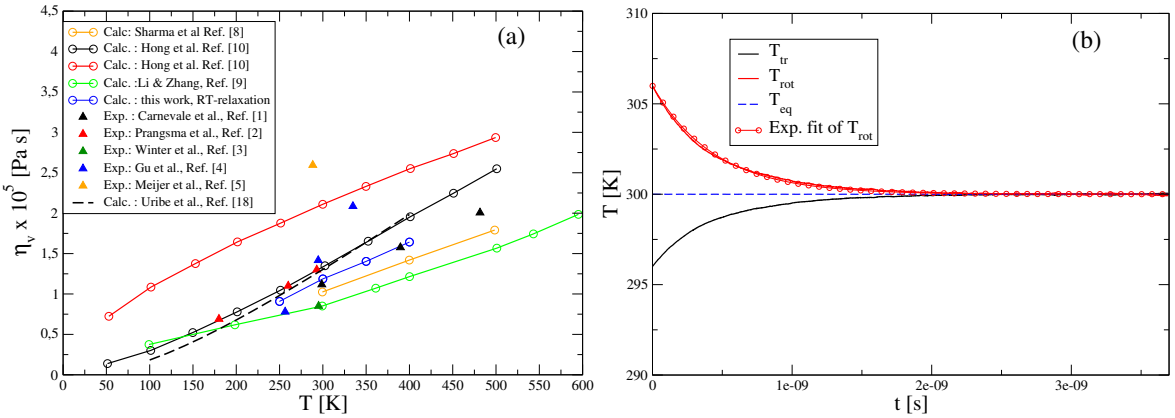

Figure 1: **(a)** - Calculated η_v compared to experimental data. **(b)** - Example of simulated RT relaxation in N_2.

is, strictly speaking, one dimensional, however it is amenable to a space homogeneous problem which describes the local gas expansion, as seen by an observer moving with the bulk velocity. The flow is governed by the following Boltzmann equation:

$$\frac{\partial f}{\partial t} - \frac{\delta}{3}\vec{v}\cdot\nabla_{\vec{v}} f = C(f,f). \tag{2}$$

In Eq. (2), $f(\vec{v},\vec{\gamma},t)$ is the distribution function of molecular velocity $\vec{v}$ and angular momentum $\vec{\gamma}$, δ is the divergence and $C(f,f)$ is the collision integral, representing binary interactions between linear rigid rotators, under the action of intermolecular forces derived by the PES. In formulating the associated CT-DSMC particle scheme it is more convenient and transparent to adopt the following equivalent form of Eq. (2):

$$\frac{\partial f}{\partial t} - \frac{\delta}{3}\nabla_{\vec{v}}\cdot(\vec{v}f) + \delta f = C(f,f) \tag{3}$$

where the third term on the lefthand side makes the density ρ vary as $\rho(t) = \rho(0)\exp(-\delta t)$, whereas the second term causes an isotropic velocity rescaling which increases or decreases T_{tr}, depending on

the sign of δ. As is clear, the two terms act only on the translational degrees of freedom; the coupling with rotational degrees of freedom is provided by the collision term, $C(f, f)$. The volume viscosity is estimated as:

$$\eta_v(T) = \lim_{\delta \to 0} \eta_v^{(est)}(T, \delta) = \frac{p - p_{tr}}{\delta} \tag{4}$$

where p and p_{tr} are the pressures calculated from the temperatures $T = (3T_{tr} + 2T_{rot})/5$ and T_{tr}, respectively. The method has been tested on the *rough* sphere gas [15], perhaps the simplest mechanical model of a polyatomic gas. Its transport coefficients have been obtained in a number of investigations by Chapman-Enskog expansions [15, 17]. Figure 2a shows the measured volume viscosity as a function of temperature during expansions with different values of the adimensional divergence, $\delta_0 = \delta\tau_0$, τ_0 being the mean free time at the beginning of the expansion. It is apparent that the curves converge to the theoretical result from [17]. The same method has been used to estimate nitrogen η_v as a function of T, during the expansion. Preliminary results are presented in Figure 2b. The simulated expansion starts from an equilibrium gas at $T_0 = 400\,K$ and $p_0 = 10^5\,Pa$. The expansion curve is obtained as extrapolation to $\delta \to 0$ of several expansions with finite δ. The results compare well with those obtained from RT relaxation. However, on the basis of the rough sphere gas convergence pattern, the curvature near the initial temperature, T_0, suggests that the values of the selected δ values are still too large to obtain accurate results on the whole temperature interval. Further calculations are underway to improve the estimations accuracy.

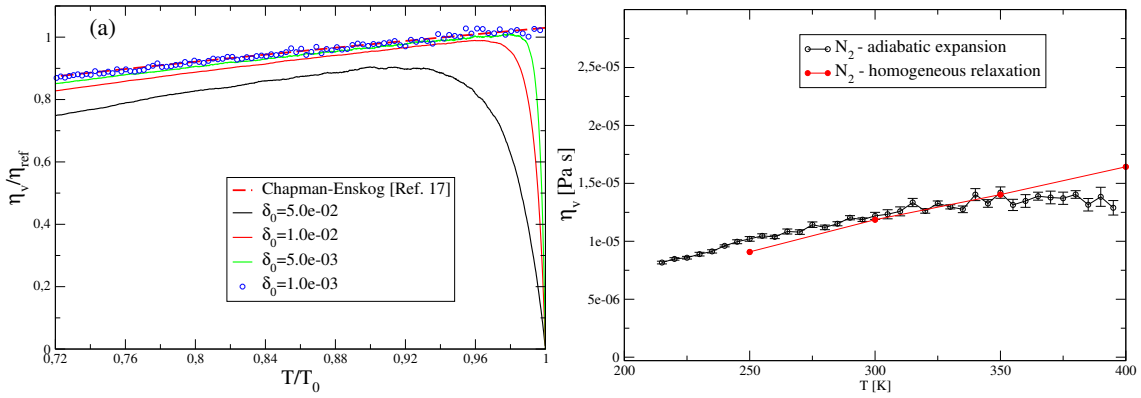

Figure 2: **(a)** - Volume viscosity of rough spheres as a function of temperature for expansions with different velocity divergence. The theoretical result from [17] is also reported for comparison.**(b)** Estimated volume viscosity of N_2 as a function of temperature.

References and citations

[1] Carnevale, E.H., Carey, C., & Larson, G. (1967). Ultrasonic Determination of Rotational Collision Numbers and Vibrational Relaxation Times of Polyatomic Gases at High Temperatures. The Journal of Chemical Physics, 47, 2829–2835.

[2] Prangsma, G., Alberga, A., & Beenakker, J. (1973). Ultrasonic determination of the volume viscosity of n2, co, ch4 and cd4 between 77 and 300 k. Physica, 64, 278–288.

[3] Winter, T.G. & Hill, G.L. (1967). High-temperature ultrasonic measurements of rotational relaxation in hydrogen, deuterium, nitrogen, and oxygen. The Journal of the Acoustical Society of America, 42, 848–858.

[4] Gu, Z. & Ubachs, W. (2013). Temperature-dependent bulk viscosity of nitrogen gas determined from spontaneous Rayleigh-Brillouin scattering. Opt. Lett., 38, 1110–1112.

[5] Meijer, A.S., de Wijn, A.S., Peters, M.F.E., et al. (2010). Coherent Rayleigh-Brillouin scattering measurements of bulk viscosity of polar and nonpolar gases, and kinetic theory. The Journal of Chemical Physics, 133, 164.315.
[6] Aquilanti, V., Bartolomei, M., Cappelletti, D., et al. (2002). The N2–N2 system: An experimental potential energy surface and calculated rotovibrational levels of the molecular nitrogen dimer. The Journal of Chemical Physics, 117, 615–627.
[7] Hellmann, R. (2013). *Ab initio* potential energy surface for the nitrogen molecule pair and thermophysical properties of nitrogen gas. Molecular Physics, 111, 387–401.
[8] Sharma, B., Kumar, R., Gupta, P., et al. (2022). On the estimation of bulk viscosity of dilute nitrogen gas using equilibrium molecular dynamics approach. Physics of Fluids, 34, 057.104.
[9] Li, Y. & Zhang, J. (2025). Gas viscosity from first principles: A case study on nitrogen. Physics of Fluids, 37, 087.137.
[10] Hong, Q., Storchi, L., Sun, Q., et al. (2023). Improved Quantum–Classical Treatment of N $_2$ –N $_2$ Inelastic Collisions: Effect of the Potentials and Complete Rate Coefficient Data Sets. Journal of Chemical Theory and Computation, 19, 8557–8571.
[11] Valentini, P., Verhoff, A.M., Grover, M.S., et al. (2023). First-principles predictions for shear viscosity of air components at high temperature. Physical Chemistry Chemical Physics, 25, 9131–9139.
[12] Bruno, D. & Frezzotti, A. (2026). Classical Trajectories Estimation of Transport Properties of $N_2 - O_2$ Mixtures. In M. Grabe, G. Oblapenko, & M. Torrilhon, eds., Rarefied Gas Dynamics, Springer Aerospace Technology. Springer.
[13] Bruno, D., Frezzotti, A., & Ghiroldi, G. (2015). Oxygen transport properties estimation by classical trajectory-direct simulation Monte Carlo. Physics of Fluids, 27.
[14] Lemmon, E.W. & Jacobsen, R.T. (2004). Viscosity and Thermal Conductivity Equations for Nitrogen, Oxygen, Argon, and Air. International Journal of Thermophysics, 25, 21–69.
[15] Chapman, S. & Cowling, T.G. (1990). The Mathematical Theory of Non-Uniform Gases. Cambridge University Press, Cambridge UK.
[16] McCourt, F., Beenakker, J., Kohler, W., et al. (1990). Nonequilibrium Phenomena in Polyatomic Gases: Volume 1. Oxford University Press.
[17] Condiff, D., Lu, W., & Dahler, J. (1965). Transport properties of polyatomic fluids, a dilute gas of perfectly rough spheres. The Journal of Chemical Physics, 42, 3445–3475.

NEGF26-682197

EVAPORATION & CONDENSATION COEFFICIENTS UNDER NON-EQUILIBRIUM CONDITIONS

M.C.W. Wolf*, S.V. Gaastra-Nedea, A.J.H. Frijns
Eindhoven University of Technology, PO Box 513, 5600 MB Eindhoven, the Netherlands
m.c.w.wolf@tue.nl

KEY WORDS

Molecular dynamics, S-model kinetic equation, Evaporation, Condensation, Liquid-Vapor interface, Mach number.

ABSTRACT

Phase change phenomena at the liquid-vapor interface, particularly evaporation and condensation play an important role across a broad range of scientific and engineering disciplines, such as biology, chemistry, and thermal systems engineering. As the demand for miniaturized, energy-efficient technologies grows, especially in confined geometries, a deeper understanding of heat and mass transfer mechanisms at the interphase becomes increasingly critical. The non-equilibrium nature of evaporation and condensation phenomena at micro- and nano-scales remains a modeling challenge. Approaches such as Molecular Dynamics (MD) are able to describe these phenomena at the liquid/vapor interface but are computationally expensive. The S-model kinetic equation offers a more efficient alternative but relies on key input parameters: the liquid temperature T_L and evaporation/condensation coefficient $\alpha_{e,c}$. This study explores the behavior of these parameters under varying vapor flow conditions, characterized by different Mach number, using the S-model.

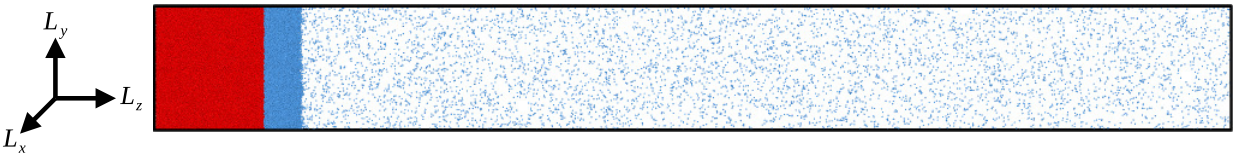

Figure 1: Schematic of the non-equilibrium MD domain.

A schematic of the non-equilibrium MD simulation is depicted in Fig.1 Its dimension parallel to the liquid/vapor interface is $L_{xy} = 200$Å, and orthogonal $L_z = 1500 - 7000$Å. It consist of an Argon liquid slab interaction with its vapor phase across a single interface modeling net-evaporation. Intermolecular forces are computed using a truncated and shifted Lennard-Jones 12-6 potential with $\sigma = 3.3916$Å,

* Corresponding author

$\epsilon/k_b = 137.90K$ and a cutoff radius $r_c = 2.5\sigma$[1]. A Nosé-Hoover[2] thermostat is applied to the liquid slab (red area) simulating a canonical ensemble (NVT) with a timestep $\Delta t = 4fs$. The liquid temperature is varied between $T_{th} = 90 - 130K$. Periodic boundary conditions are applied parallel to the interface. Orthogonal to the interface, a truncated Lennard-Jones potential holds the liquid in place at the lower wall. At the upper wall, the velocity distribution is forced to be symmetric about u_∞ which is the prescribed far-field vapor velocity[3]. Mach numbers $Ma = u_\infty/c_\infty$ range from 0.1 and 0.9, with c_∞ being the vapor speed of sound. A stationary interface position is maintained by continuously replenishing the liquid slab with new particles[4].

The steady-state form of the S-model kinetic equation [5] is defined as,

$$\mathbf{v} \cdot \frac{\partial f(z,\mathbf{v})}{\partial z} = \frac{(f^S - f)}{\tau} \tag{1}$$

where, $f(z,\mathbf{v})$ is the one particle molecular velocity distribution function, $\mathbf{v}$ is the molecular velocity vector, z is the direction orthogonal to the liquid/vapor interface, τ the relaxation time and f^S the Shakhov equilibrium distribution function. The S-model kinetic equation is solved using the discrete velocity method[6] in one-dimensional in the physical space and two dimensional in the molecular velocity space formulation. After solving Eq.(1), the velocity distribution function $f(z,\mathbf{v})$ is known. Macroscopic properties of the vapor phase such as temperature, pressure and number density are obtained by calculating the moments of the velocity distribution function f. At the lower boundary $z = 0$, the distribution function of evaporating particles is assumed to be a half range Maxwellian,

$$f(t,0,\mathbf{v}) = \left[\alpha_e n_s + (1-\alpha_c) n_r\right] \left(\frac{m}{2\pi k_b T_L}\right)^{3/2} \exp\left[-\frac{m|\mathbf{v}|^2}{2k_b T_L}\right], \quad v_z > 0 \tag{2}$$

with $\alpha_{e,c}$ the evaporation/condensation coefficients, n_r the number density of reflected particles[5] and m the molecular mass. The saturation vapor number density $n_s = p_s/(k_b T_L)$ is calculated using liquid temperature T_L saturation pressure $p_s = p(T_L)$. At the upper boundary of the simulation domain $z = L$, the vapor is assumed to be in equilibrium steady-state with prescribed far-field vapor velocity u_∞. The velocity distribution function for particles approaching the interface is,

$$f(t,L,\mathbf{v}) = \frac{p_v}{k_b T_v} \left(\frac{m}{2\pi k_b T_v}\right)^{3/2} \exp\left[-\frac{m|\mathbf{v}-\mathbf{u}_\infty|^2}{2k_b T_v}\right], \quad v_z < 0 \tag{3}$$

Results and Conclusions

The dependency of the evaporation α_e and condensation α_c coefficient and liquid temperature T_L is investigated for various vapor flow conditions using MD simulations. This requires defining a so-called liquid and vapor boundary. The position of the vapor boundary is determined using the method in Ref.[7]. For the liquid boundary position z_{L_b}, multiple locations near the liquid/vapor interface are randomly selected. For each liquid position, the corresponding liquid temperature and both coefficients are calculated. The resulting parameters are then provided as input to the S-model calculations. Its results are compared to MD results using the mean absolute percentage error (MAPE), which is defined as $100 \times \sum(|y_{MD} - y_S|/y_{MD})/N$ with y_{MD} and y_S the numerical results of MD and S-model respectively and N the number of data points. Fig.2 shows the MAPE for thermostat temperature $90K$, $Ma = 0.19$ and liquid boundary positions $-10 < z_{L_b} - z_m < 6$ where z_m is the position of the equimolar dividing surface. For higher Mach numbers and thermostat temperatures, the minimum error of pressure is almost consistently observed around $z_{L_b} = z_m$. In contrast, the density reaches its minimum deeper into the liquid phase as the thermostat temperature increases but shifts towards the liquid/vapor interface for higher Mach numbers.

Finally, the S-model simulation assumes ideal gas behavior. Using the compressibilty factor $0 < Z < 1$ (with $Z = 1$ corresponding to an ideal gas), the vapor approaches unity for lower thermostat temperatures and higher Mach numbers. Based on these observations, the liquid boundary position is chosen to be at the equimolar dividing surface for the remainder of the abstract, i.e. $z_{L_b} = z_m$.

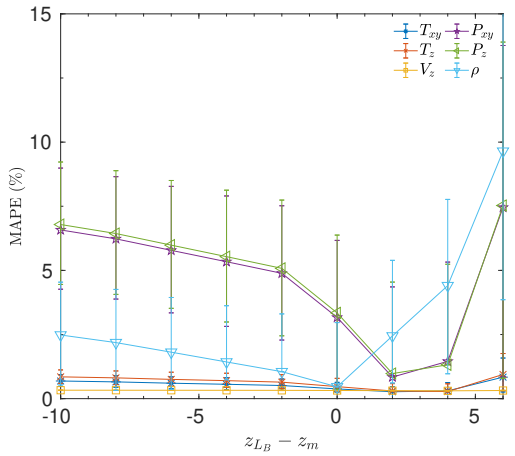

Figure 2: The mean absolute percentage error (MAPE) calculated for various liquid boundary positions using thermostat temperature $90K$ and $Ma = 0.19$. Error bars correspond to uncertainty in liquid temperature, i.e. $T_L \pm \sigma$.

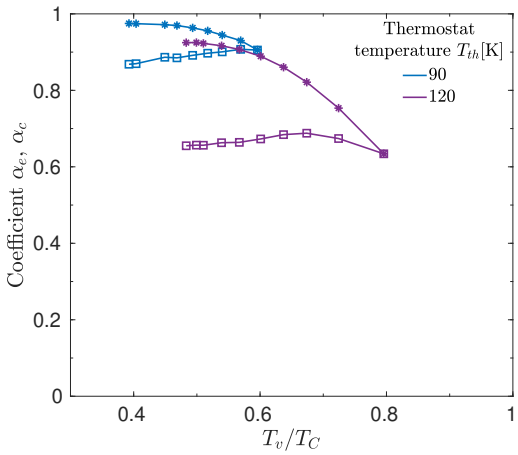

Figure 3: Evaporation (α_e,$*$) and condensation (α_c,$\square$) coefficient dependence on reduced temperature obtained from MD. Solid square corresponds to equilibrium simulation. T_C is critical argon temperature: 150.86K.

Fig.4 depicts the macroscopic profiles of density, temperature, pressure and velocity obtained both from the S-model and MD simulations at a thermostat temperature of $90K$. Each subfigure contains results for four Mach numbers, $Ma \approx 0.2, 0.4, 0.6$ and 0.8. A strong agreement is observed between the S-model and MD results for all properties and Mach numbers. For all simulations, the compressibility factor is high, with $Z > 0.95$. Evaporation and condensation coefficients obtained from MD for thermostat temperatures $90K$ and $120K$ and various Mach numbers are shown in Fig.3. Higher Mach numbers result in lower liquid temperatures T_L (i.e. more liquid cooling), leading to reduced vapor density ρ and temperature T_v. This enhances evaporation and increases the evaporation coefficient α_e. Conversely, condensation becomes more difficult, reducing its condensation coefficient α_c. For $T_{th} = 120K$, a slight increase in the condensation coefficient is observed before it decreases with increasing Mach number (i.e. lower T_v/T_C). This is most likely due to a rapid increase in liquid density near the interface (cooling effect) for $0 < Ma < 0.4$ which then saturates for $Ma > 0.4$. Vapor particles in the vicinity of the interface experience a higher attraction force from the liquid which increases the condensation coefficient.

In conclusion, positioning the liquid boundary close to the liquid/vapor interface provides better agreement between S-model and MD results. Furthermore, evaporation coefficients for both thermostat temperatures provide similar results as function of reduced temperatures T_v/T_C (i.e. Mach number). Whereas discrepancies of 0.2 or more are observed for the condensation coefficients. Further research is needed to clarify the mechanisms governing the behavior of α_e and α_c under high-Mach conditions.

Acknowledgements

This project has received funding from the European Union's Horizon 2020 research and innovation programme under the Marie Skłodowska-Curie grant agreement No. 643095.

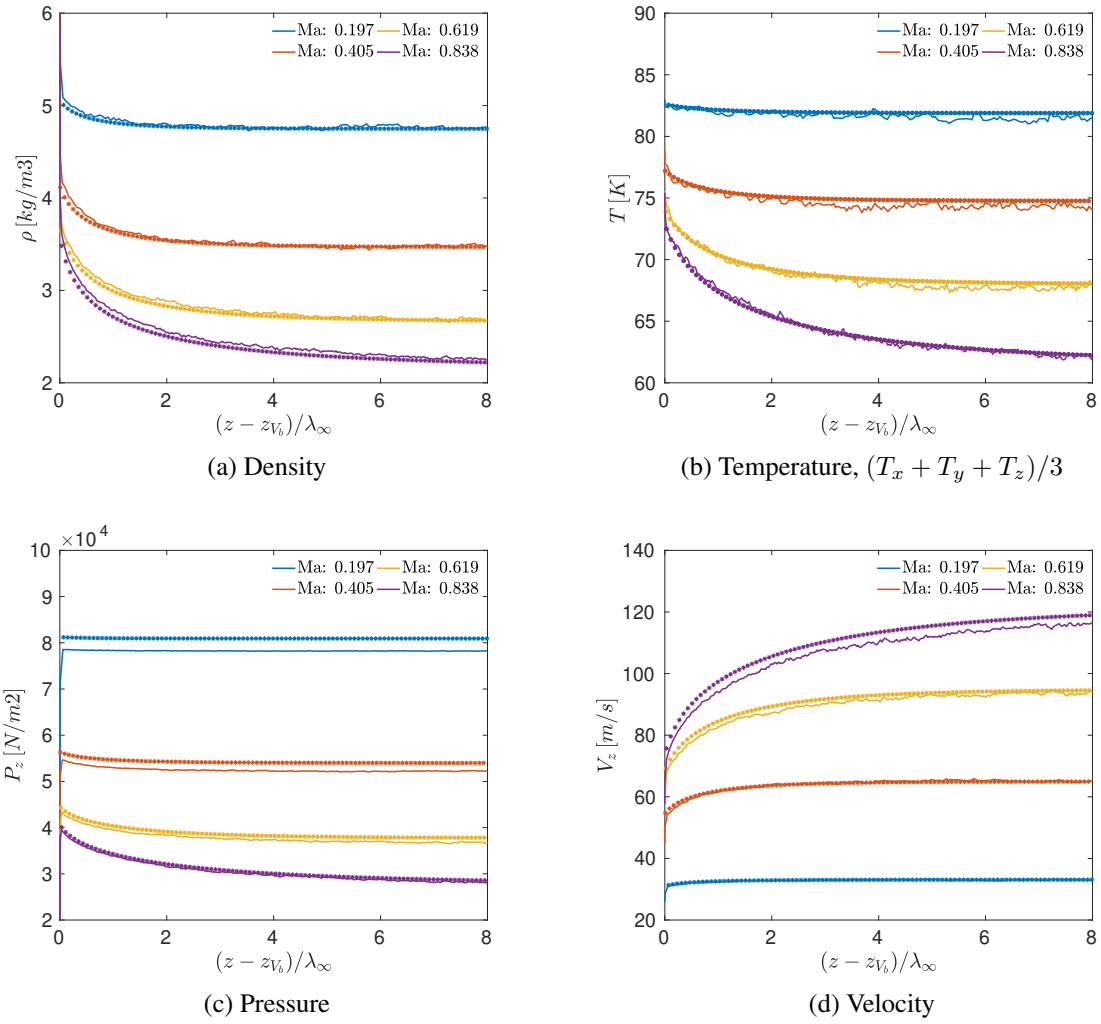

(a) Density

(b) Temperature, $(T_x + T_y + T_z)/3$

(c) Pressure

(d) Velocity

Figure 4: Comparison of the MD (solid line) results with the S-model (asterisk) results for thermostat temperature $90K$ and $Ma \approx 0.2, 0.4, 0.6$ and 0.84. S-model input parameters α_e, α_c and T_L are calculted from MD using the liquid boundary positioned at equimolar surface, i.e. $z_{L_b} - z_m = 0$. Here, λ_∞ denotes the mean free path as determined from Ref.[7] and z_{V_b} the vapor boundary position.

References and citations

[1] G. Rutkai, M. Thol, R. Span, and J. Vrabec, "How well does the lennard-jones potential represent the thermodynamic properties of noble gases?" *Molecular Physics*, vol. 115, no. 9-12, pp. 1104–1121, 2017. DOI: 10.1080/00268976.2016.1246760.

[2] G. Nosé, "A molecular dynamics method for simulations in the canonical ensemble," *Molecular Physics*, vol. 52, no. 2, pp. 255–268, 1984. DOI: 10.1080/00268978400101201.

[3] A. Frezzotti and C. Shen, "Kinetic theory description of the evaporation of multi-component substances," *Rarefied Gas Dynamics*, vol. 20, pp. 837–846, 1997.

[4] M. Heinen and J. Vrabec, "Evaporation sampled by stationary molecular dynamics simulation," *The Journal of Chemical Physics*, vol. 151, no. 4, p. 044 704, Jul. 2019. DOI: 10.1063/1.5111759. [Online]. Available: https://doi.org/10.1063/1.5111759.

[5] I. Graur and A. Polikarpov, "Comparison of different kinetic models for the heat transfer problem," *J. Heat and Mass Transfer*, vol. 46, pp. 237–244, 2009. DOI: 10.1007/s00231-009-0558-x.

[6] J. E. Broadwell, "Shock structure in a simple discrete velocity gas," *The Physics of Fluids*, vol. 7, no. 8, pp. 1243–1247, Aug. 1964. DOI: 10.1063/1.1711368.

[7] M. C. W. Wolf, R. Enright, S. V. Gaastra-Nedea, and A. J. H. Frijns, "Equilibrium evaporation coefficients quantified as transmission probabilities for monatomic fluids," *Physics of Fluids*, vol. 36, no. 6, p. 062 117, Jun. 2024. DOI: 10.1063/5.0213744.

NEGF26-679548

Experimental measurements of acetone diffusion coefficients in gas mixtures by molecular tagging

Andrea Luccon[1,2], Cathy Rond[1], Marcos Rojas-Càrdenas[1,2], John-Eric Dufour[1], Christine Barrot Lattes[1,2], Stephane Colin[1,2]
[1]Univ Toulouse, CNRS, IMT Albi, INSA Toulouse, ISAE-SUPAERO, ICA, Toulouse, France
[2]Univ Toulouse, CNRS, INP Toulouse, INSA Toulouse, FERMAT, Toulouse, France
andrea.luccon@univ-tlse3.fr, cathy.rond@insa-toulouse.fr, marcos.rojas@insa-toulouse.fr, john-eric.dufour@insa-toulouse.fr, stephane.colin@insa-toulouse.fr

KEY WORDS

microfluidics, molecular tagging velocimetry, molecular diffusion, gas microflows, phosphorescence, fluorescence

ABSTRACT

Introduction

The ability to precisely manipulate small fluid volumes, combined with compact size, low power consumption, and reduced fabrication and operating costs, has driven growing interest in the development of microfluidic systems. Among these, devices utilizing gas microflows are now employed in various applications, such as Knudsen pumps, micro heat exchangers, microactuators, and microsensors. For such systems, accurate experimental characterization of velocity and temperature fields is essential to predict and optimize their thermal and hydrodynamic performance.
At the microscale, the mean free path of gas molecules becomes comparable to the characteristic dimensions of the system, leading to flow regimes where rarefaction effects can no longer be neglected. In practice, most gas microflows fall within the slip-flow ($10^{-3} < \mathrm{Kn} < 10^{-1}$) or transitional ($10^{-1} < \mathrm{Kn} < 10$) regimes [1]. Under such conditions, non-equilibrium phenomena become significant, and the conventional continuum hypothesis coupled with the no-slip boundary condition fails to accurately describe the flow behavior. Consequently, reliable prediction of macroscopic velocity and temperature fields requires advanced theoretical and numerical models, whose validation critically relies on high-quality experimental data.
In this context, direct measurement of local flow properties is crucial both for optimizing the design of microfluidic systems and for validating models of rarefied gas dynamics. However, the availability of such data remains severely limited in the current literature, emphasizing the need for advanced experimental methodologies capable of capturing local flow characteristics with high spatial and temporal resolution.
Among the available diagnostic techniques, molecular tagging (MT) is a well-established method particularly suited for the experimental investigation of gas microflows. The method relies on the photolu-

minescent response of tracer molecules introduced into the carrier gas. When excited by a laser source with an appropriate wavelength, these molecules emit light through fluorescence or phosphorescence. By analyzing the luminescent signal (intensity and wavelength) and its temporal evolution, it is possible to extract thermodynamic and kinematic properties of the gas flow, including local temperature and velocity distributions.

Over the past decade, MT-based approaches have been increasingly applied to gas microflows, enabling both velocimetry and thermometry measurements [2, 3]. In Molecular Tagging Velocimetry (MTV), the local flow velocity is commonly estimated by dividing the average molecular displacement by the observation time interval. However, this purely advective model fails to resolve the full velocity profile, particularly near the wall, where it can artificially introduce a slip even under hydrodynamic no-slip conditions [4]. A more rigorous description requires accounting for both advective and diffusive transports, as formulated by Frezzotti et al. [5] through the advection–diffusion equation:

$$\frac{\partial s_x}{\partial t} = \bar{u}(y) + D_{2/1,2}\frac{\partial^2 s_x}{\partial y^2} \tag{1}$$

where s_x [m] is the mean molecular displacement obtained from the post-processed phosphorescence images, $\bar{u}(y)$ [m/s] is the velocity profile, and $D_{2/1,2}$ [m^2/s] is the diffusion coefficient of the tracer molecules (index 2) in the mixture with the carrier gas (index 1). The advection–diffusion formulation has been successfully applied to obtain high-quality measurements of slip velocity near solid boundaries in a 1-mm-deep rectangular microchannel [6]. However, to accurately reconstruct velocity profiles from molecular displacement data, a detailed understanding of tracer diffusion is essential, particularly under low-pressure conditions where diffusion effects play a significant role compared to advection.

In this framework, the present study provides the experimental diffusion data required to enhance the accuracy of MTV-based measurements. Acetone vapor is selected as the tracer molecule, as it is widely used in molecular tagging experiments. Both its self-diffusion and binary diffusion in helium and argon mixtures are investigated.

Measurement of diffusion coefficients in gas mixtures

The experimental determination of acetone diffusion coefficients is carried out by means of a molecular tagging approach. The technique consists in monitoring the spatial evolution of the phosphorescent emission from laser-excited tracer molecules using a high-sensitivity camera. Immediately after excitation, the tagged molecules form a narrow and well-defined emission pattern, which gradually broadens due to molecular diffusion. Figure 1 illustrates this phenomenon for acetone self-diffusion within a region of interest (ROI) along the laser beam path, showing the spatial distribution of the phosphorescent signal at 10, 20, and 50 µs after laser excitation. For each delay time, a one-dimensional intensity profile is obtained by averaging the phosphorescence signal along the laser beam direction. The resulting profiles can be spatially modeled as a Gaussian distribution, whose variance increases linearly with time as diffusion proceeds. By tracking the temporal evolution of the variance $\sigma_x^2(t)$, the diffusion coefficient $D_{2/1,2}$ can be determined from the Einstein relation [7]:

$$\sigma_x^2 = 2D_{2/1,2}t + \sigma_{x,0}^2 \tag{2}$$

where t [s] is the time after the laser excitation, $\sigma_{x,0}^2$ [m^2] is the variance of the initial light distribution. Originally developed for acetone and diacetyl self-diffusion studies by Fratantonio et al. [6] and later applied to pure acetone by Zhang et al. [8], the present work aims to improve the accuracy of acetone self-diffusion characterization and to extend the technique to binary mixtures with helium and argon.

To analyze the experimental results, the measured diffusion coefficients are compared with theoretical

predictions. A first estimate is obtained from Blanc's law [9]:

$$D_{2/1,2} = \frac{1}{\frac{x_2}{D_{22}} + \frac{x_1}{D_{21}}} \tag{3}$$

where x_i is the mole fraction of species i and D_{ij} [m^2/s] denotes the binary diffusion coefficient between species i and j.
According to the Chapman–Enskog kinetic theory [10], the binary diffusion coefficient D_{ij} is given by:

$$D_{ij} = \frac{3}{16\sqrt{\pi}} \sqrt{\frac{2k_B T}{m_{ij}}} \frac{f_D}{\sigma_{ij}^2 \Omega^{(1,1)} n} \tag{4}$$

where k_B [J/K] is the Boltzmann constant, T [K] is the absolute temperature, $m_{ij} = \frac{m_i m_j}{m_i + m_j}$ [kg] is the reduced mass, $\sigma_{ij} = \frac{\sigma_i + \sigma_j}{2}$ [m] is the average collision diameter, n the number density [m^{-3}], f_D a correction factor, and $\Omega^{(1,1)}$ the collision integral associated with the chosen intermolecular potential. The collision integral $\Omega^{(1,1)}$ is a function of the reduced temperature $T^* = \frac{k_B T}{\varepsilon_{ij}}$, where $\varepsilon_{ij} = \sqrt{\varepsilon_i \varepsilon_j}$ [J] represents the potential well depth characterizing the intermolecular interaction between species i and j, while ε_i [J] denotes the potential well depth corresponding to the self-interaction of the pure species i.
For non-polar species, the Lennard–Jones (LJ) potential is employed to compute the diffusion coefficients [11], whereas the Stockmayer (St) potential is adopted for polar molecules to account for dipole–dipole interactions [12]. The values of ε and σ adopted for acetone, helium, and argon are summarized in Table 1 for both Stockmayer and Lennard-Jones intermolecular potentials.

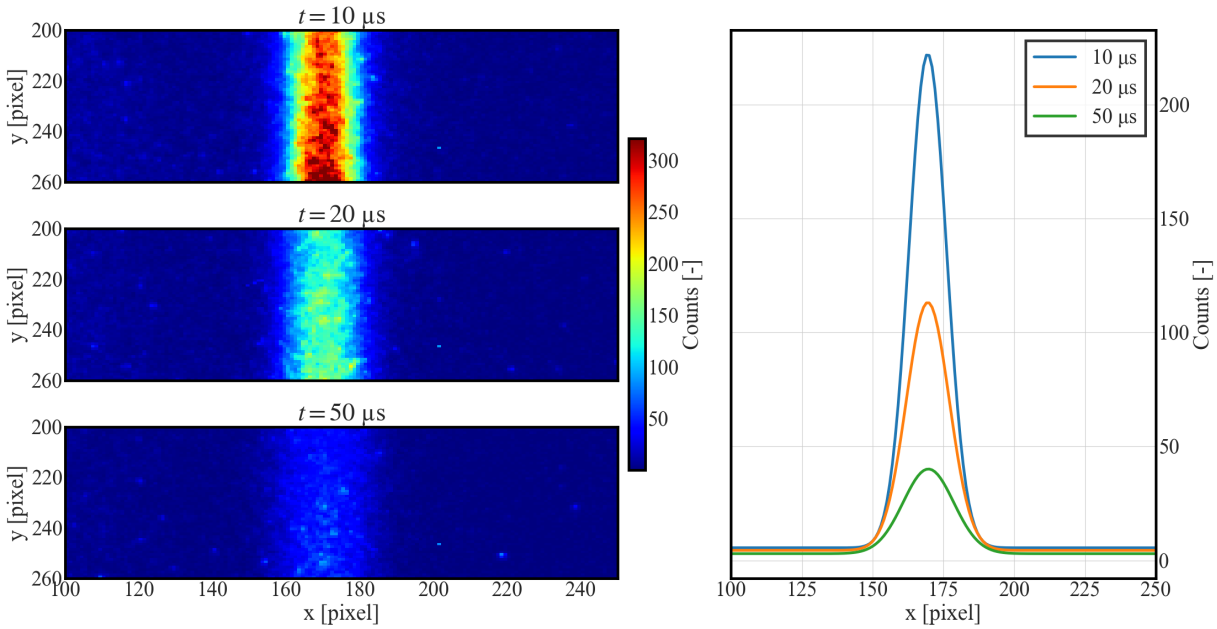

Figure 1: Two-dimensional phosphorescence intensity distributions of laser-tagged acetone within a selected region of interest (ROI) at interrogation delays of $t = 10$, 20, and 50 µs are presented, highlighting the progressive broadening of the tagged molecular line due to diffusion. The associated one-dimensional intensity profiles, obtained by averaging the phosphorescence signal along the y-direction and subsequently fitted with a Gaussian function, are reported for comparison.

Conclusions and perspectives

This study reports, for the first time, experimental measurements of acetone diffusion coefficients in gas mixtures obtained by means of molecular tagging. The present data provide a characterization of both self-diffusion and binary diffusion of acetone in helium and argon over a wide range of pressures and mixture compositions, addressing a lack of experimental data. The measured diffusion coefficients will be presented and compared with theoretical predictions based on Blanc's law and Chapman–Enskog kinetic theory during the conference presentation. Future work will focus on further improving the experimental methodology, reducing measurement uncertainties, and extending the investigation to other photoluminescence molecular tracers. The measured diffusion coefficients will then be integrated into the advection–diffusion reconstruction method, enabling accurate velocity profile measurements by molecular tagging velocimetry in gas flows.

Species	Lennard–Jones potential		Stockmayer potential	
	σ [pm]	ε/k_B [K]	σ [pm]	ε/k_B [K]
Acetone	466.9	519	450	549
Helium	257.6	10.22	—	—
Argon	343.2	122.4	—	—

Table 1: Molecular parameters adopted for acetone, helium, and argon according to the Lennard–Jones and Stockmayer intermolecular potentials. The Lennard–Jones parameters are taken from Bird [11], while the Stockmayer parameters are taken from Monchick and Mason [12]. All parameter values are derived from viscosity measurements.

Acknowledgements

Part of the work from the authors has been done with experimental facilities from Fédération de Recherche Fermat, FR 3089.

References and citations

[1] Colin, S. (2005). Rarefaction and compressibility effects on steady and transient gas flows in microchannels. *Microfluidics and Nanofluidics*, 1(3), 268–279.
[2] Yamaguchi, H., Hayashida, K., Ishiguro, Y., Takamori, K., Matsuda, Y., & Niimi, T. (2016). Micro-molecular tagging velocimetry of internal gaseous flow. *Microfluidics and Nanofluidics*, 20(2), 32.
[3] Bajić, S. (2023). Molecular Tagging Thermometry (MTT) for micro-channel gas flows (Doctoral dissertation, Université Toulouse 3–Paul Sabatier).
[4] Si Hadj Mohand, H., Frezzotti, A., Brandner, J. J., Barrot, C., & Colin, S. (2017). Molecular tagging velocimetry by direct phosphorescence in gas microflows: correction of Taylor dispersion. *Experimental Thermal and Fluid Science*, 83, 177–190.
[5] Frezzotti, A., Si Hadj Mohand, H., Barrot, C., & Colin, S. (2015). Role of diffusion on molecular tagging velocimetry technique for rarefied gas flow analysis. *Microfluidics and Nanofluidics*, 19(6), 1335–1348.
[6] Fratantonio, D., Rojas-Cárdenas, M., Barrot, C., Baldas, L., & Colin, S. (2020). Velocity measurements in channel gas flows in the slip regime by means of molecular tagging velocimetry. *Micromachines*, 11(4), 374.
[7] Einstein, A. (1956). Investigations on the Theory of the Brownian Movement. Courier Corporation.

[8] Zhang, Z., Fratantonio, D., Barrot, C., Rojas-Cardenas, M., & Colin, S. (2024). Measurements of diffusion coefficient and kinetic diameter of acetone vapor via molecular tagging. *Microfluidics and Nanofluidics*, 28(9), 62.
[9] Blanc, A. (1908). Recherches sur les mobilités des ions dans les gaz. *Journal de Physique Théorique et Appliquée*, 7(1), 825–839.
[10] Hirschfelder, J. O., Curtiss, C. F., & Bird, R. B. (1964). *The Molecular Theory of Gases and Liquids*. John Wiley & Sons.
[11] Bird, R. B. (2002). *Transport Phenomena*. Applied Mechanics Reviews, 55(1), R1–R4.
[12] Monchick, L., & Mason, E. A. (1961). Transport properties of polar gases. *The Journal of Chemical Physics*, 35(5), 1676–1697.

NEGF26-679128

EXPERIMENTALLY DETERMINING THE EFFECT OF GAS-SURFACE INTERACTIONS ON PARTICLE DYNAMICS IN RAREFIED FLOWS

Rick D.M. Jansen*[1], Rudie P.J. Kunnen[2], Herman J.H. Clercx[3]
Fluids and Flows Group and J.M. Burgers Center for Fluid Mechanics, Department of Applied Physics and Science Education, Eindhoven University of Technology, P.O. Box 513, 5600 MB Eindhoven, The Netherlands

r.d.m.jansen@tue.nl[1], r.p.j.kunnen@tue.nl[2], h.j.h.clercx@tue.nl[3]

KEY WORDS

Thermophoretic force, non-equilibrium gas, Knudsen number, energy accommodation coefficient, momentum accommodation coefficient, mean free path, particle tracking

ABSTRACT

Particle dynamics in equilibrium and non-equilibrium rarefied flows must be understood to reduce the impact of contaminants in equipment of the semiconductor industry. The particle dynamics in rarefied flows is described by the Knudsen number, which is the ratio of the mean free path of gas molecules over a characteristic length scale of the system, which in this case is the volume-equivalent radius. Gas-surface interactions are shown to be important in describing the net effect of the particle dynamics for the drag and thermophoretic forces; especially in the free-molecular limit. We conduct experiments where the momentum and energy accommodation coefficients of nitrogen, helium and argon can be measured indirectly and where we can see the effect of the accommodation coefficients on the dynamics of microparticles. This has been done by measuring settling velocities of these microparticles in low-pressure systems with and without a thermal gradient. Our measurements cover the entire transition regime and far into the free-molecular limit. Our results will contribute to an active contamination control in the semiconductor industry.

Introduction

There is a growing demand for understanding the particle dynamics in equipment used in the semiconductor industry. Friction forces in the production process of wafers lead to contaminants, which are submicron-sized particles that cause problems in the machine as the resolving resolution of the features on the wafers are becoming smaller by the day and are often smaller than the size of these contaminants. The dynamics of these contaminants must be understood to avert them from reaching vulnerable places and, therefore, reducing downtime of the machine. The machines operate at pressures from atmospheric to deep vacuum, which results in rarefied flows, where the mean free path of gas molecules, denoted by λ, becomes larger than the typical size of a particle whose characteristic length scale is described by its volume-equivalent radius r. The rarefaction for the particle can be described by the Knudsen number,

$$Kn = \lambda / r. \tag{1}$$

Gas expansions and compressions in the machine result in high thermal gradients leading to non-equilibrium states. In non-equilibrium rarefied states, gas-surface interactions become more important and are one of the dominant parameters that describe the particle dynamics. So far, there is a lack of understanding about particle dynamics in rarefied flows and how gas-surface interactions influence this. The primary cause of the limited understanding is the lack of experimental data concerning particle dynamics in the transition regime and free-molecular limit. We conduct experiments on the drag and thermophoretic force for melamine formaldehyde particles in different gases; nitrogen, argon and helium [1,2]. By measuring drag and thermophoretic forces in the free-molecular limit, we can measure the effect of the momentum and energy accommodation coefficient, respectively.

Methodology

The experiments are conducted by measuring the settling velocities of microparticles in low-pressure systems which are either filled with nitrogen, argon or helium. The setup that is being used can be seen in figure 1. The particles have sizes of (1.15±0.02) µm, (2.52±0.05) µm and (4.28±0.07) µm and the pressures range from 10 Pa to 10^5 Pa, where the accuracy of the pressures are within 0.2% of their absolute pressures.
A thermal gradient can be applied in the system by two copper plates that are placed vertically and are shielded from each other by a polystyrene window of (10.03±0.02) mm. The copper plates are kept at a fixed temperature using external water baths. The temperatures of the plates are measured by three thermistors per plate with an accuracy of 0.05 K each.
Particles are released in the system by a particle dispenser, which consists of the particle container and a shaker. The shaker vibrates the container, where a hole is made in the bottom. By shaking the container, particles are released through the hole into the system.
A vertical laser sheet (60 mW, 408 nm) illuminates the particles for their complete trajectory, which is recorded by a monochromatic CMOS camera with a maximum frame rate of 56 fps. The trajectory of the particle is reconstructed from the images by a self-made tracking program.
With the specifications of our setup, we can reach Knudsen numbers from 0.05 to 60, where the lower limit is due to the particle dispenser that creates an undesirable air flow, which is more significant at a higher pressure (small *Kn*) . The upper limit is a result of a low drag force and thus high particle velocities, which cannot be recorded by the current frame rate of the camera.

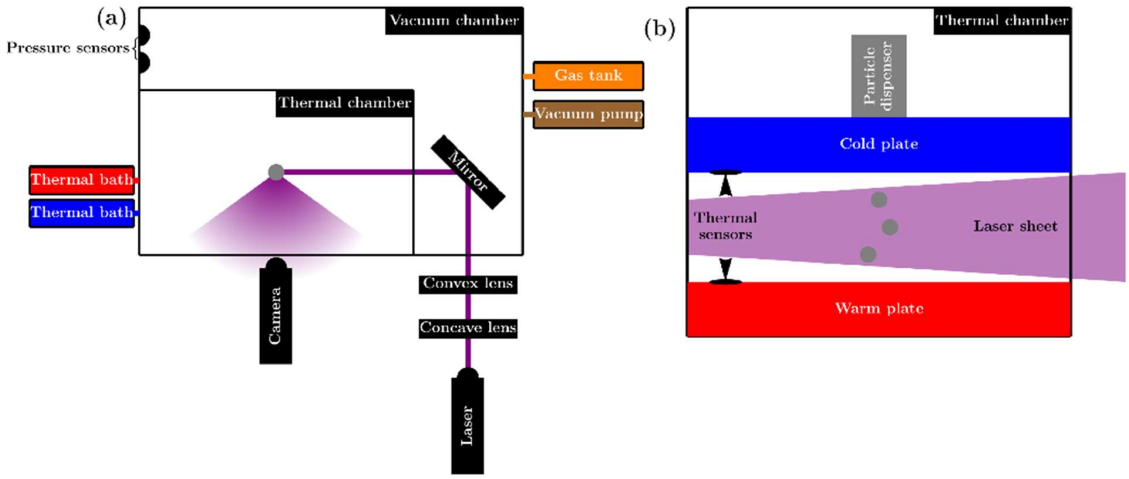

Figure 1. Experimental setup. **(a)** Top view with the vacuum chamber, thermal chamber and optical system. The thermal chamber is inside the vacuum chamber and its inside can be seen in the right figure. **(b)** Side view of the thermal chamber. The two thermal plates are set at different temperatures that are measured with three thermistors each. The particle dispenser is on top of the top plate and releases particles, which are illuminated with the vertically aligned laser sheet.

Results and discussion

The drag force is obtained by measuring the settling velocity without a temperature gradient in the system and its results can be seen in figure 2a. In the continuum limit, the drag force for a spherical particle should be equal to Stokes' drag [3]. When the system becomes more rarefied, a correction factor is needed to account for the velocity slip at the gas-surface interface described as

$$S(Kn) = F_{Stokes}/\, F_{drag}. \quad (2)$$

This is often described by the interpolation of Cunningham [4], where its constants are found experimentally by Millikan [5] and later analyzed by Allen and Raabe [6]. In the free-molecular limit, the drag is equal to the result of Epstein [7], where the momentum accommodation coefficient is included in the slip correction. By measuring the slip correction, a momentum accommodation coefficient for all used gases is found, which can be seen in table 1.

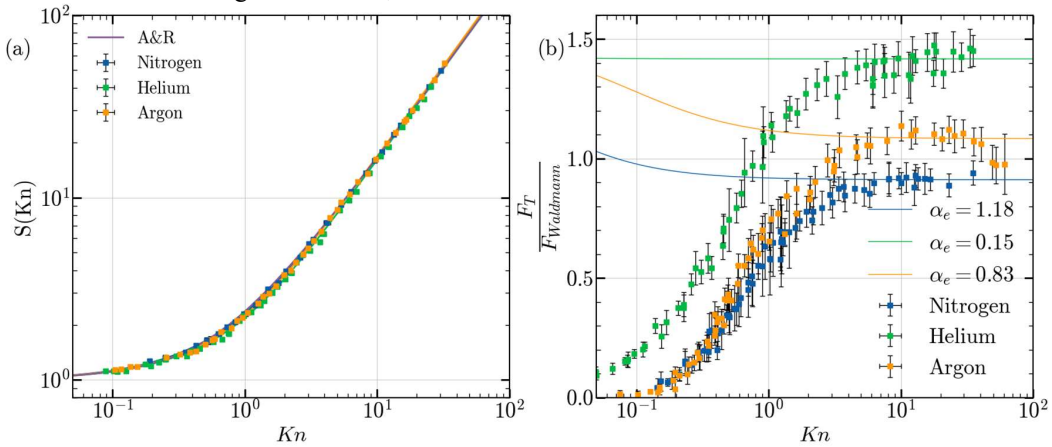

Figure 2. (a) The result of the drag measurements for nitrogen, helium and argon in blue, green and orange, respectively. The results are shown as the drag correction factor *S(Kn)* versus the Knudsen number. In purple, the result of Allen and Raabe [6] can be seen. **(b)** The result of the thermophoretic force measurements for nitrogen, helium and argon in blue, green and orange, respectively. The results are shown by normalizing the data with the result of Waldmann [8]. The solid lines are the limits of Ivchenko and Yalamov [9] with their corresponding energy accommodation coefficients (α_e).

The thermophoretic force is found experimentally in the same way as the drag measurements, but now a vertical thermal gradient is applied, which reduces the settling velocities of the particles. A well-known result of the thermophoretic force is given by Waldmann [8], where the energy accommodation coefficient is assumed to be equal to one. From the experimental results that is shown in figure 2b, we can clearly see that this is not always the case and another result given by Ivchenko and Yalamov [9], where the energy accommodation coefficient is taken into account, is suited better for predicting the thermophoretic force in the free-molecular limit. The result of nitrogen, where an energy accommodation coefficient higher than one is found, leads to the discussion if the model of Ivchenko and Yalamov is suited for the free-molecular limit. The chosen scattering kernel that Ivchenko and Yalamov use, leads to an energy accommodation coefficient higher than one. Chernyak and Sograbi [10] described the effect of the accommodation coefficients on the thermophoretic force in the free-molecular limit and found that it differs per scattering kernel. However, the experimental data, together with the result of Ivchenko and Yalamov can still be used as a proxy value for predicting the thermophoretic force. A more accurate scattering will eventually lead to better approximations for the accommodation coefficients. In the transition regime, the results [1,2] match with the predictions of Beresnev and Chernyak [11] and the results of Young [12]. Both analytical predictions are not shown in the figure for clarity.

Gas	Momentum accommodation coefficient	Energy accommodation coefficient
Nitrogen	0.96 ±0.08	1.18 ±0.01
Helium	0.9 ±0.1	0.15 ±0.03
Argon	1.0 ±0.1	0.83 ±0.03

Table 1. The results of the momentum and energy accommodation coefficients by measuring the drag and thermophoretic force in the free-molecular limit, respectively.

Conclusions

We have conducted experiments and measured the drag and thermophoretic force of microparticles in rarefied flows over the entire transition regime and into the free-molecular regime. By measuring these forces in the free-molecular limit, we can experimentally find proxy values for the momentum and energy accommodation coefficients for nitrogen, helium and argon. The effects of these coefficients can be seen in the entire transition regime. For future research, we will look into the effects of rarefaction on the drag and thermophoretic forces of nonspherical particles and rarefaction effects of the system on the particle.

Acknowledgments

The authors would like to thank F.M.R. van Uittert, G.W.J.M. Oerlemans and J.M. van der Veen for their skilful technical support. This research is co-financed by Holland High Tech with PPP allowance for research and development in the Dutch top sector of High-Tech Systems and Materials. We are grateful for our collaboration with and financial support of VDL Enabling Technologies Group.

References and Citations

[1] Jansen, R. D. M., Reinartz, R. R. L., Zhu, H., Kunnen, R. P. J., & Clercx, H. J. H. (2025). Experiments on the thermophoretic force on particles in the transition regime of rarefied flows. Physical Review E, 111, 035106.
[2] Jansen, R. D. M., Kunnen, R. P. J., & Clercx, H. J. H. (2025). Experiments on the thermophoretic force on particles in the transition regime of rarefied flows: An extension to diatomic gases. Aerosol Science and Technology, 59, 1586–1595.
[3] Stokes, G. G. (1851). On the effect of the internal friction of fluids on the motion of pendulums. Transactions of the Cambridge Philosophical Society, 9, 1–8.
[4] Cunningham, E. (1910). On the velocity of steady fall of spherical particles through a fluid medium. Proceedings of the Royal Society of London A, 83, 357–365.
[5] Millikan, R. A. (1923). The general law of fall of a small spherical body through a gas, and its bearing upon the nature of molecular reflection from surfaces. Physical Review, 22, 1–23.
[6] Allen, M., & Raabe, O. (1982*). Re-evaluation of Millikan's oil drop data for the motion of small particles in air.* Journal of Aerosol Science, 13, 537–547.
[7] Epstein, P. S. (1924). On the resistance experienced by spheres in their motion through gases. Physical Review, 23, 710–733.
[8] Waldmann, L. (1959). Über die Kraft eines inhomogenen Gases auf kleine suspendierte Kugeln. Zeitschrift für Naturforschung A, 14, 589–599.
[9] Ivchenko, I., & Yalamov, Y. I. (1973). Thermophoresis of aerosol particles in the nearly free molecular regime. Fluid Dynamics, 5, 355–360.
[10] Chernyak, V. G., & Sograbi, T. V. (2019). The role of molecule–surface interaction in thermophoresis of an aerosol particle. Journal of Aerosol Science, 128, 62–71. https://doi.org/10.1016/j.jaerosci.2018.11.012
[11] Beresnev, S., & Chernyak, V. (1995). Thermophoresis of a spherical particle in a rarefied gas: Numerical analysis based on the model kinetic equations. Physics of Fluids, 7, 1743–1756.
[12] Young, J. B. (2011). Thermophoresis of a spherical particle: Reassessment, clarification, and new analysis. Aerosol Science and Technology, 45, 927–941.

NEGF26-678798

EXTENSION OF UNIGASFOAM SOLVER TO MULTISCALE RAREFIED POLYATOMIC GAS FLOWS

Nikos Vasileiadis[*1], **Gianluca Di Staso**[1]
[1]Flow Matters Consultancy BV, Groene Loper 5, 5612 AE, Eindhoven, The Netherlands
nvasilei@flow-matters.com, gds@flow-matters.com

KEY WORDS

direct simulation Monte Carlo, unified stochastic particle, hybrid method, multiscale flow, OpenFOAM

ABSTRACT

Multiscale rarefied gas dynamics play a central role in a wide range of technological applications, from micro-electro-mechanical and micropropulsion systems (1; 2) to planetary atmosphere entry and hypersonic flight (3; 4). These flows often span the entire spectrum of gas rarefaction and thus require modeling approaches capable of capturing the continuum, slip, transition, and free-molecular flow regimes both accurately and efficiently. Conventional continuum descriptions based on the Navier-Stokes-Fourier (NSF) equations are efficient and accurate in the continuum and slip regimes but break down in transition and free-molecular flows, where reduced intermolecular interactions invalidate linear constitutive laws. On the other hand, the direct simulation Monte Carlo (DSMC) method (5) is valid across all regimes but becomes computationally prohibitive in the continuum limit due to its time-step and cell-size limitations.

To address this challenge, hybrid continuum-DSMC methods have been developed, coupling finite-volume computational fluid dynamics (CFD) solvers with DSMC to resolve continuum and rarefied regions, respectively. Domain decomposition (DD) methods (7; 6) and heterogeneous multiscale (HM) approaches (8; 9; 10) have been explored, with several general-purpose solvers now available. However, coupling distinct CFD and DSMC solvers introduces significant numerical and practical difficulties. These include the need for robust data exchange across solver boundaries, potential instabilities due to DSMC statistical noise propagating into the CFD region, and reduced efficiency in both steady and unsteady flows due to iterative coupling and large particle requirements (in the order of thousands per cell), respectively (11).

Therefore, recent efforts have focused on alternative multiscale particle-based methods. The Stochastic Particle (SP) (12), Unified Stochastic Particle (USP) (13), and Crank-Nicolson Stochastic Particle (CNSP) (14) approaches replace DSMC's collision step with BGK-type relaxation models, allowing the use of larger cells and, in the case of USP and CNSP, removing time-step constraints associated with collision dynamics. Although efficient in the continuum and slip regimes, these methods lose accuracy

[*] Corresponding author

in the transition and free-molecular regimes since simplified expressions are used to replace the original Boltzmann collision operator. To overcome this, hybrid particle-particle schemes such as SP-DSMC and USP-DSMC have been proposed, combining the efficiency of SP-type schemes in continuum regions with the accuracy of DSMC in rarefied conditions.

Recently, the uniGasFoam solver has been developed as an open-source framework for particle-based multiscale rarefied gas flows (11). Developed entirely within OpenFOAM, uniGasFoam was built on the established dsmcFoam+ solver and offered versatile simulation capabilities, including full DSMC, SP, and USP methods, as well as hybrid SP-DSMC and USP-DSMC approaches. However, uniGasFoam is restricted to monoatomic gas flows, which greatly limits its applicability to real-world problems. In this work, uniGasFoam is extended to polyatomic gas flows by implementing the polyatomic ESBGK model developed by Mathiaud et al. (15).

The algorithm of the uniGasFoam solver closely follows that of a conventional DSMC solver. Initially, simulation input data are read from their respective dictionaries, and computational particles are stochastically initialised within the flow domain. Upon starting the simulation, each time step follows a structured sequence of steps. First, particles are moved deterministically, and boundary conditions are applied. Next, macroscopic quantities of interest such as density, temperature, and velocity are sampled. In the case of a hybrid simulation, the flow domain is decomposed into continuum and rarefied regions based on the applied breakdown criteria, at a user-defined frequency. In uniGasFoam, the domain decomposition is based on the maximum gradient local-length Knudsen number criterion

$$Kn_{GLL} = \max(Kn_{\rho}, Kn_{T_{tr}}, Kn_{\mathbf{u}}), \quad Kn_{\phi} = \frac{\lambda}{\phi}|\nabla\phi|, \tag{1}$$

where λ denotes the gas mean free path, while ρ, T_{tr} and $\mathbf{u}$ denote the macroscopic gas density, translational temperature and velocity vector, respectively. In rarefied cells, binary DSMC collisions are performed, while in continuum cells, particles relax to an underlying target distribution depending on the implemented SP or USP model. After the collision step, the macroscopic quantities of interest are averaged and outputted. The algorithm then proceeds to the next time step and repeats the described process until the final simulation time is reached.

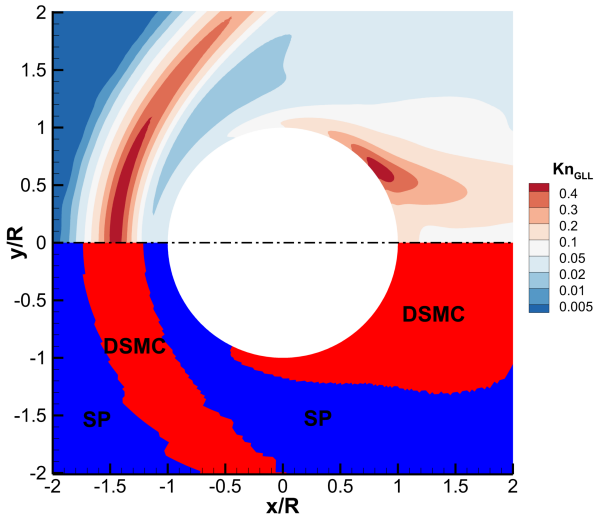

Figure 1: Maximum gradient local-length Knudsen number Kn_{GLL} (top), along with SP-DSMC regions (bottom) predicted by uniGasFoam.

The hybrid module of uniGasFoam with the implemented polyatomic ESBGK model is validated in several benchmarks, and the hypersonic flow past a cylinder is shown here (16). In the presented benchmark, nitrogen flow with number density $n_\infty = 1.61 \times 10^{21}\ m^{-3}$, temperatures $T_{tr,\infty} = T_{rot,\infty} = T_{vib,\infty} = 217.5\ K$ and velocity $u_{x,\infty} = 4510\ m/s$ past a cylinder with a diameter of $D = 0.08\ m$ and a constant temperature of 1000 K is considered. These conditions correspond to a global Knudsen number of $Kn = 0.01$ and a Mach number of $Ma = 15$. The maximum gradient local-length Knudsen number, along with the continuum (SP) and rarefied (DSMC) regions are presented in Fig. 1, where it can be seen that the domain decomposition, based on the local-length Knudsen number criterion is able to correctly identify the non-equilibrium bow shock, Knudsen layer, and wake regions. In Fig. 2 the velocity magnitude, as well as the translational, rotational, and vibrational temperatures predicted by uniGasFoam and dsmcFoam+ are provided. It is seen that the hybrid module of uniGasFoam is in excellent agreement with dsmcFoam+ for the velocity magnitude, as well as the translational and rotational temperatures, while some discrepancies can be observed for the vibrational temperature at the post-shock region. Regarding the computational cost, both simulations were run using the same numerical parameters utilizing 10 cores of an AMD Ryzen Threadripper 1950X. In this specific case, the hybrid uniGasFoam simulation was 8.5 times faster than the full DSMC one.

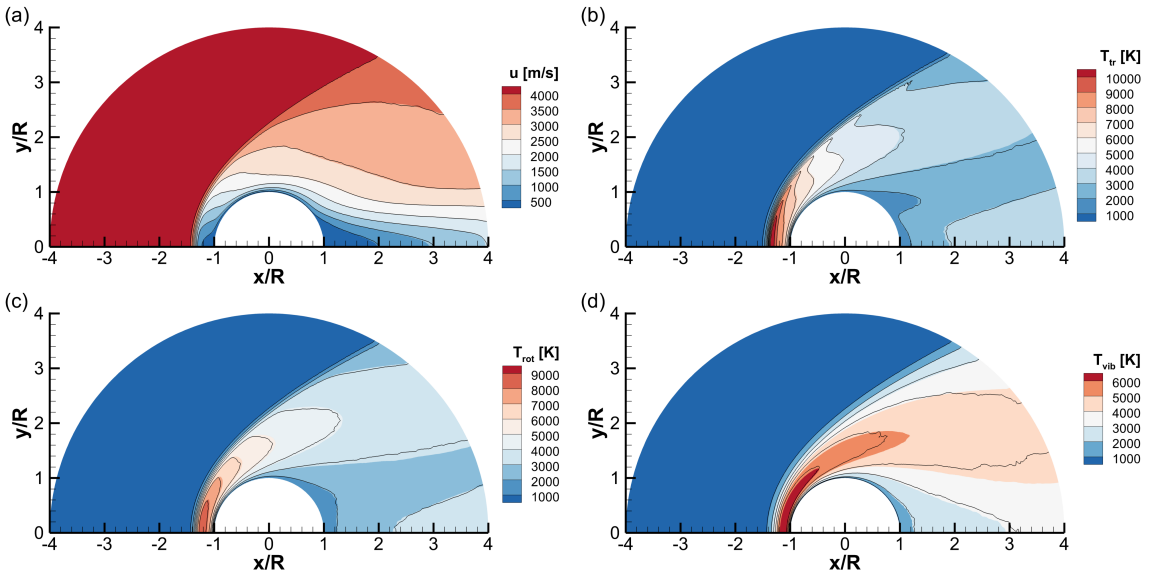

Figure 2: Comparison of (a) velocity magnitude, (b) translational, (c) rotational and (d) vibrational temperature obtained by uniGasFoam (solid lines) and dsmcFoam+ (colour flood).

In conclusion, the multiscale particle-based uniGasFoam solver has been extended to polyatomic gas flows. The polyatomic gas module of uniGasFoam has been validated in several benchmarks and the hypersonic flow past a cylinder has been presented here. It is evident that, the hybrid SP/DSMC approach accurately captures the underlying non-equilibrium phenomena, yielding results in excellent agreement with pure DSMC while significantly reducing the required computational cost. Future development of uniGasFoam will focus on extending its capabilities to include multi-species gas mixtures, further enhancing its versatility for complex gas flow simulations.

References

[1] Aktas, O., & Aluru, N. (2002). A Combined Continuum/DSMC Technique for Multiscale Analysis of Microfluidic Filters. J. Comput. Phys., 178, 342-372.
[2] Yang, Z., Tang, Z. Y., Cai, G. B., & He, B. J. (2017). Development of a Coupled NS-DSMC Method for the Simulation of Plume Impingement Effects of Space Thrusters. Thermophys. Aeromech., 24, 835-847.
[3] Wang, W. L., & Boyd, I. D. (2003). Hybrid DSMC-CFD Simulations of Hypersonic Flow over Sharp and Blunted Bodies. 36th AIAA Thermophysics Conference.
[4] Anderson, J. D. (2006). Hypersonic and High-Temperature Gas Dynamics. Reston, VA: American Institute of Aeronautics and Astronautics.
[5] Bird, G. A. (1994). Molecular Gas Dynamics and the Direct Simulation of Gas Flows. Oxford: Clarendon Press.
[6] Roveda, R., Goldstein, B. D., & Varghese, P. L. (1998). Hybrid Euler/Particle Approach for Continuum/Rarefied Flows. J. Spacecr. Rockets., 35, 258-265.
[7] Wadsworth, D., & Erwin, D. (1990). One-dimensional Hybrid Continuum/Particle Simulation Approach for Rarefied Hypersonic Flows. 5th Joint Thermophysics and Heat Transfer Conference.
[8] Garcia, L. A., Bell, J. B., Crutchfield, W. Y., & Alder, B. J. (1999). Adaptive Mesh and Algorithm Refinement Using Direct Simulation Monte Carlo. J. Comput. Phys., 154, 134-155.
[9] Docherty, S. Y., Borg, M. K., Lockerby, D. A., & Reese, J. M. (2014). Multiscale Simulation of Heat Transfer in a Rarefied Gas. Int. J. Heat Fluid Flow, 50, 114-125.
[10] Lockerby, D. A., Patronis, A., Borg, M. K., & Reese, J. M. (2015). Asynchronous Coupling of Hybrid Models for Efficient Simulation of Multiscale Systems. J. Comput. Phys., 284, 261-272.
[11] Vasileiadis, N., Tatsios, G., White, C., Lockerby, D. A., Borg, M. K., & Gibelli, L. (2025). uniGasFoam: A Particle-Based OpenFOAM Solver for Multiscale Rarefied Gas Flows, Comput. Phys. Commun., 310, 109532.
[12] Pfeiffer, M. (2018). Particle-Based Fluid Dynamics: Comparison of Different Bhatnagar-Gross-Krook Models and the Direct Simulation Monte Carlo Method for Hypersonic Flows. Phys. Fluids., 30, 106106.
[13] Fei, F., Zhang, J., Li, J., & Liu, Z. H. (2020). A Unified Stochastic Particle Bhatnagar-Gross-Krook Method for Multiscale Gas Flows. J. Comput. Phys., 400, 108972.
[14] Pfeiffer, M., Garmirian, F., & Ott, T. (2025). Crank-Nicolson Bhatnagar-Gross-Krook Integrator for Multiscale Particle-Based Kinetic Simulations. Phys. Fluids., 37, 023616.
[15] Mathiaud, J., Mieussens, L., & Pfeiffer, M. (2021). An ES-BGK model for Diatomic Gases with Correct Relaxation Rates for Internal Energies. Eur. J. Mech. B Fluids., 96, 65-77.
[16] Deschenes, T. R., & Boyd, I. D. (2011). Extension of a Modular Particle-Continuum Method to Vibrationally Excited, Hypersonic Flows. AIAA J., 49, 1951-1959.

NEGF26-678830

FABRICATION OF A KNUDSEN MICROPUMP FOR OPERATION ABOVE ATMOSPHERIC PRESSURES

Phassawat Leelaburanathanakul*[1], Thanasis Basdanis[1], Thierry Camps[2], Marcos Rojas-Cárdenas[1], Christine Barrot[1], Lucien Baldas[1], Jürgen J. Brandner[3], Stéphane Colin[1]

[1] Univ Toulouse, CNRS, IMT Mines Albi, INSA Toulouse, ISAE-SUPAERO, ICA,
3 rue Caroline Aigle, Toulouse, France
[2] CNRS, LAAS, 7 Avenue du Colonel Roche, Toulouse, 31400, France
[3] Institute of Microstructure Technology (IMT), Karlsruhe Institute of Technology,
76344 Eggenstein-Leopoldshafen, Germany
* Corresponding Author: leelabur@insa-toulouse.fr

KEY WORDS

Nanochannels, thermal transpiration, laser fabrication, rarefied gas flows, microflows, microfluidics

ABSTRACT

Introduction

Employing the thermal transpiration effect, Knudsen pumps have been demonstrated for vacuum generation and micro-gas flow delivery in micro/nanoelectromechanical systems (MEMS/NEMS) platforms, for diverse applications such as micro-gas chromatography, gas separation and gas handling [1, 2]. These pumps use temperature gradients to enable the transport of gas under rarefied conditions without moving parts, allowing for robust and vibration-free operation. Significant thermal transpiration occurs in the transitional rarefied flow regime, where channel dimensions are on the order of the molecular mean free path λ, which corresponds to a rarefaction parameter δ near = 3.5 [3, 4], with

$$\delta = pr/\mu u_0 \quad (1)$$

where p, r, μ, $u_0 = (2R_gT)^{\omega}$, R_g, T, ω correspond to the local pressure, channel radius, fluid dynamic viscosity, most probable speed, gas constant, temperature, and gas viscosity exponent, respectively.

As a consequence, obtaining effective thermal transpiration at or above atmospheric pressure will require pumping channels with hydraulic diameters of around 600 nm, which introduces significant challenges in the design and fabrication of the device. Multiple pumping stages and parallel channels can be implemented to achieve greater pressure differences (ΔP) and mass flow ($\dot{m}$). As the operating pressure increases with the number of stages, the hydraulic diameter required to maintain transitional rarefied regime decreases inversely. While a reduction in channel size is necessary to optimize the maximum pressure difference (ΔP_{max}) at mean pressure P_{mean} above 1 atm, numerical modeling indicates that the maximum mass flow ($\dot{m}_{max}$) increases monotonically with mean pressure. Hence, the 600 nm channel design is optimized for the initial atmospheric intake stage, with ΔP decreasing and $\dot{m}$ no longer limited in the subsequent stages as the P_{mean} increases above 1 atm.

Several fabrication methods reported in the literature rely on conventional MEMS techniques such as photolithography, thin-film deposition, deep reactive-ion etching (DRIE), and wafer bonding to

* Corresponding author

define and seal microchannels with integrated heaters and thermal isolation [1]. Alternative approaches employ nanoporous membranes—such as anodic aluminum oxide (AAO), silica aerogels, or polymer membranes—to achieve high pore density and surface area for thermal transpiration [5]. More recent efforts have explored additive manufacturing techniques, such as two-photo-polymerization (TPP), to create tapered flow channels from IP-Q (Immersion Photoresist, Nanoscribe GmbH) photoresists [6].

These techniques, however, present significant limits for the development of effective pumps operating around atmospheric pressure. For instance, the typical aspect ratio of DRIE is insufficient to create long, sub-micron channels required in a low-thermal-conductivity material like glass. Nanoporous materials like AAO, while offering high pore density, often introduce high flow impedance and restrict gas throughput. Furthermore, additive techniques like TPP, while precise, are serial in nature and impractically slow for fabricating over hundreds of thousands of parallel channels needed for sufficient mass flow.

To overcome these limitations, our work leverages a novel fabrication approach utilizing ultrafast femtosecond laser processing with nondiffracting Bessel beams [7, 8]. The quasi-distortion-free propagation of Bessel beams allows for the confinement of high-intensity light over extended distances, enabling the extremely fast, single-shot fabrication of taper-free nanochannels [9]. This technique directly addresses the primary challenge, as it can produce channels with sub-micron diameters (e.g., 200-800 nm), and exceptionally high aspect ratios (>100:1) at 1 kHz speed [8, 9], fulfilling the requirements to maintain the transitional rarefied regime at atmospheric pressure.

Design

The Knudsen pump design is centered on the femtosecond Bessel beam fabrication technique used to create the nanochannel pumping structure. This structure consists of approximately 300,000 nanochannels arranged in a dense hexagonal lattice to maximize channel density within a 10×10 mm² footprint, centered on a 20×25 mm² Borofloat 33 glass sample (Fig. 1b). The channel geometry was selected based on kinetic modeling of thermal transpiration flows. While the Bessel beam method allows for sub-micron-scale channels, a critical fabrication constraint is maintaining an inter-channel spacing of 10-20 µm to ensure the structural integrity of the glass and prevent cracking during processing. To create the thermal transpiration effect, a temperature gradient is established across the glass thickness. This is achieved by integrating localized heaters on the "hot side" near the nanochannels and silicon pillar heatsinks on the "cold side" (Fig. 1a). The heaters are composed of a multi-layer metal stack (titanium, titanium-tungsten, and gold). At the nanochannels locations, the top gold and titanium-tungsten layers are selectively etched away, retaining a 20-nm layer of titanium that functions as the resistive heater. Conversely, the silicon pillar heatsinks leverage the high thermal conductivity contrast between silicon and glass to efficiently diffuses heat away from the cold side. Thermal simulations validate this design, predicting that a 10 W input power to the heaters generates a 47°C temperature difference across the glass thickness.

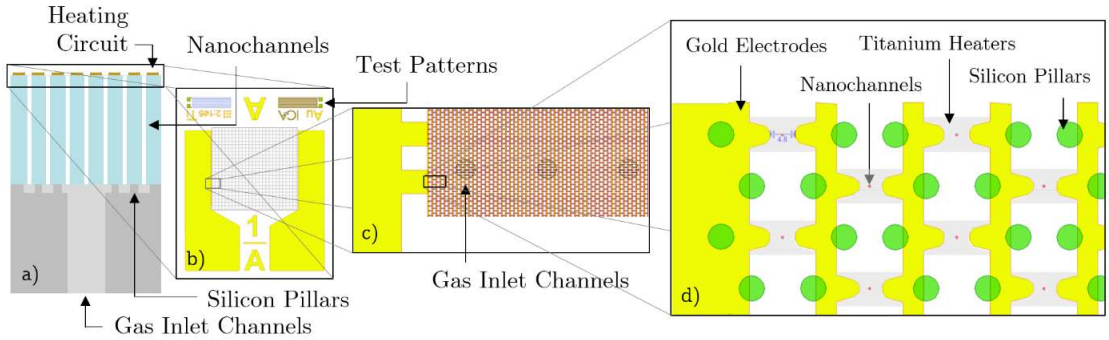

Figure 1: Schematic of the Knudsen micropump design. a) Cross-sectional view illustrating the main components for generating the thermal gradient: the top heating circuit, the central glass substrate with nanochannels, and the silicon pillars acting as a heatsink on the “cold side” of the glass. b) Top-down layout of the device, showing the electrical gold pads and the central 10×10 mm² nanochannels array. c) Magnified view of the hexagonal

nanochannel lattice and gas inlet channels. d) Detailed schematic of the "hot side", showing gold electrodes and the 20-nm titanium heaters around the nanochannels, with the underlying silicon pillars shown for reference.

Fabrication and Testing

The device fabrication follows a multi-step MEMS process (Fig. 2). First, a 400 µm silicon wafer is patterned on its top side with 15 µm-high micro-pillars (heatsinks) via RIE (Fig. 2a), and gas inlet through-holes are etched from the underside using DRIE (Fig. 2b). This structured silicon wafer is then anodically bonded to the 500 µm-thick Borofloat 33 glass wafer (Fig. 2c). Next, the core array of nanochannels (0.6 µm diameter, 500 µm deep) is fabricated in the glass using the Bessel beam technique, aligned using pre-etched markers (Fig. 2d).

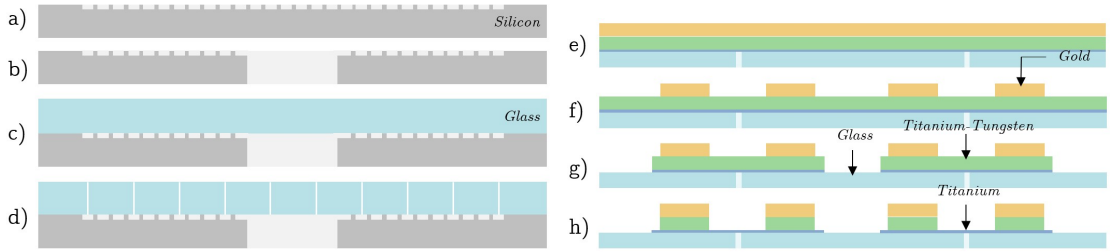

Figure 2. Cross-sectional schematic of the main fabrication steps. a) RIE patterning of 15 µm-high silicon micro-pillars (heatsinks) on the Si wafer. b) DRIE etching of gas inlet through-holes from the wafer's underside. c) Anodic bonding of the 500 µm-thick Borofloat 33 wafer to the structured silicon wafer. d) Bessel beam fabrication of the 0.6 µm diameter nanochannels through the glass. e) Deposition of the 20 nm Ti / 322 nm Ti-W / 108 nm Au metal stack. f) Wet etching of the Au layer to define the low-resistance electrodes. g) Wet etching of the Ti-W barrier layer and the 20 nm Ti layer. h) Global etching of the Ti-W to define the final high-resistance heaters.

Finally, the heating circuit is fabricated by depositing a 20 nm Ti / 322 nm Ti-W / 108 nm Au multilayer stack (Fig. 2e). This stack is patterned via three sequential photolithography and wet-etching steps: (1) the Au is patterned (KI/I_2 etchant) to define the low-resistance electrodes (Fig. 2f); (2) the Ti-W layer—which also serves as a sacrificial mask to protect the nanochannels from photoresist—is patterned (H_2O_2) (Fig. 2g); (3) the Ti layer is patterned (dilute HF) to form the high-resistance heaters (Fig. 2g). A final global etch using H_2O_2 removes all remaining exposed Ti-W (Fig. 2h).

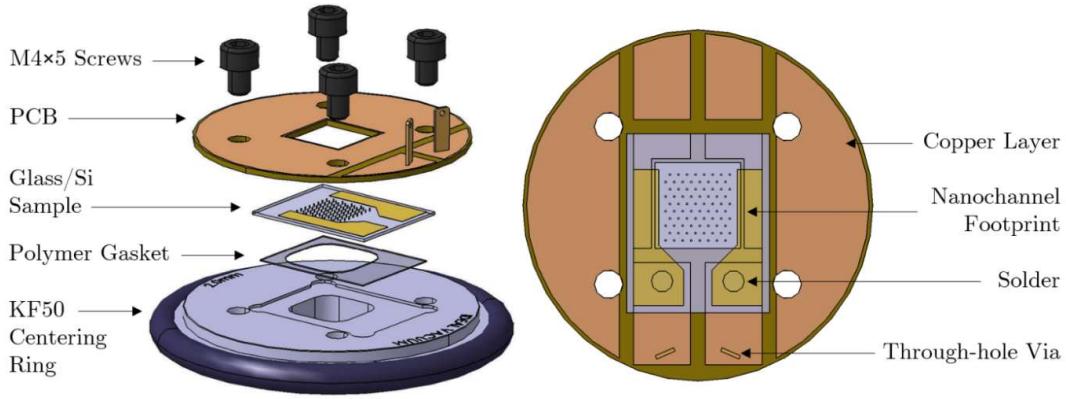

Figure 3. Device assembly for experimental testing. (Left) Exploded isometric view of the test fixture, showing the M4x5 screws, the custom PCB, the Glass/Si nanochannel sample, the polymer sealing gasket, and the machined ISO KF50 centering ring. (Right) Bottom view of the PCB layout, illustrating the copper traces, the central aperture for the nanochannel footprint, the raised solder spots for electrical contact, and the through-hole vias that route the connection.

For experimental characterization, the device is integrated into a custom test fixture designed to interface with standard ISO KF50 vacuum fittings (Fig. 3). The core of the assembly consists of the Glass/Si sample mounted onto a machined KF50 centering ring, which features a 12×12 mm² gas inlet

and blind tapped holes. A thin polymer gasket is sandwiched between the sample and the centering ring, creating a hermetic seal for microfluidic testing upon compression. Electrical contact with the device's heaters is achieved using a custom FR-4 PCB. This PCB is aligned over the sample so that its copper traces make contact with the metal pads on the glass. To ensure reliable electrical contact, small solder protrusions are deposited on the PCB's pads. Through-hole vias route the electrical paths from these bottom-side pads to top-side terminal pins, allowing for connection to an external power supply. The PCB, sample, polymer gasket, and centering ring stack are fastened and compressed by four M4x5 screws, ensuring both electrical connection and a leak-tight fluidic seal.

Conclusion and Perspectives

This work presents the design and fabrication of a Knudsen micropump optimized for operation at atmospheric and over-atmospheric pressures. To address the submicron hydraulic diameter requirement for optimal thermal transpiration at these pressures, we utilized ultrafast Bessel beam laser processing to fabricate high-aspect-ratio nanochannels in glass. Following fabrication, a series of experimental characterizations are planned. The pump performance will be evaluated through both temperature-driven and pressure-driven tests. The primary objective is to quantify the mass flow and pressure rise generated by the device. This will be achieved using the constant volume technique [10]. Mass flow rates will be calculated by measuring the rate of pressure change in a known volume, captured using two high-precision absolute capacitance diaphragm gauges (CDGs) and a differential pressure sensor placed at the pump's inlet and outlet volumes.

Acknowledgement

This work was funded by the French National Research Agency (ANR) and the German Research Agency (DFG) under the project "ANR-2022-CE92-0017-01" and “DFG BR 4175/8-1”.
This work was supported by LAAS-CNRS micro and nanotechnologies platform, a member of the Renatech French national network, under the project *Micro-actionneurs thermiques pour pompe Knudsen*, P-24-04914.

References

[1] McNamara S. and Gianchandani Y., "On-chip vacuum generated by a micromachined Knudsen pump," *J. Microelectromech. Syst.,* vol. 14, no. 4, pp. 741-746, 2005.

[2] Wang X., Tianyi S., Zhang W., Zhang Z. and Zhang S., "Knudsen pumps: a review," *Microsyst Nanoeng,* vol. 6, no. 1, p. 26, 2020.

[3] López Quesada G., Tatsios G., Valougeorgis D., Rojas-Cárdenas M., Baldas L., Barrot C. and Colin S., "Design Guidelines for Thermally Driven Micropumps of Different Architectures Based on Target Applications via Kinetic Modeling and Simulations," *Micromachines,* vol. 10, no. 4, p. 249, 2019.

[4] Rojas-Cárdenas M., Graur I., Perrier P. and Meolans J., "An Experimental and Numerical Study of the Final Zero-Flow Thermal Transpiration Stage," *Journal of Thermal Science and Technology,* vol. 7, no. 3, pp. 437-452, 2012.

[5] Cheng Q., Qin Y. and Gianchandani Y., "A Bidirectional Knudsen Pump with a 3D-Printed Thermal Management Platform," *Micromachines,* vol. 12, no. 1, p. 58, 2021.

[6] Schweizer F., Bade K., Baldas L., Bergdolt S., Colin S., Deutschbein C., Hengsbach S., Korvink J. G., Rojas-Cárdenas M. and Brandner J. J., "Rarefied gas flows in complex microfluidic 3D-structures fabricated via additive manufacturing," *Vacuum,* vol. 238, p. 114213, 2025.

[7] Bhuyan M. K., Courvoisier F., Lacourt P.-A., Jacquot M., Furfaro L., Withford M. J. and Dudley J. M., "High aspect ratio taper-free microchannel fabrication using femtosecond Bessel beams," *Optics Express,* vol. 18, no. 2, p. 566, 2010.

[8] Courvoisier F., Bhuyan M. K., Jacquot M., Lacourt P.A., Salut R., Furfaro L. and Dudley J. M., "High aspect ratio taper-free micro and nano-channel fabrication in glass with ultrafast nondiffracting Bessel beams," in *SPIE LASE*, San Francisco, 2011.

[9] Meyer R., Froehly L., Giust R., Del Hoyo J., Furfaro L., Billet C. and Courvoisier F., "Extremely high-aspect-ratio ultrafast Bessel beam generation and stealth dicing of multi-millimeter thick glass," *Applied Physics Letters,* vol. 114, no. 20, p. 201105, 2019.

[10] Rojas-Cárdenas M., Graur I., Perrier P. and Meolans J., "Time-dependent experimental analysis of a thermal transpiration rarefied gas flow," *Physics of Fluids,* vol. 25, no. 7, 2013.

NEGF26-713744

FLYING AT VERY LOW EARTH ORBIT: AN APPLICATION OF AEROTHERMOCHEMISTRY

Thierry Magin*[1,2], Pietro Parodi[2,3], Pedro Jorge[2,4], Damien Le Quang[2], Federico Bariselli[2]
[1]Aero-Thermo-Mechanics Laboratory, Université libre de Bruxelles, Brussels, Belgium
Thierry.Magin@ulb.be
[2]Aeronautics & Aerospace Department, von Karman Institute for Fluid Dynamics, Rhode-Saint-Genèse, Belgium, pedro.jorge@vki.ac.be, Damien.lequang@vki.ac.be, Federico.Bariselli@vki.ac.be
[3]Laboratoire de Physique des Plasmas, CNRS, Sorbonne Université, École polytechnique, Institut Polytechnique de Paris, Palaiseau, France, pietro.parodi@lpp.polytechnique.fr
[4]Ann and H.J. Smead Department of Aerospace Engineering Sciences, University of Colorado, Boulder, Colorado, United States

KEY WORDS

Space Platform Propulsion and Aerodynamics, Rarefied Gas Dynamics, Gas-Surface inteaction, Low-density Facility, Direct-Simulation Monte-Carlo Simulations, Particle in Cell Method.

ABSTRACT

Aerothermochemistry is a multidisciplinary domain coined by von Kármán, that integrates fluid mechanics, thermodynamics, and physical chemistry. An innovative application of aerothermochemistry is currently investigated at the von Karman Institute (VKI): satellites orbiting at lower altitudes than conventional satellites, between 120 and 300 km, in the region called Very Low Earth Orbit (VLEO). For comparison, satellites in Low Earth Orbit, such as those of the Starlink constellation, typically operate at altitudes above 340 km. Benefits can be obtained in terms of resolution performance for optical and radio instruments, as well as a more favorable link budget for communication. In VLEO, however, even using electric propulsion, the amount of propellant required to compensate for the atmospheric drag becomes economically and operationally inconvenient as mission duration increases [4]. The Air-Breathing Electric Propulsion (ABEP) concept proposes to collect the tenuous atmospheric gas and use it as the propellant, instead of carrying it from launch. The concept is illustrated in Figure 1, which shows a 3U CubeSat version of an ABEP spacecraft. In the design initially proposed by Nishiyama *et al.* [11], ABEP uses an intake to collect and compress the gas, placed either in the front or on the lateral surfaces of the spacecraft. The wing-shaped solar panels in the illustration of Figure 1 highlight the important aspect of external aerodynamics for satellites in VLEO. Aerodynamics is important for stabilization and drag reduction, but also possibly for attitude control and orbital maneuvering [5].

* Corresponding author

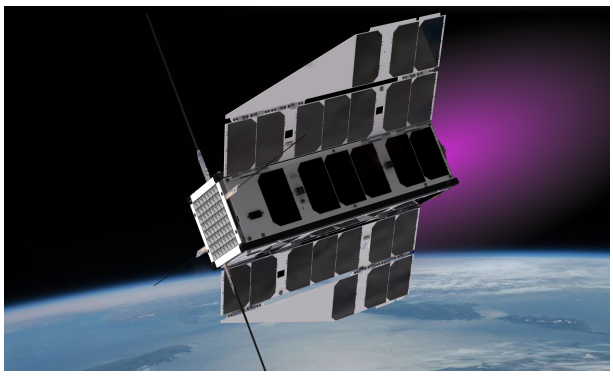

Figure 1: Artist's impression of an ABEP CubeSat in orbit. The graphics are an adaptation of the "Kelpie" 3U CubeSat from AAC Clyde Space [1]. Picture of the Earth by NASA/ISS Expedition 55. The atmospheric intake is visible as the grid aperture in the front of the spacecraft.

The high vacuum facility DRAG-ON was commissioned at VKI in 2021. It has been designed with the objective of measuring the performance of intakes for ABEP systems. As shown on the left in Figure 2, the facility is composed of bead-blasted stainless steel chambers connected by a test chamber that houses the ABEP intake model. Pressure is monitored in each chamber using MKS 370 Stabil-Ion hot-cathode gauges. The pumping system consists of two turbomolecular pumps backed by two rotary vane mechanical pumps. It provides a combined pumping capacity of 4.5 l/s which allows for reaching ultimate pressures of approximately 2 µPa and pressures of the order of 1 mPa under typical operating conditions. While the operating pressure in the facility is larger than that found in VLEO, the degree of rarefaction in the facility (Kn $\approx$ 40) is close to the free molecular flow limit, and guarantees that the flow dynamics in the intake should be dominated by gas-surface interactions.

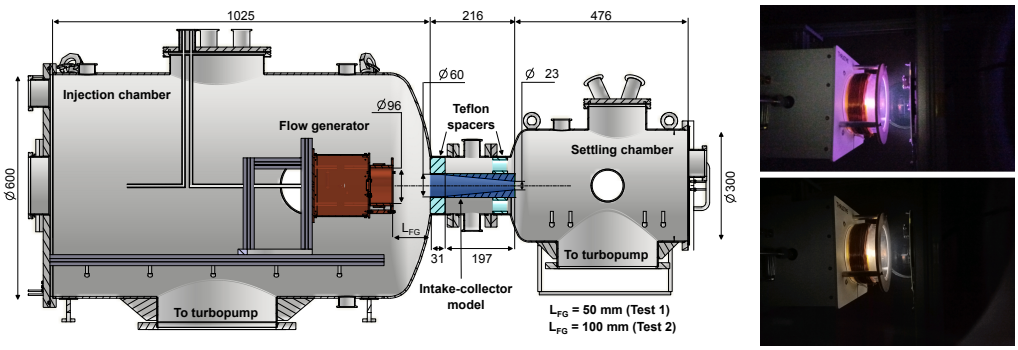

Figure 2: On the left, a drawing of the VKI DRAG-ON facility, with dimensions in mm. The facility consists of two vacuum chambers. The Particle Flow Generator is placed in the larger chamber, and the intake under test is placed in the connecting duct between the two chambers. The smaller chamber acts as a plenum to measure the pressure. The pictures on the right show the PFG in operation with argon (top) and oxygen (bottom).

In the larger chamber of the facility, the LTA100 plasma source [16] developed by ThrustMe is used to generate the flow of particles at approximately 8 km/s that aims to reproduce the flow encountered in orbit. The PFG is shown in operation in Figure 2 with argon (top) and with oxygen (bottom). The dual-chamber configuration allows us, after a calibration procedure, to measure the transmissivity of the

intake model, which is placed between the two chambers, to the particle flow [6]. Using a plasma source as a particle flow generator (PFG) has the advantage of reproducing the real flow velocity, which means that particle-surface interaction occurs at kinetic energies representative of the orbital conditions.
By measuring the transmissivity, the facility provides an indirect measure of the scattering mechanism at the intake's surface, which can, in principle, be related to more direct measurements performed in beam scattering experiments [7]. Operation with a plasma source, however, results in undesired effects due to the fact that charged particles are affected by electric fields. By developing models of the scattering process and by reproducing the experiments numerically, we aim to take these effects into account. Careful calibration of the models can then be used to extrapolate the performance measured in the facility to orbital conditions. Here, we briefly summarize the models, methods, and results of the numerical reproduction of the DRAG-ON facility.

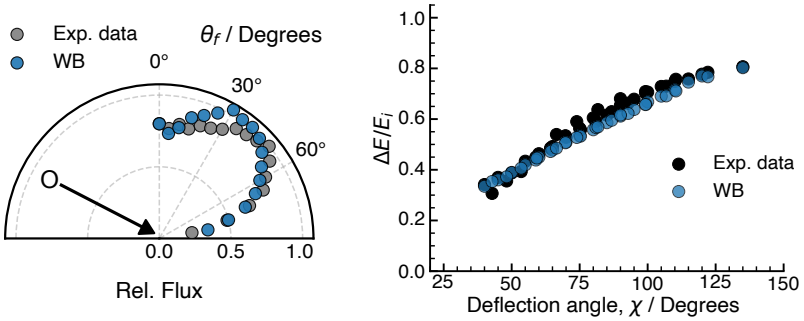

Figure 3: Angular flux distributions (left) and fractional energy transfer (right) for O + A-Al scattering at 60° incidence. Experimental data are compared the WB model. Figure adapted from Jorge et al. [7].

SURFACE SCATTERING MODELS

Charged and neutral particles can collide and react with solid surfaces according to some gas-surface interaction (GSI) model. For instance, particles can be deleted or re-emitted as a different species (according to a specified probability) to simulate absorption and reactions.
The way a particle is scattered can in general be described by a conditional probability distribution function $\mathcal{K}(\mathbf{v}' \rightarrow \mathbf{v})$ called "scattering kernel", where $\mathbf{v}'$ and $\mathbf{v}$ are the pre- and post-collision particle velocities, respectively. In particle methods, such models define how the reflected particle's velocity is sampled. In particular, in the present work, we mainly use three GSI kernels: Maxwell's model [2], the Cercignani-Lampis-Lord (CLL) kernel [10], and the "modified washboard" (WB) kernel [9].
The parameters of the WB kernel were fitted based on molecular beam-surface scattering experiments of 5 eV O atoms from a rough surface of aluminum with an Alodine chromate conversion coating [17]. The results show that scattering dynamics are broad but not diffuse, and O atoms scatter from the surface retaining significant kinetic energy. The experimental data were used to benchmark four widely used phenomenological and physics-based gas-surface interaction models [7]. The comparison revealed that none of the four models accurately reproduced the detailed angular resolved experimental data or the estimated macroscopic energy transfer. However, the WB kernel consistently outperformed the other models, providing the closest agreement with both the angular trends and the energy transfer [7].
Figure 3 shows the molecular beam-surface scattering data for the Alodine coated aluminum and the corresponding WB model fits for an incidence angle of 60 degrees. The model particularly excels at capturing the energy transfer, which exhibits a clear dependence on the deflection angle, as expected for scattering in the structure regime. Additionally, the WB model satisfies the reciprocity condition (as

well as normalization and positivity) which is particularly important for internal flows because it ensures that a non-equilibrium gas (such as the high-velocity beam entering the intake) correctly relaxes to an equilibrium distribution after successive collisions with the intake walls [9, 7].

NUMERICAL REPRODUCTION OF THE FACILITY

Plasma can be considered collisionless in the conditions at which it leaves the plasma source. The Particle-in-Cell (PIC) method [3] can accurately represent a plasma in the translational nonequilibrium state that results from a low degree of collisionality. In the present work, we will perform simulations using the PANTERA PIC-DSMC code, developed at VKI [12]. Using this method, ions and electrons are simulated fully kinetically, and evolve consistently with Poisson's equation for electrostatics, accounting for the charge density of the particles.
We simulate the flow from the exit section of the plasma source into part of the vacuum chamber and through the intake model. We consider three simulation cases: in Simulation I only neutral gas is emitted from the plasma source. In Simulation II, the accelerated ions are simulated. Simulation III considers the ideal case in which neutrals are emitted from the source in the same conditions as for the orbital flow. In all cases, the particles reaching the intake's walls are neutralized and are reflected using one of the surface scattering models described in the previous section.
We assign a uniform potential $\phi_{\text{PFG}} = 6$ V at the exit plane of the source. This, together with the ion temperature of 500 K, has been estimated by fitting the ion velocity distribution function (IVDF) acquired using a retarding potential analyzer probe placed in front of the PFG.

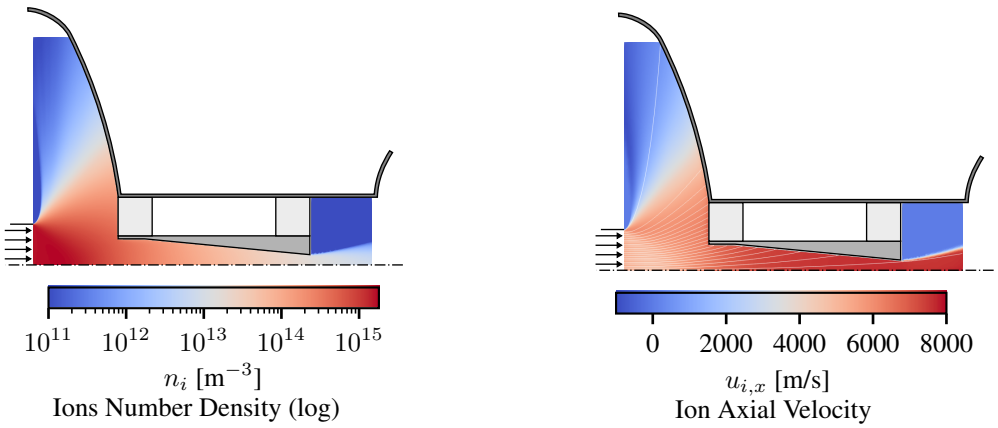

(a) (b)

Figure 4: Result of Simulation II averaged at steady-state. The panels show plots of (a) the density of ions, (b) their axial velocity and velocity streamlines.

By inspecting the results of Figure 4, one can see that the residual electron pressure at the outlet of the plasma source causes the plasma beam to expand, such that a large part of the useful flow rate is lost to the walls. In fact, only 15% of the ions emitted by the PFG enter the intake. In addition, the expansion causes the beam to reach the intake entrance with significant divergence, which is not the case for the neutral beam (or the in-orbit scenario). In addition, the plasma sheath developing at the surface of the intake model further deflects ions towards the wall, such that these reach the surface with angles of 15-25 deg with respect to the surface (Simulation II), instead of less than 5 deg when this effect is not

present (Simulation III). This negatively affects the accuracy with which the orbital flow is reproduced in DRAG-ON, and clearly is a factor to be taken into account.
We also found that the transmissivity of the intake is very sensitive to incomplete accommodation of the tangential momentum (α_t in the CLL model), even in the case where the flow is not composed of fast, directed particles but is just thermalized gas emitted from the PFG (Simulation I). The values of the transmissivity obtained with the WB model, which is calibrated using beam scattering experiments, are definitely closer to those obtained with diffuse reflections than to those obtained with the CLL model, meaning that an $\alpha_t > 0.9$ would surely be required if one chooses to adopt the CLL model. A detailed description of the numerical setup and analysis of the results can be found in [14, 13].

CONCLUSIONS AND FUTURE PERSPECTIVES

We have conducted an experimental and numerical investigation of the transmission probability of plasma beams through an intake model of an ABEP system. We find good agreement between numerical and experimental values, and illustrate how plasma beam experiments and simulations can be used to characterize the aerodynamic performance of intakes for ABEP systems. Notably, the plasma source employed in DRAG-ON successfully reaches particle energies that match those encountered in orbit.
Additionally, these simulations helped us gain more insight into the phenomena that affect this novel type of low-density plasma-based aerodynamic testing. We identified and quantified the differences between the plasma beams produced in DRAG-ON and the neutral flow encountered in orbit. While these discrepancies cannot be fully removed, calibration and input from simulations such as the ones presented here is crucial to offset them, extrapolate to flight conditions, and extract information on gas-surface scattering dynamics under complex internal flow conditions.
The biggest flaw in the simulations presented remains the uncertainty in the boundary conditions with which the plasma leaves the PFG. For instance, in the electron temperature or velocity distribution. Further plasma diagnostics, both at the PFG outlet and in proximity of the intake, are planned in the future and will help reduce these uncertainties. It should be recognized, however, that spatially resolved plasma diagnostics (e.g. using Langmuir, RFEA, and E$\times$B probes) are intrusive measurement techniques and themselves often present large uncertainties. Furthermore, future efforts will explore the development of neutralization techniques to eliminate plasma-related effects, as well as testing with oxygen [15, 8] and nitrogen beams to further improve the fidelity of orbital condition duplication.

Acknowledgements

The work of PP is funded by a Strategic Basic PhD fellowship (ref. 1S24022N) from the Research Foundation–Flanders (FWO). The work of PJ is funded by a doctoral fellowship (2020.05450BD) granted by Fundação para a Ciência e Tecnologia (FCT Portugal).

References and citations

[1] Kelpie spacecraft on nanosats database.
[2] G. A. Bird. *Molecular Gas Dynamics and the Direct Simulation of Gas Flows*. Clarendon Press, 1994.
[3] C. K. Birdsall and A. B. Langdon. *Plasma Physics via Computer Simulation*. CRC Press, 1st edition, 1991.
[4] N. H. Crisp, P. C. E. Roberts, S. Livadiotti, V. T. A. Oiko, S. Edmondson, S. J. Haigh, C. Huyton, L. A. Sinpetru, K. L. Smith, S. D. Worrall, J. Becedas, R. M. Domínguez, D. González, V. Hanessian, A. Mølgaard, J. Nielsen, M. Bisgaard, Y. A. Chan, S. Fasoulas, G. H. Herdrich, F. Romano, C. Traub, D. García-Almiñana, S. Rodríguez-Donaire, M. Sureda, D. Kataria, R. Outlaw, B. Belkouchi, A. Conte, J. S. Perez, R. Villain, B. Heißerer, and A. Schwalber. The benefits of very low

earth orbit for earth observation missions. *Progress in Aerospace Sciences*, 117:100619, 2020.

[5] Nicholas H. Crisp, Peter C. E. Roberts, Virginia Hanessian, Valeria Sulliotti-Linner, Georg H. Herdrich, Daniel García-Almiñana, Dhiren Kataria, and Simon Seminari. A method for the experimental characterisation of novel drag-reducing materials for very low earth orbits using the satellite for orbital aerodynamics research (SOAR) mission. *CEAS Space Journal*, 14(4):655–674, 2022.

[6] Pedro Jorge, P Parodi, M Spillemaekers, D Le Quang, A Hubin, and TE Magin. Performance characterization of intake-collectors for atmosphere-breathing electric propulsion systems. *Plasma Sources Science and Technology*, 34(10):105009, 2025.

[7] Pedro D. C. Jorge, Thomas E. Schwartzentruber, Annick Hubin, Thierry E. Magin, and Timothy K. Minton. Modeling hyperthermal o-atom scattering dynamics on satellite materials. *The Journal of Physical Chemistry C*, 129(27):12486–12501, 0.

[8] Pedro D. C. Jorge, Mikel Spillemaekers, Damien le Quang, et al. Relevance of an RF plasma source to satellite material testing in VLEO conditions. *CEAS Space Journal*, 2025.

[9] Tengfei Liang, Qi Li, and Wenjing Ye. A physical-based gas–surface interaction model for rarefied gas flow simulation. *Journal of Computational Physics*, 352:105–122, 2018.

[10] R. G. Lord. Some extensions to the cercignani–lampis gas–surface scattering kernel. *Physics of Fluids A: Fluid Dynamics*, 3:706–710, 1991.

[11] K. Nishiyama. Air breathing ion engine concept. In *54th International Astronautical Congress of the International Astronautical Federation, the International Academy of Astronautics, and the International Institute of Space Law*, 2003.

[12] P. Parodi, S. Boccelli, F. Bariselli, and T.E. Magin. Pantera: A PIC-MCC-DSMC software for the simulation of rarefied gases and plasmas. *SoftwareX*, 31:102244, 2025.

[13] Pietro Parodi. *Modeling and particle methods for plasma simulation applied to Air-Breathing Electric Propulsion*. PhD thesis, KU Leuven, 2025.

[14] Pietro Parodi, Damien Le Quang, Giovanni Lapenta, and Thierry Magin. Particle-in-cell simulation of the VKI DRAG-ON facility. In *AIAA SCITECH 2024 Forum*. American Institute of Aeronautics and Astronautics.

[15] D. Rafalskyi and S. Dudin. RF Plasma Flow Generator for LEO Environment Simulation: Use Cases. In *38th International Electric Propulsion Conference*, 2024. Paper IEPC-2024-337.

[16] Dmytro Rafalskyi and Stanislav Dudin. Plasma source for simulating ionosphere and upper atmosphere environments at low Earth orbits. *Vacuum*, 241:114597, 2025.

[17] Chenbiao Xu, Adriana Caracciolo, Pedro D.C. Jorge, Irina Gouzman, Marcin Pilinski, and Timothy Minton. Inelastic scattering dynamics of hyperthermal O atoms on engineering surfaces relevant to satellites in low Earth orbit. *CEAS Space Journal*, 2025.

NEGF26-679576

From 3D Tensors to 1D: A Reduction Strategy for Moment Closures in Multidimensional Systems

Eda Yilmaz[1], Manuel Torrilhon[1],
[1]yilmaz@acom.rwth-aachen.de, [1] mt@acom.rwth-aachen.de
[1]Applied and Computational Mathematics (ACoM), RWTH Aachen University, Germany

KEY WORDS

Kinetic theory of gases, moment methods, non-linear closures

ABSTRACT

Modeling rarefied gases requires frameworks beyond classical fluid descriptions, as the Navier-Stokes and Fourier equations fail in non-equilibrium regimes. Kinetic theory provides a fundamental formulation via the Boltzmann equation, describing the time evolution of the particle distribution function in phase space. Direct solution of the Boltzmann equation is computationally challenging due to the high dimensionality of the velocity space and the nonlinear nature of the collision operator.
Moment methods provide a systematic reduction by projecting the kinetic equation onto a finite set of velocity moments. Each moment corresponds to an integral of the distribution function against monomials of velocity, and represents macroscopic quantities such as density, momentum, and higher-order fluxes. The resulting system is an open hierarchy, since the evolution of the n-th moment depends on the $(n+1)$-th moment, necessitating a closure relation. Classical approaches, such as Grad's Hermite expansion [1] and maximum entropy closures [2, 3], perform well in one-dimensional problems but face difficulties in higher dimensions or far-from-equilibrium regimes. While Grad's closure fails to preserve key structural properties like hyperbolicity in these regimes, maximum entropy closures maintain many such properties at the cost of significant computational effort.
The Gramian closure [5], recently proposed for 1D moment systems, constructs orthogonal polynomials using the Gram matrix, whose entries are inner products of velocity monomials weighted by the distribution. This allows for an explicit expression of the next higher-order moment in terms of known lower-order moments, avoiding the reconstruction of the underlying distribution function. Even and odd moment orders can be treated with extended Gramian formulations, allowing control over hyperbolicity and equilibrium preservation. Numerical studies in 1D show that Gramian closures are competitive with classical closures.
Extending this methodology to three-dimensional moment tensors introduces additional challenges: the number of independent tensor components grows rapidly with the moment order, and a direct 3D Gramian closure is not straightforward. To address this, we propose a reduction strategy: the 3D moment tensor is transformed under a set of rotations exploiting symmetry and rotational invariance. Each rotation produces a one-dimensional projection along a chosen axis, allowing the 1D Gramian closure to be applied

independently. By collecting the resulting 1D closure outputs for multiple rotations, we obtain a linear system whose solution reconstructs the full 3D higher-order moment tensor.
This talk will present the method of moments for kinetic equations and introduce the Gramian closure, a novel approach based on orthogonal polynomials that provides explicit formulas for higher-order moments from given lower-order moments. We then show how this closure, originally developed for one-dimensional systems, can be extended to multidimensional moment tensors using a rotation-based reduction strategy, allowing the 1D closure to be applied along multiple axes and reconstructing the full 3D higher-order moments efficiently while preserving key tensorial properties such as symmetry and trace invariance.

Acknowledgements

This work has been supported by the German Research Foundation within the research unit DFG-FOR5409.

References and citations

[1] Grad, H. On the kinetic theory of rarefied gases. *Communications on Pure and Applied Mathematics*, 2(4):331–407, 1949.
[2] N. Böhmer and M. Torrilhon, Entropic quadrature for moment approximations of the Boltzmann–BGK equation, *Journal of Computational Physics*, vol. 401, p. 108992, 2020.
[3] Levermore, C. D. Entropy-based moment closures for kinetic equations. *Transport Theory and Statistical Physics*, 26(4–5):591–606, 1997.
[4] Torrilhon, M. Modeling nonequilibrium gas flow based on moment equations. *Annual Review of Fluid Mechanics*, 48:429–458, 2016.
[5] Yilmaz, E., Oblapenko, G., and Torrilhon, M. On nonlinear closures for moment equations based on orthogonal polynomials. *arXiv preprint arXiv:2407.05894*, 2024.
[6] Fox, R. O., Laurent, F. Hyperbolic Quadrature Method of Moments for the One-Dimensional Kinetic Equation. *SIAM Journal on Applied Mathematics*, 82:750–771, 2022.

NEGF26-686068

GAS TRANSPORT THROUGH A CAPILLARY BUNDLE INDUCED BY A TEMPERATURE GRADIENT

J.Tu*, E. Grigorov, P. Perrier, F. Topin, I. Graur
Aix-Marseille Université, CNRS, IUSTI UMR 7343, Marseille, France
junhao.TU@univ-amu.fr, emil.grigorov@univ-amu.fr, pierre.perrier@univ-amu.fr,
frederic.topin@univ-amu.fr, irina.martin@univ-amu.fr

KEY WORDS

Thermal creep, rarefied gas, porous media, experiment

ABSTRACT

The gas flow rate generated by a temperature difference across a bundle of optical fibers is studied experimentally. The measured data are compared with the mathematical model developed previously.

Introduction

A temperature gradient along the solid can induce a gas to flow from the cold side toward the hot side. This phenomenon, known as thermal transpiration or thermal creep, was first discovered by Reynolds [1] and later studied by Maxwell and Knudsen [2], [3]. The intensity of thermal creep is proportional to the Knudsen number

$$\mathrm{Kn} = \frac{\ell}{a}, \tag{1}$$

where ℓ is the equivalent free path of gas molecules, a is the characteristic flow dimension. Thermal transpiration becomes significant when the molecule-wall collisions are not-negligible compared to molecule-molecule collisions, i.e. $Kn > 0.01$. Under such conditions and starting from an initial pressure equilibrium, the gas moves macroscopically from the colder region toward the hotter one, starting from an initial pressure equilibrium. This phenomenon has recently attracted renewed interest due to the rapid development of micro-and nano-technologies. Its effects may be beneficial - enabling flow driven solely by a temperature gradient - or detrimental, for example, when inducing unwanted flows inside pressure gauge and thereby distorting measurements.

* Corresponding author

Experiment

The objective of this study is to experimentally characterize gas flows through a micro-porous sample induced by a temperature difference across it. To simplify the complex geometry of real porous medium, we first select a bundle of parallel capillaries, a porous-medium model frequently used in theoretical studies.
The experimental setup is shown in Fig. 1. This setup is an improved version of that used previously in [4], [5], [6], [7]. The sample consists of 60 optical fibers, made from pure silica, each fiber containing 60 capillaries (radius $a = 2.95 \pm 0.3\mu$m, length $L = 5$cm), Fig. 2. This bundle of capillaries is placed between two tanks whose temperatures are controlled by the hot and cold water circulations (thermal baths). The entire experimental setup is housed incide an insulated box. Three pressure sensors are used: two Capacitance Diaphragm Gauges (CDG), full scale 1000 Torr and 100 Torr, denoted by P_1 and P_2, depending on the desired initial pressure range, and a differential pressure sensor (± 100 Pa), denoted dP, which measures the pressure difference between the two tanks, with higher precision. K-type thermocouples are installed at different points in each reservoir to monitor the temperatures on both sides.

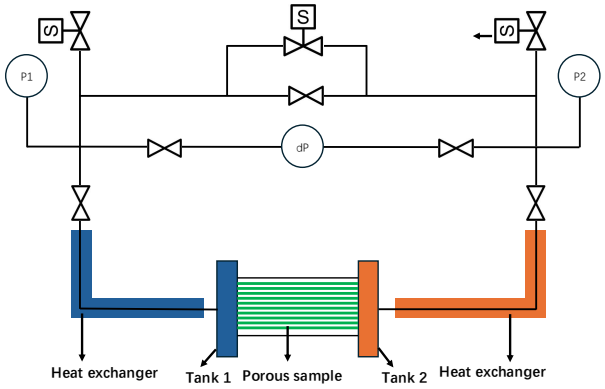

Figure 1: Experimental apparatus with two absolute pressure gauges, P1 and P2, and a differential pressure gauge dP.

The experimental procedure consists of several phases. The experiment begins by filling both reservoirs with the test gas. The bypass valve B remains open until an initial steady state is established, during which gas flows from the cold to the hot side due to temperature difference. The associated mass flow rate is denoted by M_{T}. At this stage, the pressure is uniform throughout the system and it is denoted p_{ini}. The bypass valve B is then closed while the gas continues to flow from the cold side to the hot side. This causes the pressure in the hot reservoir to increase, creating a counterflow of Poiseuille type flow, denoted by M_{P}, driven by emerging pressure difference. The final steady state is reached when both mass flow rates become equal. At this equilibrium, a constant pressure difference is established between the tanks, this is the Thermomolecular Pressure Difference (TPD).

Results and discussion

Measurements have been performed for two single gases: argon and CO_2, using a fixed temperature difference of 40°C between the hot and cold sides. Figure 3(a) shows the pressure evolution in the hot and cold reservoirs measured with the absolute pressure sensors. Figure 3(b) presents the pressure difference, $\Delta p = p_{\mathrm{h}} - p_{\mathrm{c}}$, measured by the differential pressure sensor. The asymptotic value of this curve corresponds to the TPD. The measured pressure difference is fitted using two parameters: the TPD

and the characteristic time, τ, which describes the dynamics of the pressure evolution after the bypass valve is closed. The experimental uncertainties associated with the measurements performed using the setup arise from the hot and cold tank volumes (u_V), fiber radius (u_a), fiber length (u_L), time (u_t), gas temperature (u_T), and gas pressure (u_p), the later depending on their measurement range.
The mass flow rate can be related to the measured parameters via the following equation:

$$\dot{M} = \frac{V_{T_c}^{\text{eff}}}{RT_c} \frac{\text{TPD}}{\tau} \exp\left(-\frac{t}{\tau}\right), \tag{2}$$

where V^{eff} is the effective volume.

Conclusion

The pressure variation and pressure difference across a bundle of optical fibers have been measured. From these data, the mass flow rate, the thermomolecular pressure difference, and the characteristic time have been obtained for argon and CO_2 under an applied temperature difference at the ends of the capillaries.

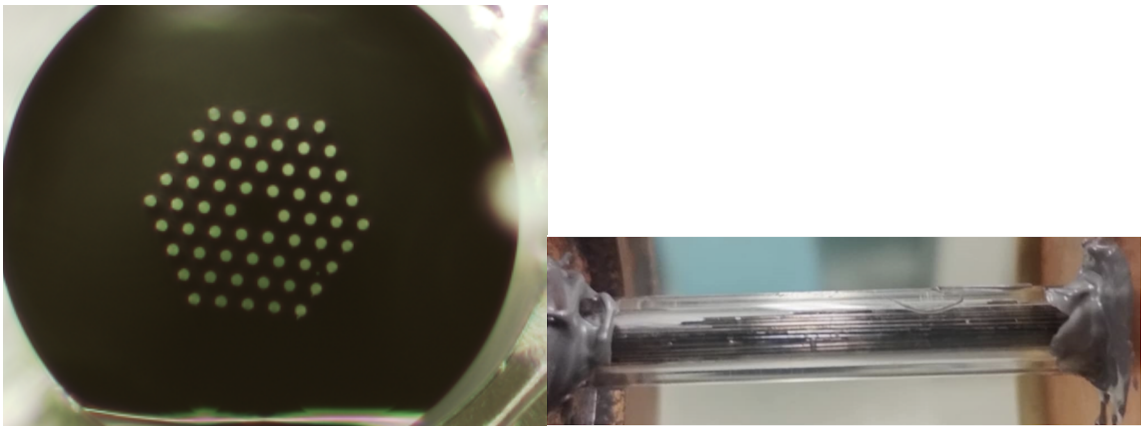

(a) (b)

Figure 2: (a) a cross-section of an optical fiber with 60 capillaries, (b) whole sample with 60 optical fibers.

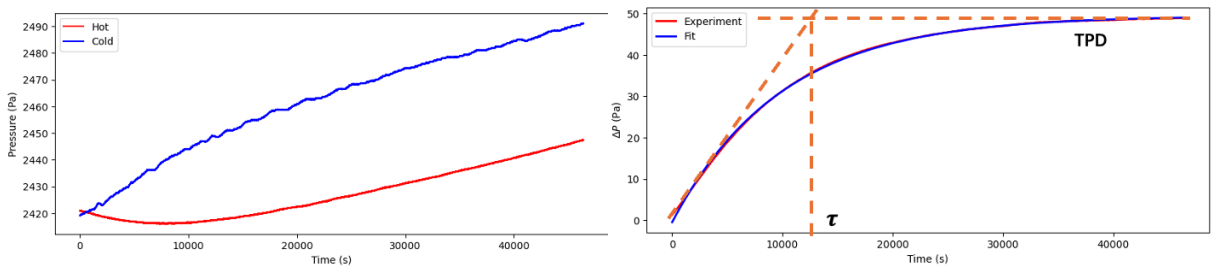

(a) (b)

Figure 3: Measurements with CO_2: (a) Pressure variation in hot and cold side, (b) the pressure difference between two tanks.

The results are compared with the previously developed numerical model [8]. Future work will include measurements of the temperature gradient driven gas-mixture flows through this bundle of capillaries as well as through real porous samples.

Acknowledgements

The study was supported by the ANR TEGTIC project number ANR-23-CE51-0055-01.

References and citations

[1] O. Reynolds, On certain dimensional properties of matter in the gaseous state, Philos. Trans. R. Soc. London 170 (1879) 727–845.
[2] J. C. Maxwell, On stress in rarefied gases arising from inequalities of temperature, Phil. Trans. R. Soc. Lond. 170 (1879) 231–256.
[3] M. Knudsen, Die Gase der Molekularströmung und der inneren Reibungsströmung der Gase durch Röhren, Annalen der Physik 333 (1) (1909) 75–130.
[4] M. Rojas Cardenas, I. Graur, P. Perrier, J. G. Méolans, Thermal transpiration flow: a circular cross-section microtube submitted to a temperature gradient, Phys. Fluids 23 (2011) 031702.
[5] M. Rojas-Cardenas, I. Graur, P. Perrier, J. G. Méolans, An experimental and numerical study of the final zero-flow thermal transpiration stage, J Therm. Sci. Technol. 7 (2012) 437–452.
[6] M. Rojas-Cardenas, I. Graur, P. Perrier, J. G. Méolans, Time-dependent experimental analysis of a thermal transpiration rarefied gas flow, Phys. Fluids 25 (2013) 072001.
[7] H. Yamaguchi, M. Rojas-Cardenas, P. Perrier, I. Graur, T. Niimi, Thermal transpiration flow through a single rectangular channel, Journal of Fluid Mechanics 744 (2014) 169–182.
[8] M. V. Johansson, H. Yamaguchi, P. Perrier, I. Graur, Some properties of a gas flow submitted to a temperature gradient, International Journal of Heat and Mass transfert 214 (2023) 124372.

NEGF26- 678891

GAS-SURFACE INTERACTION MODELS FOR VERY LOW EARTH ORBIT (VLEO) SYSTEMS

Ahilan Appar*[1], Savio Poovathingal[2]
[1]Universidad Carlos III de Madrid, Leganés, 28911, Madrid, Spain
ahilan.appar@uc3m.es
[2]University of Kentucky, Lexington, 40506, Kentucky, USA
saviopoovathingal@uky.edu

KEY WORDS

Molecular dynamics, Atomic oxygen scattering, Direct simulation Monte Carlo.

ABSTRACT

The growing population of space objects in Earth orbits, driven by increasing commercial and defense activities, poses a significant threat to existing satellites and future launches. It also raises serious concerns about the long-term sustainability of space operations. Alongside ongoing efforts in active debris removal and mitigation, exploring very low Earth orbit (VLEO, < 400 km) as a sustainable alternative platform has gained considerable momentum in recent years [1]. Operating at lower altitudes offers advantages, including increased payload and launch efficiency, improved observation capacity, as well as environmental benefits such as reduced collision risk and natural orbital self-cleaning[1]. However, VLEO environments are characterized by a high concentration of reactive atomic oxygen (AO) that interacts with spacecraft surfaces at hyperthermal orbital velocities (~7.5 km/s), resulting in increased drag and surface degradation [2]. While atmospheric drag in the VLEO regime facilitates the natural removal of orbital debris and supports the end-of-life disposal of decommissioned satellites through targeted re-entry, it also causes active satellites to lose altitude rapidly [3]. Thus, accurate estimation of the drag force is crucial for spacecraft in VLEO orbit to develop effective drag compensation and control strategies, predict orbits, avoid collisions, and aid in the development of low-drag materials [4]. Moreover, the VLEO environment is highly rarefied, resulting in a less free-molecular collision regime, characterized by a high Knudsen number, Kn=λ/L, where λ is the mean free path, and L is the characteristic length scale. In the VLEO regime (Kn > 10), where aerodynamics becomes atomistic, gas–surface interactions dominate over intermolecular gas-phase collisions. Thus, in rarefied VLEO conditions, drag and surface erosion arise not from continuum physics but from fundamental gas-surface interactions through the exchange of momentum and energy between gas particles and spacecraft surfaces [5].

* ahilan.appar@uc3m.es

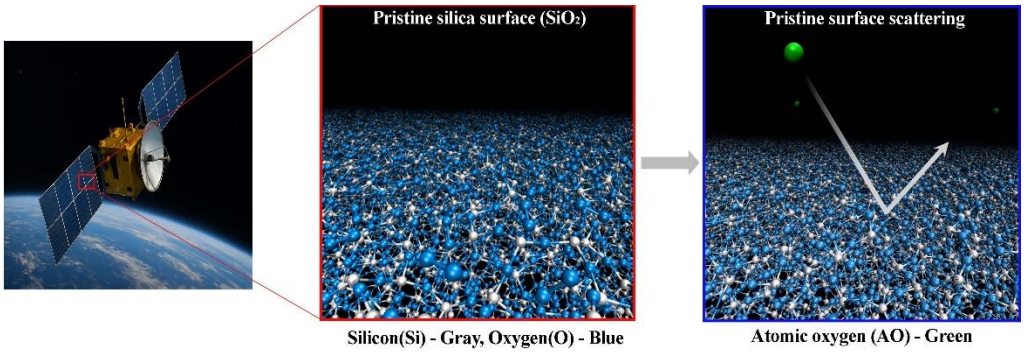

Figure 1 Schematic representation of atomic oxygen scattering on silica surface.

This work examines the scattering of atomic oxygen on amorphous silica, a common satellite material, using reactive molecular dynamics (MD) simulations (see Fig. 1). A comparison of in-plane angular scattering distributions and directional energy transfer between MD calculations and experiments reveals excellent agreement (see fig.2). Based on physical insights from MD calculations, a new accurate gas-surface interaction (GSI) model has been proposed.

Molecular Dynamics Simulations Methodology

Surface Preparation

Figure 2 illustrates the surface preparation process. Starting from the crystalline SiO_2 unit cell (mp-6945) shown in Fig. 2a, the structure was replicated to form a larger crystalline block (Fig. 2b). Through controlled annealing between 300 K and 4000 K, an amorphous bulk structure was obtained (Fig. 2c) with a final density of 2.23 g/cm³. Structural validation showed Si–O, O–O, and Si–Si bond lengths of 1.58, 2.53, and 2.98 Å, and bond angles of 109.3° (O–Si–O) and 152.3° (Si–O–Si), consistent with experimental data. Finally, periodicity along one direction was removed, and vacuum layers were introduced to form a slab geometry (Fig. 2d), which was equilibrated to produce a thermally stable amorphous SiO_2 surface for gas–surface interaction simulations.

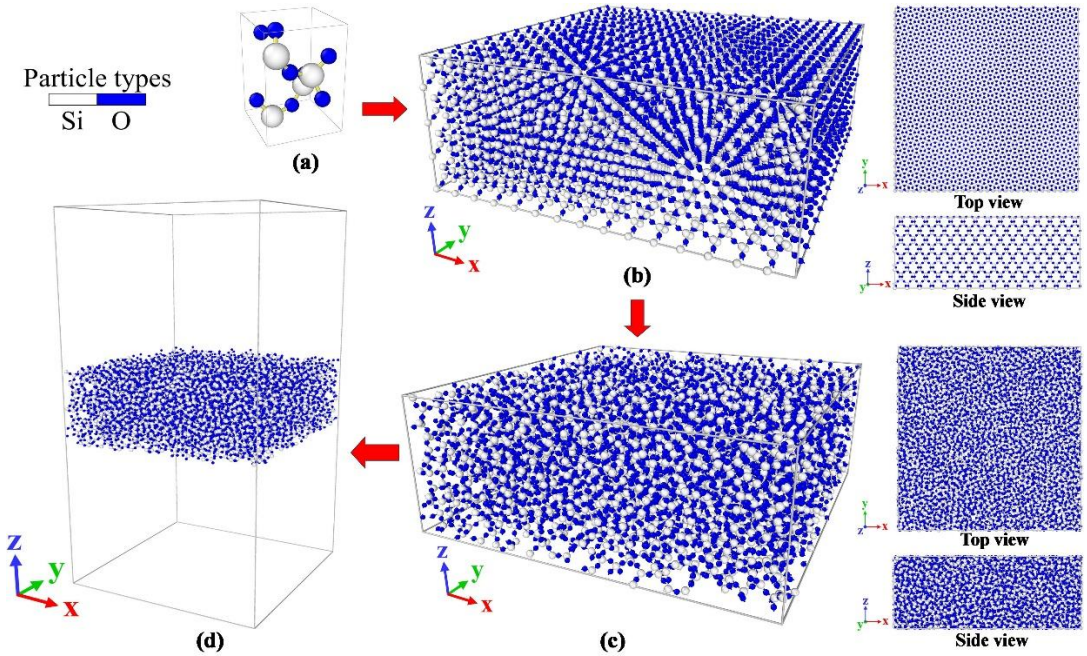

Figure 2 Amorphous silica preparation process. (a) Unit supercell of SiO_2. (b) Bulk crystalline silica structure replicated from a unit supercell of SiO_2. (c) Bulk amorphous silica after the thermal annealing process. (d) Amorphous silica slab with surface formation.

Details of Gas-Surface Interaction Simulations

Figure 4 illustrates the atomic oxygen (AO) scattering setup used to model gas–surface interactions in orbital conditions. AO particles with an incident energy of ~5 eV (corresponding to ~7.5 km/s orbital velocity) are introduced 10 Å above the SiO_2 surface at different incidence angles. The surface, equilibrated at the desired temperature, includes a 10 Å frozen bottom layer for stability, a thermostatted region to control temperature, and a free dynamic surface layer for realistic interactions. Each scattering event is simulated for 80,000 time steps with a 0.05 fs step size, ensuring complete AO–surface collisions. In total, 20,000 independent trajectories were performed to obtain statistically reliable results.

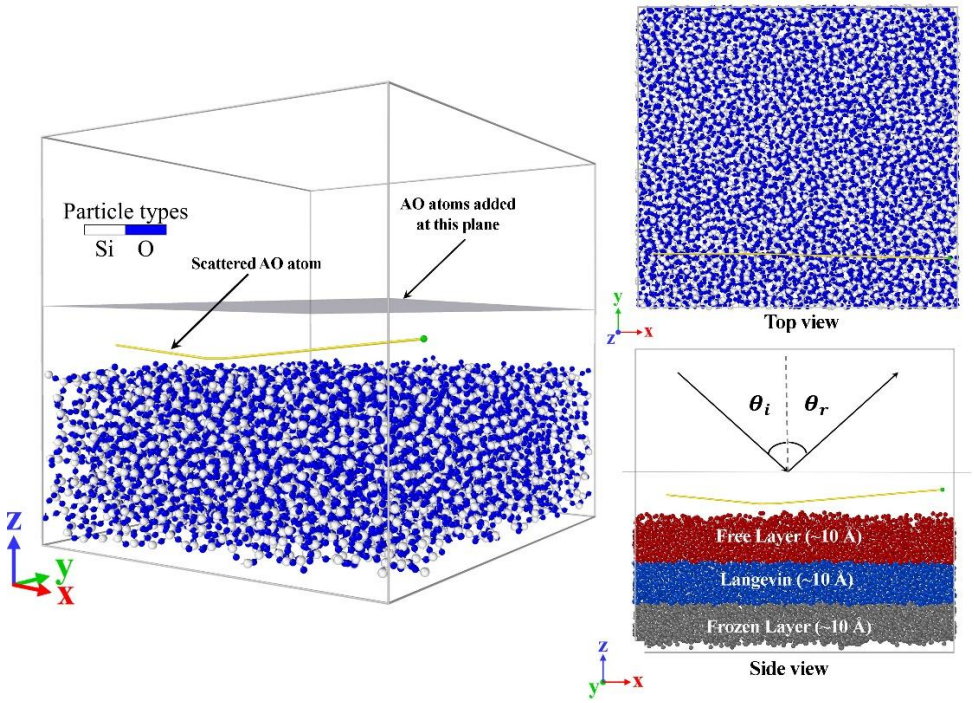

Figure 3 Illustration of the interaction of AO with the SiO2 surface. The front-view image shows that the incident angle,θi, and reflected angle, θr, are measured with respect to the are measured with respect to the surface normal axis. The detailed layer separation indicates the different regions maintained during scattering: the fixed bottom layers (gray region) ensure structural stability, the Langevin thermostat region (blue region) maintains the substrate temperature and the free, exposed layers with NVE (red region) capture the scattering dynamics.

Validation with Molecular Beam Experiments

The MD simulations of AO scattering were validated against molecular beam experiments by Minton *et al.*, which investigated AO interactions with BSF-30, a silicon-based polymer that forms a thin silica layer upon AO exposure [6]. This layer provides a realistic analog for AO scattering from silica surfaces at an incident energy of ~4.9 eV and an incidence angle of 60° at 300 K. In the simulations, particles were considered scattered if they crossed a threshold plane 10 Å above the surface, while absorbed particles were excluded from the analysis.

Figure 4a compares the in-plane angular distributions from MD and experiments. The MD results capture the characteristic lobular scattering pattern, including high-probability grazing-angle reflections and diffuse back-scattering, indicating thermal accommodation with the surface. About 23% of AO particles scattered impulsively, while the rest were temporarily adsorbed, and a small fraction (~4%) formed O_2 molecules. Figure 4b presents the directional energy transfer comparison, showing the average fractional energy loss as a function of the deflection angle. The

MD predictions (red squares) closely match the experimental data (blue circles), demonstrating that all scattering events are inelastic, with scattered particles carrying less energy than the incident flux. The MD accurately reproduces both forward- and back-scattered events across deflection angles of ~30°–210°, confirming that the simulations capture the essential physics of AO–silica interactions.

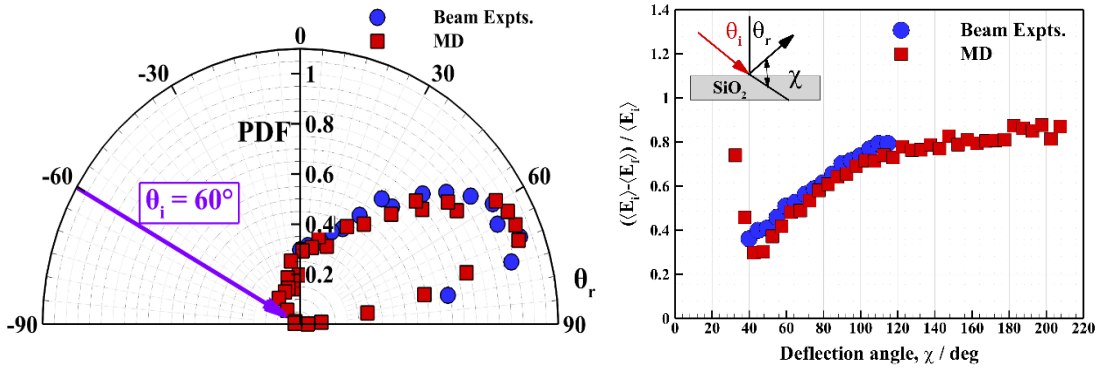

Figure 4 Validation with molecular beam experiments. **(a)** Comparison of in-plane angular distribution of scattered AO flux between MD (red squares) and the molecular beam experiment results (blue circles). The in-plane reflected angle, θr, is calculated from the velocity components in the surface-normal (z) direction, u, and the in-plane tangential (x) direction, v. **(b)** Average fractional energy transfer for in-plane scattering of AO vs. deflection angle, χ, defined as $\chi = 180^\circ - (\theta i + \theta r)$.

Further Work

The validated MD post-scattering data will be used to inform the new model, termed as diffuse-Cercignani-Lampis-Lord (DCLL). Preliminary results are promising for the new model as it reproduces angular flux distributions observed in molecular dynamics and beam experiments, while preserving a structure suitable for implementation into particle solvers. The DCLL model has been tested further with different incident angles and surface temperature.

Acknowledgments

The material is based upon the work supported by DARPA Young Faculty Award #D24AP00309 to Poovathingal. The views and conclusions contained in this document are those of the authors and should not be interpreted as representing the official policies, either expressed or implied, of DARPA or the U.S. Government. The U.S. Government is authorized to reproduce and distribute reprints for Government purposes, notwithstanding any copyright notation hereinafter.

References

[1] Crisp, N. H. *et al.* (2020). The benefits of very low earth orbit for earth observation missions. *Progress in Aerospace Sciences* 117, 100619.
[2] Jorge, P. D., *et al.* (2025). Modeling Hyperthermal O-Atom Scattering Dynamics on Satellite Materials. *The Journal of Physical Chemistry C*.
[3] Jiang, Y., *et al*. (2023). Aerodynamic drag analysis and reduction strategy for satellites in Very Low Earth Orbit. *Aerospace Science and Technology* 132, 108077.
[4] Roberts, P., *et al.* (2019). Discoverer-making commercial satellite operations in very low earth orbit a reality. *Proceedings of the International Astronautical Congress, IAC*. Vol. 2019. IAF, 2019.
[5] Livadiotti, S., *et al*. (2020). A review of gas-surface interaction models for orbital aerodynamics applications. *Progress in Aerospace Sciences* 119: 100675.
[6] Goto, A., *et al.* (2025) Atomic-oxygen effects on a siloxane-polyimide block-chain copolymer (bsf-30), *ACS Applied Polymer Materials* (2025).

NEGF26-679276

Generalized Thermodynamically Admissible 13-Moment Equations

Luke Bell [*1], **Manuel Torrilhon**[2], **Henning Struchtrup**[1]
[1]University of Victoria
lukebell@uvic.ca,struchtr@uvic.ca
[2]RWTH Aachen University
mt@acom.rwth-aachen.de

KEY WORDS

Rarefied gas dynamics, non-equilibrium thermodynamics, kinetic gas theory, entropy, moment equations.

ABSTRACT

The study of rarefied gas dynamics aims to describe phenomena occurring in flows where the ratio of the mean free path λ (length between particle collisions) and the characteristic length L of the system is relatively large. This ratio, represented by the Knudsen number $\varepsilon = \lambda/L$ quantifies the degree of rarefaction; rarefaction effects become significant for $\varepsilon \gtrsim 0.01$, marking the onset of slip and transition flow regimes [1]. These flows occur in both micro systems, where the characteristic length is small, and vacuum or high-altitude flows where pressure is low and the mean free path is large. The study of rarefied flows presents the opportunity to gain insight into the underlying phenomena, providing theoretical knowledge applicable to growing disciplines such as biomedical and aerospace engineering.
This research lies within the domain of nonequilibrium thermodynamics, where the common assumption of local thermodynamic equilibrium no longer holds [1, 2, 3]. In such regimes, the standard Navier–Stokes –Fourier (NSF) equations fail to accurately capture the observed transport phenomena. Rarefied gas flows are instead described microscopically by the integro–differential Boltzmann equation, which can be solved numerically, but only at a high computational cost, making it impractical for large-scale applications. As an alternative, macroscopic extended moment equations are derived from the Boltzmann framework. These models extend beyond the standard hydrodynamic variables (density ρ, velocity v, and temperature θ) to include higher-order moments such as the stress tensor σ_{ij} and the heat flux vector q_i to capture nonequilibrium effects. Common examples include the Grad-13 [4] and regularized R13 equations [5, 6]. These equations have proven successful but are largely restricted to the idealized Maxwell molecule model. The generalization of such models to more realistic molecular interactions is a core aspect of this study.
Traditionally, the transport equations are derived from the Boltzmann equation for a specified molecular interaction model, yielding specific values for equation coefficients [7]. This process involves lengthy mathematical derivations and requires care to ensure kinetic theory and thermodynamic principles are

* Corresponding author

preserved. Most notably, the second law of thermodynamics, which requires both the existence, and strictly non-negative generation, of entropy. The implementation of these conditions can become unclear, or even potentially neglected, in derived macroscopic equations. Instead, this research aims for thermodynamic admissibility; to strictly and explicitly enforce the second law in the foundation of transport equations by formulating a nonequilibrium entropy and its balance equation. There have been alternate approaches for thermodynamic admissibility, for example, by using the GENERIC framework, but that approach is restricted to Maxwell molecules [8].

To obtain molecular generalization and thermodynamic admissibility, we model rarefied gas flows phenomenologically by constructing the most general formulation of 13-moment equations that are compatible with kinetic gas theory and an admissible formulation of entropy and the second law. To start, we consider only linear equations and use the order-of-magnitude approach [9] to categorize Knudsen orders. We start with second order in the Knudsen number (Burnett order [10]) which will be sufficient for capturing the relevant phenomena but can and will be extended to higher orders in the future. As part of the generalized construction, we split the traditional stress tensor and heat flux vector into all possible contributions to the fluxes, and designate the so-called microscopic stress, π_{ij}, and heat flux ξ_i as only components of the general or true stress and heat flux. The transport equations contain coefficients on terms that are both familiar and not present in standard derivations [1] but maintain the integrity of the expected tensor structures [11].

We gain some insight into the restrictions on coefficients through the second law (similar process to [6]). To start, a quadratic entropy function is postulated and reads

$$\eta = \eta_0 - \frac{\alpha_\rho}{2}\rho^2 - \frac{\alpha_\upsilon}{2}\upsilon_k\upsilon_k - \frac{3\alpha_\theta}{4}\theta^2 - \frac{\alpha_\pi}{2}\pi_{ik}\pi_{ik} - \frac{\alpha_\xi}{2}\xi_k\xi_k, \tag{1}$$

with coefficients α_i that will be determined along the way. Enforcing non-negative entropy generation imposes algebraic constraints among the transport coefficients. Some coefficients are required to vanish, others to share definite signs, and the remaining form an under-constrained system to be resolved by some external approach, e.g., by fitting to existing kinetic theory data. The resulting admissible subset of coefficients guarantees that all transport processes satisfy the second law.

Further, a Chapman–Enskog (CE) expansion [12] of the microscopic stress and heat flux provides further insight on the coefficients by providing reference points for comparison to other models and coefficients [10]. After application of these techniques, the most general thermodynamically admissible transport equations to Burnett order (where stress and heat flux are implicitly first order) are presented in equations (2-8) below, with β_i representing the remaining transport coefficients. The equations are presented in Einstein tensor notation with the angled brackets denoting a symmetric and trace-free tensor, noting that the stress is implicitly symmetric. We pay particular attention to additional contributions in comparison to equations of the same order, these additional terms are found to represent Knudsen layers at the boundaries of the flow [1]. The mass balance contains no additional contributions and thus reads

$$\frac{\partial\rho}{\partial t} + \frac{\partial\upsilon_k}{\partial x_k} = 0. \tag{2}$$

The balance of momentum reads

$$\frac{\partial\upsilon_i}{\partial t} + \frac{\partial\rho}{\partial x_i} + \frac{\partial\theta}{\partial x_i} + \frac{\partial}{\partial x_k}\left(\beta_{\upsilon_1}\varepsilon\frac{\partial\upsilon_{\langle i}}{\partial x_{k\rangle}} + \beta_{\upsilon_2}\pi_{ik} + \beta_{\upsilon_3}\varepsilon\frac{\partial\xi_{\langle i}}{\partial x_{k\rangle}}\right) = G_i, \tag{3}$$

where the general stress has contributions from the velocity gradient, microscopic stress, and microscopic heat flux gradient,

$$\sigma_{ik} = \beta_{\upsilon_1}\varepsilon\frac{\partial\upsilon_{\langle i}}{\partial x_{k\rangle}} + \beta_{\upsilon_2}\pi_{ik} + \beta_{\upsilon_3}\varepsilon\frac{\partial\xi_{\langle i}}{\partial x_{k\rangle}}. \tag{4}$$

The balance of energy reads

$$\frac{3}{2}\frac{\partial\theta}{\partial t}+\frac{\partial \upsilon_k}{\partial x_k}+\frac{\partial}{\partial x_k}\left(\beta_{\theta_2}\varepsilon\frac{\partial\theta}{\partial x_k}+\beta_{\theta_3}\xi_k+\beta_{\theta_4}\varepsilon\frac{\partial\pi_{kl}}{\partial x_l}\right)=0, \tag{5}$$

where the general heat flux has contributions from the temperature gradient, microscopic heat flux, and divergence of the microscopic stress,

$$q_k=\beta_{\theta_2}\varepsilon\frac{\partial\theta}{\partial x_k}+\beta_{\theta_3}\xi_k+\beta_{\theta_4}\varepsilon\frac{\partial\pi_{kl}}{\partial x_l}. \tag{6}$$

The constitutive stress balance contains an additional second derivative of the temperature term and reads

$$\frac{\partial\pi_{ij}}{\partial t}+\beta_{\pi_1}\frac{\partial \upsilon_{\langle i}}{\partial x_{j\rangle}}+\beta_{\pi_2}\frac{\partial\xi_{\langle i}}{\partial x_{j\rangle}}-\frac{\beta_{\theta_4}}{\alpha_\pi}\varepsilon\frac{\partial^2\theta}{\partial x_{\langle i}x_{j\rangle}}=-\frac{\chi_\pi}{\varepsilon}\pi_{ij}, \tag{7}$$

where α_π remains from the entropy and χ_π is a coefficient that can be determined for specific molecular potentials.
The constitutive heat flux balance contains an additional derivative of the velocity gradient and reads

$$\frac{\partial\xi_i}{\partial t}+\beta_{\xi_2}\frac{\partial\theta}{\partial x_i}+\beta_{\pi_2}\frac{\alpha_\pi}{\alpha_\xi}\frac{\partial\pi_{ik}}{\partial x_k}-\frac{\beta_{\upsilon_3}}{\alpha_\xi}\varepsilon\frac{\partial}{\partial x_k}\frac{\partial \upsilon_{\langle i}}{\partial x_{k\rangle}}=-\frac{\chi_\xi}{\varepsilon}\xi_i, \tag{8}$$

where α_ξ remains from the entropy and χ_ξ is a coefficient that can be determined for specific molecular potentials. After construction of the general transport equations and accompanying entropy, we find that the second law enforcement created coupling between coefficients β_{υ_3} and β_{θ_4} which appear in the heat flux and stress balances respectively. We are then left with an under-constrained system of conditions for determining the following entropic and transport coefficients α_π, α_ξ, β_{υ_1}, β_{υ_2}, β_{υ_3}, β_{θ_2}, β_{θ_3}, β_{θ_4}, β_{π_1}, β_{π_2}, β_{ξ_2}, χ_π, χ_ξ. To resolve this we look to align with existing equations or tune with available experimental data. We expect alignment with well-known Grad-type moment equations [4, 13], their regularization [1, 3, 5, 6] as well as Burnett-type models [1, 12, 13, 10] which provides a sense of direction for coefficient fitting.
Further analysis comes from the construction of general boundary conditions by applying the second law to a wall-fluid interface [6, 14] which introduces additional coefficients to ensure proper structure and conditions for tuning that are coupled with the transport coefficients. Boundary conditions are tuned to reduce to the established NSF limits, while maintaining compliance with kinetic theory for Maxwell molecules [1]. From this reduction we have found further restrictions on the transport coefficients which present the opportunity to solve the equations for further analysis.
In the coming months, a reduction of the equations to standard geometries such as Couette and Poiseuille flows will be completed in time for presentation. These cases serve as valuable benchmarks because they exhibit key rarefaction effects such as velocity slip, temperature jump, and cross-coupling between stress and heat flux. The generalized model will be compared systematically with NSF, R13, and available direct Simulation Monte Carlo (DSMC) [15] or molecular dynamics [16, 17] results to assess improvements in the prediction of non-equilibrium quantities and to identify the influence of new terms introduced by the entropy-based formulation. Optimization of remaining coefficients will be guided by matching these benchmark solutions, yielding an effective closure model that captures molecular-scale information at reduced computational cost.
Beyond the immediate formulation of 13-moment equations, the present framework establishes a systematic procedure for constructing higher-order, thermodynamically consistent models. After the analysis of Burnett order, the equations will be extended to the Super-Burnett order [10, 18]. Further, the machinery used to enforce the entropy inequality can be generalized to 26 or more moments, offering a path toward

more comprehensive macroscopic equations that remain admissible by construction. Additionally, the general formulation provides a structured foundation for coupling with data-driven techniques, including artificial intelligence and machine learning, to identify coefficients. The training of general models to flow data is a developing approach [19]. By ensuring that fitted models inherently satisfy the second law, one can safely implement molecular or experimental data without violating thermodynamic consistency.

References

[1] Struchtrup, H. (2005). Macroscopic transport equations for rarefied gas flows: approximation methods in kinetic theory. Springer, Berlin, Heidelberg. doi: 10.1007/3-540-32386-4
[2] Struchtrup, H. (2024). A thermodynamic introduction to transport phenomena. Springer, Cham, Switzerland. doi: 10.1007/978-3-031-61868-0
[3] Torrilhon, M. (2016). Modeling nonequilibrium gas flow based on moment equations. Annu. Rev. Fluid Mech., 48, 429–458. doi: 10.1146/annurev-fluid-122414-034259
[4] Grad, H. (1949). On the kinetic theory of rarefied gases. Comm. Pure Appl. Math., 2, 331–407. doi: 10.1002/cpa.3160020403
[5] Struchtrup, H., & Torrilhon, M. (2003). Regularization of Grad's 13 moment equations: derivation and linear analysis. Phys. Fluids, 15(9), 2668–2680. doi: 10.1063/1.1597472
[6] Struchtrup, H., & Torrilhon, M. (2007). H-theorem, regularization, and boundary conditions for linearized 13 moment equations. Phys. Rev. Lett., 99, 014502. doi: 10.1103/PhysRevLett.99.014502
[7] Lin, B., Wang, H., Yang, S., & Cai, Z. (2025). Time-dependent regularized 13-moment equations with Onsager boundary conditions in the linear regime. arXiv preprint, arXiv:2407.12845 [math.AP]. Available at: https://arxiv.org/abs/2407.12845
[8] Struchtrup, H., & Öttinger, H.C. (2022). Thermodynamically admissible 13-moment equations. Phys. Fluids, 34(1), 017105. doi: 10.1063/5.0078780
[9] Struchtrup, H. (2004). Stable transport equations for rarefied gases at high orders in the Knudsen number. Phys. Fluids, 16(11), 3921–3934. doi: 10.1063/1.1782751
[10] Burnett, D. (1936). The distribution of molecular velocities and the mean motion in a non-uniform gas. Proc. Lond. Math. Soc., 40, 382–435. doi: 10.1112/plms/s2-40.1.382
[11] Müller, I. (1985). Thermodynamics. Pitman, Boston.
[12] Chapman, S., & Cowling, T.G. (1970). The mathematical theory of non-uniform gases. 3rd edn. Cambridge University Press, Cambridge.
[13] Kremer, G.M. (2010). An introduction to the Boltzmann equation and transport processes in gases. Springer, Berlin. doi: 10.1007/978-3-642-11617-7
[14] Rana, A.S., & Struchtrup, H. (2016). Thermodynamically admissible boundary conditions for the regularized 13 moment equations. Phys. Fluids, 28, 027105. doi: 10.1063/1.4941293
[15] Bird, G.A. (1994). Molecular gas dynamics and the direct simulation of gas flows. Oxford University Press, Oxford. online edn, Oxford Academic, 2023. doi: 10.1093/oso/9780198561958.001.0001
[16] Homes, S., & Vrabec, J. (2024). Resistivities across the vapor–liquid interface of a simple fluid: an assessment of methods. Phys. Fluids, 36(2), 022122. doi: 10.1063/5.0193522
[17] Homes, S., Frezzotti, A., Nitzke, I., Struchtrup, H., & Vrabec, J. (2025). Heat and mass transfer across the vapor–liquid interface: a comparison of molecular dynamics and the Enskog–Vlasov kinetic model. Int. J. Heat Mass Transfer, 242, 126828. doi: 10.1016/j.ijheatmasstransfer.2025.126828
[18] Reinecke, S., & Kremer, G. (1996). Burnett's equations from a (13+9N)-field theory. Cont. Mech. Thermodyn., 8, 121–130. doi: 10.1007/BF01184766
[19] Nair, A.S., Sirignano, J., Panesi, M., & MacArt, J.F. (2023). Deep learning closure of the Navier–Stokes equations for transition-continuum flows. AIAA Journal, 61(12), 1–14. doi: 10.2514/1.J062935

NEGF26-678358

H-theorems for dense inert and reactive mixtures with application to global in time existence of solutions

Jacek Polewczak[1]
[1]jacek.polewczak@csun.edu

KEY WORDS

chemically reacting fluids, simple reacting spheres, revised Enskog kinetic theory for systems

ABSTRACT

Simple reacting spheres (SRS) model has been developed in [1] and further advanced in [2], [3], and [4], In the SRS model, the molecules behave as if they were single mass points with two internal states of excitation. Collisions may alter the internal states. A dense mixture of four species A, B, A^*, B^*, consisting of hard spheres with diameters d_i and masses m_i, where indices $1, 2, 3, 4$ are for the particles A, B, A^*, B^*, respectively. In contrast to the dilute gas regime, in this work the two-particle distribution function of the mixtures, $f_{ij}^{(2)}$, is approximated (see, H. van Beijeren and M. H.Ernst, *The modified Enskog equation for mixtures*, Physica **70** (1973), 225-242) **not** by $f_{ij}^{(2)} \approx f_i f_j$ but by $f_{ij}^{(2)} \approx g_{ij}^{((2)} f_i f_j$, with f_i being a one-particle distribution function of the mixtures and $g_{ij}^{(2)}$ being the pair correlation function of hard spheres at non-uniform equilibrium, with well known algebraic expression (see (2)). I assume that when a hard-sphere A collides with another hard-sphere B, there is a probability α_R that $A + B \to A^* + B^*$, i.e., A^* and B^* are formed. I apply the same rule to the reverse reaction $A^* + B^* \to A + B$. Furthermore, m_i and d_i denote the mass and the diameter of the i-th particle, $i = 1, \ldots, 4$, and reactions take place when the reactive particles are separated by a distance $\sigma_{12} = \frac{1}{2}(d_1 + d_2) = \sigma_{34} = \frac{1}{2}(d_3 + d_4)$ and the kinetic energy associated with the relative motion exceeds the activation energy: $(1/2)\mu_{is}\big(\langle \epsilon, v - w\rangle\big)^2 \geq \gamma_i$, with $\mu_{is} = \frac{m_i m_s}{m_i + m_s}$, the reduced masses. The conservation of mass has the form $m_1 + m_2 = m_3 + m_4$, where m_i denotes the mass of the i-th particle, $i = 1, \ldots, 4$. The corresponding nonlinear kinetic system has the form

$$\frac{\partial f_i}{\partial t} + v\frac{\partial f_i}{\partial x} = J_i^E + J_i^R, \quad i = 1, 2, 3, 4, \tag{1}$$

with J_i^E, the non-reactive (hard-sphere) collision operator,

$$J_i^E = \sum_{j=1}^{4}\left\{\sigma_{ij}^2 \lambda_{ij}^E \iint\limits_{\mathbb{R}^3 \times \mathbb{S}_+^2} \left[f_{ij}^{(2)}(t, x, v', x - \sigma_{ij}\epsilon, w') - f_{ij}^{(2)}(t, x, v, x + \sigma_{is}\epsilon, w)\right] \langle \epsilon, v - w\rangle \, d\epsilon dw\right\},$$

where $\mathbb{S}_+^2 = \{\epsilon \in \mathbb{R}^3 : |\epsilon| = 1, \langle \epsilon, v - w\rangle \geq 0\}$, $\langle \cdot, \cdot \rangle$ being scalar product in $\mathbb{R}^3$, v' and w' are post-collisional velocities of elastic encounters between i and j species, and $\lambda_{ij}^E = \lambda_{ji}^E = 1 - \alpha_R$, for

$(i,j) \in \{(1,2),(2,1),(3,4),(4,3)\}$, and 1, otherwise. Here, $\sigma_{ij} = (d_i + d_j)/2$. Also, as stated above,

$$f_{ij}^{(2)}(x,v,x \pm \sigma_{ij},w) = g_{(ij)}^{(2)}(x,x \pm \sigma_{ij}) f_i(x,v) f_j(x \pm \sigma_{ij},w),$$

where $g_{ij}^{(2)}(r_1,r_2) = g_{ij}^{(2)}(r_1,r_2,\{n_i\})$ is the pair correlation function for the mixture of hard-spheres at non-uniform equilibrium with well known density expansion: $g_{ij}^{(2)}(r_1,r_2) = \exp(-\beta\phi_{ij}^{HS}(|r_1-r_2|))\times$

$$\left\{1+\sum_{k=1}^{4}\int V_{ij}^{(k)}(12\,|\,3)n_k(t,r_3)+\frac{1}{2}\sum_{k=1}^{4}\sum_{l=1}^{4}\int\int V_{ij}^{(kl)}(12\,|\,34)n_k(t,r_3)\,n_l(t,r_4)\,dr_3dr_4+\cdots\right\}, \quad (2)$$

where $n_i(t,r_j)$ are local densities of i specie at r_j, $\beta = 1/k_BT$, ϕ_{ij}^{HS} are the hard-sphere potentials, and $V_{ij}^{(k)}(12\,|\,3)$, $V_{ij}^{(lk)}(12\,|\,34)$, …, $V_{ij}^{(i_1 i_2 \ldots i_k)}(12\,|\,3\cdots k)$, $i_1,i_2,\ldots i_k = 1\ldots,4$, (Husimi functions) are the sum of all graphs of k labeled points which are biconnected, when the Mayer factor $f_{ij}(r_1,r_2) = \exp(-\beta\phi_{ij}^{HS}(|r_1-r_2|)) - 1$ is added. For hard-spheres mixture, the factors $f_{ij}(r_1,r_2) = \Theta(|r_1-r_2| - \sigma_{ij}) - 1$, where Θ is the step function. For $i = 1,2,3,4$, the reactive terms, J_i^R, are given by

$$J_i^R = \alpha_R\sigma_{ij}^2\int_{\mathbb{R}^3\times\mathbb{S}^2}\left[\left(\frac{\mu_{ij}}{\mu_{kl}}\right)^2 f_{kl}^{(2)}(t,x,v_{ij}^{\odot},x-\sigma_{ij}\epsilon,w_{ij}^{\odot}) - f_{ij}^{(2)}(t,x,v,x+\sigma_{ij}\epsilon,w)\right]\Theta(\langle\epsilon,v-w\rangle - \Gamma_{ij})\langle\epsilon,v-w\rangle d\epsilon dw.$$

Here, $\Gamma_{ij} = \sqrt{2\gamma_i/\mu_{ij}}$, where $\mu_{ij} = \frac{m_im_j}{m_i+m_j}$ are reduces masses and γ_i are the activation energies, and Θ is the Heaviside step function.
The pairs of post-reactive velocities, $(v_{ij}^{\odot},w_{ij}^{\odot}) = (v^{\ddagger},w^{\ddagger})$ for $i,j = 1,2$, with $(v^{\ddagger},w^{\ddagger})$ being post–reactive values for the (endothermic) reaction $A+B \to A^*+B^*$ and $(v_{ij}^{\odot},w_{ij}^{\odot}) = (v^{\dagger},w^{\dagger})$ for $i,j = 3,4$, with $(v^{\dagger},w^{\dagger})$ being the post-reactive velocities for the inverse (exothermic) reaction, $A^*+B^* \to A+B$. Here $0 \le \alpha_R \le 1$ is the probability for energetic enough particles to undergo reactive collisions. When $\alpha_R = 0$, the system (1) is the inert collisional operator for hard-sphere mixture.

The pairs (i,j) and (k,l) are in the set of (i,j,k,l): $\{(1,2,3,4),\ (2,1,4,3),\ (3,4,1,2),\ (4,3,2,1)\}$.

In contrast to a non-reactive four species mixtures, there is no mass conservation for the individual species in the model considered here.

The convergence of the infinite Mayer virial expansion of $g_{ij}^{(2)}$ in (2) is not known, instead, I consider a truncated series $g_{ij}^{(2)}$ in (2) with finite, but arbitrary, number of terms.

First, I show existence of an H-functional for system (1). This is the first result for dense reacting systems.

The H-functional: $H_B(t)+H_{corr}(t)$ consists of two parts: the kinetic part, $H_B(t) = \sum_{i=1}^{4}\iint f_i\log f_i\,dvdx$, and the correlational part, $H_{corr}(t)$. The structure of $H_{corr}(t)$ is similar to the algebraic structure of the equilibrium (non-uniform) entropy for the mixture of infinity system of hard–spheres. In addition, one can identify that

$$-\beta H_{corr} = \mathcal{A}^{excess} \quad \text{with} \quad \beta = 1/kT,$$

where $\mathcal{A}^{excess}$ is the excess free energy for the mixture hard-spheres in a **non-uniform** equilibrium.

Next, I construct approximate solutions to (1). Starting with L^1 initial data, I utilize the conservation laws and the H-function to show convergence of the approximate solutions to a solution of (1). This is the first such existence result for dense reactive mixture.

Additionally, when $\alpha_R = 0$ (no reactive terms), system (1) becomes an inert dense mixture of hard spheres (in this case one can consider any number of species with arbitrary masses) and this work also provides the first global in time existence of a solution for the corresponding system.

References and citations

[1] N. Xystris and J. S. Dahler, J. Chem. Phys. **68** (1978), 387–401)
[2] J. S. Dahler, L. Quin, J. Chem. Phys. (1995) **103**, 725–750
[3] J. S. Dahler, L. Quin, J. Chem. Phys. **118** (2003), 8396–8404).
[4] J. Polewczak, A. J. Soares, Kinetic and Related Models **10** (2017), No. 2, pp. 513 - 539).

NEGF26-684269

HIGH-ORDER SCHEMES FOR STOCHASTIC PARTICLE SOLUTION OF FOKKER-PLANCK KINETICS

Veronica Montanaro*[1,2], Lukas Netterdon[3], Manuel Torrilhon[3], Hossein Gorji[1],
[1] Laboratory for Computational Engineering, Swiss Federal Institute of Material Sciences (EMPA), CH- 8600 Dübendorf, Switzerland
veronica.montanaro@empa.ch, mohammadhossein.gorji@empa.ch
[2] Chair of Scientific Computing and Uncertainty Quantification, École Polytechnique Fédérale de Lausanne, CH-1015 Lausanne, Switzerland
[3] Chair of Applied and Computational Mathematics, RWTH Aachen University, D-52062 Aachen, Germany
netterdon@acom.rwth-aachen.de, mtorrilhon@acom.rwth-aachen.de

KEY WORDS

Interacting Particle Systems, Langevin Dynamics, Time Integration, Kinetic Models

ABSTRACT

In recent years, stochastic approximations of the Boltzmann equation based on simplified collision operators have gained popularity for being a computationally affordable alternative to common approaches such as Direct Simulation Monte Carlo (DSMC). Within these methods, collision operators constructed from the Fokker-Planck equation have been widely studied given their promising potentials [7]. In fact, the Fokker-Planck equation gives rise to a drift-diffusion process, which leads to a system of Stochastic Differential Equations (SDEs) of Langevin type for the velocity and position of the particles. This, in principle, allows for algorithms whose runtime is independent of the collision frequency (unlike, e.g., models based on jump processes such as the BGK method). Despite this potential, there still exist open problems on constructing high-order solution algorithms based on the Fokker-Planck equation.

In this study, we focus on devising high-order time integration scheme for particles following SDEs resulting from Fokker-Planck kinetic models. This is a relevant issue as it will be crucial for applying Fokker-Planck methods in settings where the time-step is much larger than the mean-collision-time. Currently, time integration schemes for the position and velocity SDEs may not exceed first-order accuracy [2, 3]. However improving the order of convergence is a challenging task given the statistical coupling between velocity and position updates.

Following ideas of operator-splitting in Hamiltonian systems [1], we propose here a solution algorithm

* Corresponding author

that allows high-order time integration of coupled SDE systems arising in the Fokker-Planck kinetic description. We devise second-order integrators based on splitting methods, such as the symmetric Strang schemes presented in [4, 5]. We further show that this approximation is potentially grid-free, making the integration amenable to coarser grids. Then, following the strategy introduced in [8], we build on the composition property of these schemes to design an arbitrarily high-order integrator.

Fokker-Planck equation and stochastic particle dynamics

We assume a monatomic, dilute gas. Given the molecular velocity distribution $f(v, x, t)$ describing the probability of finding a particle with velocity $v \in \mathbb{R}^3$ at time $t \in \mathbb{R}^+$ and position $x \in \mathbb{R}^3$, the linear-drift Fokker-Planck equation [3] is given by

$$\frac{\partial f}{\partial t} + v \cdot \nabla_x f = \frac{1}{\tau}\nabla_v \left((v - U)\, f\right) + \frac{k_B T}{m\tau}\Delta_{v,v} f. \tag{1}$$

Here, T is the temperature of the gas, U is the bulk velocity, k_B is the Boltzmann constant, m is the molecular mass, and τ is a relaxation parameter which is function of the temperature. The above Fokker-Planck equation gives rise to a consistent set of hydrodynamic equations with correct viscosity, yet wrong Prandtl number [3]. It can be interpreted as a diffusive approximation of the Boltzmann equation [9]. While extensions to address the Prandtl number inconsistency have been pursued (e.g. see [2, 7]), here for simplicity we focus on the linear-drift model.

The difficulty of devising a high-order time integration scheme based on Eq. 1 is already evident given that U, T, τ depend on f, through its moments. Assuming constant temperature and only focusing on variations of U, the Langevin dynamics corresponding to Eq. 1 takes the form

$$dV_t = -(1/\tau)\left(V_t - \mathbb{E}\left[V_t | X_t\right]\right) dt + \sqrt{2k_B T/(m\tau)} dW_t \tag{2}$$

$$\text{and} \quad dX_t = V_t dt, \tag{3}$$

where (V_t, X_t) are stochastic processes corresponding to a particle's velocity and position, respectively, and W_t is a 3-dimensional standard Brownian motion. The conditional expectation is given by $\mathbb{E}[.|.]$.

What is important to note here is the presence of the expectation of the velocity conditional on the position, which arises given that the bulk velocity is a moment of f. This induces a coupling between position and velocity. In the absence of position dependency, Eq. 2 can be integrated exactly (see [**?**]), however the spatial dependency renders the scheme essentially first-order when spatial variations appear.

Constructing second order splitting methods

Splitting methods rely on additive decomposition of the generator of a (stochastic) differential system such that each term can be integrated accurately. In our case, given the generator $\mathcal{L}$ corresponding to Eq. 1, we split it into three generators $\mathcal{L}_A$, $\mathcal{L}_B$ and $\mathcal{L}_O$.

$$\mathcal{L}_A(f) = -v \cdot \nabla_x f \tag{4}$$

$$\mathcal{L}_B(f) = -\frac{U}{\tau} \cdot \nabla_v f \tag{5}$$

$$\mathcal{L}_O(f) = \frac{1}{\tau}\nabla_v (vf) + \frac{k_B T}{m\tau}\Delta_{v,v} f \tag{6}$$

Note that the SDEs generated by $\mathcal{L}_A$ and $\mathcal{L}_B$ can be solved through a forward-Euler scheme and, as previously remarked, the one generated by $\mathcal{L}_O$ has an exact integrator. Of particular interest for us are

the Strang-symmetric splitting methods [6]. These methods rely on the symmetric application of the operators, evolved either with a full timestep (dt) or half a timestep ($dt/2$). For example, the ABOBA method [4] is such that the operators are applied in the following order:

$$(dt/2)\mathcal{L}_A \rightarrow (dt/2)\mathcal{L}_B \rightarrow dt\mathcal{L}_O \rightarrow (dt/2)\mathcal{L}_B \rightarrow (dt/2)\mathcal{L}_A, \tag{7}$$

and analogously, the BAOAB method can be designed in the same way [4, 5]. Following these, we achieve second-order time integration scheme of SDEs 2-3 as shown in Fig. 1.

Besides careful construction of operator splitting, we require high-order approximation of the conditional expectation. In particular, we employ a polynomial approximation $g(X_t) \approx E\left[V_t|X_t\right]$. The motivation lies in the fact that the Strang symmetric schemes are second-order accurate for drifts which are polynomial in space [4, 5]. We apply a moment matching strategy [2, 7] to determine g. Following this strategy we choose

$$g(X) = \sum_{k=1}^{N} \alpha_k H_k(X), \tag{8}$$

where N is some integer, $\{H_k(X)\}_{1\leq k\leq N}$ is a set of polynomials of increasing k-th order, and $\{\alpha_k\}_{1\leq k\leq N}$ is a set of multi-indices in $\mathbb{R}^3$. In a similar way as carried on in [2, 7], we can determine the coefficients by fixing the same number of moments $\{\mathbb{E}[H_k(V)]\}_{1\leq k\leq N}$ whose evolution in time we want to match, and solve the system of equations

$$\sum_{k=1}^{N} \alpha_k \mathbb{E}[H_k(X)H_j(V)] = \mathbb{E}[VH_j(V)],\ 1 \leq j \leq N \tag{9}$$

obtained by multiplying Eq. 1 by $H_j(v)$ and integrating over v.

An interesting aspect of this method is that, in principle, it offers a grid-free time-integration of the SDEs 2-3, since the coeffcients $\{\alpha_k\}_{1\leq k\leq N}$ are global and do not depend on space.

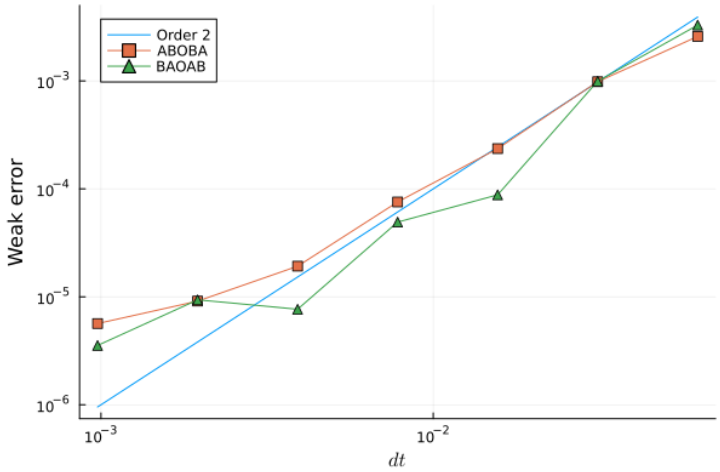

Figure 1: Weak order of convergence of methods ABOBA and BAOBA, for a test drift function $g(X) = X^2 + X^3$ and $\tau = 2k_BT/m = 1$, with averages taken over 10^5 particles.

Acknowledgements

This work was supported in part by Swiss National Science Foundation under grant 217408 and by the Deutsche Forschungsgemeinschaft (DFG, German Research Foundation) - SPP 2410 “Hyperbolic Balance Laws in Fluid Mechanics: Complexity, Scales, Randomness (CoScaRa)” within the Project 525660607 “Model Cascades for Stochastic Particle Simulations of Rarefied Polyatomic Gases”.

References and citations

[1] Channell, P. J. & Scovel, C. Symplectic integration of Hamiltonian systems. Nonlinearity 3, 231 (1990).
[2] Gorji, M. H., Torrilhon, M. & Jenny, P. Fokker–Planck model for computational studies of monatomic rarefied gas flows. J. Fluid Mech. 680, 574–601 (2011).
[3] Jenny, P., Torrilhon, M. & Heinz, S. A solution algorithm for the fluid dynamic equations based on a stochastic model for molecular motion. Journal of Computational Physics 229, 1077–1098 (2010).
[4] Leimkuhler, B. & Matthews, C. Rational Construction of Stochastic Numerical Methods for Molecular Sampling. Appl Math Res Express 2013, 34–56 (2013).
[5] Leimkuhler, B. & Matthews, C. Robust and efficient configurational molecular sampling via Langevin dynamics. J. Chem. Phys. 138, 174102 (2013).
[6] Leimkuhler, B., Paulin, D. & Whalley, P. A. Contraction and Convergence Rates for Discretized Kinetic Langevin Dynamics. SIAM J. Numer. Anal. 62, 1226–1258 (2024).
[7] Montanaro, V., Netterdon, L., Torrilhon, M. & Gorji, H. Fisher entropic Fokker-Planck model of monatomic rarefied gases. Preprint at https://doi.org/10.48550/arXiv.2509.06610 (2025).
[8] Yoshida, H. Construction of higher order symplectic integrators. Physics Letters A 150, 262–268 (1990).
[9] Pawula, R. F. Approximation of the Linear Boltzmann Equation by the Fokker-Planck Equation. Phys. Rev. 162, 186–188 (1967).

NEGF26-685871

HYBRID APPROACH TO MODELING COUPLED VIBRATIONAL–CHEMICAL RELAXATION IN CARBON DIOXIDE MIXTURES

Denis Kravchenko*[1], Elena Kustova[1]
[1]St Petersburg State University, 7–9 Universitetskaya emb., St. Petersburg, 199034, Russia
denis.kravchenko@spbu.ru, e.kustova@spbu.ru

KEY WORDS

Carbon dioxide, coupled vibrational-chemical relaxation, Chapman-Enskog method, multi-temperature approach, kinetic theory

ABSTRACT

Introduction

The kinetic theory for polyatomic gases is less developed than that for monatomic or diatomic species, despite its critical importance for modern challenges in aerospace, laser technologies, and low-temperature plasmas. For instance, simulating high-enthalpy nonequilibrium carbon dioxide flows is vital for planning missions to Mars and Venus, whose atmospheres primarily consist of CO_2. Another application is studying the mechanisms of non–thermal vibrationally-driven CO_2 decomposition.

The key difficulty in modeling such flows is the complex internal structure of molecules, which introduces additional relaxation channels due to intramode and intermode vibrational energy exchanges. In recent years, significant progress has been made in the theoretical description of nonequilibrium kinetics of carbon dioxide [1, 2]. However, accurate modeling of coupled vibrational and chemical relaxation, when each process significantly affects the others remains challenging.

Depending on the flow conditions and kinetic scaling, different modeling approaches are used, ranging from detailed state-to-state (STS) to simpler multi-temperature (MT) models. To combine the accuracy of the STS model with the efficiency of MT ones, a hybrid multi-temperature (HMT) approach based on averaging the STS relaxation terms has recently been proposed [2].

The key issue with the STS and HMT approaches is the need in accurate models for the rate coefficients of vibrational and chemical processes involving all vibrational states. The Schwartz-Slawsky-Herzfeld (SSH) model [3] and the forced harmonic oscillator (FHO) model [4] are widely used to describe state-to-state transitions due to vibrational–translational (VT) and vibrational–vibrational (VV) energy exchange in diatomic species. In this work, we use a generalization of the FHO model for carbon

* Corresponding author

dioxide. The generalized Marrone–Treanor dissociation model [5] and the preferential exchange reaction model developed for CO_2 in Ref. [6] are used to describe state-specific reaction rate coefficients.

The objectives of this study are: 1) to implement the FHO model for vibrational relaxation in pure CO_2 and in CO_2/Ar and CO_2/He mixtures, validating it against experimental data via isothermal bath relaxation simulations; 2) to apply the implemented FHO model, with intermolecular VV exchanges, to describe adiabatic bath relaxation in a five–component CO_2/CO/O_2/O/C mixture, explicitly accounting for coupled vibrational-chemical relaxation.

Theoretical model

The set of governing equations is derived from the Boltzmann equation using the Chapman–Enskog method. Equations for the two considered zero-dimensional (0D) relaxation problems (isothermal and adiabatic) differ only in the total energy equation. For an adiabatic bath, the total energy remains constant, whereas for isothermal relaxation, the translational temperature is fixed.

$$\begin{aligned}
&\frac{dU}{dt} = 0 \quad \text{or} \quad T = const, \\
&\frac{dn_c}{dt} = R_c^{react}, \quad c = \mathrm{CO_2, O_2, CO, O, C, Ar, He}, \\
&\frac{dU_{12}}{dt} = R_{12}^{v}, \quad \frac{dU_3}{dt} = R_3^{v}, \\
&\frac{dU_{vibr}^{c}}{dt} = R_c^{v}, \quad c = \mathrm{O_2, CO}.
\end{aligned} \tag{1}$$

Here, U denotes the total energy per unit volume, n_c is the number density of species c, U_{12} and U_3 are the vibrational energies per unit volume for the combined (symmetric and bending) mode and the asymmetric mode of the CO_2 molecule, respectively, and U_{vibr}^{c} is the vibrational energy per unit volume of diatomic species. The relaxation terms on the right-hand side of the equations describe the changes in number densities or vibrational energy due to molecular collisions.

Within the employed multi-temperature approach, the following slow physico–chemical processes are considered:

- Vibrational–translational (VT) energy transfer. For CO_2, VT exchange is possible for each mode (VT_m with $m = 1, 2, 3$; however, VT_2 is the most probable). Also considered are intermode vibrational exchanges VV_{2-3} and VV_{1-2-3} (VV_{1-2} is rapid due to Fermi resonance). For diatomic molecules, VT exchanges (VT_{O_2} and VT_{CO}) are included.
- Intermolecular vibrational–vibrational energy exchange (VV' processes). The most probable exchanges are VV_{3-CO}, VV_{2-CO}, VV_{1-O_2}, and VV_{O_2-CO}.
- Dissociation-recombination (DR) reactions for molecules.
- Exchange reactions (ER).

The production terms in the equations of chemical kinetics are calculated using the expression

$$R_c^{react} = \sum_{ij} \int J_{ij}^{react,c} d\mathbf{u}_c = \sum_i R_{ci}^{react}.$$

For the relaxation terms in the vibrational energy equations, we separate them into two contributions: the vibrational relaxation term ($R_c^{v,vibr}$) and the chemical relaxation term ($R_c^{v,react}$). Using the hybrid approach, all relaxation terms are first calculated in the state-to-state (STS) approximation and then summed, weighted by the vibrational energy (assuming a harmonic oscillator model):

$$R_c^{v,vibr} = \sum_{i_c} \varepsilon_{i_c}^{c} R_{ci}^{vibr}, \qquad R_c^{v,react} = \sum_{i_c} \varepsilon_{i_c}^{c} R_{ci}^{react}.$$

The STS chemical production terms are calculated using the generalized Marrone–Treanor model [5] for DR reactions and the model [6] for ER reactions. Data for the thermally averaged rate coefficients in the Arrhenius law are given by Park [7].

The vibrational relaxation terms are calculated using the following models:

1. Landau–Teller formula: a semi-empirical formula with low computational cost, but requiring knowledge of the characteristic relaxation times for each process type.

$$R_c^{v,vibr} = \sum_{\gamma_c} \frac{U^c_{vibr,eq}(T) - U^c_{vibr}\left(T_c^{vibr}\right)}{\tau_\gamma}, \quad c = 12, 3, \mathrm{CO}, \mathrm{O}_2.$$

   Here γ_c denotes some of accounted processes, and data for the characteristic relaxation times τ_γ are taken from [8].

2. The forced harmonic oscillator (FHO) model: an accurate model for calculating the integral cross-section of all possible transitions between vibrational levels with a high computational cost.

$$\tilde{\sigma}^{k\to k'}_{i\to i'}(g) = \tilde{\sigma}_{el}(g) P^{FHO,k\to k'}_{i\to i'}(g).$$

3. The Schwartz-Slawsky-Herzfeld (SSH) model: a simple and computationally efficient model for calculation of the rate coefficients for all transitions.

Results

The validation of the vibrational relaxation models is first performed by comparing the overall relaxation time in pure CO_2 without chemical reactions to eliminate vibrational-chemical coupling. The results of this isothermal bath relaxation study are presented in Fig. 1a. Spatially homogeneous

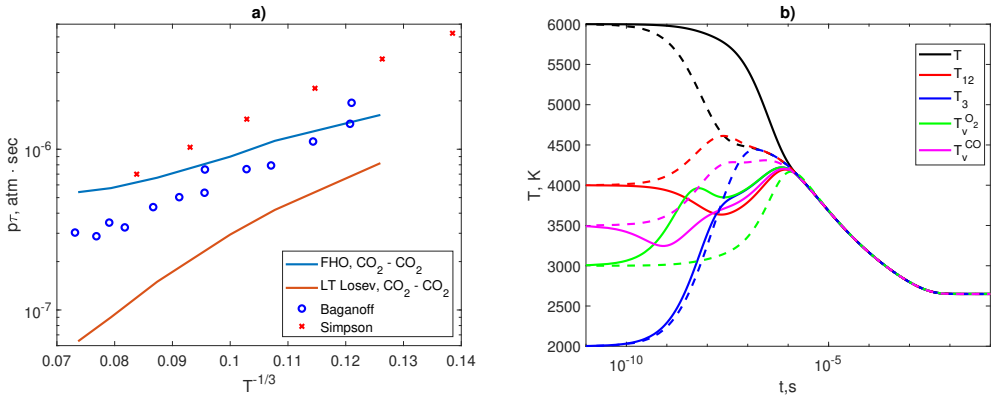

Figure 1: Overall relaxation times calculated using different models compared with experimental data [9, 10] for pure CO_2 (1a). Translational and vibrational temperatures calculated taking into account all processes (VT, VV, DR, ER) in the adiabatic bath problem (1b). Solid lines: the FHO model; dashed lines: the Landau–Teller formula with the relaxation times from [8].

isothermal bath relaxation is studied using the hybrid multi–temperature (HMT) method based on the FHO model and the Landau—Teller formula with experimental characteristic times from Losev et al. [8] (labeled LT Losev). The overall vibrational relaxation time of the mixture is determined from isothermal bath simulations using the e-folding method, allowing for direct comparison with experimental data by Simpson et. al. [9] and Baganoff [10] and validation of the approaches. The analysis shows that the

Landau–Teller formula yields the relaxation time significantly lower than the experimental data, indicating that the model overestimates the vibrational relaxation rate. In contrast, the FHO model demonstrates good agreement with the experimental data.

The capability of the models to handle complex coupled processes is then examined for an adiabatic bath problem of vibrational–chemical relaxation in a mixture CO_2/O_2/CO/O/C. Fig. 1b presents the translational and vibrational temperatures for a test case with the following initial conditions: $T(0) =$ 6000 K, $T_{12}(0) = 4000$ K, $T_3(0) = 2000$ K, $T_v^{\mathrm{CO}} = 3500$ K, $T_v^{\mathrm{O_2}} = 3000$ K; initial molar fractions $\chi_{CO_2}(0)$ = 0.98, $\chi_{CO}(0) = \chi_{O_2}(0) = 0.005$, $\chi_O(0) = \chi_C(0) = 0.005$, and the initial pressure of 10^5 Pa. A comparison between the Landau–Teller formula and the FHO model is shown. The profiles obtained with the Landau–Teller formula show usual trends; the vibrational modes attend equilibrium successively. Contrarily, the FHO model reveals significantly non-monotonic behavior of the vibrational temperatures, which can be attributed to the competing effect of various VV energy exchange processes. This demonstrates that the FHO model provides a more detailed and physically comprehensive description of the vibrational kinetics.

Acknowledgements

This work is supported by the Saint Petersburg State University, Project No. 116636233.

References and citations

[1] Kustova E.V., Nagnibeda E.A. On a correct description of a multi-temperature dissociating CO2 flow // Chem. Phys. — 2006. — Vol. 321. — Pp. 293–310.
[2] Kosareva A., Kunova O., Kustova E., Nagnibeda E.. Hybrid approach to accurate modeling of coupled vibrational-chemical kinetics in carbon dioxide // Phys. Fluids. – 2022. – Vol. 34. – No. 2.
[3] Schwartz R. N., Slawsky Z. I., Herzfeld K. F. Calculation of vibrational relaxation times in gases // J. Chem. Phys. – 1952. – Vol. 20. – No. 10. – Pp. 1591-1599.
[4] Adamovich I. V., Macheret S. O., Rich J.W., Treanor C. E. Vibrational energy transfer rates using a forced harmonic oscillator model // J. Thermophys. Heat Transf. – 1998. – Vol. 12. – No. 1. – Pp. 57-65.
[5] Marrone P. V., Treanor C. E. Chemical relaxation with preferential dissociation from excited vibrational levels // Phys. Fluids. – 1963. – Vol. 6. – No. 9. – Pp. 1215-1221.
[6] Kustova E., Savelev A., Armenise I. State-resolved dissociation and exchange reactions in CO2 flows // The Journal of Physical Chemistry A. – 2019. – Vol. 123. – No. 49. – Pp. 10529-10542.
[7] Park C., Howe J. T., Jaffe R. L., Candler G. V. Review of chemical-kinetic problems of future NASA missions. II-Mars entries // J. Thermophys. Heat transf. – 1994. – Vol. 8. – No. 1. – Pp. 9-23.
[8] Losev S.,Kozlov P., Kuznezova L., Makarov V., Romanenko Yu., Surzhikov S., Zalogin G. Radiation of CO_2–N_2–Ar mixture in a shock wave: experiment and modeling // Proceeding of the Third European Symposium on Aerothermodynamics for Space Vehicles, ESTEC, Noordwiik. - 1998. - Vol. 426. - Pp. 437–444.
[9] Simpson C. M., Bridgman K., Chandler T. R., Shock-tube study of vibrational relaxation in carbon dioxide // The Journal of Chemical Physics - 1968. - Vol. 49. - Pp. 513–522.
[10] Baganoff D., “Experiments on the wall-pressure history in shock-reflexion processes // Journal of Fluid Mechanics. - 1965. - Vol. 23. - Pp. 209–228.

NEGF26-678583

Hyperbolicity of a Hermite-Laguerre Moment Model for the Plasma Edge in Slab Geometry

Julian Koellermeier*[12], Nikita Mischenko[34], Josefine H. E. Proll[35]
[1]Ghent University, Sint-Pietersnieuwstraat 33, 9000 Gent, Belgium
[2]Rijksuniversiteit Groningen, Broerstraat 5, 9712 CP Groningen, The Netherlands
j.koellermeier@rug.nl
[3]Eindhoven University of Technology, De Zaale, 5612 AZ Eindhoven, The Netherlands
[4]Delft University of Technology, Mekelweg 15, 2628 CD Delft, Nederland
[5]Max Planck Institute for Plasma Physics, Wendelsteinstr. 1, 17491 Greifswald, Germany

KEY WORDS

Gyrokinetic, drift-kinetic moment model, hyperbolic regularization

ABSTRACT

Simulating the plasma edge of magnetic confinement fusion devices requires a stable and efficient numerical approach. Particle dynamics can be modeled by a kinetic equation, which is difficult to solve due to the high dimensionality of the phase space. In this paper we derive a moment model for a reduced kinetic equation to elucidate the question of hyperbolicity of the system, which is necessary to create a stable numerical model. The system matrix of an infinite set of moment equations is derived, after which the hyperbolicity of the model is investigated through the characteristic polynomial of said matrix. Hyperbolicity regions of the models are calculated and loss of hyperbolicity is investigated in scenarios relevant to magnetic confinement fusion. Regularization procedures that make the system globally hyperbolic are used to overcome that loss of hyperbolicity leading to a stable moment model hierarchy for plasma edge simulations.

A drift-kinetic moment model in slab geometry

A drift-kinetic moment model for the description of the plasma edge at arbitrary collisionality was recently proposed by Jorge et al. [10]. The drift-kinetic equation is derived using a Lagrangian approach to the equations of motion, which are presented in a guiding center framework. This framework describes particle motion with a velocity parallel to the magnetic field, $v_{||}$, a velocity perpendicular to the magnetic field, $v_\perp$, and an angle of gyration θ. The drift-kinetic equation is given by

$$\partial_t \langle f \rangle + \dot{\mathbf{R}} \cdot \nabla \langle f \rangle + \dot{v}_{||} \partial_{v_{||}} \langle f \rangle = \langle C(f) \rangle, \tag{1}$$

* Corresponding author

where f is the distribution function, $C(f)$ is the collision operator (for the purposes of this paper chosen to be zero), $\dot{\mathbf{R}}$ is the guiding center velocity, and $\langle f \rangle$ is the gyroaveraged distribution function.
Slab geometry is widely used in studies of astrophysical plasmas [7, 11] and fusion plasmas alike [5, 1]. It is usually defined as a geometry in which two spatial directions are homogeneous. After some assumptions and simplifications, the transport equation in slab geometry is reduced to one direction given by

$$\partial_t f(t, x, v_{||}, v_\perp) + v_{||} \partial_x f(t, x, v_{||}, v_\perp) = 0, \tag{2}$$

where ∂_x is a derivative in one spatial direction, which is analogous to the 1D quasilinear collisionless Boltzmann equation that is familiar from literature [4, 3, 6]. While the equation is reduced to one spatial derivative, *two* velocity dimensions remain relevant for analysis.

Hermite-Laguerre basis expansion

In this work, we consider extended fluid dynamics equations, so-called moment equations, based on the expansion of the unknown distribution function in a Hermite-Laguerre basis defined by

$$f(t, x, v_{||}, v_\perp) = \sum_{p,j=0}^{\infty} \frac{N^{p,j}}{\sqrt{2^p p!}} F_M H_p(s_{||}) L_j(s_\perp^2), \tag{3}$$

Where H_p is the physicists's Hermite polynomial of order p and L_j is the Laguerre polynomial or order j. Equation (3) introduces the bi-Maxwellian distribution function with velocities:

$$F_M = N \frac{e^{-s_{||}^2 - s_\perp^2}}{\pi^{3/2} v_{th||} v_{th\perp}^2}, \tag{4}$$

where $s_{||}$ is the normalized and shifted parallel velocity defined by

$$s_{||} = \frac{v_{||} - U_{||}}{v_{th||}}, \qquad v_{th||}^2 = \frac{2T_{||}}{m}, \tag{5}$$

with background bulk velocity $U_{||}$, and $s_\perp$ is the normalized perpendicular velocity

$$s_\perp^2 = \frac{v_\perp^2}{v_{th\perp}} = \frac{\mu B}{T_\perp}, \qquad v_{th\perp}^2 = \frac{2T_\perp}{m}. \tag{6}$$

Note that the velocities depend on $U_{||}, T_{||}$, and $T_\perp$, which themselves correspond to moments of the distribution function and are thus not known a priori. This makes (3) a highly non-linear ansatz.
The moment equations, i.e. evolution equations for the unknown macroscopic and microscopic variables, can be derived in the following form

$$\partial_t \mathbf{w} + A_{sys} \partial_x \mathbf{w} = 0, \tag{7}$$

where A_{sys} is the so-called *system matrix* representing the infinite moment equations, and the vector $\mathbf{w}$ can be identified as containing the moments of the distribution function.
We note that the moment models used in this work are traditionally applied in near-continuum regimes and their extension to stronger non-equilibrium regimes like the free-molecular flows in the plasma edge requires careful consideration. However, in contrast to many existing models from the literature, we do consider *non-linear* moment expansions. These models theoretically increase accuracy, but also comes at the price of potential stability issues due to lack of hyperbolicity. Therefore, the model stability needs to be ensured before an assessment of accuracy of the models can even be made. This is why in this

work we first focus on the stability of moment models. An assessment of accuracy requires extensive numerical testing and is left for future work.
In our presentation, we derive the moment equations for a suitably scaled vector of variables and analyse the properties of the system matrix with respect to hyperbolicity for equilibrium and non-equilibrium. We investigate the loss of hyperbolicity in scenarios relevant to magnetic confinement fusion. Loss of hyperbolicity is already well-studied for related problems in rarefied gas dynamics, where it is typically overcome by a technique called hyperbolic regularization [2, 8, 9]. We perform examples of hyperbolic regularization similar to the one developed in [2] using a careful study of the characteristic polynomial of A_{sys}. This then leads to a new regularized system matrix A^H_{sys}, which ensures the system's hyperbolicity.

Acknowledgements

The authors thank Rogerio Jorge for clarifications and fruitful discussions regarding their related work [10]. This work has been carried out within the framework of the EUROfusion Consortium, funded by the European Union via the Euratom Research and Training Programme (Grant Agreement No 101052200 — EUROfusion). Views and opinions expressed are however those of the author(s) only and do not necessarily reflect those of the European Union or the European Commission. Neither the European Union nor the European Commission can be held responsible for them.

References and citations

[1] A. J. Brizard and T. S. Hahm, *Foundations of nonlinear gyrokinetic theory*, Reviews of modern physics, 79 (2007), p. 421.
[2] Z. Cai et al., *Globally hyperbolic regularization of Grad's moment system in one-dimensional space*, Communications in Mathematical Sciences, 11 (2013), pp. 547–571.
[3] C. Cercignani, *The boltzmann equation and fluid dynamics*, in Handbook of mathematical fluid dynamics, Vol. I, 2002, pp. 1–69.
[4] C. Cercignani and C. Cercignani, *The boltzmann equation*, Springer, 1988.
[5] Z. Chang and J. Callen, *Unified fluid/kinetic description of plasma microinstabilities. part i: Basic equations in a sheared slab geometry*, Physics of Fluids B: Plasma Physics, 4 (1992), pp. 1167–1181.
[6] F. Golse, *The boltzmann equation and its hydrodynamic limits*, Evolutionary equations, 2 (2005), pp. 159–301.
[7] G. G. Howes, S. C. Cowley, W. Dorland, G. W. Hammett, E. Quataert, and A. A. Schekochihin, *Astrophysical gyrokinetics: basic equations and linear theory*, The Astrophysical Journal, 651 (2006), p. 590.
[8] J. Koellermeier and M. Torrilhon, *Numerical solution of hyperbolic moment models for the Boltzmann equation*, European Journal of Mechanics - B/Fluids, 64 (2016).
[9] ——, *Numerical study of partially conservative moment equations in kinetic theory*, Communications in Computational Physics, 21 (2017), pp. 981–1011.
[10] N. F. L. R. Jorge, P. Ricci, *A drift-kinetic analytical model for scrape-off layer plasma dynamics at arbitrary collisionality*, Journal of Plasma Physics, 83 (2017), p. 905830606.
[11] A. Schekochihin, S. Cowley, W. Dorland, G. Hammett, G. G. Howes, E. Quataert, and T. Tatsuno, *Astrophysical gyrokinetics: kinetic and fluid turbulent cascades in magnetized weakly collisional plasmas*, The Astrophysical Journal Supplement Series, 182 (2009), p. 310.

NEGF26-686074

Interfacial resistivities from a Shakhov-Enskog kinetic model

Gaëtan Brunetto*[1], Stéphane Blanco[1], Richard Fournier[1],
Pascal Lavieille[1], Marc Miscevic[1]
[1]Mailing address
name@laplace.univ-tlse.fr

KEY WORDS

Nanoscale flow, Hydrodynamic regime, Liquid-vapor interface, Kinetic theory.

ABSTRACT

The modelling of strong density gradient regions in fluids is a challenging task. It becomes even more complex when the fluid is fairly dense and out of equilibrium. It is however a central question in order to address the exchanges of heat and mass across a liquid vapor interface, which is fundamental to meet the design requirements of modern technological needs. For small departure from equilibrium, one could expect close equilibrium approaches, i.e., hydrodynamic regime, to be an appropriate description of the system, giving access to the interfacial resistivities and their dependence to the state of the fluid. In this work, using a BGK-Shakhov model, we show that we can obtain the same hydrodynamic equations as Enskog for dense fluids. The close equilibrium limit of the resulting set of equations is then shown to be reducible to linear relations between fluxes and thermodynamical forces. The link between those quantities is associated with resistivities.

1. Introduction

The fine modelling of interfacial resistivities for a liquid vapor system has become more and more important over the past years. The miniaturisation of cooling devices and the need to handle higher and higher fluxes have made necessary to reduce the liquid layer in multiphase systems, up to a point where the main contribution to the thermal resistance of the overall system may be controlled in certain situations by the interfacial region. Understanding the behavior of the fluid in this area is however a challenging task. It is indeed the siege of the phase transition over a scale of only a few molecular diameters, inheriting a physical as well as geometrical complexity.
The accurate prediction of the mass and heat transfers across the interface is mostly based on two possible images for the interface, i.e. the sharp and the diffuse interface. Sharp interfaces show jumps in the physical properties of the fluid between the two phases. The most used model for this question is

* Corresponding author

the Hertz-Knudsen-Schrage (HKS) one. Using Kinetic Theory (KT), it prescribes the form of the distribution function in the vapor and at the interface, and deduces the fluxes at stationary regime [2]. Some coefficients are finally added to the model to take into account the complex nanoscale dynamics, e.g. the accommodation coefficients. This model is close to other macroscopic model based on the Thermodynamics of Irreversible Processes (TIP) [1]. While fruitful, this approach is limited by the capacity to find values for those coefficients. Experimental measurements have been conducted to find those missing quantities [3, 4], but the practical difficulties associated with the interface is responsible of a strong scattering of the resulting values even for the same fluid [5].
The other image for the interface is the diffuse interface [6]. The two bulk phases are here linked by continuous density, velocity and temperature profiles. In the context of KT, the hydrodynamics limit gives access to the macroscopic transport equations, with expressions for the transport coefficients valid at any points of the flow. The only physical parameters entering this modelling are the characteristic of the particles, which can be found by simple critical point measurements. The interfacial resistivities, and their functional dependences to the state of the fluid are accessible by solving the macroscopic equations. In this work, a method to derive the thermal resistance of a liquid vapor system starting from a KT base on the Enskog-Vlasov equation is proposed. The non local collision term is replaced by a Shakhov term, in order to simplify the hydrodynamic limit computation. We then tune the parameters of the Shakhov model to obtain the same macroscopic transport coefficients as Enskog's for liquids. We finally use the resulting equations in a perturbative regime around the equilibrium to obtain the resistivities.

2. Kinetic theory and hydrodynamics limit

We choose to describe the fluid using the Enskog-Vlasov equation [7], a generalisation of the Enskog equation for dense fluids of hard spheres [8] to include intermolecular attraction between the constituents [9]. For particles of molecular mass m and diameter d_0, this equation reads

$$\frac{\partial f}{\partial t} + \mathbf{c}\cdot\boldsymbol{\nabla} f + \mathbf{F}\cdot\boldsymbol{\nabla}_{\mathbf{c}} f = \mathcal{S}_{\text{En}}(f,f), \tag{1}$$

where $\mathbf{r}$, $\mathbf{c}$ and t denotes space, microscopic velocity and time and $f(\mathbf{r},\mathbf{c},t)$ is the velocity distribution function. The vector $\mathbf{F}$ is the Vlasov force per unit mass, describing the total force experienced by a particle at position $\mathbf{r}$ due to the contribution all other particles through an inverse power attractive potential

$$\mathbf{F} = -\frac{1}{\rho}\boldsymbol{\nabla}\cdot\mathsf{T} = \frac{1}{\rho}\boldsymbol{\nabla}\cdot\left[a\rho^2 + \kappa\rho\boldsymbol{\nabla}^2\rho + \frac{1}{2}\kappa\boldsymbol{\nabla}\rho\cdot\boldsymbol{\nabla}\rho\right]\mathbb{I}_3 - \kappa\boldsymbol{\nabla}\rho\boldsymbol{\nabla}\rho], \tag{2}$$

with $\rho(\mathbf{r}_1,t)$ the mass local density, $a = \frac{4\pi {d_0}^3}{3m^2}\phi_0$, $\kappa = \frac{5\pi {d_0}^5}{6m^2}\phi_0$ and $\mathbb{I}_3$ is the three dimensional unit tensor and ϕ_0 is the strength of the attractive potential.
The collision term $\mathcal{S}_{\text{En}}$ derived from the Enskog proposition for hard spheres reads

$$\mathcal{S}_{\text{En}} = -\frac{1}{\tau}(f - f_{\text{Sha}}) - b\rho Y f_M \left[\begin{array}{l} \mathbf{C}\cdot\left(\boldsymbol{\nabla}\ln\left(\rho^2 Y\theta\right) + \frac{3}{5}\left(\frac{\mathbf{C}^2}{2\theta} - \frac{5}{2}\right)\boldsymbol{\nabla}\ln\theta\right) \\ +\frac{2}{5}\left(2\frac{\mathbf{CC}}{2\theta} : \boldsymbol{\nabla}\mathbf{v} + \left(\frac{C^2}{2\theta} - \frac{5}{2}\right)\boldsymbol{\nabla}\cdot\mathbf{v}\right) \end{array}\right], \tag{3}$$

where $\theta = rT$ is the temperature times the specific gas contant, $\mathbf{v}$ the hydrodynamic velocity, $\mathbf{C} = \mathbf{c} - \mathbf{v}$ is the molecular speed in the reference frame of the flow, $b = \frac{2\pi {d_0}^3}{3m}$ is the molecular volume per unit mass and $Y(\rho)$ is the pair correlation function. The first part is a relaxation term with characteristic time τ towards a Shakhov velocity distribution function [10]

$$f_{\text{Sha}} = f_M\left[1 + (1-\text{Pr})\frac{\mathbf{C}\cdot\mathbf{J}_Q}{5\rho\theta^2}\left(\frac{\mathbf{C}^2}{\theta} - 5\right)\right], \tag{4}$$

with $\mathbf{J}_Q$ being the heat flux vector, Pr the Prandtl number and f_M the local maxwellian distribution function. The second member of the collision operator is an excess part containing information about the non locality of the original Enskog collision operator [11]. Following a procedure used in [12], the hydrodynamic equations at Navier-Stockes-Fourier level reads

$$\begin{cases} \frac{\partial \rho}{\partial t} & +\boldsymbol{\nabla}\cdot(\rho\mathbf{v}) = 0 \\ \frac{\partial(\rho\mathbf{v})}{\partial t} & +\boldsymbol{\nabla}\cdot(\rho\mathbf{v}\mathbf{v} + \rho\theta(1+b\rho Y) + \mathsf{T} - 2\rho\theta\tau\mathsf{S}) = 0 \\ \frac{\partial\left(\frac{3\rho\theta}{2}\right)}{\partial t} & +\boldsymbol{\nabla}\cdot\left(\frac{3\rho\theta}{2}\mathbf{v} - \frac{5}{2\mathrm{Pr}}\rho\theta\tau\boldsymbol{\nabla}\theta\right) = -\rho\theta(1+b\rho Y)\boldsymbol{\nabla}\cdot\mathbf{v} + 2\rho\theta\tau\mathsf{S}:\boldsymbol{\nabla}\mathbf{v} \end{cases}, \tag{5}$$

where S is the rate of shear stress tensor $\mathsf{S}_{\alpha\beta} = \frac{1}{2}\left(\frac{\partial v_\alpha}{\partial x_\beta} + \frac{\partial v_\beta}{\partial x_\alpha}\right) - \frac{1}{3}\boldsymbol{\nabla}\cdot\mathbf{v}\delta_{\alpha\beta}$. Matching those equations with the usual flow equations, one recognizes the thermal conductivity and dynamical viscosity coefficients $\lambda = \frac{5}{2}\frac{\rho\theta}{\mathrm{Pr}}\tau$ and $\mu = \rho\theta\tau$.
The last step is the tuning of the free functions. The pair correlation function will impose the state equation of the fluid, we do not need to specify it for the purpose of this work. For the transport coefficients, we want them to be identical to the one found by Enskog at first order in the Chapman-Enskog method, thus it imposes

$$\begin{cases} \tau &= \frac{1}{\rho\theta Y}\frac{5m}{16{d_0}^2}\sqrt{\frac{\theta}{\pi}}\left(1 + \frac{4}{5}b\rho Y + \frac{4}{25}\left(1+\frac{12}{\pi}\right)(b\rho Y)^2\right), \\ \mathrm{Pr} &= \frac{2}{3}\frac{1+\frac{4}{5}b\rho Y+\frac{4}{25}\left(1+\frac{12}{\pi}\right)(b\rho Y)^2}{1+\frac{6}{5}b\rho Y+\frac{9}{25}\left(1+\frac{32}{9\pi}\right)(b\rho Y)^2}. \end{cases} \tag{6}$$

This model is supposed to be valid at any point of the flow, in particular the interfacial region, as long as the hydrodynamic limit conditions are ensured. At equilibrium, i.e. $\mathbf{v} = \mathbf{0}$ and $\theta = \theta_0$ a constant, the equations 5 reduce to the well known diffuse interface equation which defines the equilibrium density profile ρ_0

$$\boldsymbol{\nabla}\cdot[\rho_0\theta_0(1+b\rho_0 Y(\rho_0))\mathbb{I}_3 - \mathsf{T}] = 0 \tag{7}$$

3. Linear perturbation and resistivities

We now look at the hydrodynamic equations at linear order in perturbation around the equilibrium along a one dimensional axis z and at stationary regime. Including those conditions, the energy balance equation decouples from the momentum one, leading to

$$\partial_z q(z) = -\partial_z\left(\lambda_0\partial_z\tilde{\theta}\right) = j_m\theta_0\left(\frac{1}{\rho_0} + bY_0\right)\partial_z\rho_0, \tag{8}$$

with $q(z)$ the heat flux, $\tilde{\theta}$ the temperature perturbation and j_m an imposed mass flux. Changing variable from z to ρ_0 and integrating from the bulk vapor density ρ_v up to a density in the interface $\rho_0(z)$, and then a second time on z from the vapor to the liquid bulk altitude, the temperature jump for the whole region gives

$$\Delta\tilde{\theta} = -q_v\int_{z_v}^{z_l}\mathrm{d}z\,\frac{1}{\lambda_0} - j_m\theta_0\int_{z_v}^{z_l}\mathrm{d}z\,\frac{1}{\lambda_0}\left[\ln\left(\frac{\rho_0(z)}{\rho_v}\right) + b\int_{\rho_v}^{\rho_0(z)}\mathrm{d}\rho_0\;Y_0\right] \tag{9}$$

This jump however takes also contributions of part of the bulk phases and can be made arbitrary big by increasing the gap between z_v and z_l. To remove them, one can subtract the bulk temperature profiles extrapolated up to an arbitrary altitude. This altitude z_i is chosen to be the point of steepest slope of the equilibrium density. At linear order in perturbation, the bulk temperature jumps are simply given by the imposed heat flux times the ratio between the conductivity and the thickness of the layer $\Delta\tilde{\theta}_{v/l} =$

$\frac{q_{v/l}\, e_{v/l}}{\lambda_{v/l}}$, and the latent heat is define by $j_m L_v = q_l - q_v$. Using these, we are left with the temperature jump at the interface

$$\Delta\tilde{\theta}_i = j_m L_v R_1 + q_v R_2, \tag{10}$$

with R_1 and R_2 the resistivities that reads

$$\left\{ \begin{array}{rcl} R_1 & = & \frac{\theta_0}{L_v} \int_{z_v}^{z_l} \frac{1}{\lambda_0} \left(\ln\left(\frac{\rho_v}{\rho_0}\right) + b \int_{\rho_0}^{\rho_v} \mathrm{d}\rho_0 \; Y_0 \right) \mathrm{d}z + \int_{z_i}^{z_l} \frac{\theta_0 L_v}{\lambda_l} \, \mathrm{d}z \\ R_2 & = & \int_{z_v}^{z_i} \left(\frac{1}{\lambda_v} - \frac{1}{\lambda_0} \right) \mathrm{d}z + \int_{z_i}^{z_l} \left(\frac{1}{\lambda_l} - \frac{1}{\lambda_0} \right) \mathrm{d}z \end{array} \right. . \tag{11}$$

It is possible to show that these relations depend on the location dividing surface z_i but not on the thickness of the bulk regions chosen by showing that the integral arguments cancels in the bulks. Moreover, those coefficients are independent of the fluxes and of the temperature jump, as expected in linear response around an equilibrium.
We showed that it is possible to obtain interfacial resistivities for the interface starting from a KT. Those coefficients are dependent on the characteristic of the particles only through the state functions. They allow for a simple computation of the transfer coefficients between phases in an engineering context. Of course, work needs to be done in order to validate or not our approach. We need to characterise the limit of the perturbative regime and check if it is sufficient to describe the system for most engineering contexts. Then those results needs to be confronted the resolution to the kinetic theory without going to the hydrodynamic regime, in order to check if this regime can be applied for the interface. Last, this proposition should be compared to other approaches, for example to the well known HKS model.

References and citations

[1] Kjelstrup, S. & Bedeaux, D. (2008). Non-equilibrium thermodynamics of heterogeneous systems. World Scientific.
[2] Schrage, R. W. (1953). A Theoretical Study of Interphase Mass Transfer. Columbia University Press.
[3] Fang, G. & Ward, C. A. (1999). Temperature measured close to the interface of an evaporating liquid. Physical Review E, 59(1), 417-428.
[4] Badam, V.K, Kumar, V., Durst, F. & Danov, K. (2007). Experimental and theoretical investigations on interfacial temperature jumps during evaporation. Experimental Thermal and Fluid Science, 32, 276-296.
[5] Marek, R. & Straub, J. (2001). Analysis of the evaporation coefficient and the condensation coefficient of water. International Journal of Heat and Mass Transfer, 44(1), 39-53.
[6] Anderson, D. M., McFadden, G. B., & Wheeler, A. A. (1998). Diffuse-interface methods in fluid mechanics. Annual review of fluid mechanics, 30(1), 139-165.
[7] Sobrino, L. D. (1967). On the kinetic theory of a van der Waals gas. Canadian Journal of Physics, 45(2), 363-385.
[8] D. Enskog, (1921). The numerical calculation of phenomena in fairly dense gases, Ark. Mat. Astron. Fys. 16 (1).
[9] Vlasov, A.A. (1961). Many-Particle Theory and Its Application to Plasma, Gordon and Breach.
[10] Shakhov, E. M. (1972). Generalization of the Krook kinetic relaxation equation, Fluid Dynamics, 3(5), 95-96.
[11] Chapman, S., Cowling, T. G., Burnett, D. & Cercignani, C. (1990). The mathematical theory of non-uniform gases: an account of the kinetic theory of viscosity, thermal conduction and diffusion in gases, Cambridge mathematical library, 3rd edition.
[12] Wang, P., Wu, L., Ho, M. T., Li, J., Li, Z.-H. & Zhang, Y. (2020). The kinetic Shakhov–Enskog model for non-equilibrium flow of dense gases, Journal of Fluid Mechanics, 883, A48.

NEGF26-679178

IONIC WIND INDUCED BY A DIELECTRIC BARRIER DISCHARGE BETWEEN A NEEDLE TIP AND THE SURFACE OF A LIQUID

Eric MOREAU
eric.moreau@univ-poitiers.fr

KEY WORDS

Ionic wind, non-thermal plasma, DBD, plasma-water interaction, PIV measurements

ABSTRACT

Over the past decade, the interaction between non-equilibrium plasmas and liquids has gained increasing significance due to various applications, such as water treatment for instance. In this context, we developed a simple design consisting of a high-voltage needle placed a few millimetres above the surface of the liquid to be treated, whereas the grounded electrode is located below the glass tank containing the liquid (Figure 1). Therefore, between the two conductive electrodes, there is an air gap of a few millimetres, three centimetres of water and a 2-mm thick dielectric barrier of glass. Depending on the values of the applied voltage and its frequency, three different types of discharges may be observed between the needle tip and the water surface: a corona discharge, a transient regime and a filamentary discharge. Moreover, due to different physical phenomena, several mechanical effects can occur: a gas flow induced by the discharge, a deformation of the liquid surface and a flow inside the liquid, all these electrohydrodynamic phenomena being investigated by our team. The present experimental study focuses on the ionic wind produced between the needle tip and the water surface when a corona-type DBD is ignited. The velocity of this gas flow is measured with a high-frequency PIV system (particle image velocimetry), that allows us to obtain 2D velocity fields with a spatial resolution smaller than 100 µm (see the field of view, FOV, in Figure 1). The input parameters that have been investigated are the distance between the needle tip and the water surface (from 11 mm down to 4 mm), the values of the applied voltage and its frequency (from 20 Hz up to 2 kHz), and the water conductivity (from 2 µS/m to 400 µS/m). The results highlight that the characteristics of the produced ionic wind jet depend strongly on all these parameters. Moreover, time-resolved measurements show that the positive corona discharge (occurring during the positive half-cycle) results in a fast and stable ionic wind jet when the ionic wind produced during the negative discharge is strongly unstable.

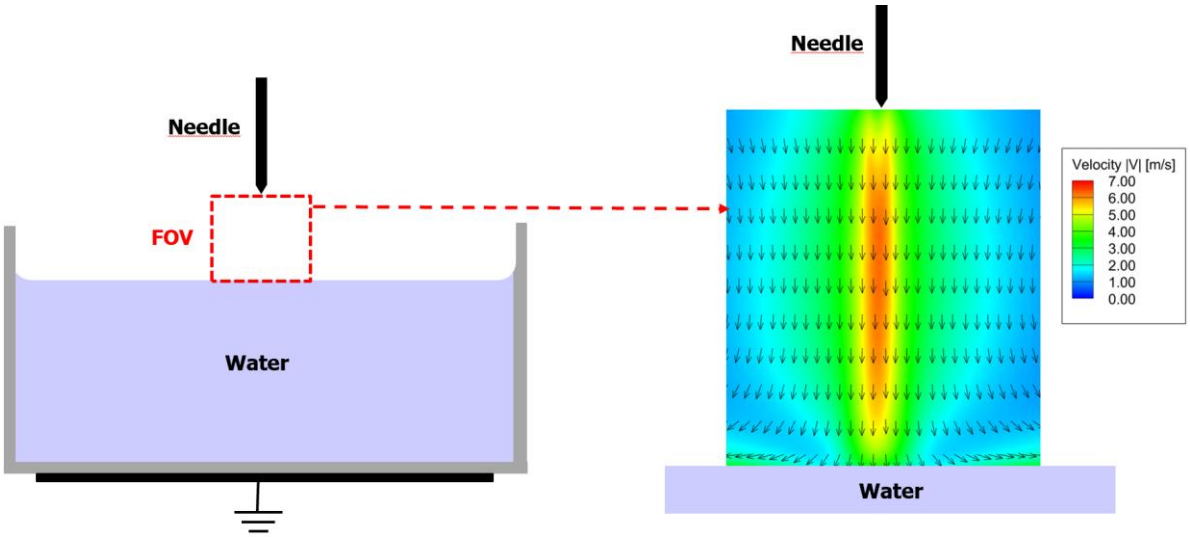

Figure 1: Scheme of the discharge setup and example of a time-averaged velocity fields of the ionic wind produced between the needle tip and the water surface.

RESULTS

In this section, we present two examples of velocity fields of the produced ionic wind. The needle tip is at x = y = 0. The water surface is at x = 11 mm. For all the cases, the background color corresponds to the modulus of the ionic wind velocity (from 0 to 7 m/s, see the legend in Figure 1), and the black arrows to the flow direction (they do not corresponds to the velocity vectors as their length is constant).

Figure 2 shows time-averaged velocity fields for three different voltage amplitudes V_{AC}, the gap between the needle tip and the water surface being equal to 11 mm (water conductivity $\sigma = 400$ µS/cm). The frequency of the sine high voltage here equals 1 kHz. We can see that a gas flow is induced from the needle tip toward the water surface, resulting in an ionic wind jet perpendicular to the water surface. Moreover, the velocity increases with the applied high voltage.

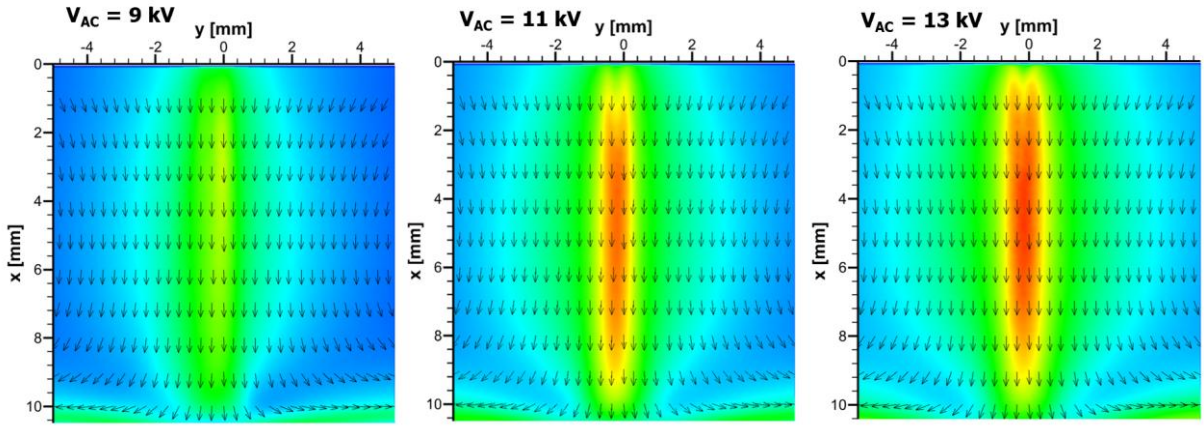

Figure 2: Time-averaged velocity fields for three different voltage amplitudes V_{AC} (voltage frequency f_{AC} = 1 kHz, needle-to-water gap = 10 mm, water conductivity $\sigma = 400$ µS/cm).

Figure 3 shows an example of the time-resolved behavior of the ionic wind. The high voltage frequency is 20 Hz, and the PIV frequency equals 400 Hz, resulting in 20 instantaneous velocity fields during one voltage period (every 2.5 ms). Here, only six are shown. Between t = 0 and 25 ms (positive half-priod of the voltage), a positive discharge takes place when a negative discharge occurs between 25 and 50 ms. At t = 5 ms, the ionic wind jet starts to develop from the needle tip. Its velocity is around 4 m/s. However, it has not reached the water surface. At t = 15 ms, a fully developed jet is visible. It is perpendicular to the water surface and its velocity is about 7 m/s. During the negative discharge, the jet is unstable, its direction being not perpendicular to the water surface. Moreover, the velocity during the negative half-period is smaller than the one during the positive half-period.

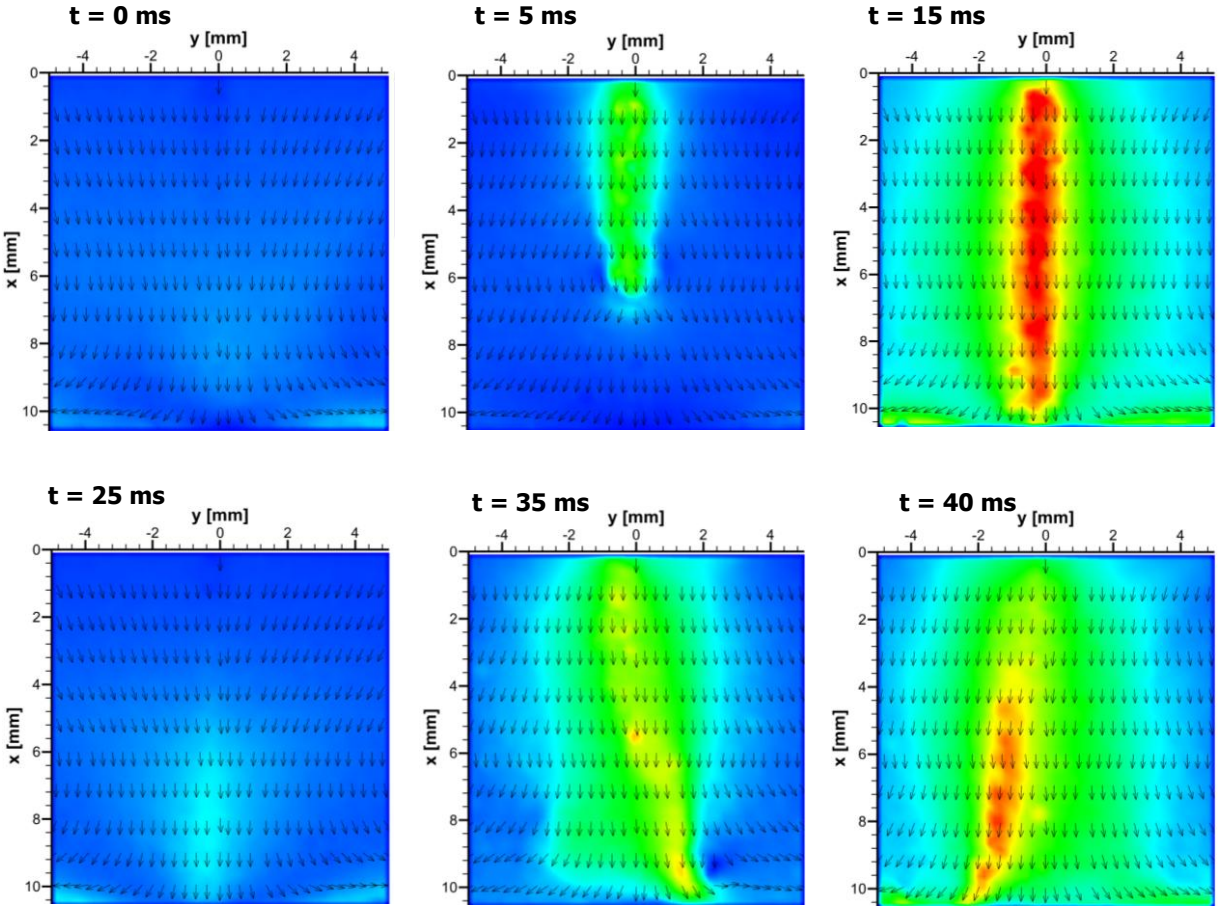

Figure 3: Instantaneous velocity fields at different moments during one voltage period.

CONCLUSION

In this abstract, we have shown only two results from a much more comprehensive study. The complete study will be presented in greater detail during the oral presentation. The main finding of this work is as follows. First, the ionic wind jet produced between the needle and the water surface is roughly similar to that generated between a needle and a flat plate. However, its behavior over time is different. Indeed, the positive charges deposited on the water surface during the positive half-cycle of the applied voltage cause the jet to become unstable during the negative half-cycle.

Acknowledgments

This work was supported by ANR-11-LABX-0017-01 and ANR-18-EUR-0010.

NEGF26-679197

KINETIC MODELING OF CHEMICALLY REACTING MIXTURES: A BGK-TYPE APPROACH

Marzia Bisi[1], Maria Groppi[1], Anna Macaluso[*1]
[1]Department of Mathematical, Physical and Computer Sciences, University of Parma,
Parco Area delle Scienze 53/A, Parma, 43124, Italy
marzia.bisi@unipr.it, maria.groppi@unipr.it, anna.macaluso@unipr.it

KEY WORDS

Kinetic theory, BGK equations, Reactive mixtures, Exchange rates

ABSTRACT

In classical kinetic theory the dynamics of gas mixtures is naturally described through integro-differential Boltzmann equations for species distribution functions [1]. However, the analytical and numerical study of these equations is rather difficult due to the complexity of the nonlinear integral Boltzmann operator that describes the collision mechanisms in detail. For this reason, simpler kinetic descriptions have been built up starting from the BGK relaxation model for a single gas proposed by Bhatnagar, Gross, and Krook [2] in 1954, that replaces the nonlinear integral operator with a linear operator which prescribes the relaxation of the distribution function towards a proper Maxwellian attractor.

The description was originally formulated for a single gas, however it was highly desirable to develop consistent generalizations applicable to gas mixtures, whether inert or reactive, and composed of monatomic or polyatomic species, particularly for use in physical processes. Indeed, the ability to model gas mixtures within a reactive kinetic framework is of considerable importance for practical applications, such as atmospheric re-entry phenomena [3, 4] and various industrial processes [5, 6].

Among the different formulations that can be found in the literature, we refer to [7], where a BGK-type model for inert mixtures is proposed, reproducing the structure of the Boltzmann formulation. In this approach, the collision operator is expressed as a sum of binary terms of relaxation type, each representing the exchanges between pairs of components due to mechanical interactions. Such a formulation has the notable advantage of distinguishing between collisions involving different pairs of species and, therefore, enables the study of multiple-scale hydrodynamic regimes [8], which are frequently encountered in mixtures of components with disparate masses, as it occurs in plasma physics.

[*] Corresponding author

In this work, we aim at introducing a new BGK-type model for a gas mixture undergoing a simple chemical reaction. We consider a mixture of four monatomic rarefied gases G_s, $s = 1, 2, 3, 4$, each of them endowed with its own molecular mass m_s and internal energy E_s, undergoing binary elastic mechanical collisions and a bi-molecular reversible reaction,

$$G_1 + G_2 \leftrightarrows G_3 + G_4, \tag{1}$$

such that $\Delta E = E_3 + E_4 - E_1 - E_2 > 0$. Let $f_s = f_s(\mathbf{x}, \mathbf{v}, t)$ be the distribution function of the particles of the s-th gas depending on position $\mathbf{x} \in \mathbb{R}^3$, molecular velocity $\mathbf{v} \in \mathbb{R}^3$, and time $t \in \mathbb{R}^+$. The evolution of the mixture, in absence of external forces, is governed by a system of kinetic BGK-type equations of the form

$$\frac{\partial f_s}{\partial t} + \mathbf{v} \cdot \nabla_{\mathbf{x}} f_s = \mathcal{Q}_s\left[\mathbf{f}\right] = \mathcal{Q}_s^{ME}\left[\mathbf{f}\right] + \mathcal{Q}_s^{CH}(f_s), \qquad s = 1, 2, 3, 4,$$

where $\mathbf{f} = [f_1, f_2, f_3, f_4]$ is a vector collecting all distribution functions. The collision operators on the right-hand-side mimic the structure of the Boltzmann collision terms for the same mixture [9], taking into account both mechanical and chemical interactions separately, analogously to [10]. The mechanical BGK operator is the sum of binary terms, according to [7],

$$\mathcal{Q}_s^{ME}\left[\mathbf{f}\right] = \sum_{r=1}^{4} \mathcal{Q}_{sr}^{ME} = \sum_{r=1}^{4} \nu_{sr}(\mathcal{M}_{sr} - f_s), \tag{2}$$

and even the chemical operator is assumed of BGK type,

$$\mathcal{Q}_s^{CH}(f_s) = \nu_s^{CH}(\mathcal{M}_s - f_s), \tag{3}$$

where ν_{sr} and ν_s^{CH} represent the frequencies of mechanical and reactive collisions obeying the chemical law (1), respectively.

In (2) and (3), $\mathcal{M}_{sr}$ and $\mathcal{M}_s$ are Maxwellian attractors, depending on auxiliary (fictitious) densities, velocities, and temperatures that have to be properly computed in order to make the BGK model consistent, namely compatible with conservation laws, correct equilibrium solutions and entropy dissipation principle ($\mathcal{H}$-Theorem). This is done by assuming that the exchange rates for momentum and total energy of BGK mechanical and chemical operators coincide with the corresponding exchange rates of each Boltzmann integral operator. Under the hypothesis of Maxwell molecule potential, we explicitly calculate the production terms in the mechanical contributions for both Boltzmann and BGK formulations, resulting in an explicit relationship between the auxiliary parameters of local attractors and the macroscopic fields of each species. Concerning chemical contributions, an appropriate input distribution function is necessary to compute explicitly the production terms in the Boltzmann setting. To this end, the distribution function is approximated by the elastic Maxwellian equilibrium, under the assumption of slow chemical reaction.

We prove that such model correctly reproduces by construction the conservation laws and admits the correct equilibrium solutions, namely Maxwellians with a common mean velocity and temperature, with number densities related to temperatures by the mass action law. To conclude, some numerical simulations of the kinetic BGK system in space homogeneous conditions are performed to investigate the asymptotic trend of the reacting mixture to the equilibrium.

Acknowledgements

This work was performed in the frame of activities sponsored by the Italian National Group of Mathematical Physics (GNFM-INdAM) and by the University of Parma (Italy). The authors thank the support of the project PRIN 2022 PNRR "Mathematical Modelling for a Sustainable Circular Economy in Ecosystems" (project code P2022PSMT7, CUP D53D23018960001) funded by the European Union - NextGenerationEU PNRR-M4C2-I 1.1 and by MUR-Italian Ministry of Universities and Research.

References

[1] Cercignani C. (1988). The Boltzmann equation and its applications. Springer, New York.
[2] Bhatnagar P. L., Gross E.P., & Krook M. (1954). A model for collision processes in gases. I. Small amplitude processes in charged and neutral one-component systems. Phys. Rev., 94 , 511–525.
[3] Baranger C., Dauvois Y., Marois G., Mathé J., Mathiaud J., & Mieussens L. (2020). A BGK model for high temperature rarefied gas flows, Eur. J. Mech. B Fluids, 80, 1–12.
[4] Li Z. H., & Zhang H. X. (2009). Gas-kinetic numerical studies of three-dimensional complex flows on spacecraft re-entry. J. Comput. Phys., 228 (4), 1116–1138.
[5] Cercignani C., Frezzotti A., & Lorenzani S. (2008). Using the Kinetic Equations for MEMS and NEMS. Advances in multiphysics simulation and experimental testing of MEMS, 37–80.
[6] Lorenzani S. (2019). A microchannel flow application of a linearized kinetic Bhatnagar-Gross-Krook-type model for inert gas mixtures with general intermolecular forces. Phys. Fluids, 31 (7).
[7] Bobylev A.V., Bisi M., Groppi M., Spiga G., & Potapenko I.F. (2018). A general consistent BGK model for gas mixtures, Kinet. Relat. Models, 11, 1377–1393.
[8] Bisi M., Groppi M., & Martalò G. (2021). Macroscopic equations for inert gas mixtures in different hydrodynamic regimes, J. Phys. A: Math. Theor., 54 (8), 085201.
[9] Rossani A., & Spiga G. (1999). A note on the kinetic theory of chemically reacting gases. Physica A, 272, 563–573.
[10] Martalò G., Soares A. J., & Travaglini R. (2024). A BGK-type model for multi-component gas mixtures undergoing a bimolecular chemical reaction. J. Stat. Phys., 192 (1).

NEGF26-677682

MASS AND HEAT TRANSFER AT LIQUID-VAPOR INTERFACES: REAL GAS AND NON-LINEARITY

Henning Struchtrup[1]
[1]Dept. of Mechanical Engineering, University of Victoria, Victoria, British Columbia, Canada
struchtr@uvic.ca

KEY WORDS

Nonequilibrium, Evaporation, Condensation, Interface resistivities, Kinetic Theory, Enskog-Vlasov Gas,

ABSTRACT

This contribution concerns evaporation and heat transfer processes at liquid vapor interfaces in thermodynamic nonequilibrium, as depicted in Fig. 1. In the case of small scales, i.e., large resolution, and/or large heat and mass fluxes, these processes are accompanied by marked temperature jumps $T_V - T_L$ between vapor and liquid, and deviation of pressure from saturation, so that $p_V \neq p_{\rm sat}\,(T_L)$.

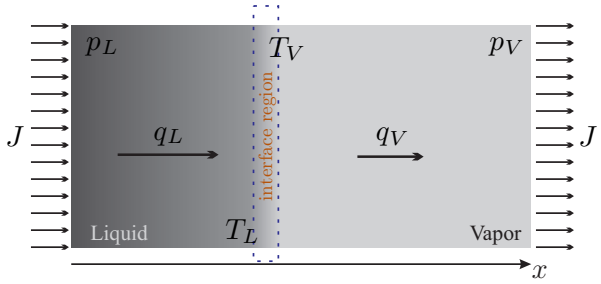

Figure 1: Geometry, properties, and fluxes in one-dimensional mass and heat transfer across a liquid-vapor interface.

Thermodynamic modelling of these jumps introduces interfacial resistivities $r_{\alpha\beta}$ [1], while kinetic theory models rely on condensation and accommodation coefficients [2]. The jumps are microscale effects and thus difficult to measure, with experimental uncertainties making it almost impossible to verify models or extract reliable data [3]. Molecular dynamics (MD) simulations provide high resolution on the molecular scale but unavoidable stochastic noise affects determination of resistivities [4, 2].
Kinetic theory models are typically restricted to ideal gases, while MD simulations are often run in denser gases, where real gas effects affect the results, and, in order to reduce noise, in strong non-equilibrium with large fluxes. In this presentation, I combine elements of the Hertz-Knudsen-Schrage model of kinetic theory [5] with the Tsuruta condensation coefficient [6] and the Enskog-Vlasov model for real gases [7, 8] to the non-linear Tsuruta–EV–HKS model, which is valid up to the critical point . The resulting interfacial

resistivities markedly decrease with temperature towards the critical point, and depend non-linearly on mass and heat flux. Details on the derivation and evaluation can be found in Refs. [2, 9, 10]
The well-known approach of classical linear irreversible thermodynamics (LIT) [1] yields the interface conditions as relations between the thermodynamic forces, i.e., the deviations from equilibrium, and the thermodynamic fluxes, which push the system towards equilibrium,

$$\begin{bmatrix} \frac{g_L}{\theta_L} - \frac{g_V}{\theta_V} + h_V\left(\frac{1}{\theta_V} - \frac{1}{\theta_L}\right) \\ \frac{\theta_L}{\theta_V} - 1 \end{bmatrix} = \begin{bmatrix} \hat{r}_{11} & \hat{r}_{12} \\ \hat{r}_{21} & \hat{r}_{22} \end{bmatrix} \begin{bmatrix} \hat{J} \\ \hat{q}_V \end{bmatrix} . \tag{1}$$

On the left hand side of the above are the thermodynamic forces, with Gibbs free energy g, enthalpy h and temperature in energy units $\theta = RT$, where R is the gas constant and T thermodynamic temperature in Kelvin. Equation (1) is written for dimensionless mass and heat fluxes $\hat{J} = \frac{\sqrt{2\pi\theta_L}}{p_{\mathrm{sat}}(\theta_L)} J$, $\hat{q}_V = \frac{\sqrt{2\pi\theta_L}}{p_{\mathrm{sat}}(\theta_L)} \frac{q_V}{\theta_L}$.
The relation between forces and fluxes is given by the dimensionless resistivity matrix $\hat{r}_{\alpha\beta}$, which should be symmetric due to the Onsager relations. While in simple models the resistivities are assumed to be constants, in general they depend on the local temperature, and possibly on the fluxes $\hat{J}, \hat{q}_V$, see Ref. [11].
As a phenomenological approach, LIT can only predict the form of the interface relations, but cannot make detailed statements on the values of the resistivities, which therefore must be obtained from experiments or microscopic models.
The Hertz-Knudsen-Schrage (HKS) model is derived from kinetic theory modelling based on assumptions on condensation and accommodation coefficents, e.g., see [2]. Typically only a relation for mass flux is given, but for a complete interface model a relation for heat flux must be included. Evaluation of Eq. (1) with the HKS model yields the corresponding resistivities [2, 9].
For a constant accommodation coefficient ψ and considering non-linearities in mass flux [9], one finds mass and kinetic heat flux at the interface as, with mass density ρ and the abbreviation $p_{\mathrm{sat}} = p_{\mathrm{sat}}(\theta_L)$,

$$\hat{J} = \frac{2\psi}{2-\psi}\left[\frac{\rho_{V,\mathrm{sat}}\theta_L}{p_{\mathrm{sat}}} - \frac{\rho_V\theta_L}{p_{\mathrm{sat}}}\sqrt{\Theta} - \frac{1}{4\pi}\frac{p_{\mathrm{sat}}}{\rho_V\theta_L}\frac{\hat{J}^2}{\sqrt{\Theta}}\right] , \tag{2}$$

$$\begin{aligned} \hat{\mathrm{q}}_V = {} & \frac{2\psi}{2-\psi}\left(2 - \frac{5}{2}\Theta\right)\left[\frac{\rho_{V,\mathrm{sat}}\theta_L}{p_{\mathrm{sat}}} - \frac{\rho_V\theta_L}{p_{\mathrm{sat}}}\sqrt{\Theta}\right] + 4\frac{\rho_V\theta_L}{p_{\mathrm{sat}}}\left[1-\Theta\right]\sqrt{\Theta} \\ & + \frac{1}{4\pi}\left[8\frac{1-\psi}{2-\psi}\left(\frac{\rho_V\theta_L}{p_{\mathrm{sat}}}\sqrt{\Theta}\left(1 - \frac{7}{4}\Theta\right) + \frac{1}{2}\frac{\rho_{V,\mathrm{sat}}\theta_L}{p_{\mathrm{sat}}}\Theta\right) - \Theta\left(\frac{\rho_V\theta_L}{p_{\mathrm{sat}}}\sqrt{\Theta} + 2\frac{\rho_{V,\mathrm{sat}}\theta_L}{p_{\mathrm{sat}}}\right)\right]\frac{p_{\mathrm{sat}}^2}{\rho_V^2\theta_L^2}\frac{\hat{J}^2}{\Theta} \\ & + \frac{1}{8\pi^2}\frac{\psi}{2-\psi}\frac{p_{\mathrm{sat}}^3}{\rho_V^3\theta_L^3}\frac{\hat{J}^4}{\sqrt{\Theta}} . \end{aligned} \tag{3}$$

With MD simulations typically run at higher temperatures, the HKS model must be extended to account for deviation from the ideal gas law for the vapor as well as compressibility of the liquid. Furthermore, based on MD simulations Tsuruta and co-workes have shown that for higher temperatures the condensation coefficient is a decreasing function of temperature and depends on impact velocity [6].
To include these effects, in Ref. [10] we have extended the non-linear HKS model (2, 3) by accounting for Tsuruta's impact dependent condensation coefficient, and we used the Enskog-Vlasov gas model [7, 8] to describe compressible liquid and non-ideal vapor.
Resistivities were determined numerically from this model for the special cases of mass transfer with adiabatic vapor, and heat transfer across the interface for zero mass flux, as depicted in Fig. 2. For low temperatures, these results agree with Eqs. (2, 3).
Since accurate data from experiments or microscopic simulations is scarce, a detailed comparison of the modeling results with data is not possible. Figure 3 shows the resistivities determined from MD

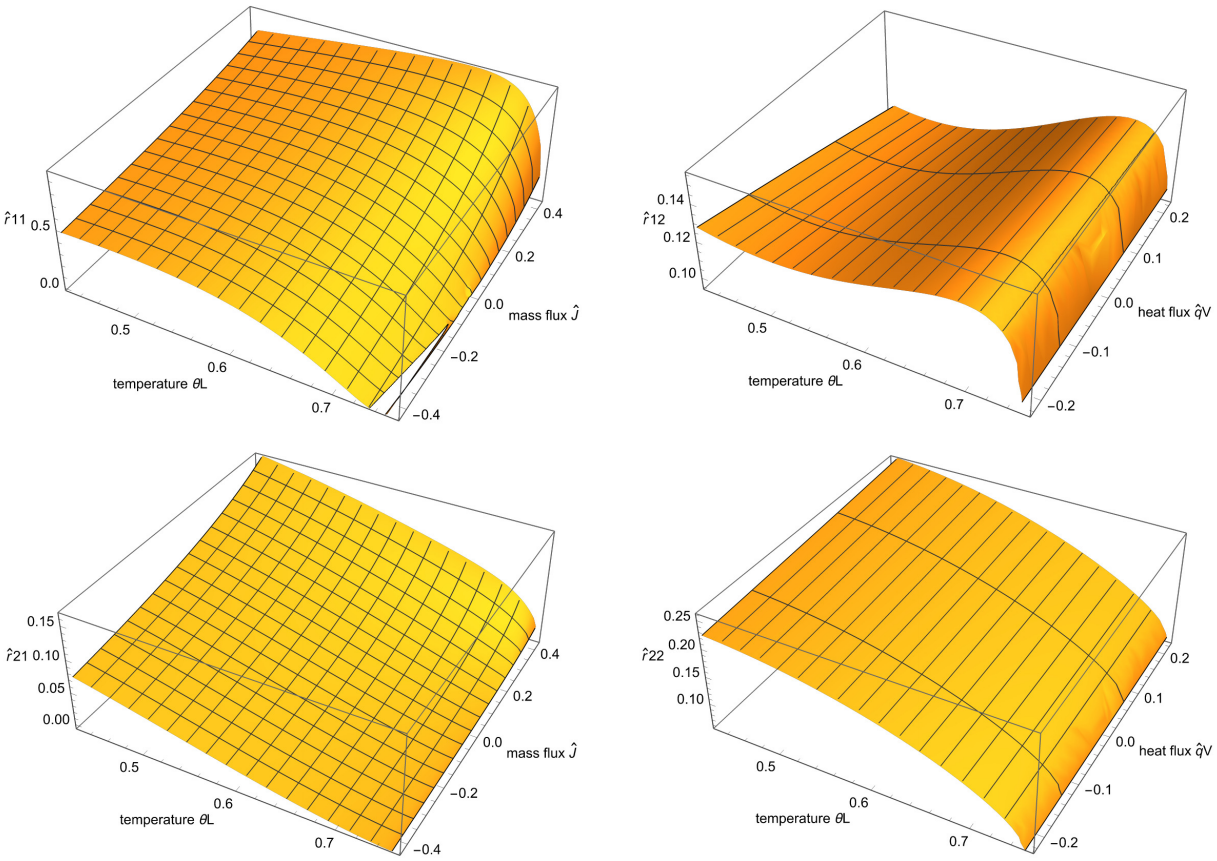

Figure 2: Resistivities $\hat{r}_{\alpha\beta}$ for the Tsuruta-EV-HKS model as functions of temperature and mass flux $\hat{J}$ (for $\hat{r}_{11}$, $\hat{r}_{21}$) or heat flux $\hat{q}_V$ (for $\hat{r}_{12}$, $\hat{r}_{22}$). Critical temperature for the EV gas is $\theta_{\rm cr} = 0.754$.

simulations [4] as functions of relative temperature $\theta_{\rm L}/\theta_{\rm cr}$, where the relative size of fluxes is indicated by gray levels. The temperatures are below the region where in Fig. 2 resistivities are strongly decreasing. The MD resistivities stand in principal agreement with the modelling results in Fig. 2: For large mass fluxes, the resistivity $\hat{r}_{11}$ is a slowly decreasing function of temperature, while the heat transfer resistivity $\hat{r}_{22}$ exhibits comparatively faster decrease. Both off-diagonal resistivities decrease rather weakly with increasing temperature, with $\hat{r}_{21}$ appearing to be larger for larger mass fluxes.
The presentation will give details on derivation of the model and its evaluation, as well as a deeper discussion of MD results in terms of non-linearity and non-ideality. It will be highlighted that the predicted behavior—marked temperature dependence, in particular for temperatures approaching the critical point, and non-linearity—will affect experiments and molecular dynamics simulations and thus must be carefully considered in evaluation of experimental and simulation data.

References

[1] Struchtrup, H. (2024). A Thermodynamic Introduction to Transport Phenomena, Springer Cham.
[2] Caputa, J.P., & Struchtrup, H. (2011) Interface model for non-equilibrium evaporation, Physica A, 390, 31–42
[3] Rauter, M.T., Aasen, A., Kjelstrup, S., & Wilhelmsen, Ø. (2023). A comparative study of experiments and theories on steady-state evaporation of water, Chem. Therm. Therm. Anal., 8, 100091.
[4] Homes, S., & Vrabec, J. (2024). Resistivities across the vapor–liquid interface of a simple fluid: An assessment of methods, Phys. Fluids, 36, 022122.

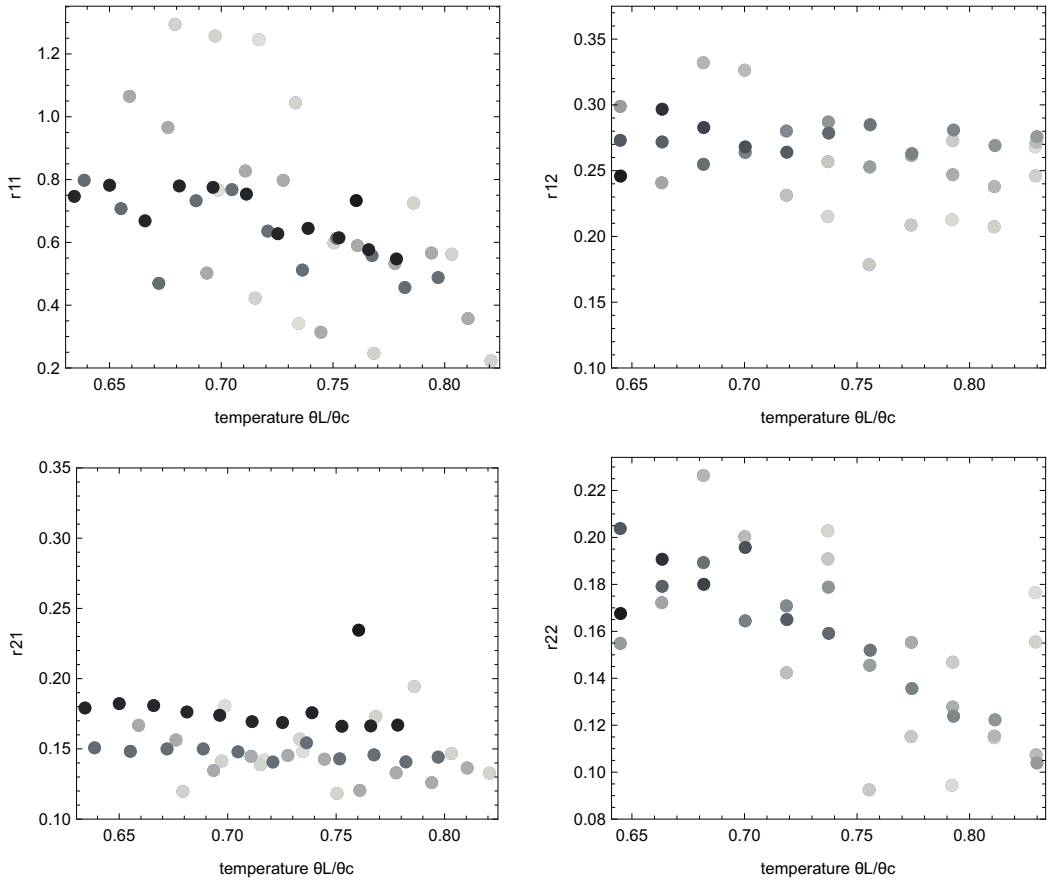

Figure 3: Dimensionless resistivities $\hat{r}_{\alpha\beta}$ determined from MD simulations [4] plotted over relative temperature $\theta_{\mathrm{L}}/\theta_{\mathrm{cr}}$. The gray level indicates the strength of dimensionless mass and heat flux, respectively, with darker colors indicating larger absolute fluxes.

[5] Schrage, R.W. (1953). A Theoretical Study of Interphase Mass Transfer. Columbia University Press, New York.
[6] Tsuruta, T., Tanaka, H., & Masuoka, T. (1999). Condensation/evaporation coefficient and velocity distributions at liquid–vapor interface, Int. J. Heat Mass Trans., 42, 4107-4116.
[7] Struchtrup, H., & Frezzotti, A. (2022). Twenty-six moment equations for the Enskog-Vlasov equation, J. Fluid Mechanics, 940, A-40.
[8] Struchtrup, H., Jahandideh, H., Couteau, A. & Frezzotti, A. (2024). Heat Transfer and Evaporation Processes from the Enskog-Vlasov Equation, and its Moment Equations, Int. J. Heat Mass Trans., 223, 125238.
[9] Feyzi Oskouei, P., & Struchtrup, H. (2025). Nonlinear mass and heat transfer across liquid-vapor interfaces. Phys. Rev. E, 112, 025501.
[10] Struchtrup, H. (2025). Mass and heat transfer resistivities at liquid–vapor interfaces: Beyond the ideal gas. Int. J. Heat Mass Trans., 256, 127943.
[11] Struchtrup, H. & Öttinger, H.C. (2023). Nonequilibrium liquid-vapor interfaces: Linear and nonlinear descriptions, Phys. Rev. E, 108, 064801.

NEGF26-679608

MEASUREMENTS OF HELIUM ARGON MIXTURE USING CONSTANT VOLUME TECHNIQUE

Emil Grigorov[1], Felix Sharipov[2], Pierre Perrier[1], Frédéric Topin[1], Irina Graur*[1]
[1]Aix-Marseille Université, CNRS, IUSTI UMR 7343, 5 rue E. Fermi, 13453, Marseille, France
emil.grigorov@univ-amu.fr, pierre.perrier@univ-amu.fr, frederic.topin@univ-amu.fr,
irina.martin@univ-amu.fr
[2]Departamento de Física, Universidade Federal do Paraná, Curitiba, 81531-980, Brazil
sharipov@fisica.ufpr.br

KEY WORDS

gas flow through a microchannel, rarefaction parameter, gas mixture, transitional and slip flow regimes

INTRODUCTION

In many applications involving gas flows it is far more common to encounter gaseous mixtures rather than a single gas. The Knudsen number (or the rarefaction parameter) of a gas mixture, defined as the ratio between the molecular mean free path of the mixture and a characteristic flow dimension, determines the properties of such a flow. In the free molecular flow regime ($Kn \gg 1$) the intermolecular collisions can be neglected and the components of a gas mixtures are independent of each other. In this case the analytical solutions [1] or the collision-less modeling using the Molflow software [2] or collision-less Direct Simulation Monte Carlo (DSMC) method [3] could be used to predict the behaviors of gas mixture flows. This flow regime is related to the vacuum technology applications, as leak detection [4], [5], gas composition determination via mass spectrometer [6] and the pumping speed analysis [7]. When the Knudsen number is larger then 0.1, $Kn > 0.1$, i.e. a gas mixture is in the slip and viscous flow regimes, a single gas approximation could be suitable to simulate the mixture behaviors. These gas flow regimes can be found in various MEMS applications related to the gas analysis [8]. Both approaches presented above come with limitations and assumptions, which often do not hold - or hold only partially - in the transitional flow regime.
The single gas approach is also discussed in Refs. [9], [10]. The authors of Ref. [9] shown an example of application of this approach for the case of He-Ar binary mixture and the deviation less than 3% was found between the single gas approximation with the velocity slip coefficient calculated for the gas mixture and the numerical solution of the McCormack model up to the rarefaction parameter equal 2. More complete numerical study is carried out in Ref. [10], where the numerical simulations of He-Xe gas mixture are realized to complete the data base for He-Ne, He-Ar and He-Kr, provided in Ref. [11]. Different length/radius ratios, namely $L/R = 1$, 5 and 10 are considered. The tube conductance is

* Corresponding author

analyzed using single gas approach. The estimation of the error made applying the single gas approach is provided and it depends on the ratio of the molar masses of the mixture, the initial concentration and the rarefaction level.
To apply this single gas approximation approach the value of the velocity slip coefficient must be known. As it was mentioned above it was calculated numerically by several authors. However, due to the additional difficulties related to the experiments with the mixture there are only very few data on the measurements of this coefficients. To our best knowledge, only two articles report the data on the velocity slip coefficient for the gas mixture, see Refs. [12], [13]. The authors of [12] have measured the velocity slip coefficient using the Spinning Rotor Gauge (SRG). The data on the velocity slip coefficients for the mixtures of He-Ar, He-N_2 and He-Ne for three different concentration of each are reported. The viscous slip coefficient for a helium - argon binary gas mixture was determined based on mass flow rate measurements through a microtube operating in the slip flow regime in Ref. [13]. The constant-volume method was employed for this purpose, relating the pressure variations in two connected chambers. The results showed that the extracted viscous slip coefficients exhibit a concave dependence on the molar ratio of the mixture.

EXPERIMENTAL SETUP

The improved constant-volume technique [14] is used to measure the gas mass flow rate through the microtube settled between two reservoirs. The experimental setup is shown in Fig. 1. The volumes of the inlet and outlet tanks (which consist of pipes) are equal to $(29.6 \pm 1.42) \times 10^{-6}$ m^3 and $(22.6 \pm 1.08) \times 10^{-6}$ m^3, respectively.

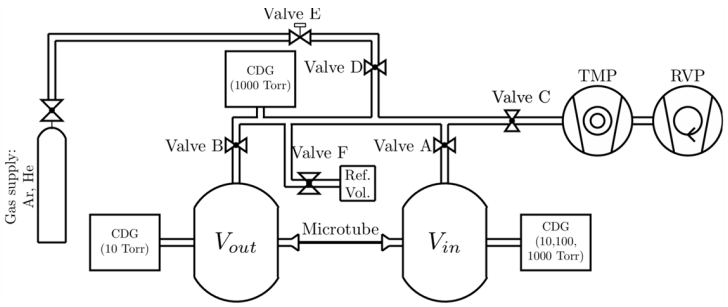

Figure 1: Experimental setup.

The outlet reservoir is pumped down using the turbomolecular pump. Absolute pressure variations in both tanks are measured using capacitance diaphragm gauges (CDG), with full-scale ranges of 1000 Torr for the inlet chamber and 10 Torr for the outlet one. Since each sensor has a different internal volume (3.6 and 4.2 $\times 10^{-6}$ m^3, respectively), these volumes are added to the pipes volumes to determine the total volume of each tank. The total inlet volume (V_{in}) is 30.1 and 30.7 $\times 10^{-6}$ m^3, respectively, depending on the sensor used. Similarly, the total outlet volume (V_{out}) is 26.2 and 26.8 $\times 10^{-6}$ m^3, respectively.
The temperatures of the external walls of both tanks are monitored using thermocouples. During each experiment, the variation at room temperature does not exceed 0.2°C, ensuring isothermal conditions.
The stainless steel tube, with a circular cross-section, is positioned between the two tanks. Its dimensions were previously determined in Ref. [15] using an electron microscope to be 2a = 239.73 $\pm$2.39μm for the internal diameter, a is the tube radius, and L = 10.33 $\pm$0.05cm for the length.
The binary mixture of two noble gases is considered, namely, helium and argon.

RESULTS AND DISCUSSION

The pressure variation over time in the inlet tank was measured for five different initial concentrations C_0 of argon-helium mixture defined as

$$C_0 = \frac{n_1}{n_1 + n_2}, \tag{1}$$

where n_1 and n_2 are the number densities of helium and argon respectively. All measurements were conducted within the viscous, slip and transitional flow regimes. Figure 2 shows measured inlet pressure and rarefaction parameter vs. time. The rarefaction parameter for the mixture is defined as

$$\delta = \frac{ap}{\mu v_{\mathrm{m}}}, \tag{2}$$

where a is the tube radius, p is the reference pressure, μ is the gas viscosity of the mixture, v_{m} is the characteristic molecular speed of the mixture, calculated via the mean molar mass.

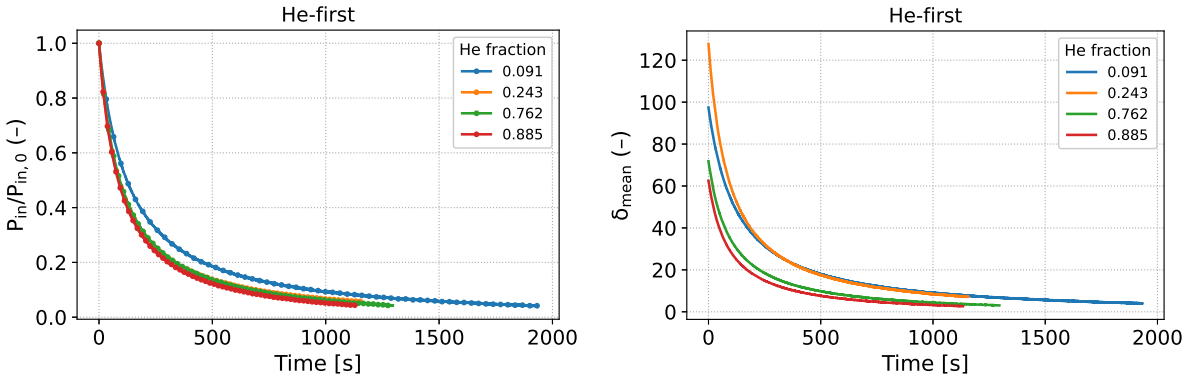

Figure 2: (a) Measured inlet pressure $p_{\mathrm{in}}/p_{\mathrm{in0}}$ vs. time, (b) rarefaction parameter vs. time.

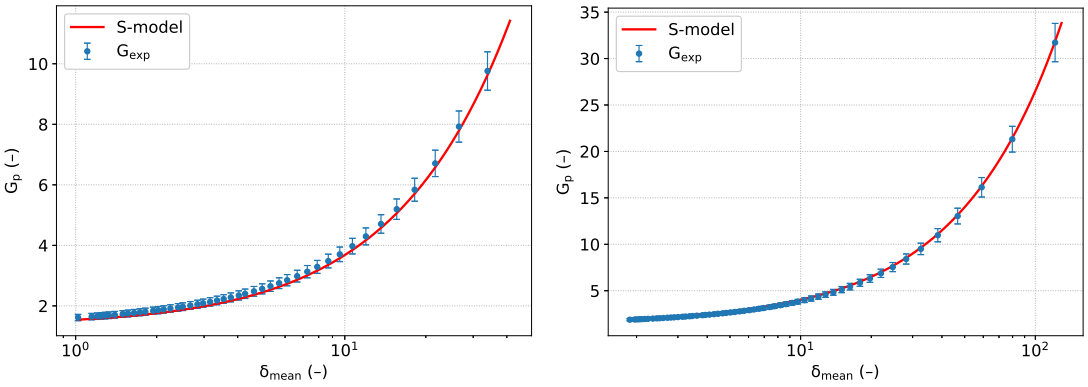

Figure 3: (Measured dimensionless mass flow rate, G_{exp}, mass flow rate obtained from the fitting of the S-model results for a single gas, denoted "S-model", with the velocity slip coefficient, σ_{p}, from Ref. [16]: (a) $C_0 = 10\%$, (b) C_0=50%.

Figure 3 shows the dimensionless mass flow rate extracted from the pressure measurements in the inlet tank, the fitting formula [17] of the results obtained from the S-model with velocity slip coefficient calculated for He-Ar mixture in [16]. Very good agreement is found for all data even up the beginning of transitional flow regime.

Acknowledgements

The study was supported by the ANR TEGTIC project number ANR-23-CE51-0055-01. One of the authors, Felix Sharipov, thanks the Aix Marseille University for the support of his stay at the IUSTI laboratory in July 2024 and CNPq (Brazil, Grant No. 303429/2022-4).

References and citations

[1] F. Sharipov, Gaseous mixtures in vacuum systems and microfluidics, J. Vac Sci. Technol. A 31 (5) (2013) 050806–1.
[2] M. Ady, R. Kersevan, Introduction to the latest version of the test-particle, ACC 2014-0249, CERN, Geneva, Switzeland (October 2014).
[3] G. A. Bird, Molecular Gas Dynamics and the Direct Simulation of Gas Flows, Oxford Science Publications, Oxford University Press Inc., New York, 1994.
[4] K. McCulloh, C. Tilford, C. Ehrich, F. Long, Low-range flowmeters for use with vacuum and leak standards, Journal of Vac. Sci. Technol. A, Surfaces, and Films 5 (6) (1987) 376–381.
[5] M. Bergoglio, A. Calcatelli, Gas flow rate measurements for leak callibration, Vacuum 46 (8-10) (1995) 763–765.
[6] W. Sun, C. Wu, Y. Cheng, M. Dong, M. Guo, Y. Li, Z. Ren, W. Jia, N. Wei, Study on calibrating the quadrupole mass spectrometers with gas mixture, Measurements 164 (2020) 108099.
[7] K. Jousten, H. Menzer, R. Niepraschk, A new fully automated gas flowmeter at the ptb for flow rates between 10^{-13} mol/s and 10^{-6} mol/s, Metrologia 39 (6) (2002) 519.
[8] C. Zhang, T. Wang, G. Zhang, R. Gao, C. Gao, Z. Wang, F. Xuan, Rational design and fabrication of MEMS gas sensors with long-term stability: A comprehensive review, Adv. Sci. 12 (e11555) (2025).
[9] F. Sharipov, D. Kalempa, Velocity slip and temperature jump coefficients for gaseous mixtures. I. Viscous slip coefficient, Phys. Fluids 15 (6) (2003) 1800–1806.
[10] D. Valougeorgis, M. Vargas, S. Naris, Analysis of gas separation, conductance and equivalent single gas approach for binary gas mixture flow expansion through tubes of various lengths into vacuum, Vacuum 128 (2016) 1–8.
[11] M. Vargas, S. Naris, D. Valougeorgis, S. Pantazis, K. Jousten, Time-dependent rarefied gas flow of single gases and binary gas mixtures into vacuum, Vacuum 109 (2014) 385–396.
[12] J. A. Bentz, R. V. Tompson, S. K. Loyalka, Viscosity and velocity slip coefficients for gas mixtures: Measurements with a spinning rotor gauge, J. Vac. Sci. Technol. 17 (1999) 235.
[13] H. Yamaguchi, K. Takamori, P. Perrier, I. Graur, Y. Matsuda, T. Niimi, Viscous slip coefficient for binary gas mixtures mesured from mass flow rate through a single microtube, Physics of Fluids 28 (2016) 092001.
[14] E. Grigorov, F. Sharipov, P. Perrier, F. Topin, I. Graur, Measurements of the poiseuille coefficient in the slip and transitional flow regimes, Journal of Fluid Mechanics accepted (2025).
[15] M. Hadj Nacer, I. Graur, P. Perrier, J. G. Méolans, M. Wüest, Gas flow through microtubes with different surface coating, Journal of Vac. Sci. Technol. A 32 (2) (2014) 021601–9.
[16] F. Sharipov, D. Kalempa, Gaseous mixture flow through a long tube at arbitrary Knudsen number, J. Vac. Sci. Technol. A 20 (3) (2002) 814–822.
[17] F. Sharipov, I. Graur, C. Day, Leak rate of water into vacuum through microtubes, Journal of Vac. Sci. Technol. A 28 (3) (2010) 443–448.

NEGF26-685635

MICROREGENERATORS DESIGNED FOR OSCILLATORY GAS FLOWS INSIDE CRYOCOOLERS

Frederic Ayela*[1], Samuel Bonnet[1,2], Damien Colombet[1], Nicolas Luchier[2], Manuel Medrano-Munoz[2]

[1]LEGI, Univ. Grenoble Alpes, CNRS, 38000 Grenoble, France
[2]IRIG DSBT, CEA, 38000 Grenoble, France
frederic.ayela@univ-grenoble-alpes.fr, samuel.bonnet@univ-grenoble-alpes.fr, damien.colombet@univ-grenoble-alpes.fr, nicolas.luchier@cea.fr, manuel.medrano@univ-grenoble-alpes.fr

KEY WORDS

Diamond shaped cylinders, pressure oscillation, cut-off frequency, Stirling engines.

ABSTRACT

Regenerators used in Stirling engines or cryocoolers are usually composed of a cluster of spheres or metallic fibers. Gas flow inside such devices is a problem that couples heat transfer and hydrodynamics, as it requires determining the configuration that will optimize heat exchange and minimize pressure drops—and thus the required hydraulic power. Nowadays, microfabrication techniques make possible to perform microregenerators that integrate various networks with perfectly controlled geometries into microchannels, allowing to study the influence of aspect ratios and porosity on both the pressure drop of the flowing gas and thermal exchange. In that way, our teams have studied numerically the flow and heat transfer around a diamond-shaped cylinder at moderate Reynolds number [1], and experimentally the pressure losses at moderate Reynolds numbers in diamond-shaped cylinders arrays [2, 3], with helium gas as the working fluid. Steady-state flow experiments and heat transfer simulations have demonstrated that such geometries are indeed more efficient than those of conventional regenerators. Experimental studies of the flow have confirmed and quantified the influence of porosity on associated pressure drops.
Oscillatory flows have then been considered. This is a key point because the miniaturization of the size of the cryocoolers, for spatial applications for example, induces a necessary increase of the frequency of the cycles in order to keep the heat power extracted from the cold source at a constant level.

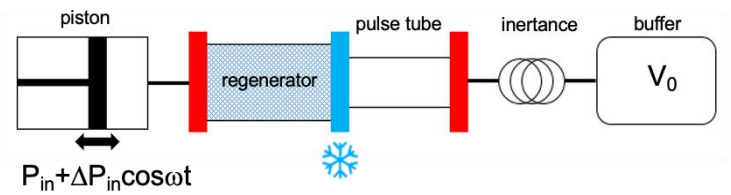

Figure 1: Sketch of a cryocooler.

* Corresponding author

A simplified sketch of a cryocooler is presented in Figure 1. The inertance and the buffer act as a second piston of a Stirling engine.
The microregenerators we have designed have been micromachined by deep reactive ion etching of a silicon substrate. The silicon part is then anodically bonded by a Pyrex cap. A SEM snapshot of the array of a periodic set of diamond shaped cylinders is presented in Figure 2.

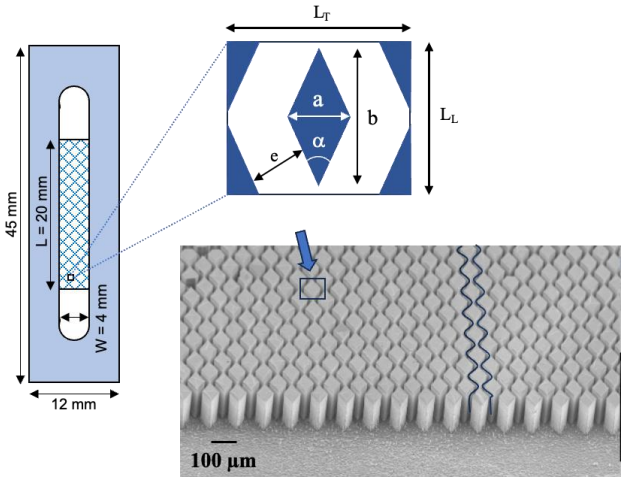

Figure 2 : Micromachined silicon regenerator consisting of an array of single cells. The blue path illustrates the tortuous way of the gaseous laminar flow through elementary cells.

We have developped a model establishing the cut-off frequency above which the pressure modulation ΔP_{out} in the volume V_0 is damped, in isothermal and laminar flow conditions. Such microregenerators coupled with an output volume V_0 and submitted to an oscillatory gaseous flow, behave as an electrical RC circuit. The buffer volume V_0 acts as a capacitance and the viscosity of the gas flowing through the microchannels in the regenerator is similar to a resistance. In this model, the cut-off frequency obeys :

$$f_c \approx \frac{8}{\pi\mu}\frac{n_T}{n_L}\frac{H}{P_{ois}V_0}\frac{P_{in}e^3}{g(\alpha)} \qquad (1)$$

where µ is the dynamic viscosity of the gas, n_L and n_T are the number of elementary cells in the lenght and width direction respectively, H is the height of the channel, P_{ois} is the Poiseuille number for each microchannel (value around 96), e is the smallest distance between two neihbouring cylinders (Figure 2) and g(α) is a function of the geometrical characteristics of the cylinders. As the cut-off frequency varies as e^3, it is obvious that it is difficult to combine size reduction of microregenerators and high working frequency. No rarefaction effect is expected as $P_{in} \approx 10$ bar.

A double-piston oscillator (Thales, LSF9310), generates stable pressure waves in the frequency range of 15–120 Hz, with an amplitude on the order of 1 bar. To measure cut-off frequencies, pressure measurement (P_{in} and P_0) were performed using two dynamic pressure sensors (Kistler 211B4) and two static pressure sensors (Keller PAA-23). Temperature measurements were carried out using K-type micro-thermocouples (250 µm in diameter). Pressure and temperature values were continuously monitored and recorded using an oscilloscope (Keysight DSOX1204A) and two data acquisition cards (NI-USB309, cDAQ9171).

We have tested such a model with several microregenerators exhibiting different a, e and α values, with $V_0 = 2$ cm^3 and $V_0 = 15$ cm^3, and input pressures 8 bar < P_{in} < 15 bar, $\Delta P_{in} \approx 1$ bar. Theoretical cut-off frequencies calculated from Eq. (1) ranged from 0.1 Hz to 14 Hz. All the devices under test

have presented a damping of the output pressure modulation when increasing the frequency up to 100 Hz, with experimental cut-off frequencies which are all in very good agreement with the calculated ones. An illustration is presented in Figure 3.

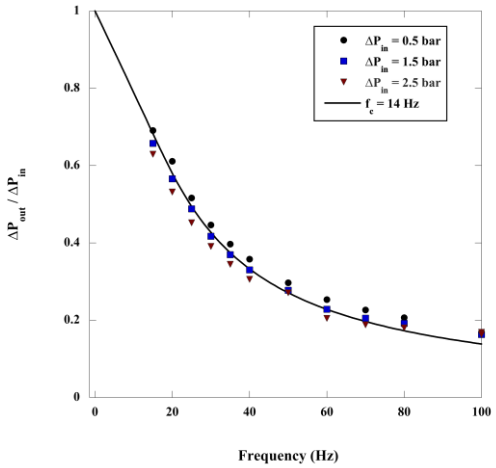

Figure 3 : Spectrum of the ratio $\Delta P_{out}/\Delta P_{in}$ for a microregenerator having a theoretical cut-off frequency f_c = 14Hz (straight line). The evolution of the experimental data, when increasing ΔP_{in}, is the consequence of an increase of the viscosity because isothermal conditions are no more respected. Experimental uncertainties about ΔP_{out} and ΔP_{in} are included in the size of the plots.

A key finding of this work is the importance of the transient regime and the possibility of controlling the operating frequency through the network arrangement. With similar geometries but with parameters b and a slightly smaller than those used in the current work presented here, cut-off frequencies of ≈ 600 Hz are theoretically reachable. This research continues with experimental studies of heat transfer.

References and Citations

[1] Sochinski, A., Colombet, D., Ayela, F., Medrano-Munoz, M., Luchier, N., Duval, J._M. (2018). *Hydrodynamic experimental and numerical study of micro-fabricated regenerators*. NEGF 18, 3th European Conference on Non-Equilibrium Gas Flows, Strasbourg.

[2] Sochinski, A., Colombet, D., Medrano-Munoz, M., Ayela, F., Luchier, N. (2019). *Flow and heat transfer around a diamond-shaped cylinder at moderate Reynolds number*, Int. J. Heat Mass Transf. **142**, 118435.

[3] Sochinski, A., Colombet, D., Medrano-Munoz, M., Ayela, F., Luchier, N. (2021). *Pressure losses at moderate Reynolds numbers in diamond-shaped cylinders arrays : application to micro-regenerators*, Journal of Fluids Engineering **143**(6), 061203.

NEGF26-679212

Model-Adaptive Simulation of Moment Equations for Capturing Nonequilibrium Regions in Rarefied Gas Flows

Rik Verbiest*[1], Julian Koellermeier[1,2]
[1] Rijksuniversiteit Groningen, Broerstraat 5, 9712 CP Groningen, the Netherlands
r.verbiest@rug.nl
[2] Ghent University, Sint-Pietersnieuwstraat 33, 9000 Gent, Belgium

KEY WORDS

Multiscale modelling, domain decomposition, model order reduction, hyperbolic relaxation systems.

ABSTRACT

The need for space- and time-adaptivity in simulations of rarefied gases arises because different time-variable subdomains within a rarefied gas domain often require varying levels of modelling complexity. Different-order moment models are effective at describing rarefied flows with respective levels of complexity in each subdomain. In this work, an adaptive numerical method for simulating the non-linear Hyperbolic Moment Equations (HME) model is proposed to simulate a rarefied gas flow using a HME model with time- and space-dependent model order. The first step of the adaptive procedure is a domain decomposition into subdomains each modelled by an HME model of an appropriate order, using a combination of a distribution-based nonequilibrium criterion and a gradient-based nonequilibrium criterion. In the second step of the adaptive procedure, a non-linear adaptation of a recently developed padded buffer cell approach is proposed to couple these varying-order HME models. The proposed adaptive numerical method yields accurate results compared to a high-order HME model while obtaining a computational speedup.

Introduction

Many rarefied gas flows are characterized by the presence of both near-equilibrium regions and nonequilibrium regions. Examples are high-altitude flights and atmospheric reentry flights, in which the dimensionless Knudsen number (Kn) varies in time and space. In regions of small Kn, the gas can be assumed to be in equilibrium and standard fluid dynamics models for the macroscopic quantities yield sufficient accuracy. The nonequilibrium effects in regions of large Kn need models beyond the standard fluid equations that include microscopic effects. This motivates the need for adaptive simulation techniques and hybrid methods for the numerical simulation of rarefied gas flows.

* Corresponding author

Rarefied gas flows in the mesoscopic regime are represented by a particle distribution function $f(t, \vec{x}, \vec{c})$, that describes the probability of finding a gas particle at time t in position $\vec{x}$ and with particle velocity $\vec{c}$. The evolution of the function $f(t, \vec{x}, \vec{c})$ is governed by the Boltzmann transport equation (BTE)

$$\partial_t f + \vec{c} \cdot \nabla_{\vec{x}} f = Q(f, f), \tag{1}$$

where the right-hand side collision operator $Q(f, f)$ describes collisions between gas particles. Existing methods for the numerical simulation of the BTE (1) can be divided into two main categories: 1) particle-based solvers and 2) deterministic solvers. In particle-based solvers, the gas is represented by simulating sampled gas particles whose free flow streaming and collision mimic the BTE (1). Deterministic solvers compute approximate solutions of the BTE (1) by either deterministically discretizing the phase space $(t, \vec{x}, \vec{c})$ of the BTE (1) directly, or describing the evolution of macroscopic quantities by a reduced order model and discretizing the resulting partial differential equations of the reduced order model. Many hybrid methods couple fluid dynamics models in regions of small Kn with a particle representation in regions of large Kn. The fluid dynamics equations are typically solved by *deterministic* solvers, while the particle description employs *particle-based* solvers, which complicates the coupling.
Deterministic moment models for kinetic equations, first introduced by Grad in [6], have proven to be a powerful class of models for the simulation of rarefied gases in the mesoscopic regime [3, 9]. These moment models are reduced order models for the BTE (1) that achieve increasing accuracy by successively including more and more variables and evolution equations. A moment model is therefore characterized by its order, measuring the number of variables or equations. A higher-order moment model is often more accurate but computationally more expensive than a lower-order moment model as more variables are included in the model. It is thus desirable to always use the moment model with the smallest possible order. This directly calls for adaptivity. Moment models are ideally suited for adaptivity because they have a hierarchical structure.
In this study, a model-adaptive method that is adaptive in time and space for the simulation of the one-dimensional hyperbolic moment equations (HME) [2] is discussed. The adaptive procedure consists of a domain decomposition criterion and a spatial coupling formula. The spatial coupling formula has recently been applied to moment models for free-surface flows in [10] and is a non-linear adaptation of the spatial coupling proposed in [11]. In particular, the same numerical solver is used in the entire domain, which simplifies the coupling.

Hyperbolic Moment Equations

The one-dimensional HME model [2] is derived by assuming $f(t, x, c)$ to be a truncated Hermite expansion of order $M \geq 3$ given by

$$f(t, x, c) = \sum_{i=0}^{M} f_i(t, x) \frac{1}{\sqrt{2\pi}} \theta^{-\frac{i+1}{2}} He_i\left(\frac{c-u}{\sqrt{\theta}}\right) \exp\left(-\frac{(c-u)^2}{2\theta}\right), \tag{2}$$

were He_i and f_i are the $i-$th Hermite polynomial and moment, respectively, u is the macroscopic velocity, and θ is the temperature. The first three moments read $f_0 = \rho$, where ρ is the density, and $f_1 = f_2 = 0$. The density ρ, velocity u, and temperature θ are governed by the Euler equations. The equations for the remaining moments are obtained by taking higher-order moments of the BTE (1):

$$\begin{aligned} &\partial_t f_k - f_{k-1}\frac{\theta}{\rho}\partial_x \rho + (k+1) f_k \partial_x u + \left(\frac{1}{2}\theta f_{k-3} + \frac{k-1}{2} f_{k-1}\right)\partial_x \theta \\ &- \frac{3}{\rho} f_{k-2}\partial_x f_3 + \theta \partial_x f_{k-1} + u \partial_x f_k + (k+1)\partial_x f_{k+1} = -\frac{1}{\tau} f_k, \qquad k \geq 3, \end{aligned} \tag{3}$$

with relaxation time $\tau \in \mathbb{R}^+$ [2]. The derivation of the equations (3) uses the BGK collision operator [1]. The system of partial differential equations (3) together with the Euler equations is closed by setting

$f_{M+1} = 0$. It is well-know that this system of equations is not hyperbolic. To obtain a hyperbolic system, the HME model adds a regularization term to the equation for the last moment f_M. For details, we refer the reader to [2]. The HME model of order M can be written in compact form as

$$\partial_t \vec{w}_M + A_M(\vec{w}_M)\partial_x \vec{w}_M = S\vec{w}_M, \tag{4}$$

with state variable vector $\vec{w}_M = (\rho, u, \theta, f_3, \ldots, f_M) \in \mathbb{R}^{M+1}$. The transport matrix $A_M(\vec{w}_M) \in \mathbb{R}^{(M+1)\times(M+1)}$ and the matrix $S \in \mathbb{R}^{(M+1)\times(M+1)}$ are defined in [2].

Domain Decomposition Criterion

In every time step t_n, the computational domain $\Omega \subset \mathbb{R}$ is decomposed into subdomains that are each modelled by an HME model of an appropriate order. We propose a domain decomposition criterion that is a combination of a distribution-based criterion for model-coarsening and a gradient-based criterion for model-refining.

Model-coarsening

The order of the HME model is reduced from higher order M_H to lower order M_L in a spatial subdomain if, in that subdomain, the highest-order moment f_{M_H} is small in magnitude, i.e.,

$$|f_{M_\mathrm{H}}| < \epsilon_\mathrm{f}, \tag{5}$$

where ϵ_f is a chosen tolerance level. This distribution-based model-coarsening criterion (5) has previously been studied in [7].

Model-refinement

The order M of the HME model is increased from lower order M_L to higher order M_H in a spatial subdomain if, in that subdomain, the gradients of the moments are small in magnitude. We propose the model-refinement criterion

$$Kn\sqrt{\left(\frac{\partial_x \rho}{\rho}\right)^2 + \left(\frac{\partial_x u}{u}\right)^2 + \left(\frac{\partial_x T}{T}\right)^2 + \left(\frac{\partial_x f_3}{f_3}\right)^2 + \ldots + \left(\frac{\partial_x f_{M_\mathrm{L}}}{f_{M_\mathrm{L}}}\right)^2} > \epsilon_\partial, \tag{6}$$

where ϵ_∂ is a chosen tolerance level. This gradient-based criterion (6) is similar to the criterion proposed in [8], for example.

Spatial Coupling

For the spatial coupling of two different-order HME moment models at their boundary interface, we propose a non-linear adaptation of the Padded Buffer Cell coupling proposed in [11].
The HME equations (4) are discretized in space and approximated in the finite volumes $[x_i - \Delta x/2, x_i + \Delta x/2]$ with equidistant cell centers x_i, $i = 1, 2, \ldots, N_x$, and discretized in time with time step Δt and approximated at the discrete times t_n, $n = 0, 1, \ldots, N_t$. The discretized variable vectors at time t_n in cell $[x_i - \Delta x/2, x_i + \Delta x/2]$ are denoted by w_i^n. The overarching numerical scheme for the transport part of (4) is the polynomial viscosity method (PVM) [5]

$$w_i^{n+1} = w_i^n - \frac{\Delta t}{\Delta x}\left(D^+_{i-\frac{1}{2}} + D^-_{i+\frac{1}{2}}\right), \qquad i = 1, \ldots, N_x, \tag{7}$$

with fluctuations $D^\pm_{i+\frac{1}{2}} = A^\pm_\Phi(w_i^n, w_{i+1}^n)$ given by, for example, the PRICE scheme [4]

$$A^\pm_\Phi(w_\mathrm{l}, w_\mathrm{r}) = \frac{1}{2}\left(A_\Phi(w_\mathrm{l}, w_\mathrm{r}) \cdot (w_\mathrm{r} - w_\mathrm{l}) \pm Q_\Phi(w_\mathrm{l}, w_\mathrm{r}) \cdot (w_\mathrm{r} - w_\mathrm{l})\right), \tag{8}$$

with generalized Roe linearization $A_\Phi = A_\Phi(w_\mathrm{l}, w_\mathrm{r})$ given by

$$A_\Phi(w_\mathrm{l}, w_\mathrm{r}) \cdot (w_\mathrm{r} - w_\mathrm{l}) = \int_0^1 A_M(\Phi(s; w_\mathrm{l}, w_\mathrm{r})) \frac{\partial \Phi}{\partial s}(s; w_\mathrm{l}, w_\mathrm{r}) ds, \tag{9}$$

with a linear path $\Phi(s; w_\mathrm{l}, w_\mathrm{r}) = (1-s) \cdot w_\mathrm{l} + s \cdot w_\mathrm{r}$, and with numerical viscosity matrix

$$Q_\Phi(w_\mathrm{l}, w_\mathrm{r}) = \frac{\Delta x}{2\Delta t} I + \frac{\Delta t}{2\Delta x} A_\Phi^2(w_\mathrm{l}, w_\mathrm{r}). \tag{10}$$

At a boundary interface located at $x = x_L + \Delta x/2$ between a lower-order HME model of order M_L and a higher-order HME of order $M_\mathrm{L}+1$, the fluctuations $D_{L+\frac{1}{2}}$ are computed by padding the left lower-order state variable vector $w_L^n = (\rho_L^n, u_L^n, \theta_L^n, (f_3)_L^n, \ldots, (f_{M_L})_L^n)^T \in \mathbb{R}^{M_L+1}$ with an additional moment $(f_{M_L+1})_L^n$ such that it has the same length as the right higher-order state variable vector $w_{L+1}^n \in \mathbb{R}^{M_L+2}$.

Acknowledgements

This work is part of the project *HiWAVE* with file number VI.Vidi.233.066 of the *ENW Vidi* research programme, funded by the *Dutch Research Council (NWO)*.

References and citations

[1] P. L. Bhatnagar, E. P. Gross, and M. Krook. A model for collision processes in gases. i. small amplitude processes in charged and neutral one-component systems. *Phys. Rev.*, 94:511–525, May 1954.
[2] Z. Cai, Y. Fan, and R. Li. Globally Hyperbolic Regularization of Grad's Moment System in One-Dimensional Space. *Commun. Math. Sci.*, 11:547–571, 2013.
[3] Z. Cai, Y. Fan, and R. Li. A Framework on Moment Model Reduction for Kinetic Equation. *SIAM J. Appl. Math.*, 75(5):2001–2023, 2015.
[4] A. Canestrelli, A. Siviglia, M. Dumbser, and E. Toro. Well-balanced high-order centred schemes for non-conservative hyperbolic systems. applications to shallow water equations with fixed and mobile bed. *Adv. Water Resour.*, 32:834–844, 06 2009.
[5] M. J. Castro Díaz and E. Fernández-Nieto. A Class of Computationally Fast First Order Finite Volume Solvers: PVM Methods. *SIAM J. Sci. Comput.*, 34(4):A2173–A2196, 2012.
[6] H. Grad. On the kinetic theory of rarefied gases. *Commun. Pure Appl. Math.*, 2(4):331–407, 1949.
[7] J. Koellermeier. Error estimators for adaptive simulation of rarefied gases using hyperbolic moment models. *AIP Conf. Proc.*, 2132(1):120004, 2019.
[8] V. Kolobov, R. Arslanbekov, V. Aristov, A. Frolova, and S. Zabelok. Unified solver for rarefied and continuum flows with adaptive mesh and algorithm refinement. *J. Comput. Phys.*, 223(2):589–608, May 2007.
[9] M. Torrilhon. Modeling Nonequilibrium Gas Flow Based on Moment Equations. *Annu. Rev. Fluid Mech.*, 48(48):429–458, 2016.
[10] R. Verbiest and J. Koellermeier. Model-adaptive simulation of hierarchical shallow water moment equations in one dimension. submitted.
[11] R. Verbiest and J. Koellermeier. Spatially adaptive moment model using padded buffer cell for linear hierarchical moment equations. accepted.

NEGF26-677749

Molecular Dynamics-Informed Collision Kernels for Polyatomic Gases

Bas Gieling[1], Michael Abdelmalik[2], Harald van Brummelen[3], Arjan Frijns[4], Torsten Keßler[5], Marwa Shahine[6]
Department of Mechanical Engineering, Eindhoven University of Technology
5600MB Eindhoven, the Netherlands
[1]b.w.t.gieling@tue.nl, [2]m.abdel.malik@tue.nl, [3]e.h.v.brummelen@tue.nl, [4]a.j.h.frijns@tue.nl,
[5]t.kessler@tue.nl, [6]m.shahine@tue.nl

KEY WORDS

Boltzmann equation, discontinuous Galerkin finite-element method, kinetic theory, machine learning, method of moments, rarefied gas dynamics.

ABSTRACT

Non-equilibrium effects arise in numerous industrial applications. Rarefied gas flows, for example, occur in environments where the molecular mean free path becomes comparable to the characteristic length scale of the system. Their ratio is called the Knudsen number (Kn), and continuum models such as the Navier-Stokes equations begin to break down as Kn approaches unity [3]. This breakdown occurs in applications ranging from spacecraft reentry (low-pressure environment), or microporous systems (small length scale), to semiconductor lithography in vacuum chambers (low-pressure and microscale).

The Boltzmann equation (1) provides a kinetic description of gases across the entire range of Knudsen numbers, from the continuum to the free-molecular regime.

$$\partial_t f + \nabla_x \cdot \mathbf{v} f = \mathcal{C}(f, f) \tag{1}$$

This equation gives a statistical description of the gas through the single-particle distribution function f. It was originally derived from Molecular Dynamics by letting the number of particles approach infinity under the Boltzmann-Grad limit [4]. This derivation also gives rise to a collision operator $\mathcal{C}$, which is consistent with conservation laws and entropy dissipation by definition.

This operator has an exact formulation up to an unknown collision kernel. Traditional formulations of this kernel have relied on their mathematical properties, such as detailed balance and non-negativity. Using these properties, the collision operator can be proven to dissipate entropy [2]. However, these kernels often significantly simplify the actual molecular interactions.

In the present work, we propose a data-driven approach to fit a parametrized collision kernel to high-fidelity Molecular Dynamics data. We thereby aim to exploit the fundamental relationship between the

Boltzmann equation and the MD formulation from which it is originally derived. Exact conservation of mass, momentum, and energy, as well as entropy dissipation, are guaranteed a priori by the mathematical properties of the chosen parametrization. We facilitate the simulation of polyatomic gases by extending phase space with an additional dimension, representing the internal energy of the particle. The collision operator can be extended accordingly, using the Larsen-Borgnakke parametrization of collisions [2].

To solve the resulting Boltzmann equation, we employ the Discontinuous Galerkin Method of Moments (DGMoM) approach [1]. This computational framework combines the spatial discretization of the Discontinuous Galerkin finite element method, with the velocity and internal energy discretization of the Method of Moments [5]. The macroscopic quantities of the gas - density, bulk velocity, temperature, etc. - appear as moments of the distribution function, which allows for comparison with experimental results.

These comparisons are carried out for a one-dimensional heat flux problem, and for two-dimensional mass flow through a micro-channel. Through the incorporation of accurate microscopic effects, we are able to obtain good agreement between simulation and experimental results. In the continuum and free molecular limits, we re-obtain the analytic results derived from kinetic theory. Finally, conservation and dissipation laws are maintained analytically and will be numerically verified.

Acknowledgements

This research is funded through NWO Emerging Key Enabling Technologies (KIC) program under project name “Accelerating Rarefied Gas Dynamics” (file number KICH1.ST04.22.017).

References

[1] M.R.A. Abdelmalik, D.A.M. Van der Woude, and E.H. Van Brummelen. “Entropy bounds for the space–time discontinuous Galerkin finite element moment method applied to the BGK–Boltzmann equation”. In: *Computer Methods in Applied Mechanics and Engineering* 398 (2022), p. 115162. DOI: https://doi.org/10.1016/j.cma.2022.115162.

[2] J.F. Bourgat et al. “Microreversible collisions for polyatomic gases and Boltzmann’s theorem”. In: *European Journal of Mechanics B-fluids* 13 (1994), pp. 237–254.

[3] S. Kokou Dadzie and H. Brenner. “Predicting enhanced mass flow rates in gas microchannels using nonkinetic models”. In: *Phys. Rev. E* 86 (3 2012). DOI: 10.1103/PhysRevE.86.036318.

[4] H. Grad. “Principles of the Kinetic Theory of Gases”. In: *Thermodynamik der Gase / Thermodynamics of Gases*. 1958, pp. 205–294. DOI: 10.1007/978-3-642-45892-7_3.

[5] C. David Levermore. “Moment closure hierarchies for kinetic theories”. In: *Journal of Statistical Physics* 83.5-6 (1996), pp. 1021–1065. DOI: 10.1007/BF02179552.

NEGF26-679318

MOLECULAR KINETIC MODELLING OF SURFACE-CONFINED EVAPORATIVE FLOWS

Baochao Shan[1], Shaokang Li[2,3], Yonghao Zhang[*2,3]
[1]Applied and Computational Mathematics, RWTH Aachen University, Aachen 52062, Germany
shan@acom.rwth-aachen.de
[2]Centre for Interdisciplinary Research in Fluids, Institute of Mechanics, Chinese Academy of Sciences, Beijing 100190, China
[3]School of Engineering Science, University of Chinese Academy of Sciences, Beijing 101408, China
lishaokang@imech.ac.cn; yonghao.zhang@imech.ac.cn

KEY WORDS

Non-equilibrium evaporation, micro/nano-flow, molecular kinetic theory, fluid surface interaction.

ABSTRACT

Surface-confined non-equilibrium evaporative flows play a central role in new technologies that exploit nanoscale confined flows, ranging from nanoporous membranes for distillation, hydrogen/carbon dioxide storage, to evaporative cooling in electronics. Understanding of non-equilibrium liquid-vapour phase changes and fluid-solid molecular interactions that are critical to these and other such technologies is still at an early stage. In this work, we propose a molecular kinetic model that consistently resolves the coupled interactions among vapour, liquid and solid surface in such flows. This 'bottom up' approach can describe the formation of the liquid-vapour, liquid-solid and vapour-solid interfaces and the effects of non-equilibrium and real fluids, which does not need empirical models depending on ad hoc parameters such as the evaporation/condensation coefficients and contact angle. In addition, fluid-solid molecular interactions are explicitly considered in the transport equations, eliminating the reliance on pre-defined boundary conditions. This mesoscopic framework bridges the gap between molecular-scale dynamics and macroscopic hydrodynamics, striking a balance of computational accuracy and efficiency.

Molecular kinetic model

By appropriately modelling fluid-fluid and fluid-surface interactions, the transport equations governing the nano-scale confined flows (NCFs) can be expressed as

$$\left.\begin{aligned} D_t f &= Q_{ff} + Q_{fs}^{lg} + Q_{fs}^{m}, \\ D_t g &= 0.5|\boldsymbol{\xi}|^2 (Q_{ff} + Q_{fs}^{lg}) + Q_{fs}^{e}, \end{aligned}\right\} \tag{1}$$

* Corresponding author

where Q^m_{fs} and Q^e_{fs} drive the momentum (f) and energy (g) distribution functions toward the wall Maxwellian f^{eq}_w and g^{eq}_w via fluid-solid molecular collisions. Therefore, the boundary conditions at solid surface are an integral part of the governing equation. During fluid-surface collisions, only the temporal evolution of distribution functions is considered, as the spatial advection term vanishes due to the fixed position of the solid surface. As a result, Q^m_{fs} and Q^e_{fs} can be singled out from the molecular kinetic model (1) and expressed separately as:

$$\partial_t f = -\tau_m^{-1}(f - f^{eq}_w), \tag{2a}$$

$$\partial_t g = -\tau_e^{-1}(g - g^{eq}_w), \tag{2b}$$

where τ_m and τ_e are relaxation times for the momentum and energy. Linking the relaxation times with the accommodation coefficients, the above governing equations become

$$f(\boldsymbol{\xi}_t, \xi_n) - f(\boldsymbol{\xi}_t, -\xi_n) = -\omega_m \left[f(\boldsymbol{\xi}_t, -\xi_n) - f^{eq}_w\right], \tag{3a}$$

$$g(\boldsymbol{\xi}_t, \xi_n) - g(\boldsymbol{\xi}_t, -\xi_n) = -\omega_e \left[g(\boldsymbol{\xi}_t, -\xi_n) - g^{eq}_w\right]. \tag{3b}$$

Here, $-\xi_n$ and ξ_n denote the normal velocities of incoming and outgoing molecules, while $\boldsymbol{\xi}_t$ represents the tangential velocity component. The momentum and energy accommodation coefficients ω_m and ω_e measure the momentum and energy transfer rates between the fluid and the solid. These coefficients can be determined experimentally, through MD simulations, or via theoretical calculations. More details can be found in Shan et al. [1].

Results and discussion

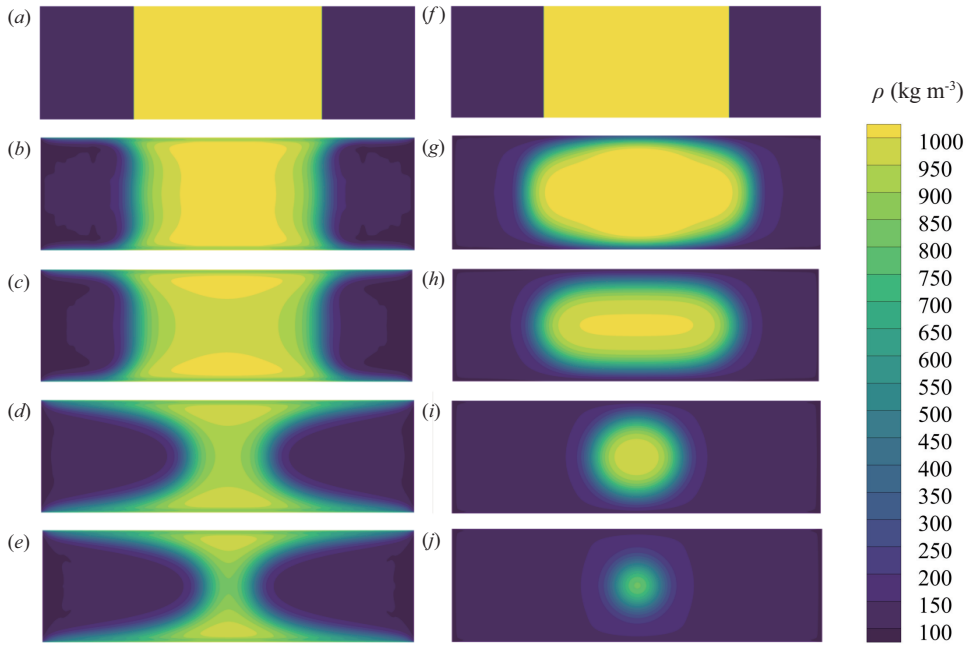

Figure 1: Density contour in the hydrophilic ($a - e$) and hydrophobic ($f - j$) nanochannels. Figures (a) to (e) correspond to time at $t = 0.00$ ns, 0.01 ns, 0.03 ns, 0.47 ns, 0.67 ns, respectively. Figures (f) to (j) correspond to time at $t = 0.00$ ns, 0.02 ns, 0.52 ns, 1.40 ns, and 1.76 ns, respectively.

When a liquid-vapour interface meets a solid boundary, a three-phase contact line forms. Here, we consider a nanochannel initially filled with a central liquid region bounded by the vapour regions at the two open ends, as illustrated in figure 1. The distinct confinement characteristics lead to different meniscus evolution behaviours. In the hydrophilic confinement (figure 1($a-e$)), the strong liquid-solid adhesion, surpassing the liquid cohesive force, enhances surface wetting, so liquid molecules are pulled to the solid surface to form an adsorbed film and a concave meniscus. Since liquid molecules are more stable at the liquid-solid interface, it becomes kinetically hindered to replenish the evaporating liquid at the centreline. This inefficient mass transfer ultimately leads to the meniscus rupture at a critical point (see figure 1(e)), when molecular cohesion overcomes the momentum input from non-local liquid-vapour collisions. By contrast, for the hydrophobic channel (figure 1($f-j$)), liquid cohesion prevails over adhesion. Hence, the liquid de-wets from the solid surface, forming a convex meniscus and creating a vapour gap near the wall. Liquid molecules near the liquid-vapour interface are in a higher energy state and thus more prone to evaporate than those in the bulk. Consequently, the convex meniscus evolves into an isolated droplet, as shown in figure 1(i). The liquid molecules at the droplet centre are the most stable and last to evaporate, after which the droplet disappears and no liquid exists (figure 1(f)).
Figure 2 shows the simulated ripening process of two droplets, where the density contour plots with the velocity vector fields at different times for the temperature of $T = 0.6$, non-dimensionalized by the critical temperature. Initially, the liquid-vapour interfaces of the two droplets evaporate rapidly to reach the average saturate pressure. Then, the ripening process takes place, as can be seen from the velocity field, which clearly shows the mass transfer from the smaller droplet to the larger one (t=100, 1800, 4000). Note that, during the ripening process, the larger droplet grows at the expense of the smaller one, with no liquid bridge forming between them, and the transfer rate increases significantly as the smaller droplet becomes smaller (t=4000). Eventually the system reaches a steady state and only one stationary droplet remains in the domain (t=5400).

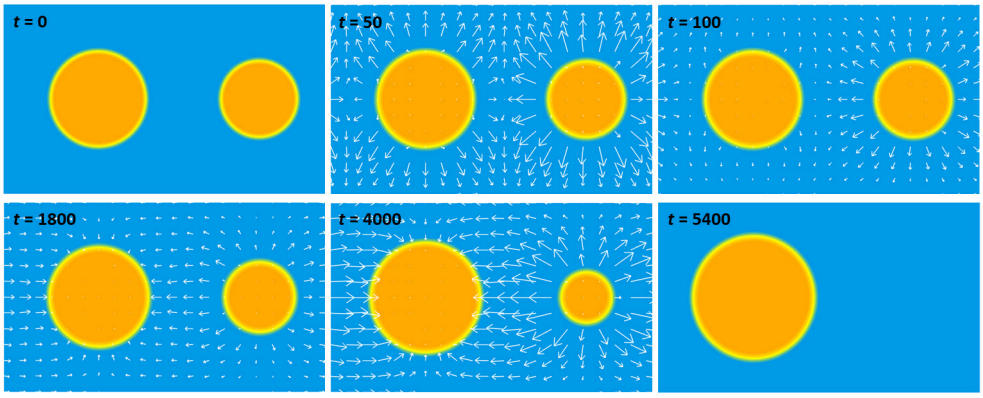

Figure 2: Simulated droplet ripening process at $T = 0.6$. The time of each image is displayed in the top left corner, and the velocity vector is represented by a white arrow.

Acknowledgements

We would like to thank Manuel Torrilhon, Zhaoli Guo, Livio Gibelli for insightful discussions.

References and citations

[1] Shan, B., & Torrilhon, M., & Guo, Z. & Zhang, Y.H. (2025). Molecular kinetic modelling of nanoscale confined flows. J. Fluid Mech., 1012, A20

NEGF26-683429

NON-EQUILIBRIUM THERMODYNAMICS OF ORIENTED GRANULAR GASES

Meitham Amereh[1], Henning Struchtrup[2], Ben Nadler*[3]
Department of Mechanical Engineering, University of Victoria, Victoria, BC V8P 5C2, Canada
mamereh@uvic.ca[1], struchtr@uvic.ca[2] , bnadler@uvic.ca[3]

KEY WORDS

Oriented particles, orientation tensor, evolving anisotropy, granular kinetic theory.

ABSTRACT

In this work, we develop a continuum model for the thermodynamics of granular systems consisting of rigid oriented particles by extending the state variables to account for the additional granular state variables. The state variables to describe oriented granular gas are the granular temperature and the granular orientation in addition to the standard state variables which are density, velocity and thermodynamic temperature. The granular temperature is a nonnegative scalar value that represents the energy of the agitated particles (energy of the translation and rotation velocities fluctuations). The orientation is a symmetric, trace-free and bounded second order tensor representing the particles orientation distribution. The orientation tensor measures the deviation from isotropic orientation distribution.
The two additional granular state variables are governed by associated balance laws that are the granular energy and orientation which are in addition to the conservation of mass, balances of linear momentum, thermal energy and entropy. Defining the orientation entropy contribution in terms of the orientation tensor, the Gibbs equation is used to identify entropy thermodynamic fluxes (driving to equilibrium) in terms of the thermodynamic forces (deviation from equilibrium) and the state variables. Using the non-negative entropy production requirement, the constitutive laws are constructed for all the fluxes. The constitutive laws for the fluxes, as first order approximation, are constructed by taking the fluxes to be linear combinations of the forces. The phenomenological coefficients matrix is obtained using the Onsager-Casimir reciprocity principles, which is required to be positive semi-definite. The general representation of the phenomenological coefficients matrix includes all the possible coupling, and the phenomenological coefficients are tensor of up to sixth order.
This formulation is too general and can only serve as a reference to generalize the constitutive laws if needed. To obtain a meaningful model we must make substantial simplifications by neglecting, what we consider, secondary effects. The developed constitutive laws are compared with models available in the literature for spherical particles as a special case. It is shown that the developed constitutive laws can

* Corresponding author

describe spherical particles, and more importantly, to provide a systematic framework to generalize these laws to oriented particles.

Orientation tensor

The particle orientations are represented by the second moment of the orientations [1] defined by

$$A_{ij} = \oint_{s^2} f(\mathbf{k}) k_i k_j d\mathbf{k} - \frac{1}{3}\delta_{ij} \quad , \quad \oint_{s^2} f(\mathbf{k}) d\mathbf{k} = 1 \tag{1}$$

where $f(\mathbf{k})$ is the probability density function in the direction $\mathbf{k}$, s^2 is the unit sphere and δ_{ij} is the identity matrix. It follows that the orientation tensor is a symmetric, trace-free and bounded second order tensor, which measures the deviation from isotropic orientation distribution. The two non-linear invariants of A_{ij} are

$$i_1 = A_{lm}A_{lm} \quad , \quad i_2 = A_{lm}A_{ln}A_{ln} \ , \tag{2}$$

where $i_1 = 0, i_2 = 0$ for isotropic distribution and $i_1 = 2/3, i_2 = 2/9$ for completely aligned distribution.

State variables and balance laws

For granular systems of oriented particles the extended state variables [2, 3] are density, thermodynamical temperature, granular temperature and orientation

$$\{\rho, v_i, \theta, T, A_{ij}\} \ , \tag{3}$$

respectively. The associated balance laws are conservation of mass, balance of linear momentum, balance of thermodynamic energy, balance of granular energy, balance of orientation and balance of entropy

$$\begin{aligned}
\dot{\rho} + \rho v_{l,l} &= 0 \ , \\
\rho \dot{v}_i + t_{il,l} &= 0 \quad , \quad t_{ij} = p\delta_{ij} - t^v_{ij} \ , \\
\rho c_v \dot{\theta} + q_{l,l} &= r \\
\rho \frac{5}{2}\dot{T} + Q_{l,l} &= -r - t_{lm}d_{lm} \quad , \quad d_{lm} = v_{(l,m)} \ , \\
\rho \mathring{A}_{ij} + G_{ijl,l} &= P_{ij} \quad , \quad \mathring{A}_{ij} = \dot{A}_{ij} + A_{il}v_{[l,j]} - v_{[i,l]}A_{lj} \ , \\
\rho \dot{s} + \phi_{l,l} &= \Sigma \ \geq 0 \ ,
\end{aligned}$$

respectively, which must be closed with constitutive laws for the stress t_{ij}, heat flux q_l, rate of energy exchange between thermal and granular energies, granular heat flux Q_l, orientation flux G_{ijk}, orientation production P_{ij}, entropy flux ϕ_i and entropy production Σ.

Entropy

The additional entropy contribution associated with the orientation is take as

$$s = \frac{a_1}{2} i_1 + \frac{a_2}{3} i_2 + \frac{a_3}{4} (i_1)^2 + \dots \ , \tag{4}$$

such that the Gibbs equation takes the form

$$ds = -\frac{p}{T\rho^2}\, d\rho + \frac{1}{\theta}\, du + \frac{1}{T}\, dU + \Lambda_{lm}\, dA_{lm} \ , \tag{5}$$

where by (4)

$$\Lambda_{ij} = a_1 A_{ij} + a_2 A_{ij}^2 + a_3 i_1 A_{ij} + \dots \,. \tag{6}$$

It follows that the entropy production is

$$\Sigma = r\left(\frac{1}{\theta} - \frac{1}{T}\right) + q_l \left(\frac{1}{\theta}\right)_{,l} + Q_l \left(\frac{1}{T}\right)_{,l} + \frac{1}{T} t^v_{lm} d_{lm} + P_{lm}\Lambda_{lm} + G_{lmn}\Lambda_{lm,n} \tag{7}$$

where t^v_{ij} is the viscous stress.

Constitutive laws

It follows form (7) that the thermodynamic forces are

$$\mathcal{F}_\alpha = \left[\, 1/\theta - 1/T \;,\; (1/\theta)_{,i} \;,\; (1/T)_{,i} \;,\; d_{ij} \;,\; \Lambda_{ij} \;,\; \Lambda_{ij,k} \,\right] \;, \tag{8}$$

and the conjugate thermodynamic fluxes are

$$\mathcal{J}_\alpha = \left[\, r \;,\; q_i \;,\; Q_i \;,\; t^v_{ij}/T \;,\; P_{ij} \;,\; G_{ijk} \,\right] \;. \tag{9}$$

Taking the thermodynamic fluxes to be linear functions of the thermodynamic forces

$$\mathcal{J}_\alpha = \sum_\beta L_{\alpha\beta}\mathcal{F}_\beta \;, \tag{10}$$

where the phenomenological matrix $L_{\alpha\beta}$ must be positive-semi definite. Invoking the Onsager-Casimir reciprocity principle, the force-flux relations are

$$\begin{bmatrix} r \\ q_i \\ Q_i \\ t^v_{ij}/T \\ P_{ij} \\ G_{ijk} \end{bmatrix} = \begin{bmatrix} \mathcal{A}^1 & 0 & 0 & \mathcal{B}^1_{lm} & \mathcal{B}^2_{lm} & 0 \\ 0 & \mathcal{B}^3_{il} & \mathcal{B}^4_{il} & 0 & 0 & \mathcal{C}^1_{ilmn} \\ 0 & \mathcal{B}^4_{il} & \mathcal{B}^5_{il} & 0 & 0 & \mathcal{C}^2_{ilmn} \\ -\mathcal{B}^1_{ij} & 0 & 0 & \mathcal{C}^3_{ijlm} & -\mathcal{C}^4_{lmij} & \mathcal{D}^1_{ijlmn} \\ \mathcal{B}^2_{ij} & 0 & 0 & \mathcal{C}^4_{ijlm} & \mathcal{C}^5_{ijlm} & \mathcal{D}^2_{ijlmn} \\ 0 & \mathcal{C}^1_{lijk} & \mathcal{C}^2_{ijkl} & -\mathcal{D}^1_{ijklm} & \mathcal{D}^2_{ijklm} & \mathcal{E}_{ijklmn} \end{bmatrix} \begin{bmatrix} 1/\theta - 1/T \\ (1/\theta)_{,l} \\ (1/T)_{,l} \\ d_{lm} \\ \Lambda_{lm} \\ \Lambda_{lm,n} \end{bmatrix} . \tag{11}$$

Using the isotropic functions representation theorem, the components of phenomenological matrix

$$\{\mathcal{A}, \mathcal{B}_{ij}, \mathcal{C}_{ilmn}, \mathcal{D}_{ijlmn}, \mathcal{E}_{ijklmn}\} \tag{12}$$

are constructed by products of the identity matrix, δ_{ij}, the Levi-Civita symbol, ϵ_{ijk}, and the orientation tensor, A_{ij}, and can only depend on the objective scalar quantities $\{\rho, \theta, T, i_1, i_2\}$, which simplifies the mathematical structure.

Summary

The formulation of the thermodynamic of oriented granular gases in terms of the phenomenological transport coefficients is completed by determining these coefficients from available results and experiments. Here, the transport coefficients are determined by comparison with results available in the literature for spherical and non-spherical particles. It is shown that the proposed formulation can capture all the available results by determining the relevant associated phenomenological transport coefficients. In addition, the proposed formulation provides a systematic framework to further generalized thermodynamics of granular gases which is consistent with the second law of thermodynamics.

Acknowledgements

This work was supported by the Natural Sciences and Engineering Research Council of Canada (NSERC) through Discovery Grant RGPIN-2022-03188 (Struchtrup) and RGPIN-2018-04573 (Nadler).

References and citations

[1] Nadler B., Guillard F. & Einav I. (2018). Kinematic model of Transient Shape-induced anisotropy in dense granular flow. Phys. Rev. Lett., 120, 198003.
[2] Amereh M. & Nadler B. (2022). A generalized model for dense axisymmetric grains flow with orientation diffusion. J. Fluid Mech., 936, A40.
[3] Vescovi D., Nadler B. & Berzi D. (2024). Simple generalization of kinetic theory for granular flows of nonspherical, oriented particles. Phys. Rev. Fluids, 9, L012301.

NEGF26-677758

Nonlocal Moment Equations for Liquid-vapor Flows

Aldo Frezzotti*[1], Henning Struchtrup[2]
[1]aldo.frezzotti@polimi.it, [2] struchtr@uvic.ca

KEY WORDS

Enskog-Vlasov equation, moment methods, vapor-liquid interface, shear flows

ABSTRACT

Introduction

Recently, a system of moment equations [1] has been derived from Enskog-Vlasov equation (EV) [2] and applied to various types of nonequilibrium flows in which liquid and vapor regions coexist, being separated by a fully resolved interface [3, 4]. The EV equation has an intrinsic nonlocal structure, inherited from Enskog's kinetic theory of the dense hard sphere fluid. Grad-26 moment equations, derived in Ref. [1], are based on a local (differential) expansion of the hard sphere collision integral and self-consistent field term, generated by the potential attractive tail. Expanding nonlocal terms is fully justified in regions where flow variations are small across a distance on the order of the range of molecular forces. However, expansions accuracy must be confirmed in the liquid-vapor interface region, whose thickness is on the order of ten molecular diameters. Here, higher order moments, crucial for the description of kinetic layers in the vapor, are produced in an extremely narrow region, corresponding to the vapor-side half of the interface [1, 3].
The present work aims at obtaining a set of moment equations, based on the linearized EV equation, in which fluxes and sources keep their *exact*, nonlocal form. Then, the accuracy of the moment approximation depends only on the number of moments, not on the order of the expansion turning nonlocal into local terms.

Test problem: two-phase Couette flow

Comparing local and nonlocal forms of moment equations is easier in the case of a two-phase Couette flow, in which shear is imposed to the liquid and vapor phases, separated by an interface (see Fig. 1). When shear rate is small, energy and momentum transfer decouple [1] and it is possible to consider an isothermal Couette flow. In this case, the density keeps its equilibrium profile $n_0(x)$ determined by the

* Corresponding author

following equations [5], for each temperature T_0 below the critical temperature T_{crit}:

$$k_B T_0 \frac{dn_0}{dx} = n_0(x) F_x^{(0)}(x) + 2\pi a^2 n_0(x) k_B T_0 \int_{-1}^{+1} k_x Y\left[n_0(x - \frac{a}{2}k_x)\right] n_0(x - ak_x)\, dk_x \quad (1)$$

$$F_x^{(0)}(x) = -2\pi \left[\phi_t(a) \int_{|y-x|\le a} (y-x) n_0(y)\, dy + \int_{|y-x|>a} (y-x)\phi_t(|y-x|) n_0(y)\, dy\right]. \quad (2)$$

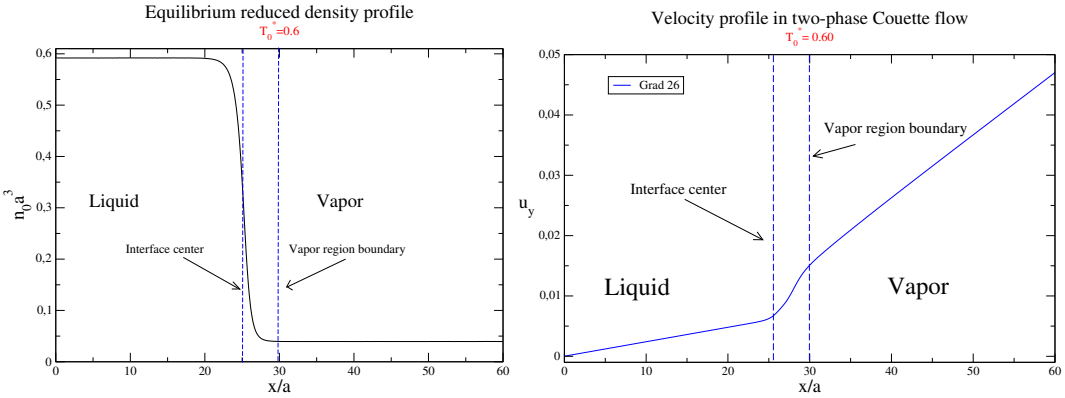

Figure 1: **Left** - Equilibrium density profile at reduced temperature $T_0^* = k_B T_0/\epsilon = 0.6$. **Right** - Velocity profile, parallel to the interface, from Grad$_{26}$, local moment approximation [1]

.

In Eqs. (1,2), $F_x^{(0)}(x)$ is the mean field generated by the soft tail of the intermolecular potential ϕ_t, wheras a is the diameter associated with the hard sphere potential.
The assumed small shear rate allows writing the fluid distribution function as $f(x, \mathbf{v}, t) = f_0(x, \mathbf{v})[1 + h(x, \mathbf{v}, t)]$, being $f_0(x, \mathbf{v})$ the nonuniform equilibrium Maxwellian:

$$f_0(x, \mathbf{v}) = n_0(x)\omega_0(\mathbf{v}), \quad \omega_0(\mathbf{v}) = \frac{1}{(2\pi RT_0)^{3/2}} \exp\left(-\frac{\mathbf{v}^2}{2RT_0}\right) \quad (3)$$

and $h(x, \mathbf{v}, t)$ the shear induced perturbation. Linearized fluid flow equations are obtained from the following, general balance equation for a molecular property $\psi(\mathbf{v})$:

$$\frac{\partial M_\psi}{\partial t} + \frac{\partial}{\partial x}\left(J_\psi^{(k)} + J_\psi^{(c)}\right) - \frac{F_x^{(0)}(x)}{m} \int \frac{\partial \psi}{\partial v_x} f_0(x, \mathbf{v}) h(x, \mathbf{v}, t)\, d\mathbf{v} = S_\psi^{(c)}(x, t) \quad (4)$$

where:

$$M_\psi(x, t) = \int \psi(\mathbf{v})\omega_0(\mathbf{v}) h(x, \mathbf{v}, t)\, d\mathbf{v} \quad (5)$$

$$J_\psi^{(k)}(x, t) = n_0(x) \int v_x \psi(\mathbf{v})\omega_0(\mathbf{v}) h(x, \mathbf{v}, t)\, d\mathbf{v} \quad (6)$$

$$J_\psi^{(c)}(x, t) = \frac{a^2}{4} \int d\mathbf{v}\, d\mathbf{v}_1\, d^2\mathbf{k}(\mathbf{g}\cdot\mathbf{k})^+ \int_0^a d\lambda k_x \Delta_\psi(\mathbf{v}, \mathbf{v}_1, \hat{\mathbf{k}}) Y\left[n_0\left(\frac{x_1 + x_2}{2}\right)\right] \times$$
$$n_0(x_1) n_0(x_2)\omega_0(\mathbf{v}_1)\omega_0(\mathbf{v}_2)[h(x_1, \mathbf{v}_1, t) + h(x_2, \mathbf{v}_2, t)] \quad (7)$$

$$S_\psi^{(c)}(x, t) = \frac{a^2}{2} \int d\mathbf{v}\, d\mathbf{v}_1\, d^2\mathbf{k}(\mathbf{g}\cdot\mathbf{k})^+ \Sigma_\psi(\mathbf{v}_1, \mathbf{v}_2, \hat{\mathbf{k}}) Y\left[n_0\left(x - \frac{a}{2}k_x\right)\right] \times$$
$$n_0(x) n_0(x - ak_x)\omega_0(\mathbf{v}_1)\omega_0(\mathbf{v}_2)[h(x, \mathbf{v}_1, t) + h(x - ak_x, \mathbf{v}_2, t)] \quad (8)$$

where:

$$\Delta_\psi(\mathbf{v}_1,\mathbf{v}_2,\hat{\mathbf{k}}) = [\psi(\mathbf{v}^*)-\psi(\mathbf{v})]-[\psi(\mathbf{v}_1^*)-\psi(\mathbf{v}_1)]$$
$$\Sigma_\psi(\mathbf{v}_1,\mathbf{v}_2,\hat{\mathbf{k}}) = [\psi(\mathbf{v}^*)-\psi(\mathbf{v})]+[\psi(\mathbf{v}_1^*)-\psi(\mathbf{v}_1)]$$

As shown in Ref. [1], for the isothermal Couette flow, Grad$_{26}$ closure is based on the five moments $u_y(x,t)$, σ_{xy}, $q_y(x,t)$, $m_{xxy}(x,t)$ and $R_{xy}(x,t)$. The associated perturbation $h(x,\mathbf{v},t)$ takes the form:

$$h(x,\mathbf{v},t) = u_y(x,t)\frac{v_y}{RT_0}+\sigma_{xy}(x,y)\frac{v_xv_y}{\rho_0(RT_0)^2}+q_y(x,t)\frac{v_y}{5\rho_0(RT_0)^2}\left(\frac{\mathbf{v}^2}{5RT_0}-1\right)+$$
$$m_{xxy}(x,t)\frac{5}{8}\frac{v_y}{\rho_0(RT_0)^3}\left(v_x^2-\frac{\mathbf{v}^2}{5}\right)+R_{xy}(x,t)\frac{v_xv_y}{7\rho_0(RT_0)^3}\left(\frac{\mathbf{v}^2}{2RT_0}-\frac{7}{2}\right) \quad (9)$$

In Eq. (9), $u_y(x,t)$ is the shear flow velocity, σ_{xy} is the *kinetic* tangential stress, $q_y(x,t)$ is the y component of the *kinetic* heat flux, whereas $m_{xxy}(x,t)$ and $R_{xy}(x,t)$ are two additional third and fourth order moments, respectively. Setting $\psi(\mathbf{v})$ equal to the polynomials corresponding to each field u_y,σ_{xy}, q_y, m_{xxy}, R_{xy} and inserting the above expression for h into the sources and fluxes expressions, Eqs. (4) are turned into a system of five linear integro-differential equations[1]. For simplicity, we give below the form of the equation of conservation of momentum along the direction y, paralell to the liquid-vapor interface:

$$\rho_0\frac{\partial}{\partial t}u_y+\frac{\partial}{\partial x}\left(\sigma_{xy}+\sum_{l=1}^{5}J_{1l}^{(c)}\right)=0 \quad (10)$$

$$J_{11}^{(c)}(x,t) = ma^2\sqrt{\pi RT_0}\int_{-1}^{+1}dk_x\int_0^a d\lambda\, k_x\left(1-k_x^2\right)W_0(x_1,x_2)\times[u_y(x_2)-u_y(x_1)] \quad (11)$$

$$J_{12}^{(c)}(x,t) = \frac{\pi a^2}{2}\int_{-1}^{+1}dk_x\int_0^a d\lambda\, k_x^2\left(1-k_x^2\right)W_0(x_1,x_2)\times\left[\frac{\sigma_{xy}(x_1)}{n_0(x_1)}+\frac{\sigma_{xy}(x_2)}{n_0(x_2)}\right] \quad (12)$$

$$J_{13}^{(c)}(x,t) = \frac{a^2}{10}\sqrt{\frac{\pi}{RT_0}}\int_{-1}^{+1}dk_x\int_0^a d\lambda\, W_0(x_1,x_2)k_x(1-k_x^2)\left[\frac{q_y(x_2)}{n_0(x_2)}-\frac{q_y(x_1)}{n_0(x_1)}\right] \quad (13)$$

$$J_{14}^{(c)}(x,t) = -\frac{a^2}{16}\sqrt{\frac{\pi}{RT_0}}\int_{-1}^{+1}dk_x\int_0^a d\lambda\, W_0(x_1,x_2)k_x(1-k_x^2)(1-5kx^2)\times$$
$$\left[\frac{m_{xxy}(x_2)}{n_0(x_2)}-\frac{m_{xxy}(x_1)}{n_0(x_1)}\right] \quad (14)$$

$$J_{15}^{(c)}(x,t)=0 \quad (15)$$

where $x_1=x+\lambda k_x$, $x_2=x+(\lambda-a)k_x$ and $W_0(x_1,x_2)\equiv n_0(x_1)n_0(x_2)Y\left[n_0\left(\frac{x_1+x_2}{2}\right)\right]$. As shown by the expressions above, collisional sources and fluxes at x are obtained by weighting macroscopic field over the interval $[x-a,x+a]$. Weighting functions are specific to the particular balance equation and and macroscopic field contribution. It is also interesting to note that total fluxes result from the sum of a kinetic and a collisional contribution. Hence, the total tangential stress (the quantity within brackets in Eq. (10)) is not given by σ_{xy}, as in the dilute gas limit, but it contains contributions from other moments. In spite of their relatively complicated structure, the numerical solution of the moment equations is greatly simplified by expressing each macroscopic field as superposition of base functions. Then, the numerical calculation of sources and fluxes is reduced to vector-matrix products, in which matrices

[1] Analytical manipulations have been done by open source Maxima platform

can be precomputed and stored.

As examples, Figure 2 shows the profiles of nonlocal sources $S_{22}^{(c)}(x)$ and $S_{32}^{(c)}(x)$:

$$S_{22}^{(c)}(x) = a^2\sqrt{\pi RT_0}\int_{-1}^{+1} dk_x W_0'(x_1,x_2)\left(1-3k_x^2+4k_x^4\right)\times\left[\frac{\sigma_{xy}^{(k)}(x_1)}{n_0(x_1)}+\frac{\sigma_{xy}^{(k)}(x_2)}{n_0(x_2)}\right] \tag{16}$$

$$S_{32}^{(c)}(x) = \frac{\pi a^2}{2}RT_0\int_{-1}^{+1} dk_x W_0'(x_1,x_2)k_x\left(1-2k_x^2\right)\times\left[\frac{\sigma_{xy}^{(k)}(x_2)}{n_0(x_2)}-\frac{\sigma_{xy}^{(k)}(x_1)}{n_0(x_1)}\right] \tag{17}$$

$$x_1 = x, \qquad x_2 = x - ak_x$$

giving the contribution of σ_{xy} to the tangential stress and heat flux equation, respectively. Nonlocal profiles are compared to the corresponding local approximation, up to terms of degree a^4, as done in Refs. [1, 4]. The field σ_{xy} is provided by solutions of the linearized, *local* Grad$_{26}$ equations [1].
As expected, discrepancies are more pronounced at lower temperature, where the density profile is steeper, in the interface region. Also, as suggested by previous results [1, 4], nonlocal and local expressions present discrepancies that reduce on approaching the critical temperature. The complete (numerical) solution of the nonlocal form of the balance equation is underway to understand whether the observed discrepancies [1] between moment equations and EV-DSMC solutions, at low reduced temperatures, are caused by the moments choice or by the order of local expansions.

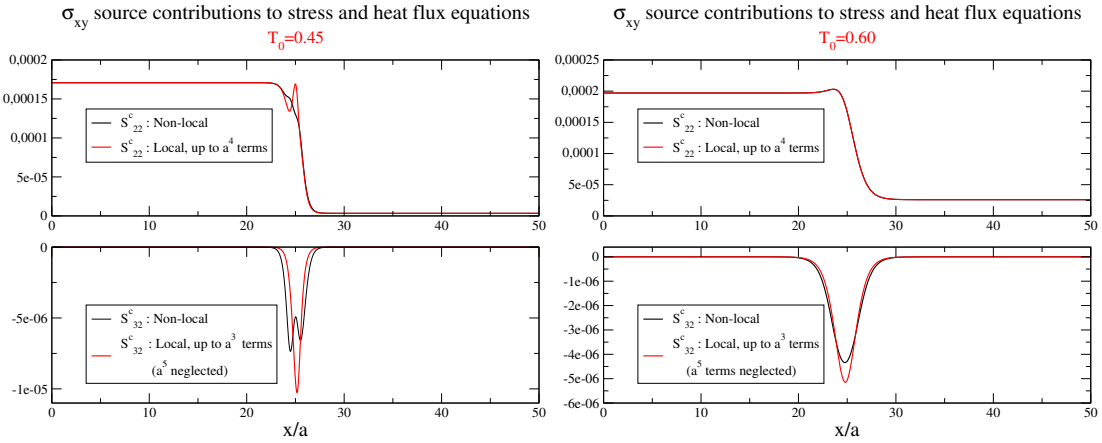

Figure 2: Comparisons of nonlocal and local expressions of source terms $S_{22}^{(c)}$ and $S_{22}^{(c)}$. **Left** - $T_0^* = 0.45$. **Right** - $T_0^* = 0.60$.

References and citations

[1] Struchtrup, H., & Frezzotti, A. (2022). Twenty-six moment equations for the Enskog–Vlasov equation. Journal of Fluid Mechanics, 940, A40.
[2] de Sobrino, L, (1967). On the kinetic theory of a van der Waals gas. Can. J. Phys., 45(2), 363–385.
[3] Frezzotti, A., & Struchtrup, H. (2023). Kinetic Effects in Non-ideal, Two-Phase Shear Flows. Springer Indam Series, Vol. 51, 107–117
[4] Struchtrup, H., et al. (2024). Heat transfer and evaporation processes from the Enskog-Vlasov equation and its moment equations. International Journal of Heat and Mass Transfer, 223,125238.

[5] Frezzotti, A., Gibelli, L., & Lorenzani, S. (2005). Mean field kinetic theory description of evaporation of a fluid into vacuum. Phys. Fluids, 17, 012102.

NEGF26-678651

ON THE GENERATION OF CORNER FLOW CIRCULATION AT HIGHLY RAREFIED CONDITIONS

Din Ben-Adva[1], Avshalom Manela*[1]
[1]The Stephen B. Klein Faculty of Aerospace Engineering, Technion, Haifa 3200003, Israel
din-ben-adva@campus.technion.ac.il, amanela@technion.ac.il

KEY WORDS

Free-molecular flows, Moffatt vortices, Maxwell boundary condition, direct simulation Monte Carlo.

ABSTRACT

We investigate the occurrence of flow circulation in an open triangular cavity filled with a gas at highly rarefied conditions. The cavity is subject to an external shear flow that is either in the circular or linear direction at its inlet. The problem is studied analytically in the free-molecular limit and numerically based on the direct simulation Monte Carlo (DSMC) method. The corner walls are modelled based on the Maxwell boundary condition, as either specular or diffuse. The results are obtained for arbitrary values of the outer flow speed and corner angle. Remarkably, it is found that multiple recirculation zones occupy the corner domain in the absence of molecular interactions. In the specular-corner setup, such topologies occur at non-large outer-flow speeds and distinct corner-angle intervals. In the diffuse-wall case, the cavity flow field contains two recirculation zones at sufficiently low corner angles for both circular and straight outer flows. The results are rationalized based on the ballistic particle kinematics, suggesting insight into the relation between the microscopic description and the hydrodynamic (observed) generation of circulation. The effects of molecular collisions on the corner flow pattern is inspected via DSMC calculations.

Introduction

The occurrence of 'corner eddies', a sequence of vortices of decreasing size and strength in the vicinity of a sharp edge, has been initially revealed and analyzed by Moffatt in the 1960s, in the context of continuum incompressible flows [1]. Ever since, follow-up continuum-flow investigations have been carried out (see Ref. [2] and works cited therein), considering the two-dimensional wedge-confined problem, as well as the three-dimensional cone-edge configuration. Both free-surface (external-flow-induced) and lid-driven setups have been examined, and the impacts of solid walls dynamic and thermodynamic conditions have been investigated in detail, to examine their effect of the developed flow field.

* Corresponding author

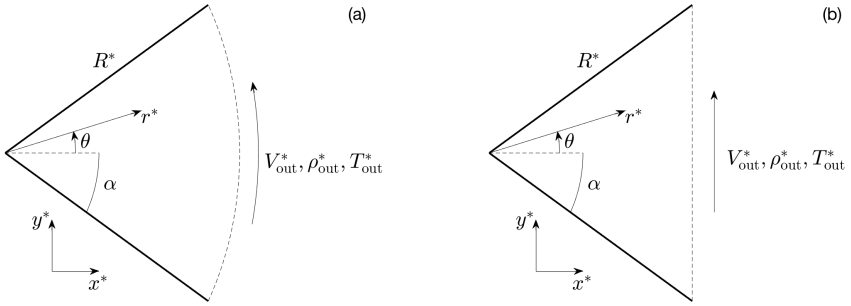

Figure 1: Schematic of the problem. A two-dimensional corner of length R^* and angle opening 2α is affected by an external uniform flow in the azimuthal $\hat{\boldsymbol{\theta}}$ (Fig. 1a) or vertical $\hat{\mathbf{y}}$ (Fig. 1b) directions, set at density $\rho^*_{\rm out}$, temperature $T^*_{\rm out}$ and speed $V^*_{\rm out}$.

Lid-driven and non-lid-driven (open) cavity flows have also been considered in the context of rarefied gas flows. The latter are primarily encountered in grooved microchannel geometries, and are also ubiquitous in outer-space flight objects, where design constraints result in non-smooth surface structures. In the former, flows passing through rough channels have been analyzed (e.g.,Refs. [3, 4]). In the latter, the effect of surface grooves on the vehicle drag force has been examined [5, 6]. Almost invariably, all works studying rarefied gas cavity flows rely on numerical simulations, applying the direct simulation Monte Carlo (DSMC) method [7], which is routinely used for the description of dilute gas flows. While DSMC calculations are known to converge to the solution of the Boltzmann kinetic equation, they require considerable computational efforts and lack the insight that may be gained through rigorous analysis. In particular, corner-flow DSMC calculations are formidably challenging, as low flow speeds are expected, resulting in an inevitable decrease in the signal-to-noise ratio. This prohibits a detailed description of vortex formation near the sharp corner, which is a main focus of the current study.
In view of the above, the objective of the present work is to investigate the formation of corner circulation in the highly-rarefied gas-flow regime. To this end, we consider the high-Knudsen limit of the two-dimensional gas flow developed in the vicinity of a sharp edge and driven by an external stream. Closed-form analysis is made in the free-molecular limit, where the impact of corner side wall conditions is detected based on the Maxwell boundary model. The results obtained are compared with DSMC calculations, to test their validity and examine the effect of few molecular collisions (at large yet finite Knudsen numbers) on the vortical flow field.

Statement of the problem

Schematic of the problem is presented in Figure 1. Consider a perfect monatomic gas passing in the vicinity of a two-dimensional corner confined between solid walls of length R^* (hereafter, asterisks denote dimensional quantities) with angle opening $0 < 2\alpha < \pi$. The outer flow is set at uniform density $\rho^*_{\rm out}$ and temperature $T^*_{\rm out}$. Using the marked cartesian (x^*, y^*) or polar (r^*, θ) coordinate systems, two setups are examined, where the outer flow velocity $\mathbf{V}^*_{\rm out}$ is directed either in the azimuthal $\hat{\boldsymbol{\theta}}$ (Fig. 1a) or vertical $\hat{\mathbf{y}}$ (Fig. 1b) directions. These represent the open-cavity counterparts of circular- and straight-wall lid-driven flows, respectively, that may be generated by the corresponding motion of a far-field wall, not modelled in the present work. Placing the axes origin at the corner edge, we seek to describe the steady gas motion inside the corner in the highly rarefied flow regime, where the corner length R^* is assumed small compared with the gas mean free path.

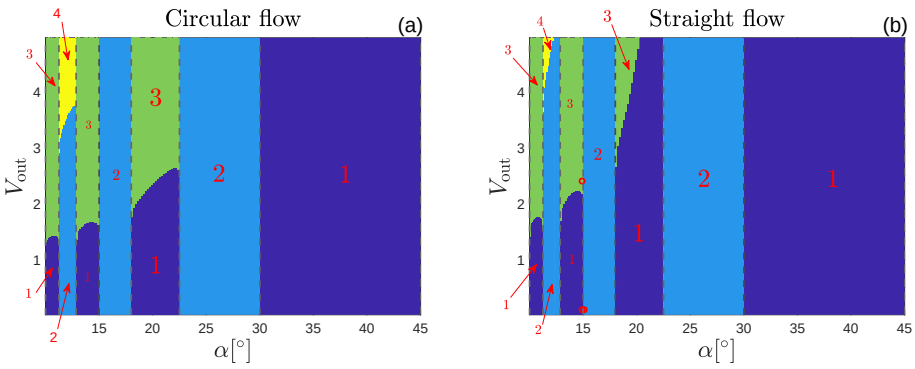

Figure 2: Division of the (α, V_{out}) plane for a specular-wall corner in the free-molecular regime into subdomains with different numbers of vortical structures. The blue, light blue, green and yellow zones mark parameter subdomains with one, two, three and four vortices, respectively, as indicated. Fig. 2a presents results for circular outer flow and Fig. 2b shows counterpart data for straight external flow. The red circles in Fig. 2b mark the parameter combinations referred to in Fig. 3.

To render the problem dimensionless, we scale the position by the corner walls length R^*, the velocity by the outer-temperature-based most probable molecular speed U^*_{mp}, and the density and temperature by ρ^*_{out} and T^*_{out}, respectively. The system non-dimensional description is subsequently governed by the outer flow reduced velocity V_{out} and the corner semi-angle α. In addition, the gas mean Knudsen number is introduced, $\mathrm{Kn} = \lambda^*/R^*$, where λ^* marks the mean free path of a gas molecule at the outer flow conditions. Assuming a hard-sphere gas model, $\lambda^* = m^*/(\pi\sqrt{2}\rho^*_{out}d^{*2})$, where m^* and d^* denote the gas molecular mass and diameter, respectively [8]. For simplicity, we model the gas-surface interaction via the Maxwell wall condition, and study the specular- and diffuse-surface cases separately. The detailed formulation of the wall conditions, as well as the inlet Maxwellian distribution, are skipped for brevity.

Results

Figs. 2 and 3 illustrate some of our results in the free-molecular ($\mathrm{Kn} \to \infty$) limit for a specular-wall corner, where our analysis enables kinematic rationalization of the observed vortical flow-field. The details of rationalization are skipped and will be discussed in the full-paper version.
Remarkably, Figs. 2 and 3 indicate the occurrence of multi-vortex fields in the free-molecular limit. Figure 2 presents the division of the (α, V_{out}) plane of parameters into domains with different numbers of vortical structures, where the blue, light blue, green and yellow subdomains mark parameter areas with one, two, three and four vortices, respectively. The results for the cases of circular and straight outer flows are shown in Figs. 2a and 2b, respectively, and are based on the free-molecular solution. In common to both setups, at sufficiently low V_{out} speeds ($V_{out} \lesssim 1$), we find an alternating change in the number of vortices between one and two. At a fixed (and sufficiently low) value of α, an increase in V_{out} yields the appearance of multiple vortical structures, which are added in pairs.
To complement Fig. 2, Fig. 3 presents the free-molecular velocity amplitude colormaps and streamlines in a specular-wall corner at the indicated combinations of α and V_{out}, also marked by circles in Fig. 2b. Figs. 3a and 3b show characteristically low $V_{out} = 0.1$ results at α values that are slightly below and above $\alpha = 15^\circ$. Fig. 3c then shows counterpart data at $\alpha = 14.9^\circ$ and large $V_{out} = 2.4$. In line with Fig. 2, Figs. 3a and 3b show flow fields with one and two vortices, respectively, where the added vortex appearing at $\alpha = 15.1^\circ$ is confined to the proximity of the corner origin. The maximum flow speed observed in all cases is significantly lower than the outer V_{out} value, due to the strong effect of particles arriving at

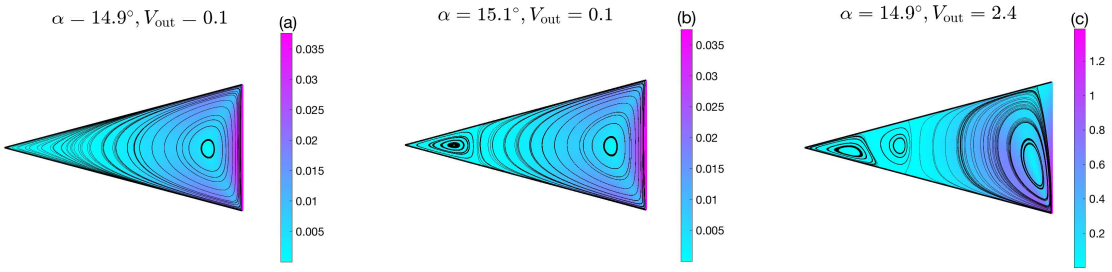

Figure 3: Free-molecular velocity amplitude colormaps and streamlines in a specular-wall corner at the indicated combinations of the corner semi-angle α and outer-flow speed V_{out} for straight outer flow.

the outlet section from inside the corner, which reduce the total speed. At $\alpha = 14.9°$ and $V_{\text{out}} = 2.4$, the flow contains three circulation zones. While the vortices are approximately symmetrically located about the $\theta = 0$ axis in Figs. 3a and 3b, they are asymmetrically distributed in Fig. 3c. This, as well as additional observations, will be rigorously rationalized in the full-paper version of our work, based on the free-molecular solution.

Acknowledgements

The research was supported by the Israel Science Foundation (grant No. 412/21).

References and citations

[1] Moffatt, H. (1964). Viscous and resistive eddies near a sharp corner. J. Fluid Mech., 18, 1-18.
[2] Shankar, P., & Deshpande, M. (2000). Fluid mechanics in the driven cavity. Ann. Rev. Fluid Mech., 32, 93-136.
[3] Rovenskaya, O., & Croce, C. (2018). Heat transfer in rough microchannels under rarefied flow conditions. Eur. J. Mech. B Fluids, 72, 706-715.
[4] Sazhin, O. (2020). Rarefied gas flow through a rough channel into a vacuum. Microfluid. Nanofluidics, 24, 27.
[5] Guo, G., & Luo, Q. (2018). DSMC investigation on flow characteristics of rarefied hypersonic flow over a cavity with different geometric shapes. Int. J. Mech. Sci., 148, 496-509.
[6] Nabapure, D., Singh, A., & Kalluri, R. (2023). Investigation of rarefied flow over an open cavity using direct simulation Monte Carlo. Aeronaut. J., 127, 1009-1036.
[7] Bird, G. (1994). Molecular Gas Dynamics and the Direct Simulation of Gas Flows. Oxford: Clarendon Press.
[8] Sone, Y. (2007). Molecular Gas Dynamics: Theory, Techniques, and Applications. Boston: Birkhäuser.

NEGF26-678764

PARTICLE REDUCTION SCHEMES FOR BINNING-BASED MERGING APPROACHES IN VARIABLE-WEIGHT DSMC

Georgii Oblapenko*[1], Minyi Qian[2], Shijie Xu[2], Yanliang Zhu[2], Manuel Torrilhon[1]
[1]Applied and Computational Mathematics, RWTH Aachen, Schinkelstrasse 2, 52062 Aachen, Germany
oblapenko.georgii@acom.rwth-aachen.de
[2]RWTH Aachen, Templergraben 55, 2062 Aachen, Germany
minyi.qian@rwth-aachen.de, shijie.xu@rwth-aachen.de, yanliang.zhu@rwth-aachen.de
mt@acom.rwth-aachen.de

KEY WORDS

Direct Simulation Monte Carlo, numerical simulation, Boltzmann equation

ABSTRACT

The Direct Simulation Monte Carlo (DSMC) method is a state-of-the art numerical approach to simulating the Boltzmann equation governing the behaviour of non-equilibrium gas flows [1] that models the gas as a collection of stochastically interacting computational particles, each representing a large number of actual gas atoms or molecules. Its conceptual simplicity, high parallel efficiency, and extensive modelling capabilities, such as modelling of chemical reactions, radiation, and coupling to particle-in-cell solvers for plasma simulations, have led to its widespread adoption.
However, the standard DSMC method assumes that each computational particle represents a single fixed number of actual gas particles. This potentially leads to issues in modelling of multi-species flows where some of the species' molar fractions are significantly lower [2], and of flows with strong density gradients [6], as very large numbers of simulation particles are required to resolve these trace species. It also may lead to poor resolution of high-energy particle populations (high-speed particles or particles in excited internal energy states), affecting reaction rates and simulation fidelity. To solve these issues, various schemes have been proposed: species-wise weighting methods [2, 3], and the stochastic weighted particle method (SWPM) [15]. Whilst these approaches resolve the issues associated with resolution of trace populations, they require creation of addition particles during the particle collision process, which, if left unchecked, leads to an exponential growth in the number of computational particles, making a simulation impossible.
To resolve this issue of particle number growth, merging approaches have been developed, that reduce the number of particles in the simulation by replacing the original set of particles with a new, smaller set of particles [14]. Although the conservation of basic invariants such as mass, momentum, and energy

* Corresponding author

during a merging procedure is relatively easy to ensure, the distortion introduced into the particle distribution by the merging can lead to erroneous results, even if the procedure itself is conservative [12, 6]. Therefore, recent works have focused on conservation of higher-order moments of the distribution function [4, 5, 10]. However, these approaches are oftentimes associated with a significantly higher cost compared to methods that only conserve the lowest-order moments and use semi-empirical particle grouping algorithms to reduce the induced error [17, 8, 7] by applying the reduction procedure to small groups of particles.
In the present work, we investigate and compare several simple particle reduction algorithms coupled with non-adaptive grid-based and adaptive octree-based particle grouping strategies within variable-weight DSMC. The methods are implemented in an open-source variable-weight DSMC code and applied to the simulation of Couette and Fourier flows, where their performance is evaluated in terms of computational efficiency and numerical accuracy.

Particle reduction

We investigate three approaches to particle reduction: 1) the $N : 2$ method of Martin and Cambier [8], which replaces N particles with 2 and conserves mass, momentum, and energy, as well as the independent x, y, z components of the energy; 2) a $N : 3$ method that conserves the full stress tensor by replacing N particles with 3 and utilizing the additional degrees of freedom; 3) a $N : 1$ method that conserves mass and momentum and the results of which are rescaled to conserve energy as well. We denote these methods as "C", "ST", "R".
The possibility of conserving energy when using the $N : 1$ approach is due to the fact that although in each particle group, only 1 particle remains after merging, the whole system of post-merge particles contains at least 2 particles; thus, it is possible to additionally rescale the post-merge velocities of the particles to ensure conservation of energy. In a similar fashion, the post-merge particle positions can also be rescaled to ensure conservation of the second spatial moments of the pre-merge particle distribution.

Particle grouping

The particle reduction methods described above are applied to groups of particles close in phase space, as this reduces the simulation error [6]. In the present work, we consider the adaptive octree-based grouping of Martin and Cambier [8], which we denote as "OC", as well as a simpler and faster non-adaptive grouping based on a uniform grid in velocity space [17, 11], which we denote as "G".
The adaptive octree merging routine automatically refines the particle clusters until a target post-merge number of particles is reached. The grid-based approach requires setting the number of grid elements in advance, as well as the grid extent. In the present work, we consider the grid extent to be governed by a multiple of the mean thermal velocity $\sqrt{2kT/m}$. The impact of the choice of the grid extent will be studied in the present work.

Numerical results

We consider the one-dimensional microscale flows, and compare the different grouping approaches coupled with the different particle reduction schemes. The merging approaches were implemented in the open-source variable-weight DSMC code Merzbild.jl [9].
The preliminary results are shown for the simulation of a Couette flow with the following parameters: the domain length is 5×10^{-4} m, the velocity of the left wall in y-direction is -500 m/s, the velocity of the right wall in the y-direction is 500 m/s, and the wall temperatures are 300 K. An argon gas is considered using the VHS potential. The flow was initialized with 150 particles/cell, and octree merging ("OC") was performed with the target number of particles set to 100 each time the number of particles in a cell exceeded 150. The timestep size was chosen as 2.59×10^{-9} s. The number density was taken

to be 5×10^{22} m^{-3}, corresponding to a Knudsen number of approximately 6×10^{-2}. The variable-weight collision scheme of Schmidt and Rutland was used for the simulations [16]. The SPARTA fixed-weight DSMC code [13] was used to compute reference values against which the other approaches are benchmarked.

Merging method	Normal pressure, Pa	Shear stress, Pa
OC+R ($N:1$)	327.8	61.6
OC+C ($N:2$)	314.2	56.1
OC+ST ($N:3$)	321.8	56.8
G+C ($N:2$)	319.0	56.0
Reference	306.1	53.8

Table 1: Values of normal pressure and shear stress on the left wall for various merging methods, Couette flow. "Reference" denotes values obtained from a fixed-weight DSMC simulation.

Table 1 shows the time-averaged computed values of the normal pressure and the (x, y) component of the shear stress tensor on the left wall. The time averaging was performed for 36000 steps after the system had reached steady state. It can be seen that the use of rescaled $N:1$ ("OC+R") merging leads to stronger deviations in the computed shear stress values, whereas for the normal pressure the impact of the choice of merging procedure is less clear. The grid-based merging approach ("G+C") also exhibits higher deviations than the octree merging routine using the same $N:2$ particle reudction scheme. Even though the grid-based merging is approximately 25% faster than the octree-based merging, the resulting particle weight distribution is less uniform, leading to higher costs in the evaluation of collisions, thus resulting in a 40% higher simulation cost overall.
The full work is planned to include more detailed analysis of the role of the merging schemes for the bulk and surface quantities for microscale flows, both in terms of simulation accuracy as well as computational efficiency, as well as guidelines as to the optimal choice of particle merging schemes for the simulation of such flows.

Acknowledgments

This work has been supported by the German Research Foundation within the research unit SFB 1481.

References and citations

References to published literature should be quoted in the text by enclosing between two brackets the number of the referencePlease refer to the following examples:

[1] Bird, G. A. (1994). Molecular gas dynamics and the direct simulation of gas flows. Oxford: Clarendon press Oxford.
[2] Boyd, I. D. (1996). Conservative species weighting scheme for the direct simulation Monte Carlo method. J. Thermophys. Heat Transfer, 10, 4, 579–585.
[3] Charton, V., Yamaoka, E., Morimoto, T., and Kinefuchi, K. (2025). Species weighting scheme in direct simulation Monte Carlo applied to jet plume simulations. J. Comput. Phys., 542, 114354.
[4] Faghihi, D., Carey, V., Michoski, C., Hager, R., Janhunen, S., Chang, C.-S., and Moser, R. (2020). Moment preserving constrained resampling with applications to particle-in-cell methods. J. Comput. Phys., 109317.
[5] Gonoskov, A. (2022). Agnostic conservative down-sampling for optimizing statistical representations and PIC simulations. Comput. Phys. Commun., 271, 108200.

[6] Hong, A. Y. and Gallis, M. A. (2024). An improved stochastic weighted particle method for boundary driven flows. J. Comput. Phys., 517, 113353.
[7] Lama, S., Zweck, J., and Goeckner, M. (2020). A higher order moment preserving reduction scheme for the Stochastic Weighted Particle Method. SIAM Journ. Sci. Comp., 42, 5, A2889–A2909.
[8] Martin, R. S. and Cambier, J.-L. (2016). Octree particle management for DSMC and PIC simulations. J. Comput. Phys., 327, 943–966.
[9] Oblapenko, G. Merzbild.jl: A Julia DSMC code. https://github.com/merzbild/Merzbild.jl.
[10] Oblapenko, G. (2024). A non-negative least squares-based approach for moment-preserving particle merging. arXiv preprint arXiv:2412.12354.
[11] Oblapenko, G., Goldstein, D. B., Varghese, P., and Moore, C. (2020). A velocity space hybridization-based Boltzmann equation solver. J. Comput. Phys., 408, 109302.
[12] Oblapenko, G., Goldstein, D. B., Varghese, P., and Moore, C. (2022). Improving PIC-DSMC simulations of electrical breakdown via event splitting. In AIAA Scitech 2022 Forum, 215.
[13] Plimpton, S. J., Moore, S. G., Borner, A., Stagg, A. K., Koehler, T. P., Torczynski, J. R., and Gallis, M. A. (2019). Direct simulation Monte Carlo on petaflop supercomputers and beyond. Phys. Fluids, 31, 8, 086101.
[14] Rjasanow, S., Schreiber, T., and Wagner, W. (1998). Reduction of the number of particles in the stochastic weighted particle method for the Boltzmann equation. J. Comput. Phys., 145, 1, 382–405.
[15] Rjasanow, S. and Wagner, W. (1996). A stochastic weighted particle method for the Boltzmann equation. J. Comput. Phys., 124, 2, 243–253.
[16] Schmidt, D. P. and Rutland, C. (2000). A new droplet collision algorithm. J. Comput. Phys., 164, 1, 62–80.
[17] Vranic, M., Grismayer, T., Martins, J. L., Fonseca, R. A., and Silva, L. O. (2015). Particle merging algorithm for PIC codes. Comput. Phys. Commun., 191, 65–73.

NEGF26-678812

Performance study on a Knudsen pump prototype fabricated via two-photon-polymerization

Franz Schweizer*[1,2], Klaus Bade[2,3], Lucien Baldas[1], Samuel Bergdolt[2,3], Jürgen J. Brandner[2,3], Stéphane Colin [1], Celine Deutschbein[2,3], Stefan Hengsbach[2,3], Jan G. Korvink[2], Marcos Rojas-Cárdenas[1]

[1]Univ Toulouse, CNRS, IMT Mines Albi, INSA Toulouse, ISAE-SUPAERO, ICA, Toulouse, France
schweizer@insa-toulouse.fr, lucien.baldas@insa-toulouse.fr, colin@insa-toulouse.fr, marcos.rojas@insa-toulouse.fr

[2]Institute of Microstructure Technology (IMT), Karlsruhe Institute of Technology, Eggenstein-Leopoldshafen, Germany
jan.korvink@kit.edu

[3]Karlsruhe Nano Micro Facility (KNMFi), Karlsruhe Institute of Technology, Eggenstein-Leopoldshafen, Germany
klaus.bade@kit.edu, samuel.bergdolt@kit.edu, juergen.brandner@kit.edu, celine.deutschbein@kit.edu, stefan.hengsbach@kit.edu,

Key words

Microfluidics, rarefied gas flow, two-photon-polymerization, thermal transpiration

Abstract

Thermal transpiration flow is characterized by the displacement of a rarefied gas along a temperature gradient applied to the bounding wall.
The exploitation of thermal transpiration flow for gas pumping was initially proposed in the work by Knudsen [1], who presented a prototype of a multistage Knudsen pump.
Knudsen pumps displace gas without any moving parts. Enabling vibration-free operation and robust performance over long periods. These key features make Knudsen pumps attractive for integration with often mechanically delicate sensing devices [2].
Sensing applications typically require low but precise flow rates, which can be provided by a Knudsen pump. Knudsen pumps have also been proposed as compressors for refrigeration [3] systems, an application demanding higher performance in terms of pressure head and flow rate.
Performance enhancement of Knudsen pumps is a key factor in their wider application. The main driver of performance is the temperature gradient, which must be applied along the pumping channels of the device, typically micrometer in size. The creation and maintenance of considerable temperature gradients on such a small scale are challenging. One of the main strategies to increase the temperature gradient is to

* Corresponding author

enhance the thermal resistance of the channel structure itself, which can be achieved using low-thermal-conductivity materials and by reducing the material cross-sections. The proposed Knudsen pump design consists of three main parts, as shown in Fig. 1a: (1) Silicon substrate with a central opening for hydraulic connection; (2) Low-thermal-conductivity polymer structure with an array of vertical channels connecting the two sides of the substrate, fabricated by two-photon-polymerization additive manufacturing [4, 5]; (3) Metal heater deposited on the polymer structure and spanning the channel array, microscope image shown in Fig 1b. The honeycomb channels have a hydraulic diameter of roughly 40 µm and are sep-

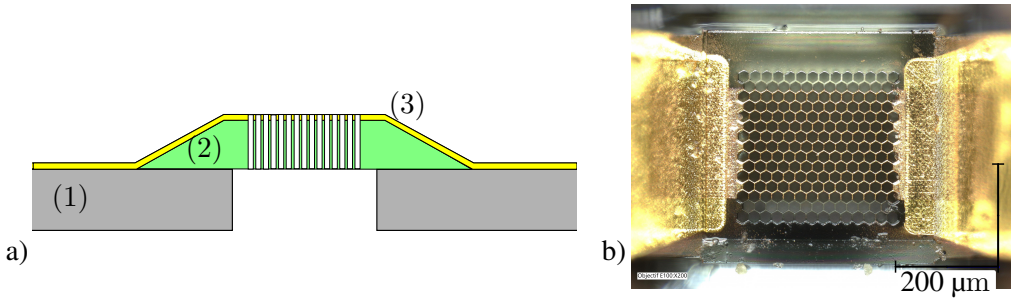

Figure 1: (a) Schematic cross-section of the Knudsen pump; (b) Microscope image of the top view of the Knudsen pump.

arated by 5 µm thick polymer walls. The prototype comprises $N = 203$ parallel channels. The heater width decreases in the channel area, as visible in Fig. 1b, and the separation walls of the channels serve as micro-tracks carrying the heating current. In this work, we have solved the heat transfer equation to obtain the temperature maps created by the thin film heater inside the micrometric polymer structure. The simulations were carried out using Comsol Multiphysics 6.1. Owing to its symmetry, only a quarter of the pump geometry is modeled. The simulation includes two domains, the polymer structure and the gas, in this case nitrogen, filling the channels. Both solid and gas phases are modeled as solids and are shown in Fig. 2. The obtained temperatures are moderate. Furthermore, with this channel size, the pump

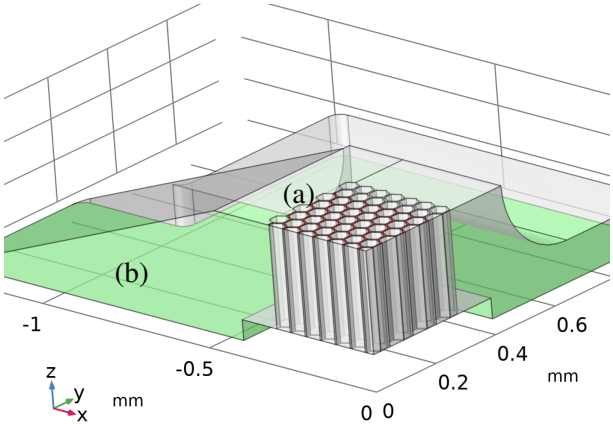

Figure 2: Simulation domain with boundary conditions: (a) constant heat flux (red), (b) ambient temperature (green).

should be operated under vacuum conditions to ensure a sufficient level of rarefaction. Therefore, the

influence of radiative and convective cooling of the sample are neglected in this simplified investigation, as the main mode of heat transfer is conduction through the gas and polymer structure. The thermal conductivity of the polymer is roughly three orders of magnitude lower than that of silicon. Thus, in this work, the silicon substrate is assumed to be isothermal at the ambient temperature of 298 K (see boundary condition (b) in Fig. 2). Furthermore, the heater power is assumed to be equally distributed over the area of the thin film heater (see boundary condition (a) in Fig. 2). The thermal simulation yields the temperature distribution along the centerline of each channel. The extracted temperature gradients along two channels and three different heater powers are shown in Fig. 3 (left). The presented channels are the central channel at $x = 0$, $y = 0$ (solid lines) and the channel in the corner of the array farthest away from the center channel at $x = -290$ µm, $y = 270$ µm (dashed lines). It is clearly visible that an increased heater power P_h leads to higher temperature gradients, however it also results in higher mean temperatures. Furthermore, the temperature gradients of the channels farthest from the center are almost negligible, resulting in a lower overall performance of the pump. The pressure distribution and the mass

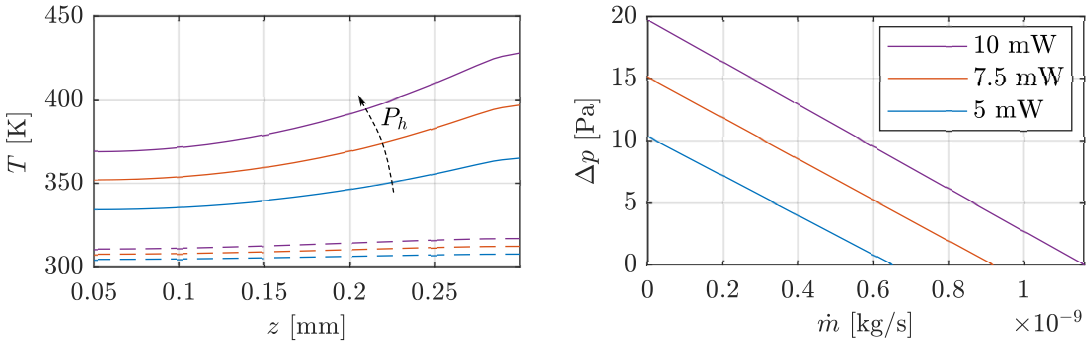

Figure 3: Temperature distribution along two channels: At the center $x = 0$, $y = 0$ (solid lines) and at one corner $x = -290$ µm, $y = 270$ µm (dashed lines) of the array (left) and characteristic curve of the overall pump (right) for different heater powers.

flow rate of the thermal transpiration flow can be solved via the infinite capillary theory [6]. The applied temperature boundary conditions correspond to the temperature distribution results obtained via the thermal simulation. The set of kinetic flow coefficients used can be found in [7] and was obtained with the Shakhov model for a circular cross-section, assuming full accommodation at the wall. For the simulation, the hydraulic diameter of the honeycomb shape is used. Owing to the non-uniform temperature field in the structure, each channel of the pump exhibits a different temperature distribution. This is taken into account in the flow modeling, where each channel is associated with its own temperature distribution in the parallel channels system. The ith channel displays the characteristic curve

$$\dot{m}_i = \dot{m}_i \left(\Delta p, p_m\right), \quad i = 1...203, \tag{1}$$

where $\dot{m}_i$ is the mass flow rate that the channel can maintain at a pressure head Δp and a mean pressure p_m.
The overall characteristic curve of the pump is obtained through the sum of the mass flow rates of all channels

$$\dot{m}(\Delta p, p_m) = \sum_{i=1}^{N} \dot{m}_i(\Delta p, p_m). \tag{2}$$

The characteristic curve of the overall pump for three different heater powers is shown in Fig. 3 (right). The results were obtained at a mean pressure of 1000 Pa using nitrogen as the working gas. The maximum mass flow rate, as well as the maximum pressure head, increases with the heater power.

The presented work demonstrates that reasonable temperature gradients can be achieved with low heater input power, highlighting the great potential of low thermal-conductivity materials for Knudsen pump construction. Furthermore, the simulation results reveal significant differences in temperature gradients between channels located at the center and at the edge of the array, which compromise the device performance. Lateral thermal insulation of the channel area would therefore be advisable.
Future work should include more comprehensive modeling of the overall Knudsen pump system. This should include possible fabrication related defects of the structure, including real channel sizes and alignment tolerances of different structures. Particularly the influence of the alignment precision between polymer structure and thin film heater on the system performance should be investigated. Additionally, this method can be used to improve the design, particularly to achieve a more uniform temperature difference across all channels in the array.

Acknowledgements

This work was carried out with the support of the Région Occitanie Pyrénées Méditerranée under the agreement n°00138088 / 22009727 (ProtOtype de Micro Pompe Knudsen à HYdrogène -HOMER), the Karlsruhe Nano Micro Facility (KNMFi, www.knmf.kit.edu), a Helmholtz Research Infrastructure at Karlsruhe Institute of Technology (KIT, www.kit.edu) and the Deutsche Forschungsgemeinschaft (DFG) for funding the CRC 1527 “HyPERiON”. The collaboration between ICA and KNMFi was realized under a long term grant agreement “2022-027-031254” and a short term grant agreement “2020-024-029397”. The authors gratefully acknowledge the Renatech network for their support and access to LAAS-CNRS micro and nanotechnologies platform, under the project: Micro-actionneurs thermiques pour pompe Knudsen, P-24-04914.

References

[1] Martin Knudsen. Eine Revision der Gleichgewichtsbedingung der Gase. Thermische Molekularströmung. *Annalen der Physik*, 336(1):205–229, 1909.
[2] V. Martini-Laithier, I. Graur, S. Bernardini, K. Aguir, P. Perrier, and M. Bendahan. Ammonia detection by a novel Pyrex microsystem based on thermal creep phenomenon. *Sensors and Actuators B: Chemical*, 192:714–719, March 2014.
[3] Wenjie Zhang, Wei Lu, and Botao Wang. Performance analysis of a novel thermal transpiration vacuum cooling system. *International Journal of Green Energy*, 19(2):149–158, January 2022.
[4] Dingdong Zhang, Guillermo López-Quesada, Samuel Bergdolt, Stefan Hengsbach, Klaus Bade, Stéphane Colin, and Marcos Rojas-Cárdenas. 3D micro-structures for rarefied gas flow applications manufactured via two-photon-polymerization. *Vacuum*, 211:111915, May 2023.
[5] Franz Schweizer, Klaus Bade, Lucien Baldas, Samuel Bergdolt, Stéphane Colin, Celine Deutschbein, Stefan Hengsbach, Jan G. Korvink, Marcos Rojas-Cárdenas, and Jürgen J. Brandner. Rarefied gas flows in complex microfluidic 3D-structures fabricated via additive manufacturing. *Vacuum*, 238:114213, August 2025.
[6] Felix Sharipov. Rarefied gas flow through a long tube at arbitrary pressure and temperature drops. *Journal of Vacuum Science & Technology A: Vacuum, Surfaces, and Films*, 15(4):2434–2436, July 1997.
[7] Guillermo López Quesada. *Thermally Driven Vacuum Micropumps*. PhD thesis, University of Toulouse, Toulouse, France, September 2019.

NEGF26-694028

PHOTOPHORETIC LEVITATION: FROM AEROSOLS TO AIRCRAFT

Benjamin Schafer*[1,2]
[1]Rarefied Technologies Inc., Albuquerque, NM, USA, 87111
[2]Harvard University John A. Paulson School of Engineering and Applied Sciences, Cambridge, MA, USA, 02138
schafer@g.harvard.edu

KEY WORDS

Photophoresis, thermal transpiration, near-space, remote sensing, aerospace

ABSTRACT

Photophoresis is a phenomenon that occurs when an object surrounded by a low-pressure gas is illuminated. An asymmetry in the object's temperature or accommodation coefficient (AC) causes the gas to transfer more momentum to one side, resulting in a force [1]. This explains why a radiometer spins when illuminated and how aerosol layers remain aloft in the stratosphere and mesosphere (20–100 km altitudes) under sunlight [2,3]. Photophoresis was largely considered a novelty throughout the 20th century, but recent advancements in nanofabrication are spurring interest in new photophoretic devices [4].

My colleagues and I recently showed, for the first time, that lightweight devices with engineered surfaces generate sufficient photophoretic lift to sustain near-space flight when illuminated by sunlight (Fig. 1a,b,i) [5]. As a novel propulsion mechanism, photophoresis will enable new observational capabilities for atmospheric and space science. The lofting forces are strongest in the mesosphere, a region of the atmosphere too high for planes and balloons to fly, but too low for satellites to orbit. Photophoretically flying devices could bridge this observational gap without fuel, batteries, or photovoltaics to sustain flight. These "flyers" could be deployed via stratospheric balloons or rocketsondes and remain aloft for up to months at a time, depending on their size, weight, and deployment latitude. While passive flyers without payloads can be fabricated today at low cost, scaling up current photophoretic designs would achieve > 100 mg payloads within 5 years (Fig. 1g,h). This payload capacity is enough to loft lightweight sensors to send real-time atmospheric data to the ground or satellites. We also lay a blueprint for practical photophoretic flight by describing deployment methods, device lifetimes, and active payload integration to enable in situ data collection and wireless communication. Photophoretic flyers could also serve as remote sensing tools in the mesospheres of Mars and Venus, with comparable lofting efficiencies to those on Earth.

To predict the photophoretic forces and drag of our structures under atmospheric environments, we developed a computational approach that blends analytical temperature calculations with direct simulation Monte Carlo (DSMC) simulations (Fig. 1c) [6,7]. We used this approach to design new photophoretic devices with some of the largest experimentally-measured lofting forces to date (Fig. 1d). These photophoretic materials also exhibit among the highest strength-to-weight ratios of any structures reported (Fig. 1e,f) [8], and they can host a variety of engineered optics, metamaterials, and MEMS to manipulate the photophoretic force. Investigating new device designs, materials, and coatings will open new frontiers in materials science and create new electronic and mechanical structures for systems with strict size, weight, and power (SWAP) requirements.

Remote sensing at altitudes above 30 km is limited by the low concentration of natural aerosols, with few exceptions [9]. Because the motion of photophoretic flyers is a function of the ambient wind, temperature, and pressure, these quantities can be determined by either remotely tracking their position using satellites or collecting the data in situ with active payloads. Data on incident UV flux, electron density, and atomic oxygen concentration can similarly be inferred from the devices' lifetimes or optical changes over time. These data are critical for understanding mesospheric circulation patterns and the effects of space weather on the lower ionosphere. They can also be used to calibrate global models of the atmosphere. High-altitude balloons or rocketsondes would deploy photophoretic flyers in at least the mid-stratosphere, which is at a low enough pressure for them to continue rising to their target altitude. The specific flight altitude, lifetime, and reflectivity of a tracer can be tailored by changing its materials, size, and microscale features. We surveyed hundreds of materials, fabrication methods, and payloads to show that a wide envelope of flyer performance is achievable with well-established fabrication methods. Furthermore, flyers can be made with inert, non-toxic materials like silica glass and carbon, mitigating concerns about stratospheric warming and pollution.

In this lecture, I will give an overview of work towards photophoretic flight, starting with basic concepts of photophoretic levitation and a motivation for macroscopic flying platforms based on fundamental studies of atmospheric aerosols. I will focus on the recent work towards proof-of-concept flight of cm-scale structures in the lab, discuss practical concepts for near-space flight including persistence and deployment, and describe several use cases for atmospheric data collection and remote sensing.

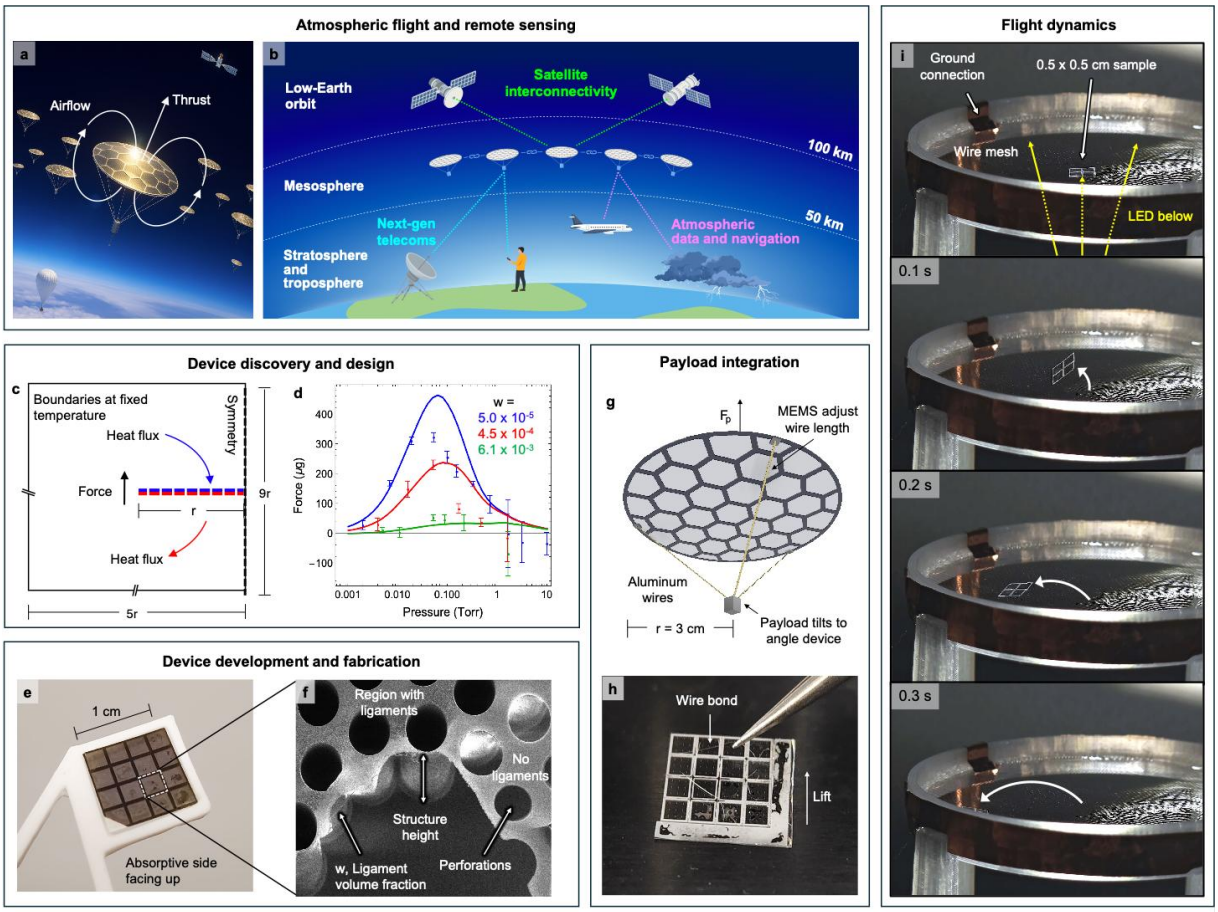

Figure 1: **a)** Atmospheric levitation of a conceptual device caused by photophoretic airflow through perforations in the device. **b)** Applications of photophoretic flyers include climate data collection, next-generation communications, and satellite relays. **c)** DSMC model of the lofting force on a perforated membrane with a temperature difference between its top and bottom sides. **d)** Experimentally measured data of three membrane-like structures with varying ligament densities overlaid with model predictions. **e)** 1 cm^2 test sample and **f)** SEM

image of its perforations. **g)** A 3 cm-radius disk structure with 10 mg payload capacity that could change its attitude by moving the payload. **h)** Wire-bonding is an effective way to attach an arbitrary payload. **i)** Time-lapse of a 0.5 cm^2 sample flying when exposed to 750 W/m^2 (55 % the intensity of sunlight) from a white LED at 26.7 Pa.

Acknowledgments

Thanks to A. J. Feldhaus, J. F. M. Hardigree, J. Kim, F. Sharipov, G. S. Hwang, J. J. Vlassak, and D. W. Keith. This work was supported by the Star-Friedman Challenge for Promising Scientific Research at Harvard University, the Harvard University Grid Accelerator, the New Mexico Lab Embedded Entrepreneurship Program, and Breakthrough Energy.

References and Citations

[1] Horvath, H. (2014). *KONA Powder Part. J.* **31**, 181–199.
[2] Keith, D. W. (2010). *Proc. Natl. Acad. Sci. USA* **107**, 38.
[3] Cheremisin, A. A. (2019). *J. Aerosol Sci.* **136**, 15–35.
[4] Cortes, J., Stanczak, C., Azadi, M., Narula, M., Nicaise, S. M., Hu, H., & Bargatin, I. (2020) Photophoretic levitation of macroscopic nanocardboard plates. *Adv. Mater.* **32**, 16, 1906878.
[5] Schafer, B. C., Kim, J., Sharipov, F., Hwang, G. S., Vlassak, J. J., & Keith, D. W. (2025). Photophoretic flight of perforated structures in near-space conditions. *Nature*, **644**, 362-369.
[6] Sharipov, F., & Schafer, B. C. (2025). Radiometric forces exerted on a membrane with different accommodation coefficients on its sides. *Phys. Rev. Appl.* **24**, 044050.
[7] Sharipov, F., & Schafer, B. C. (2024). Radiometric forces exerted on a perforated membrane. *Phys. Fluids* **36**, 117155.
[8] Kim, J., Jin, L., Schafer, B. C., Jiao, Q., Bertoldi, K., Keith, D. W., & Vlassak, J. J. (2023). Ultralight and ultra-stiff nano-cardboard panels: Mechanical analysis, characterization, and design principles. *Acta Mater.* **248**, 118782.
[9] Mlynczak, M. G., Yue, J., McCormack, J., Liebermann, R. S., & Livesey, N. J. (2021). An observational gap at the edge of space. *Eos*. https://eos.org/opinions/an-observational-gap-at-the-edge-of-space

NEGF26-678339

RADIOMETRIC FORCES ON STRUCTURES COMPOSED OF COAXIAL RINGS

Felix Sharipov*[1], Benjamin C. Schafer[2,3],
[1]Departamento de Física, Universidade Federal do Paraná, Curitiba, Brazil
sharipov@fisica.ufpr.br
[2] Rarefied Technologies Inc., Albuquerque, NM, USA
[3] John A. Paulson Sch. of Eng. and Appl. Sci., Harvard University, Cambridge, MA, USA
schafer@g.harvard.edu

KEY WORDS

Direct simulation Monte Carlo, *ab initio* potential, photophoresis, levitation, structure optimization

ABSTRACT

Recent work suggests that photophoretic forces could levitate thin, 10 centimeter-scale membranes in near-space [1, 2]. Such devices could be useful for atmospheric science or telecommunications on Earth and Mars. Generally, the photophoretic force reaches its maximum value when the molecular mean-free-path (MFP) of the surrounding gas is about the same as the size of a solid, non-porous structure [3, 4]. This restricts photophoretic levitation to mm-scale or smaller structures at high altitudes. However, numerical calculations of the radiometric force exerted on perforated membranes [5, 6] suggest that the perforations increase the force when the membrane radius is significantly larger than the MFP. This is in line with experimental data comparing the forces on porous and non-porous structures [7]. A main assumption throughout these calculations and experiments is that the perforation size should be much smaller than the MFP. However, the costs and difficulty of fabricating membranes increases as the perforations are made smaller. In other words, it is easier to drill or cut fewer holes with larger sizes. To study the trade-off between perforation size and photophoretic force, we study a circular membrane composed of coaxial rings, with varying ring sizes, numbers of rings, and distances between the rings.

The aim of the present work is to model gas flows near a circular membrane of radius a composed of N_r coaxial rings as is shown in Figure 1. The environment temperature and pressure are fixed at T_0 and p_0, respectively. Following the previous work [5, 6], we assume that the membrane has different temperatures at its sides, i.e., the top side is maintained at T_0, while the bottom side has a different temperature T_w. The width of the rings h is the same for all of them and related to the porosity β as

$$h = \frac{a}{2N_r}\left[\sqrt{(N_r-1)^2+4\beta N_r}-(N_r-1)\right]. \qquad (1)$$

* Corresponding author

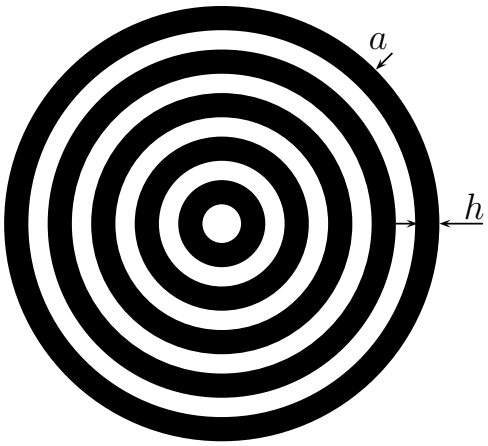

Figure 1: Diagram of the modeled membrane.

Besides the number of rings N_r and porosity β, the solution is determined by the rarefaction parameter

$$\delta = ap_0/\mu v_0, \quad v_0 = \sqrt{2R_g T_0/\mathcal{M}}, \tag{2}$$

where μ is the dynamic viscosity of the gas, v_0 is the most probable speed of the gas molecules, R_g is the universal gas constant, and $\mathcal{M}$ is the molar weight of the gas. We calculate the force F exerted on the membrane. The results are presented in terms of the dimensionless force $\mathcal{F}$ defined as

$$\mathcal{F} = F\frac{T_0}{\pi a^2 p_0 \Delta T}, \quad \Delta T = T_w - T_0. \tag{3}$$

The direct simulation Monte Carlo method based on *ab initio* potential [8] is applied to calculate the flow-field and photophoretic force exerted on the membrane. Diffuse gas-surface interactions are assumed. The calculations are performed for helium and for the same values of porosity β of the works [5, 6]. The environment temperature is assumed to be $T_0 = 300$ K, while the membrane's bottom surface temperature is $T_w = 400$ K. Preliminary results are shown in Figure 2, where the data on perforated membrane [6] are also plotted. As expected, the force $\mathcal{F}$ for a membrane composed from rings becomes close to that for perforated membrane when N_r increases. We compare these results to recent experimental studies of the photophoretic force on membranes with varying perforation area densities and sizes, which suggest that the maximum photophoretic forces are only marginally reduced when the perforations are up to several times larger than the MFP of the surrounding gas. We will also present how varying perforation density and size affect structures for atmospheric flight at different altitudes.

Acknowledgements

F. Sh. is supported by CNPq, Brazil, Grant No. 303429/2022-4. B. Sch. is supported by Rarefied Technologies Inc.

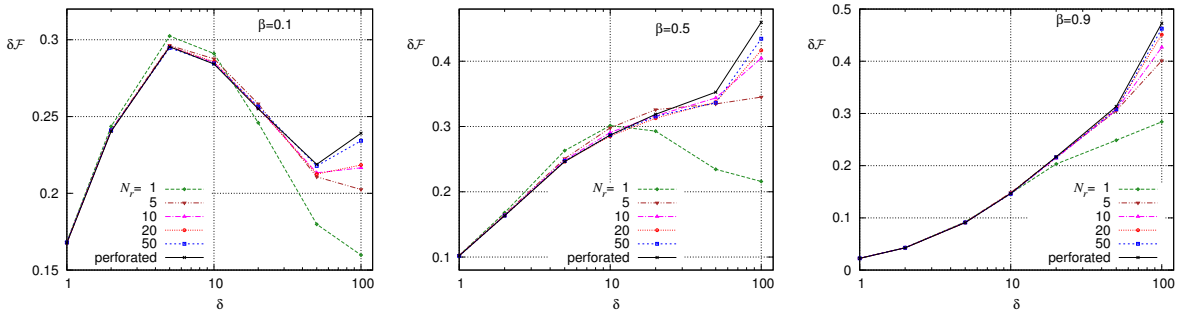

Figure 2: Dimensionless force $\mathcal{F}$ vs. rarefaction parameter δ for three different values of the membrane porosity β.

References and citations

[1] J. Kim, L. Jin, B. C. Schafer, Q. Jiao, K. Bertoldi, D. W. Keith, and J. J. Vlassak, "Ultralight and ultra-stiff nano-cardboard panels: Mechanical analysis, characterization, and design principles," Acta Mater. **248** (2023).

[2] B. C. Schafer, J. Kim, F. Sharipov, G.-S. Hwang, J. J. Vlassak, and D. W. Keith, "Photophoretic flight of perforated structures in near-space conditions," Nature **644**, 362–369 (2025).

[3] S. F. Gimelshein, N. E. Gimelshein, A. D. Ketsdever, and N. P. Selden, "Analysis and Applications of Radiometeric Forces in Rarefied Gas Flows," in *27th Int. Symp. Rarefied Gas dyn., 2010*, D. A. Levin, I. J. Wysong, and A. L. Garcia, eds. (2011), p. 693.

[4] D. Kalempa and F. Sharipov, "Radiometric force on a sphere in a rarefied gas based on the Cercignani-Lampis model of gas-surface interaction," Phys. Fluids **33**, 073 602 (2021).

[5] F. Sharipov, B. C. Schafer, and D. W. Keith, "Modelling the photophoretic force on a perforated membrane," Phys.Fluids **36**, 081 707 (2024).

[6] F. Sharipov and B. C. Schafer, "Radiometric forces exerted on a perforated membrane," Phys.Fluids **36**, 117 155 (2024).

[7] C. Duermann, G. Wurm, and M. Kuepper, "Radiative forces on macroscopic porous bodies in proto-planetary disks: laboratory experiments," Astron. Astrophys. **558**, A70 (2013).

[8] F. Sharipov, "Direct simulation Monte Carlo method based on *ab initio* potential: Recovery of transport coefficients of multi-component mixtures of noble gases," Phys. Fluids **34**, 097 114 (2022).

NEGF26-686060

RAMAN THERMOMETRY OF CONFINED GAS MICROFLOWS

José M. Fernández*[1], Carlos Alvarez[1,2], Guzmán Tejeda[1]
[1]Laboratory of Molecular Fluid Dynamics, Instituto de Estructura de la Materia IEM-CSIC, Serrano 121, 28006 Madrid, Spain
jm.fernandez@csic.es, g.tejeda@csic.es
[2]Institut de Physique de Rennes, 263 Av. du général Leclerc, 35042 Rennes Cedex, France
carlos.alvarez@univ-rennes.fr

KEY WORDS

Raman spectroscopy, experimental techniques, temperature maps, nitrogen, carbon dioxide, slip regime.

ABSTRACT

Microfluidics devices with internal gas flows are nowadays subject of a rapid development. These devices often operate in rarefied gas flow regimes, since the ratio (Knudsen number, Kn) of the molecular mean free path over the channel dimensions becomes non-negligible. In those rarefied flows, non-equilibrium effects are expected to occur, like temperature-jumps near the wall. However, there is a lack of experimental techniques capable of measuring the internal properties, such as temperature, in gas flows confined in small channels [1].

Raman spectroscopy is an optical tool based on the inelastic light scattering process, and has become a powerful non-intrusive technique to probe gas flows at the molecular level with spatial resolution of a few microns. These capabilities have been widely demonstrated in gas free microjets of small molecules at the Laboratory of Molecular Fluid Dynamics of the IEM-CSIC [2-7].

Raman spectroscopy relies on the structure of the Quantum-Mechanical energy levels of the gas molecules, like other molecular spectroscopies based on the absorption or emission of microwave or infrared radiation. Therefore, it can access the population of the energy levels of their internal motions (rotation and vibration), even when those populations deviate from the equilibrium Boltzmann distribution [8].

In order to extend the diagnostics capabilities of Raman spectroscopy to confined gas flows, we present here several examples of the application of Raman thermometry to gas flows within millimeter-sized channels. For this work, we have designed several channels with different geometries, and forced thermal gradients between some of their surfaces while flowing gases through the channels. The pressures ranged from atmospheric down to 20 mbar, and the flow velocities ranged from 10 to 300 cm/s. The most rarefied flows lie in the slip regime ($Kn \geq 10^{-3}$).

The experiments carried out so far have demonstrated that the gas temperature in the flow can be mapped with high spatial resolution, from the rotational and vibrational Raman spectra of molecules like N_2, CO_2 and H_2. The recorded temperature maps of the confined flows under thermal gradients show

* Corresponding author

a different thermal behavior for gases like CO_2, that absorbs IR radiation, versus those like N_2 or H_2 which are transparent to it.

Acknowledgments

This work was funded by the Spanish MCIN/AEI/10.13039/501100011033/ through grant No. PID2021-123752NB-I00.

References and Citations

[1] S. Colin, J. M. Fernández, C. Barrot, L. Baldas, S. Bajic, M. Rojas-Cárdenas (2022). "Review of Optical Thermometry Techniques for Flows at the Microscale towards Their Applicability to Gas Microflows". *Micromachines* **13**, 1819.

[2] S. Montero, B. Maté, G. Tejeda, J.M. Fernández, A. Ramos (2001). Raman studies of free jet expansion (Diagnostics and mapping), in *Atomic and Molecular Beams. The State of the Art 2000*, R. Campargue (Ed.), Springer, Berlin; pags. 295–306.

[3] A. Ramos, G. Tejeda, J. M. Fernández, S. Montero (2009). Non-equilibrium processes in supersonic jets of N_2, H_2, and N_2+H_2 mixtures. I. Zone of silence. *Journal of Physical Chemistry A.* **113**, 8506–8512.

[4] A. Ramos, G. Tejeda, J. M. Fernández, S. Montero (2010). Non-equilibrium processes in supersonic jets of N_2, H_2, and N_2+H_2 mixtures. II. Shock waves. *Journal of Physical Chemistry A.* **114**, 7761-7768.

[5] G. Tejeda, E. Carmona-Novillo, E. Moreno, J. M. Fernández, M. I. Hernández, S. Montero (2015). Laboratory study of rate coefficients for H_2O:He inelastic collisions between 20 and 120 K. *Astrophysical Journal Supplement Series* **216**(1), 3.

[6] F. Gámez, J. M. Fernández, E. Moreno, G. Tejeda, M. I. Hernández, S. Montero (2019). Inelastic Collisions of O_2 with He at Low Temperatures. *Journal of Physical Chemistry A* **123**, 8496-8505.

[7] C. Álvarez, G. Tejeda, J. M. Fernández (2024). Laboratory study of rotationally inelastic collisions of CO_2 at low temperatures. *Journal of Chemical Physics* **160**, 164307.

[8] S. Montero, G. Tejeda, J. M. Fernández (2020). Laboratory Study of Rate Coefficients for H_2:H_2 Inelastic Collisions between 295 and 20 K. *Astrophysical Journal Supplement Series* **247**:14.

NEGF26-679329

REALIZATION OF FRICTION REDUCTION ACTING ON AN OBJECT UTILIZING KNUDSEN FORCE

Hiroki Yamaguchi*[1,2], Tatsuki Hanai[2], Shigeru Yonemura[3]
[1] Toyota Technological Institute, 2-12-1 Hisakata, Tempaku, Nagoya, Aichi 468-8511, JAPAN
hiroki@toyota-ti.ac.jp
[2]Nagoya University, Furo-cho, Chikusa, Nagoya, Aichi 464-8603, JAPAN
hanai.tatsuki.b0@s.mail.nagoya-u.ac.jp
[3]Chubu University, 1200 Matsumoto-cho, Kasugai, Aichi 487-8501, JAPAN
yonemura@fsc.chubu.ac.jp

KEY WORDS

Thermal transpiration flow, Thermal creep flow, Rarefied gas dynamics, Gas lubrication, Micro/nano-channels

ABSTRACT

In high Knudsen number environments, such as rarefied gas flows or micro / nano gaseous flows, the existence of temperature difference / gradient induces a flow called a thermal transpiration flow. This thermally driven flow has been extensively studied for a long time [1], and it has been utilized in Knudsen pumps / compressors [2]. As a reaction of this flow, the Knudsen force acts on the surface.

Recently, several researchers have achieved levitation of an object with the photophoretic force [3,4]. Photophoresis is induced by a non-uniform temperature distribution, similar to the thermal transpiration flow. A particle is known to levitate by a temperature gradient [5]. Thus, it would be possible to realize a reduction in the friction acting on an object by inducing the Knudsen force through a temperature distribution.

In this study, we followed the numerical study by the DSMC in which an object with narrow perpendicular channels placed above a heated flat plate was subjected to a lift force [6]. We observed an object on a inclined heated flat plate to evaluate the friction reduction.

A flat plate with a heater attached was placed on a goniometer stage. By installing it inside a vacuum desiccator made of acrylic, the pressure inside the desiccator could be varied. The friction

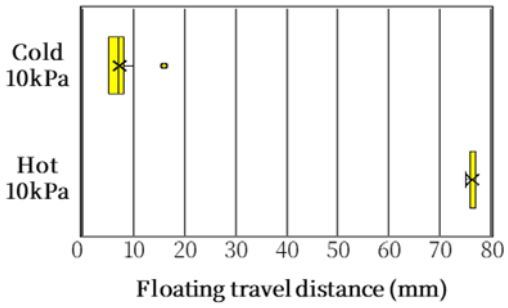

Figure 1: The travel distances of the object with different conditions.

acting on an object was investigated by dropping the object down the inclined flat plate and observing its subsequent behavior.

The observations were performed at slightly low pressure of 10 kPa under two conditions: left at room temperature without heating and heated up to 100℃. We measured the travel distance of the object sliding down the inclined flat plate. Figure 1 shows that while the object hardly moves under the unheated condition, it moves significantly when heated. It suggests that heating the flat plate induced a thermal transpiration flow and a Knudsen lift force, reducing the friction acting on the object.

Acknowledgments

This work was supported by JSPS KAKENHI Grant Numbers JP17K06141, JP20K04279, JP23K03666, and JP25K01171.

References and Citations

[1] Akhlaghi, H., Roohi, E., & Stefanov, S. A (2023). Comprehensive review on micro- and nano-scale gas flow effects: Slip-jump phenomena, Knudsen paradox, thermally-driven flows, and Knudsen pumps. *Phys. Rep.*, **997**, 1–60.

[2] Wang, X., Su, T., Zhang, W., & Zhang, S. (2020). Knudsen pumps: A review. *Microsyst. Nanoeng.*, **26**, 2–28.

[3] Cortes, J., Stanczak, C., Azadi, M., Narula, M., Nicaise, S. M., Hu, H., Bargatin, I. (2020). Photophoretic Levitation of Macroscopic Nanocardboard Plates, *Adv. Mater*., **32**, 1906878.

[4] Schafer, B. C., Kim, J.-h., Sharipov, F., Hwang, G.-S., Vlassak. J. J., & Keith, D. W. (2025). Photophoretic flight of perforated structures in near-space conditions. *Nature*, **644**, 362–369.

[5] Kelling, T., & Wurm, G. (2009). Self-Sustained Levitation of Dust Aggregate Ensembles by Temperature-Gradient-Induced Overpressures. *Phys. Rev. Lett.*, **103**, 215502.

[6] Yonemura, S., & Kawagoe, Y. (2018). A Study on a Force Exerted on Microscale Object due to a Non-Uniform Temperature Field, *31st International Symposium on Rarefied Gas Dynamics*.

NEGF26-679355

SHOCK THICKNESS ANALYSIS IN MULTI-TEMPERATURE NAVIER-STOKES EQUATIONS FOR BINARY INERT MIXTURES

Marzia Bisi[1], Maria Groppi[1], Anna Macaluso[1], Giorgio Martalò*[2]
[1]Department of Mathematical Physical and Computer Sciences, University of Parma, Parco Area delle Scienze 53/A, 43124 Parma, Italy
marzia.bisi@unipr.it, maria.groppi@unipr.it, anna.macaluso@unipr.it
[2]Department of Mathematics "F. Casorati", University of Pavia, Via A. Ferrata 5, 27100 Pavia, Italy
giorgio.martalo@unipv.it

KEY WORDS

Multi-temperature Navier-Stokes equations, Shock wave analysis, Shock thickness

ABSTRACT

The shock wave structure is a widely investigated topic in the literature, especially among researchers working on hyperbolic systems of conservation and balance laws. In recent years, their attention has been focused on the emergence, of discontinuities (subshocks) that compromise the physical admissibility of the solutions. In particular, for multi-velocity and multi-temperature mixtures, it has been observed that fields profiles may exhibit several discontinuities, and that the critical Mach number at which the physical meaning of the solution is lost depends on the masses and concentrations of the components.
In this presentation, we instead consider the shock wave structure for Navier–Stokes descriptions, which, unlike hyperbolic systems, provide smooth solutions for any value of the Mach number. Our focus will be on the analysis of the shock thickness, which gives a measure of the transition region where the solution rapidly passes from an equilibrium state to another. This parameter, which quantifies the strength of the shock, depends on the Mach number and is expected to exhibit a monotonic behavior as the Mach number increases. However, as known since the '50s [1], in the case of a single gas, the thickness decreases up to a certain Mach number, after which it unexpectedly begins to increase again; it is also shown that the choice of the intermolecular potential affects the critical value. Such result has been extended to inert binary mixtures whose evolution is modeled by single-velocity and single-temperature descriptions [2].
Now, our main aim is to discuss this issue for multi-velocity and multi-temperature Navier-Stokes equa-

* Corresponding author

tions for species mass densities n_s, mean velocities $\mathbf{u}_s$ and temperatures T_s

$$\frac{\partial n_s}{\partial t} + \nabla_{\mathbf{x}} \cdot (n_s \mathbf{u}_s) = 0 \tag{1}$$

$$\frac{\partial}{\partial t}(\rho_s \mathbf{u}_s) + \nabla_{\mathbf{x}} \cdot (\rho_s \mathbf{u}_s \otimes \mathbf{u}_s + n_s T_s \underline{\mathbf{I}}) + \nabla_{\mathbf{x}} \cdot \underline{\mathbf{P}}_s^{(1)} = \mathbf{R}_{sr} \tag{2}$$

$$\frac{\partial}{\partial t}\left(\frac{1}{2}\rho_s u_s^2 + \frac{3}{2} n_s T_s\right) + \nabla_{\mathbf{x}} \cdot \left[\left(\frac{1}{2}\rho_s u_s^2 + \frac{5}{2} n_s T_s\right)\mathbf{u}_s\right] + \nabla_{\mathbf{x}} \cdot \left[\underline{\mathbf{P}}_s^{(1)} \cdot \mathbf{u}_s + \mathbf{q}_s^{(1)}\right] = S_{sr}\,, \tag{3}$$

$s = 1, 2$, $r \neq s$, obtained as hydrodynamic limit of recent BGK [3] and hybrid Boltzmann-BGK [4] kinetic formulations. We point out that conservations of global momentum and energy can be recovered by summing over the index s. Source terms at the right-hand side are given by

$$\mathbf{R}_{sr} = \lambda_{sr}^{[1]} \alpha_{rs} m_s n_s n_r \left(\mathbf{u}_r - \mathbf{u}_s\right) \tag{4}$$

$$S_{sr} = \lambda_{sr}^{[1]} \alpha_{sr} \alpha_{rs} n_s n_r \left[3(T_r - T_s) + (m_s \mathbf{u}_s + m_r \mathbf{u}_r) \cdot (\mathbf{u}_r - \mathbf{u}_s)\right], \tag{5}$$

where $\lambda_{sr}^{[k]}$ is a proper moment (of order k) of the inter-species cross section and $\alpha_{sr} = m_s/(m_s + m_r)$ is the mass ratio; the 1st order corrections of species pressure tensor and heat flux are given explicitly as

$$\underline{\mathbf{P}}_s^{(1)} = -\mu_s \underline{\Upsilon}_s + \frac{4}{3 n_s \lambda_{ss}^{[2]}} \sum_{\substack{r=1 \\ r \neq s}}^{N} \nu_{sr}^{(0)} \rho_s a_{sr}^2 \left[(\mathbf{u}_r - \mathbf{u}_s) \otimes (\mathbf{u}_r - \mathbf{u}_s) - \frac{1}{3}|\mathbf{u}_r - \mathbf{u}_s|^2 \underline{\mathbf{I}}\right] \tag{6}$$

$$\mathbf{q}_s^{(1)} = -\xi_s \nabla_{\mathbf{x}} T_s + \frac{10}{\lambda_{ss}^{[2]}} \sum_{\substack{r=1 \\ r \neq s}}^{N} \alpha_{sr} \nu_{sr}^{(0)} a_{sr}^2 (T_r - T_s)(\mathbf{u}_r - \mathbf{u}_s) + \\ + \frac{2 m_s}{3 \lambda_{ss}^{[2]}} \sum_{\substack{r=1 \\ r \neq s}}^{N} \nu_{sr}^{(0)} a_{sr}^2 (5\alpha_{rs} - a_{sr}) |\mathbf{u}_r - \mathbf{u}_s|^2 (\mathbf{u}_r - \mathbf{u}_s), \tag{7}$$

with

$$\Upsilon_{s,hk} = \frac{\partial u_{s,h}}{\partial x_k} + \frac{\partial u_{s,k}}{\partial x_h} - \frac{2}{3} \nabla_{\mathbf{x}} \cdot \mathbf{u}_s \delta_{hk} \tag{8}$$

being the strain rate tensor, $\mu_s = 4T_s/(3\lambda_{ss}^{[2]})$ and $\xi_s = 5T_s/(m_s \lambda_{ss}^{[2]})$ the viscosity and heat conductivity coefficients, respectively.

The 1-D steady shock wave problem consists in finding the solution of the associated ODEs system, with limiting conditions at $\pm\infty$ of equilibrium, characterized by the equalization of species velocities and temperatures, and vanishing viscous stress and heat flux; the shock thickness can be measured as

$$\Delta = \frac{u_- - u_+}{\max |du/dx|}\,, \tag{9}$$

where u is the one-dimensional mixture velocity and $u_\pm$ its limiting values at $\pm\infty$.

We present a detailed analysis of the shock thickness problem for different inert mixtures of noble gases, and diverse concentrations of the two components at the equilibrium. The investigation extends the results obtained for the single-gas case, confirming the non-monotonic behavior of the shock thickness for increasing Mach number, also for a simplified single-velocity and multi-temperature model (see Figure 1). In addition, it is shown that the critical value of the Mach number at which the shock thickness profile reaches its minimum is not unique, but depends on the mass ratio and on the constituents' concentrations at the equilibrium, as shown for example in Table 1 for a single-velocity description.

Some slight discrepancies emerge between the single- and the multi-velocity formulations [5], particularly when small mass ratios are considered, i.e. when mixtures components have very disparate masses. In the model which accounts for all species fields, the transition proceeds more gradually and appears less steeply; moreover, temperature overshoot effects are reduced or entirely absent, suggesting that describing different species to evolve with distinct velocities smooths the equilibration process. The minimum of the shock thickness in the multi-velocity model occurs at slightly higher critical Mach numbers, especially for small mass ratios (see Figure 2). This behavior is expected, since mixtures containing both light and heavy species display distinctive features that can only be captured with an accurate description.

Acknowledgements

This work was performed in the frame of activities sponsored by the Italian National Group of Mathematical Physics (GNFM-INdAM) and by the Universities of Parma (Italy) and Pavia (Italy). MB, MG and AM thanks the support of the project PRIN 2022 PNRR *Mathematical Modelling for a Sustainable Circular Economy in Ecosystems* (project code P2022PSMT7, CUP D53D23018960001) funded by the European Union - NextGenerationEU PNRR-M4C2-I 1.1 and by MUR-Italian Ministry of Universities

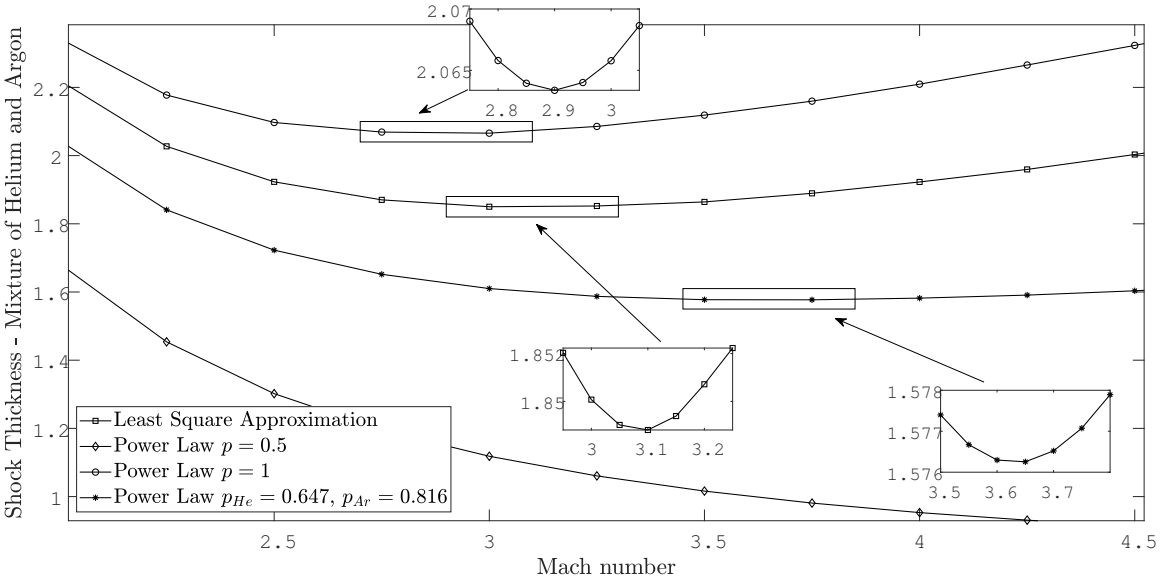

Figure 1: Shock thickness Δ versus Mach number for a mixture of Helium (75%) and Argon (25%) and different models of viscosity.

Mixture	m_1/m_2	$\chi_1^{\pm}$	$\chi_2^{\pm}$	LSA	Realistic	Maxwell
Helium - Xenon	0.03	0.25	0.75	3.55	3.05	3.65
		0.75	0.25	3.1	2.3	2.7
Helium - Argon	0.1	0.25	0.75	3.9	4.9	3.15
		0.75	0.25	3.1	3.65	2.9
Krypton - Xenon	0.64	0.25	0.75	3.28	3.55	3.38
		0.75	0.25	3.49	3.73	3.1

Table 1: Critical Mach number for mixtures of Helium and Xenon, Helium and Argon, and Krypton and Xenon at different concentrations for three types of interaction potential.

and Research. This research benefits from the *High Performance Computing* facility of the University of Parma, Italy (HPC.unipr.it).

References and citations

[1] Gilbarg, D., & Paolucci, D. (1953). The structure of shock waves in the continuum theory of fluids. Arch. Ration. Mech. Anal., 2, 617-642.
[2] Bisi, M., Groppi, M., & Martalò, G. (2021). On the shock thickness for a binary gas mixture. Ric. Mat., 70(1), 251-266.
[3] Bisi, M., Groppi, M., & Martalò, G. (2021). Macroscopic equations for inert gas mixtures in different hydrodynamic regimes. J. Phys. A: Math. Theor., 54(8), 085201.
[4] Bisi, M., Groppi, M., Macaluso, A., & Martalò, G. (2025). Multi-temperature hydrodynamic limits derived from a hybrid Boltzmann-BGK model. J. Phys. A: Math. Theor.
[5] Macaluso, A., & Martalò, G. (2025). Shock Thickness Analysis in Multi-temperature Navier-Stokes Equations for Binary Gas Mixtures. In press

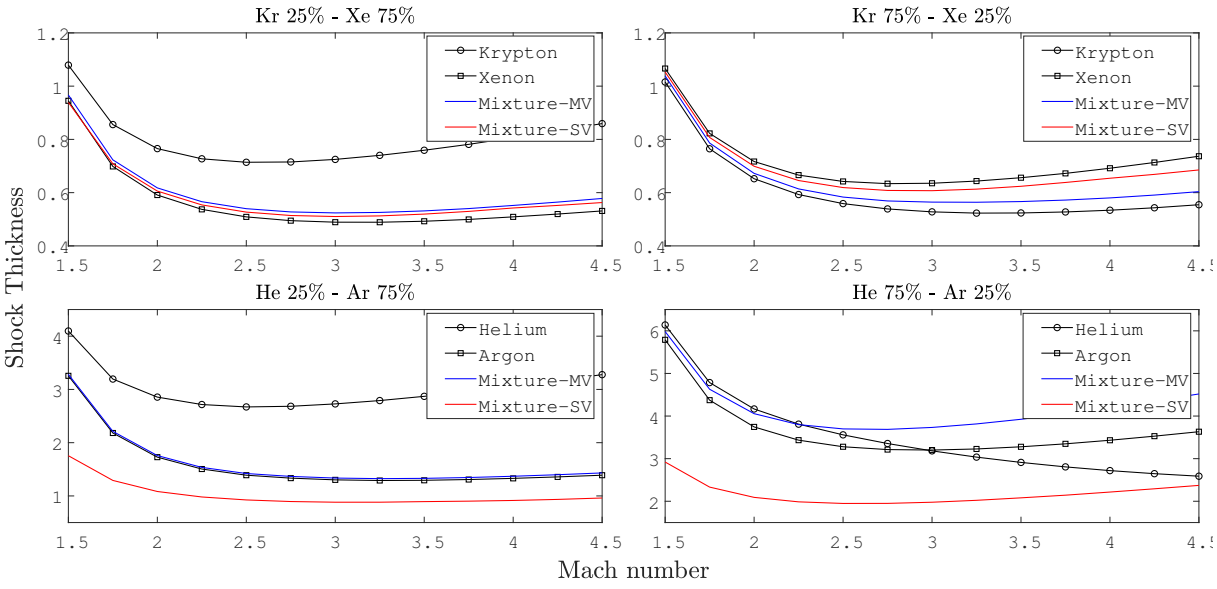

Figure 2: Shock thickness Δ and corresponding species quantities Δ_s for mixtures of Krypton and Xenon (top line) and Helium and Argon (bottom line) at different concentrations in both single-velocity and multi-velocity formulations.

NEGF26-686098

Shock Wave Dynamics in Non-Equilibrium Gas Flow Regimes: Insights from Grad-Type Moment Systems

Satyvir Singh[*], **Manuel Torrilhon**
Institute for Applied and Computational Mathematics, RWTH Aachen University, Germany
singh@acom.rwth-aachen.de, mt@acom.rwth-aachen.de

KEY WORDS

Kinetic theory of gases, rarefied gas dynamics, discontinuous Galerkin approximation, Grad-models, Knudsen number.

ABSTRACT

Shock waves in rarefied and non-equilibrium gas flow regimes exhibit complex multi-scale structures that cannot be accurately described by classical continuum models such as the Navier–Stokes–Fourier (NSF) equations [1]. In the transition regime, characterized by moderate to high Knudsen numbers, strong thermodynamic non-equilibrium leads to anisotropic stresses, non-Fourier heat flux, and higher-order transport effects within the shock layer. Capturing these phenomena requires modeling frameworks derived from kinetic theory. In this work, shock wave dynamics are investigated using Grad-type moment systems to provide improved physical insight and predictive capability for non-equilibrium gas flows [2]. Extended moment equations, including Grad's 13-moment system and higher-order variants, are employed to resolve rarefied shock structures. These models retain higher-order tensorial moments representing stress, heat flux, and non-equilibrium energy transport, enabling a more accurate description of shock-layer physics than continuum models. To resolve steep gradients and nonlinear wave interactions, a high-order Discontinuous Galerkin (DG) method is developed for the moment system. The DG framework provides high-resolution shock capturing, geometric flexibility, and numerical robustness for solving hyperbolic moment equations [3].
A series of numerical experiments is performed for one- and multi-dimensional shock problems across a range of Mach and Knudsen numbers. The results are compared with DSMC simulations and continuum solutions [4]. The Grad-based formulation demonstrates improved prediction of shock thickness, temperature overshoot, stress relaxation, and nonlinear heat-flux behavior. In particular, the simulations capture non-monotonic temperature profiles and higher-order moment oscillations that are not represented in NSF-based models [5]. Representative flow behavior predicted by the moment system is illustrated in Fig. 1, which shows Mach-number contours for supersonic flow over an aerospike blunt body at $Ma = 3$ and $\alpha = 10^{\circ}$ for two Knudsen numbers. The comparison between $Kn = 0.0001$ and $Kn = 0.01$ demonstrates the influence of rarefaction on the bow-shock structure, shock thickness, and

[*] Corresponding author

downstream expansion region, highlighting the growing importance of non-equilibrium transport effects as the flow transitions from near-continuum to rarefied conditions.
These results highlight the capability of Grad-type moment systems, combined with high-order DG discretization, to model transitional and rarefied shock flows efficiently. The study demonstrates that moment-based approaches provide a computationally efficient alternative to particle methods while retaining essential non-equilibrium physics. The findings contribute toward advancing hybrid kinetic–continuum modeling strategies for applications in hypersonic aerothermodynamics, micro-scale gas transport, and high-speed flow systems.

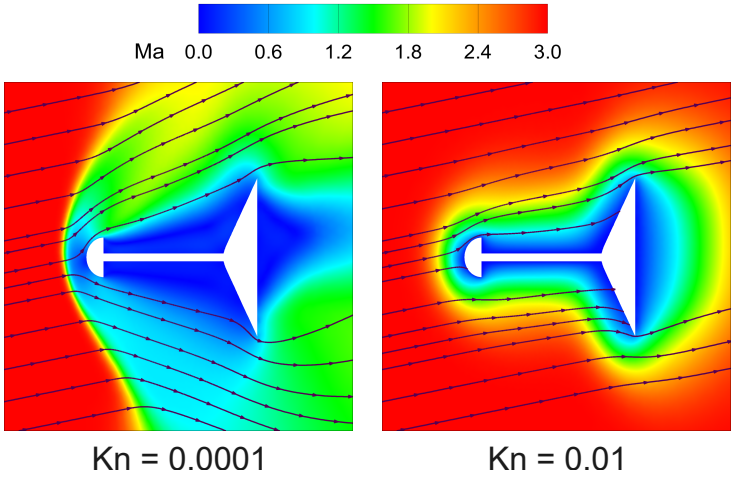

Figure 1: Mach number contours for supersonic flow over an aerospike blunt body at $Ma = 3$ and angle of attack $\alpha = 10°$, computed using a Grad-type moment system. Results are shown for two Knudsen numbers, $Kn = 0.0001$ (near-continuum regime) and $Kn = 0.01$ (transition regime). The comparison illustrates rarefaction-induced modifications of the bow-shock structure, shock thickness, and downstream flow expansion in non-equilibrium gas flows.

Acknowledgements

The authors acknowledge the support provided by the German Research Foundation within the research unit DFG–FOR5409.

References

[1] Torrilhon, M., & and Struchtrup, H. (2004). Regularized 13-moment equations: shock structure calculations and comparison to Burnett models. J. Fluid Mech., 513, 171–198.
[2] Torrilhon, M. (2016). Modeling nonequilibrium gas flow based on moment equations. Annu. Rev. Fluid Mech., 48, 429–458.
[3] Singh, S., Karchani, A., Chourushi, T., & Myong, R. S. (2022). A three-dimensional modal discontinuous Galerkin method for the second-order Boltzmann-Curtiss-based constitutive model of rarefied and microscale gas flows. J. Comput. Phys., 457, 111052.
[4] Singh, S., Song, H., & Torrilhon, M. (2024). Modal discontinuous Galerkin simulations for Grad's 13 moment equations: Application to Riemann problem in continuum-rarefied flow regime. J. Comput. Theor. Trans., 53, 398–422.
[5] Song, H., Singh, S., & Torrilhon, M. (2025). Non-equilibrium flow simulations based on Grad-14 and Grad-17 moment equations for polytropic gases. Phys. Fluids, 37, 036140.

NEGF26-686105

SIMULATION OF THE ENTRY OF A SPHERE INTO A NITROGEN ATMOSPHERE WITH A VIBRATIONAL-SPECIFIC MODEL

Marie-Claude Druguet*[1], Arnaud Bultel[2]
[1]Aix-Marseille Université, CNRS UMR 7343, IUSTI, 5 rue Enrico Fermi, 13453 Marseille, France
marie-claude.druguet@univ-amu.fr
[2]Normandie Université, CNRS UMR 6614, CORIA, Site du Madrillet, 76801 St Etienne du Rouvray, France
arnaud.bultel@coria.fr

KEY WORDS

State-to-state modeling, hypersonic flow, aerothermodynamics, computational fluid dynamics.

1. Introduction

During the atmospheric entry of a spacecraft at hypervelocity the gas in the shock layer goes through high temperatures and through various thermochemical non-equilibrium states. For decades, the scientific community has worked to better understand the behavior of excited species in non-equilibrium plasmas. In the widely used global chemical mechanism approaches – among them the well-known models developed by Park [1, 2] – the modeling consists in considering the chemical species as a whole without distinguishing their excited states. The population number density of their excited states is then estimated either by assuming a Boltzmann distribution at an excitation temperature or by assuming the quasi-steady state. For the past recent years, another methodology has been developed, [3]–[7], based on a complete description of the flow field with considering every (or several) excited states of each particle as independent species. This approach is very attractive because of its expected accuracy in giving a detailed description of a plasma, but it is very challenging to implement in CFD codes.
In this framework, the present study is a contribution to the progressive work for computing a reactive and non-equilibrium gas flow through the shock layer surrounding an axi-symmetric blunt body, with detailed collisional-radiative models. The selected state-to-state model recently implemented in our in-house code PINENS (Parallel Implicit Non-Equilibrium Navier-Stokes) [8] is a state-specific vibrational model, that is a simplified version of CoRaM-N_2, a collisional-radiative (CR) model developed for nitrogen [7]. This model takes into account the species N_2 and N, and is vibrationnally specific for the N_2 molecules on their ground electronic state. It allows to simulate the phase of ladder-climbing vibrational excitation and the resulting dissociation of N_2.
The first step in attempting to simulate the composition and the vibrational state of the gas around a space body with the detailed chemical kinetics model was done for an entry velocity of a sphere at 10.6

* Corresponding author

km/s. The results then obtained surprisingly showed that some of the processes had no visible effect on the gas vibrational state, unless a close-up view of the results was done. Because of that, it was decided to perform the simulations at a lower entry speed of 8 km/s to assess the potential effect of these processes at lower temperatures in the shock layer. Again, the results showed that some of the processes had negligible effect on the gas composition and vibrational state. This is why, before concluding that some of these processes are inefficient in a shock layer, one wants to test once more the vibrational-state specific model for nitrogen, for the entry of the sphere at other entry speeds, one at 6.19 km/s and the other one at 11.25 km/s. The present work shows the results for an atmospheric entry at 6.19 km/s.

2. Vibrational-state specific model, mathematical formulation, and entry conditions

The vibrationally specific model subject of the present work takes into account heavy, neutral particles. It considers each of the 68 vibrational states of N_2 ($0 \leq v \leq v_{max} = 67$) on the ground electronic state – pointed out by Armenise et al. – as well as the ground electronic state of N. The terms *"species-states"* or *"pseudo-species"* refer to the chemical species N and N_2(v) on its excited states v. In comparison, the global modeling for such a gas mixture would only include the molecule N_2 and the atom N.
According to the CoRaM-N_2 model that is used as the basis to derive the present vibrational-state specific model, the vibrational excitation of molecules N_2 takes place through vibration–translation processes under molecular impact (VT-m processes), through vibration–vibration processes under molecular impact (VV-m processes), or through vibration–translation processes under atomic impact (VT-a processes). It results 6817 forward collisional elementary processes. The data used for the rate coefficients for these processes were calculated by Armenise et al.and Esposito et al. The backward collisional elementary processes are calculated from the forward rate coefficient and the corresponding equilibrium constant using the detailed balance principle. In comparison, the usual global modeling for the chemical reactions between N_2 and N includes 2 reactions of dissociation of N_2.
The equations to be solved are the usual Navier-Stokes equations, except that a mass conservation equation is written for each vibrational level of N_2(v) instead of one conservation equation of mass for N_2. As for the equation of vibrational energy of N_2 usually used in the global models (Landau-Teller, Millikan-White), it is no longer needed in the detailed model. Each species s on its excited state v – named *"pseudo-species"* and noted sv – has a mass density ρ_{sv} and the total mass density of the gas mixture is $\rho = \sum_{sv=1}^{n_{sv}} \rho_{sv}$. For an axi-symmetric flow, one then has to solve 72 equations: 69 conservation equations for the *"species-state"* N and N_2(v), two equations for the conservation of the momentum, and one equation for the conservation of the total energy. The set of conservative equations is closed with an adequate equation of state. In comparison, the global model relies on the same equations, except that they refer to the species s (N_2 and N in their entirety), instead of the *"species-states"* sv. In that case, there are only 6 conservation equations to solve.

3. Results

For an atmosphere initially composed of 100% of N_2 on v=0 vibrational level and according to the considered vibrational state-to-state model, the molecules N_2 on their zero-vibrational level collide, get excited, and – depending on the type of collisions – get dissociated across the shock wave. These collisional processes lead to a gas mixture composed of the two species N_2 and N, N_2 being on various vibrational levels depending on the excitation processes considered. The vibrational-state specific model – split into several groups of reactions – is implemented in PINENS code step-by-step in order to show the specific effect of each process group on the population densities of the 68 vibrational levels of N_2 and of the atomic species N, throughout the shock layer. The results presented hereafter correspond to an entry of the sphere at V_∞ = 6.19 km/s.

3.1 VT-m (67 processes).

The first step consists in taking into account the VT exchanges by molecular impact (VT-m). The results then obtained are shown in Fig. 1. Interestingly, the temperature profile along the stagnation line is similar to that obtained when no chemical reactions are taken into account in the gas flow: the temperature is maximum in the entire shock layer, with a maximum of 19,000 K reached near the stagnation area of the flow, just in front of the boundary layer. This means that the VT-m processes do not take much thermal energy from the gas.
In this figure, one can also follow the evolutions of the mass fractions of each vibrational level of N_2 (from v = 0 to 67) along the stagnation line throughout the shock layer, down to the boundary layer. The population density of N_2(v=0) decreases across the shock wave to the profit of the excited states v=1 to 67, noting that the vibrational levels are more widely spread at the lower entry speed of 6.19 km/s than higher entry velocities [9].

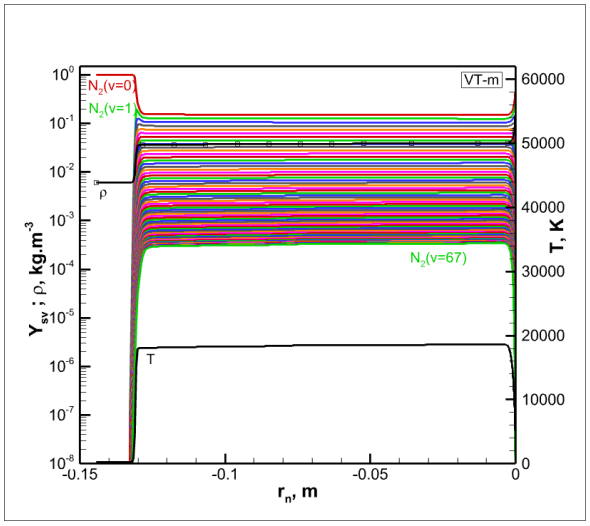

Figure 1: Temperature and mass fractions of N_2(v=0,67) along the stagnation line, obtained with 67 processes (VT-m). V_∞=6.19 km/s.

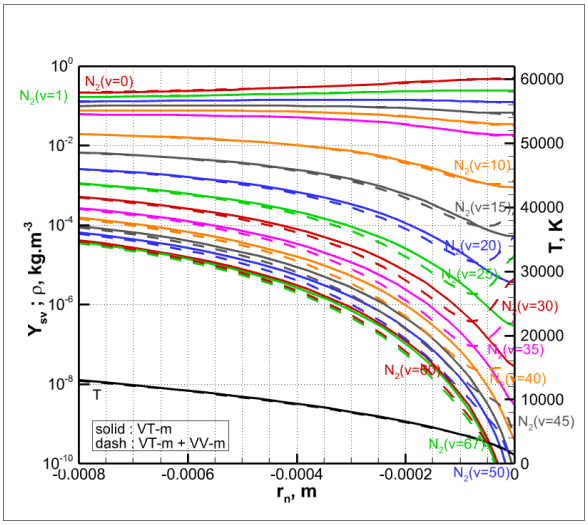

Figure 2: Temperature and mass fractions of N_2(v=0,67) along the stagnation line. Comparison between 67 processes (VT-m) and 4556 processes (VT-m + VV-m). Close-up view near the boundary layer. V_∞=6.19 km/s.

3.2 VT-m + VV-m (4556 processes).

The addition of the processes modeling the vibration–vibration exchanges by molecular impact (VV-m) does not show any visible difference on the population densities when compared to those obtained with the (VT-m) processes only, unless a very close-up view of the population curves is done near the boundary layer (Fig. 2). This observation is similar to that made with V_∞ = 10.6 km/s [9] and V_∞ = 8 km/s. The reason to that little effect of the VV-m processes is not fully understood, but a preliminary explanation may lie in the slow VV rates compared to the transit time in the shock layer. Because of the little effect of the VV-m processes and because these processes are numerous – which make the computations very long –, we decided to no longer take into account the VV-m processes in the remaining of the simulations.

3.3 VT-m + VT-m-D (68 processes).

The introduction of the VT-m-D process makes a major change in the temperature and densities profiles of the vibrational levels of N_2(v) throughout the shock layer and specifically along the stagnation line (Fig. 3 compared to Fig. 1). Adding this single process of dissociation tends to reduce the shock layer width from approximately 13 cm to 10.5 cm, and changes the temperature profile across the shock layer: the temperature is no longer maximum at 19,000 K throughout the shock layer (Fig. 1) but peaks at 18,000 K in the shock wave then decreases slightly to 10,000 K (Fig. 3). This means that the single (VT-m-D) processe absorbs a large amount of thermal energy, and that it is a very efficient process among the many reactions of the vibrational-state specific model implemented in the CFD code. This new temperature profile is similar to the those usually observed when chemical reactions are taken into account in global models, and is typical of shock layer where dissociation processes take place. Regarding the species profiles within the shock layer, N is now in equivalent quantity with N_2(v=0). Most of the vibrational levels of N_2 are less populated, especially the highest levels – because of the dissociation of N_2 from the highest vibrational levels – to the profit of N.
Moreover, it has to be noted that the addition of the 67 VV-m-D processes to the 68 processes (VT-m + VT-m-D) do not make visible changes on the population densities nor on the temperature profile throughout the shock layer (figures not shown). It is as if the VT-m-D process already did the major work of dissociation, not allowing the VV-m-D processes do their part of the dissociation. However, when the sole processes VV-m-D are added to the VT-m processes (without adding the VT-m-D process), the 67 VV-m-D processes do the same job of dissociation as the single VT-m-D process would have done. Therefore, the 67 processes VV-m-D are no longer included in the remaining of the simulations.

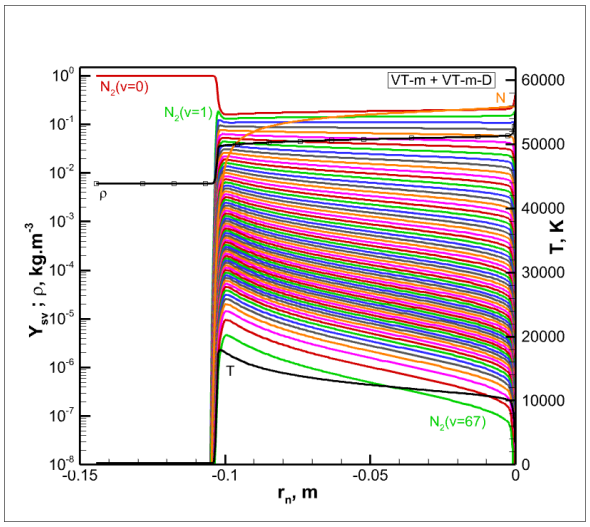

Figure 3: Temperature and mass fractions of N and N_2(v=0,67) along the stagnation line, obtained with 68 processes (VT-m + VT-m-D). V_∞=6.19 km/s.

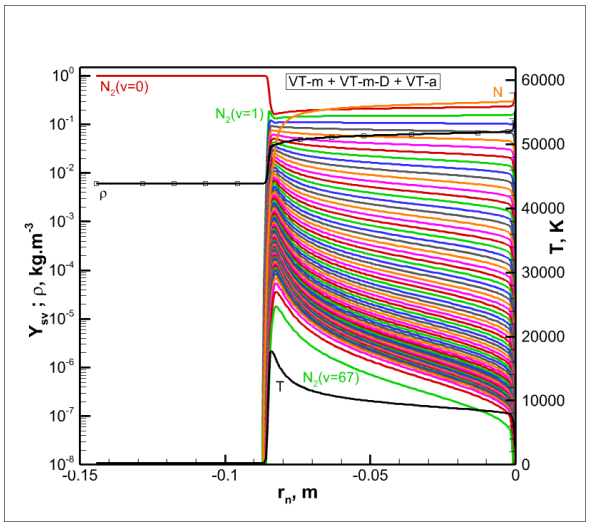

Figure 4: Temperature and mass fractions of N and N_2(v=0,67) along the stagnation line, obtained with 2193 processes (VT-m + VT-m-D + VT-a). V_∞=6.19 km/s.

3.4 VT-m + VT-m-D + VT-a (2193 processes).

Adding the 2125 VT-a processes (Vibration-Translation exchanges by atomic impact) has a noticeable effect on the flow fields (Fig. 4 compared to Fig. 3). The shock layer width decreases from 10.5 cm

to 8.5 cm, but the temperature peak decreases very little from 18,000 to 17,700 K. Interestingly, the high vibrational levels are more populated right behind the shock wave than they were without the VT-a processes, then most of the vibrational levels get depopulated faster in the shock layer when the VT-a processes are included (Fig. 4) than when they are not (Fig. 3).

3.5 VT-m + VT-m-D + VT-a + VT-a-D (2261 processes).

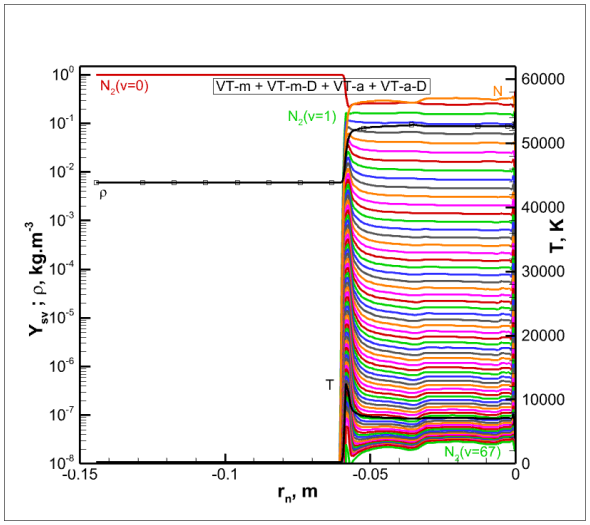

Figure 5: Temperature and mass fractions of N and N_2(v=0,67) along the stagnation line, obtained with 2261 processes (VT-m + VT-m-D + VT-a + VT-a-D). V_∞=6.19 km/s.

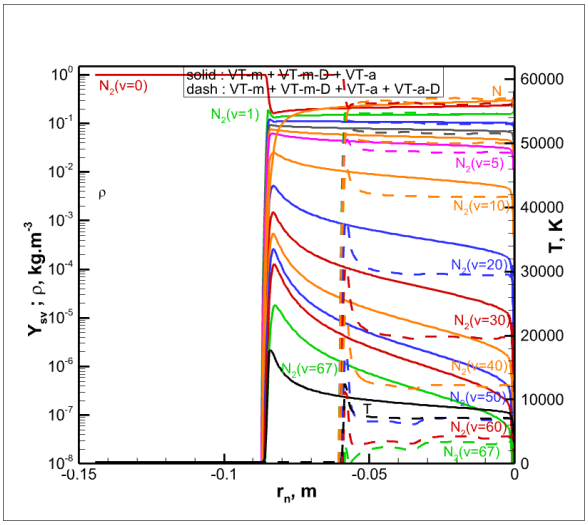

Figure 6: Temperature and mass fractions of N and N_2(v=0,67) along the stagnation line. Comparison between 2261 processes (VT-m + VT-m-D + VT-a + VT-a-D) and 2193 processes (VT-m + VT-m-D + VT-a). V_∞=6.19 km/s.

The addition of the 68 processes VT-a-D (VT processes by atomic impact leading to dissociation) makes the shock layer width decreases from 8.5 cm to 6 cm approximately and the temperature peak decreases from 17,700 to 12,500 K. As for the species densities, the various vibrational levels are strongly populated through the shock wave, then depopulate slightly right behind the shock wave. Interestingly, for this entry velocity, the vibrational levels remain populated and the nitrogen molecules do not dissociate completely – the mass fraction of N is far from being equal to unity as it can be for higher entry velocities–, likely because the temperature in the shock layer is not as high as in cases of higher entry velocities. A comparison of the results obtained with and without the VT-a-D processes is presented in Fig. 6, where only a few vibrational level population densities are displayed for clarity reasons.

3.6 Boltzmann diagrams

The Boltzmann diagrams that draw the densities of N_2(v) versus the energy of the vibrational levels expressed in eV are plotted at different positions along the stagnation line across the shock wave (positions 1 to 12 in Figs. 7 and 9) and across the boundary layer (positions A to L in Fig 8 and 10). The Boltzmann distribution is reached when the curves representing the level populations (or mass fractions) – expressed in logarithmic scale – versus the energies of the levels – expressed in linear scale – are linear. Results in Figs. 7 and 8 correspond to simulations done with the 68 processes VT-m + VT-m-D, while

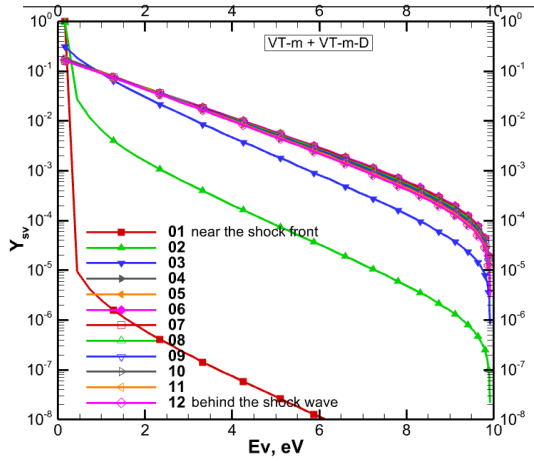

Figure 7: Boltzmann diagram at various positions across the shock wave, obtained with 68 processes (VT-m + VT-m-D). V_∞=6.19 km/s.

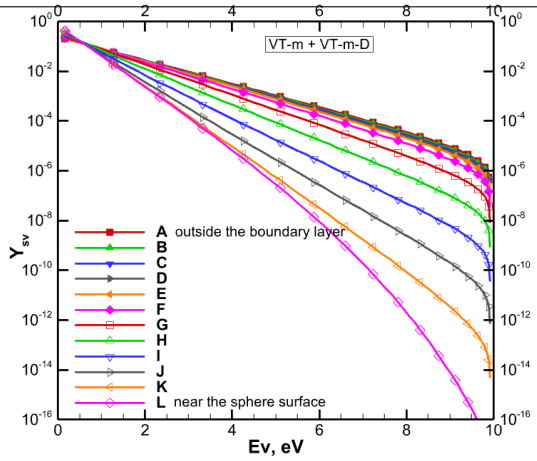

Figure 8: Boltzmann diagram at various positions across the boundary layer, obtained with 68 processes (VT-m + VT-m-D). V_∞=6.19 km/s.

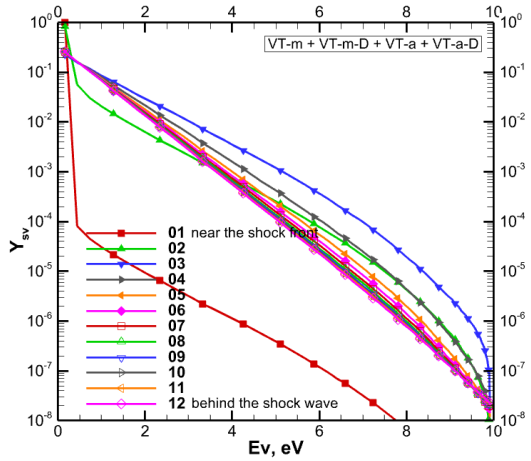

Figure 9: Boltzmann diagram at various positions across the shock wave, obtained with 2261 processes (VT-m + VT-m-D + VT-a + VT-a-D). V_∞=6.19 km/s.

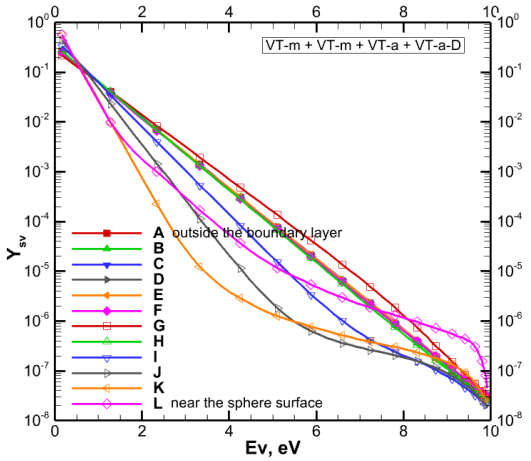

Figure 10: Boltzmann diagram at various positions across the boundary layer, obtained with 2261 processes (VT-m + VT-m-D + VT-a + VT-a-D). V_∞=6.19 km/s.

those in Figs. 9 and 10 correspond to simulations done with all the efficient processes (VT-m + VT-m-D + VT-a + VT-a-D).

In Figs. 7 and 8 – case (VT-m + VT-m-D) – the Boltzmann diagrams show that the Boltzmann distribution is not reached, as none of the curves are linear. On the other hand, for the case (VT-m + VT-m-D + VT-a + VT-a-D), the Boltzmann distribution is reached for the curves 07 to 12 (Fig. 9) that correspond to a few mm behind the shock front. The Boltzmann distribution is also reached outside of the boundary layer,

for the curves H to A, H corresponding to the distance of 2 mm from the stagnation point.
More results will be presented and analyzed in the oral presentation and in the paper.

4. Preliminary Conclusions

A vibrational-state specific model issued from the collisional radiative model CoRaM-N_2 implemented in the PINENS code was used for simulating the non-equilibrium flow past a sphere entering a Nitrogen atmosphere at 6.19 km/s. Vibrational-state population densities and temperature in the shock layer surrounding the sphere and particularly along the stagnation line were presented and analysed. The main conclusion is that the vibration-vibration exchanges through molecular impact, leading or not to dissociation, have very little effect on the population densities. On the other hand, clear evidence was shown of the progressive effect of the vibration-translation exchanges through molecular and atomic impacts. The study also showed that the Boltzmann distribution is obtained only in specific positions in the shock layer. Obtaining such results in reasonable computational time showed that it is possible to predict the vibrational level population distributions throughout an axi-symmetric shock layer with a detailed kinetics model.

Acknowledgements

Centre de Calcul Intensif d'Aix-Marseille is acknowledged for granting access to its high performance computing resources.

References and citations

[1] Park, C. (1988) "Assessment of a Two-Temperature Kinetic Model for Dissociating and Weakly Ionizing Nitrogen," *Journal of Thermophysics*, Vol. 2, No. 1, pp. 8–16.

[2] Park, C. (1993) "Review of Chemical-Kinetic Problems of Future NASA Missions, I: Earth Entries," *Journal of Thermophysics and Heat Transfer*, Vol. 7, No. 3, pp. 385–398.
doi:10.2514/3.431

[3] Armenise, I., Capitelli, M., and Gorse, C. (1998) "Nitrogen Nonequilibrium Vibrational Distributions and Non-Arrhenius Dissociation Constants in Hypersonic Boundary Layers," *Journal of Thermophysics and Heat Transfer*, Vol. 12, No. 1, pp. 45–51.
doi:10.2514/2.6300

[4] Pierrot, L., Yu, L., Gessman, R.J., Laux, C.O., and Kruger, C.H. (1999) "Collisional-Radiative Modeling of Nonequilibrium Effects in Nitrogen Plasmas," *AIAA 99-3478*, 30th AIAA Plasmadynamics and Lasers Conference, Norfolk, VA, June 28-July 1, 1999.

[5] Bultel, A., Chéron, B. G., Bourdon, A., Motapon, O., and Schneider, I.F. (2006) "Collisional-Radiative Model in Air for Earth Re-Entry Problems," *Physics of Plasmas*, Vol. 13, No. 4, Paper 043502.
doi:10.1063/1.2194827

[6] Esposito, F., Armenise, I., and Capitelli, M. (2006) "N - N2 State to State Vibrational-Relaxation and Dissociation Rates Based on Quasiclassical Calculations," *Chemical Physics*, Vol. 331, No. 1, pp. 1–8.
doi:10.1016/j.chemphys.2006.09.035

[7] Annaloro J., Bultel A., Omaly P. (2014) "Collisional-Radiative Modeling Behind Shock Waves in Nitrogen", *J. of Thermophysics and Heat Transfer*, Vol. 28, No. 4, pp. 608-622. doi: 10.2514/1.T4263.

[8] Druguet M.-C., Candler G.V., Nompelis I. (2005) "Effects of Numerics on Navier-Stokes Computations of Hypersonic Double-Cone Flows", *AIAA Journal*, Vol. 43, No. 3, pp. 616-623.

[9] Druguet, M.-C., Bultel, A., Morel, V., and Annaloro, J. (2019) "Non-equilibrium Nitrogen Re-entry Flow Computed with a Vibrational-Specific Kinetics Model", *AIAA 2019-2283*, doi: 10.2514/6.2019-2283.

NEGF26-694060

SPACE CHARGE COMPENSATION OF HYDROGEN ION BEAMS: A PARTICLE-IN-CELL STUDY

Benzi John[1*], Kiran Jonathan[1], Olli Tarvainen[2], Erin Flannigan[2], Daniel Faircloth[2] and David Emerson[1]
[1]Scientific Computing Department, STFC Daresbury Laboratory, Warrington, United Kingdom.
benzi.john@stfc.ac.uk
[2]ISIS Neutron and Muon Source, STFC Rutherford Appleton Laboratory, Didcot, United Kingdom.

KEY WORDS

Space Charge Compensation, Hydrogen Ion beams, Particle-in-cell, Plasma.

ABSTRACT

Hydrogen ion sources are extensively used in particle accelerators worldwide for a range of applications, such as high-energy particle physics at CERN and in spallation neutron source facilities like the ISIS Neutron and Muon Source. A typical problem encountered in the low energy beam transport (LEBT) region of such particle accelerators is beam divergence and transport losses due to space charge effects. Space Charge Compensation (SCC) is a process that helps to minimise transport losses by lowering the space charge of the ion beam. In the SCC process of a negative hydrogen ion beam, the H^- beam ionises the background gas, trapping positive ions within the negative beam forming a low-density "beam-plasma" [1]. A joint experiment-simulation campaign is currently underway to study the space charge compensation process to support ISIS operations and upgrades to the facility in the ion source regions. The authors recently studied the effect of magnetic field on the SCC process of a H^- ion beam [2]. The focus of the present study is to investigate the SCC process of both positive and negative hydrogen ion beams under various operating conditions using the Particle-in-Cell (PIC) method.

The Particle-in-Cell technique is a high-fidelity tool to study the kinetic properties of plasmas from first principles and is well-suited for coupling electromagnetic fields with the transport and collision of neutral and charged particles. The PIC simulations to study the SCC process have been carried out using the well-established, open-source code, PICLas [3]. PICLas enables high-fidelity, large-scale three-dimensional simulations using high-performance computing (HPC) and is well suited for a wide range of applications involving plasma simulations and non-equilibrium rarefied gas flows. To enable the current work, PICLas has been customised with the multi-reaction and cross-section-based chemistry framework to handle the chemical reactions associated with the SCC process of negative hydrogen ion beams [2].

A three-dimensional electrostatic PIC model has been considered here for investigating the space charge compensation of negative hydrogen ion beams. An example of a three-dimensional computational grid representation of a LEBT region is shown in Fig. 1. To enable a H^- beam passing centrally through this domain, beam particles are emitted from the entrance of the domain at a uniform

* Corresponding author

density corresponding to the beam properties (typically 65 keV, 30 mA with a beam radius of 2.5 cm). Open Neumann boundary conditions have been considered at the beam entrance and exit, while all other boundaries are grounded.

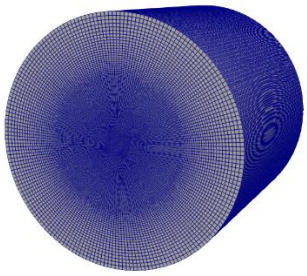

Figure 1: 3D computational grid employed for the simulations.

The H^- beam interacts with a background hydrogen gas at a constant background gas pressure. Typical operating pressures in the LEBT region are of the order of 10^{-5} mbar, implying highly rarefied non-equilibrium conditions. Interactions of the beam with the H_2 gas is modelled using the Monte Carlo Collision (MCC) model. To study the effect of a magnetic LEBT, a uniform background magnetic field (B=0.35T) along the direction of beam propagation is considered. A multi-reaction framework is considered (Eqs. (1-3)) with cross-section-based chemistry models, which produces secondary electrons, compensating H_2^+ particles, and neutral H particles. To ensure accuracy, the smallest cell sizes considered for the simulation are a fraction of the Debye length and the time step considered is much smaller than the inverse of the plasma frequency, typically of the order of 10^{-10} s.

$$H^- + H_2 \rightarrow H^- + H_2^+ + e^- \quad (1)$$
$$H^- + H_2 \rightarrow H + H_2 + e^- \quad (2)$$
$$e^- + H_2 \rightarrow H_2^+ + 2e^- \quad (3)$$

The three-dimensional particle distribution of all species at steady state for a compensated beam due to the interaction of the beam with a background H_2 gas and the presence of a uniform magnetic field is shown in Fig. 2. The compensating positive ions are effectively bound to the magnetic field lines, which helps in their confinement within the beam. Illustrative simulation results showing H^- beam number density of an uncompensated beam due to space charge effects and corresponding results for a compensated beam due to the interaction with a background gas and the production of compensating positive ions is shown in Fig. 3. Future work will compare the SCC process of a negative hydrogen ion beam with a positive hydrogen ion beam for a wide range of operating conditions.

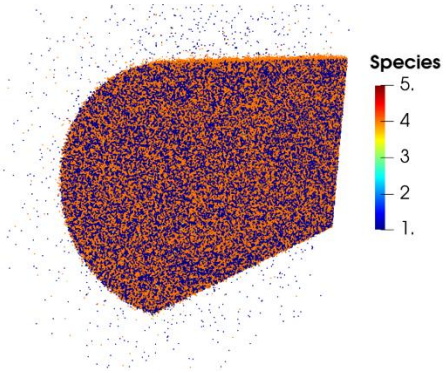

Figure 2: H_2^+ Particle accumulation at steady state within the beam. Species colour: 1=H^-, 3=electron, 4=H_2^+, 5=H.

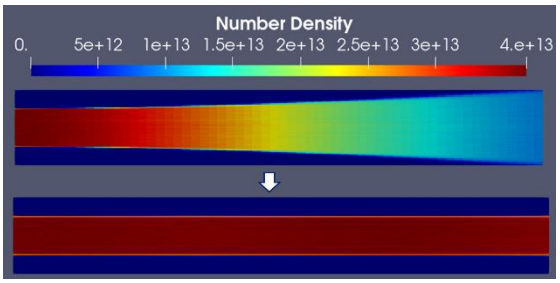

Figure 3: H^- beam number density of an uncompensated beam (top) and for a compensated beam (bottom).

Acknowledgments

This work has been supported by an International Science Partnerships Fund grant awarded by UK Research and Innovation and STFC's Ada Lovelace Centre. The authors also acknowledge the use of resources provided by the Isambard 3 Tier-2 HPC Facility.

References and Citations

[1] Valerio-Lizarraga, C. A., Leon-Monzon, I., & Scrivens, R. (2015). Negative ion beam space charge compensation by residual gas, *Phys. Rev. ST Accel. Beams* 18, 080101.

[2] John, B., Jonathan, K., Tarvainen, O., Flannigan, E., Faircloth, D., & Emerson, D. (2025). Effect of magnetic field on space charge compensation in negative hydrogen ion beams: a computational study, *J. Instrumentation* 20, C05024.

[3] Fasoulas, S., Munz, C., Pfeiffer, M., Beyer, J., Copplestone, T., Mirza, A., Nizenkov, P., Ortwein, P., & Reschke, W. (2019). Combining particle-in-cell and direct simulation Monte Carlo for the simulation of reactive plasma flows, *Phys. Fluids* 31, 072006.

NEGF26-684533

THE KEY ROLE OF NON-EQUILIBRIUM GAS FLOWS ON EDGE PLASMA BEHAVIOR AND EXHAUST EFFICIENCY IN NUCLEAR FUSION REACTORS

Stylianos Varoutis[1], Georg Schlisio[1], Dieter Boeyaert[2], Christopher C. Klepper[3], Felix Warmer[1] and W7-X Team*
[1]Max Planck Institute for Plasma Physics, 17491 Greifswald, Germany
[2]Department of Nuclear Engineering and Engineering Physics, University of Wisconsin-Madison, US
[3]Oak Ridge National Laboratory, Oak Ridge, Tennessee, US
*see author list in O. Grulke et al., Nuclear Fusion 64 (2024) 112002
stylianos.varoutis@ipp.mpg.de

KEY WORDS

Wendelstein 7-X, stellarator, ITER, tokamak, particle exhaust, vacuum pumping, DSMC method, neutral gas dynamics, kinetic models

ABSTRACT

The control of neutral particle dynamics in the edge and divertor regions is one of the critical challenges in the operation of magnetic confinement fusion devices, including tokamaks and stellarators. In these regions, where plasma interacts with material boundaries, the gas density can drop by several orders of magnitude relative to the core plasma. Under such conditions, the mean free path of neutral particles becomes comparable to or even larger than characteristic geometrical dimensions such as the divertor pumping port width. This transition from continuum to non-continuum behavior defines the regime of rarefied gas flows, which plays a fundamental role in determining particle recycling, neutral exhaust, impurity transport, and overall plasma confinement performance.

In fusion devices the complexity of rarefied flow phenomena is particularly pronounced. ITER's divertor must handle exhaust power exceeding 10 MW/m^2, while maintaining sufficient neutral pumping efficiency to remove helium ash and tritium. The narrow geometry of its pumping ducts, combined with the high degree of vacuum required, creates flow conditions that are strongly rarefied, with Knudsen numbers spanning the transitional to free-molecular regimes. Similarly, Wendelstein 7-X, with its fully three-dimensional magnetic configuration and modular divertor design, exhibits non-uniform neutral pressure and particle recycling patterns that can only be accurately captured through kinetic or hybrid modeling approaches. These features make rarefied flow modeling indispensable to predicting the behavior of neutral atoms and molecules that escape the confined plasma and interact with plasma-facing components.

Traditional fluid models, based on continuum assumptions, cannot capture the essential characteristics of these flows, as the molecular collisions are insufficient to maintain local thermodynamic equilibrium. Consequently, the Boltzmann transport equation must be solved or approximated through numerical schemes. In the context of fusion research, one of the most widely used approaches is the Direct Simulation Monte Carlo (DSMC) method [1], which statistically samples particle trajectories and

collisions to approximate the solution of the Boltzmann equation under rarefied conditions. DSMC simulations can resolve local variations in density, temperature, and velocity distributions that are inaccessible to macroscopic fluid descriptions. This method has been successfully applied to model neutral gas behavior in various tokamak and stellarator devices and pumping systems, providing insight into molecular backflow, pressure distribution, and the efficiency of cryogenic pumping schemes.

A central component of integrated modeling in fusion edge physics is the coupling of plasma fluid solvers with neutral kinetic codes. The SOLPS-ITER for tokamak devices [2] as well as EMC3-EIRENE [3,4,5] packages represent a state-of-the-art example of this approach, where a multi-fluid magnetized plasma code is dynamically coupled with the EIRENE Monte Carlo solver [6] for neutrals. EIRENE is based on the classical BGK kinetic model and tracks the trajectories and collisions of neutral atoms and molecules, including charge-exchange and ionization events, while B2.5 or EMC3 respectively compute the plasma background fields. This coupling enables a self-consistent description of plasma–neutral interactions, incorporating both continuum and rarefied flow regimes within the same computational framework.

When EIRENE code is applied with a velocity-independent collision frequency, the classical BGK model fails to accurately determine the transport coefficients' ratio, specifically the ratio of thermal conductivity to viscosity. As a result, employing the classical BGK kinetic model yields a Prandtl number of unity for a monoatomic gas, rather than the expected 2/3. Consequently, the classical BGK kinetic model is typically applied only for isothermal and pressure-driven flows. This limitation of the EIRENE highlights the necessity for alternative numerical methods that can more precisely describe non-isothermal conditions, as anticipated in the exhaust system of a fusion reactor.

An alternative to EIRENE is the DIVertor GAs Simulator (DIVGAS) [7,8], which offers a powerful and reliable framework for optimizing and evaluating the particle exhaust in fusion reactors. The DIVGAS framework features two powerful solvers, a deterministic and a stochastic one, which require a plasma background as boundary conditions. The stochastic module is based on the DSMC method, while the deterministic module on the Discrete Velocity Method (DVM) [9]. Both methods accurately capture neutral gas behavior across the entire range of collisionality, establishing DIVGAS as the leading tool for plasma exhaust research. Within the European Fusion program, DIVGAS has been validated based on experimental results from JET [8] and W7-X [10,11] and has been employed in modelling the particle exhaust of JT60-SA [12] and DEMO [13,14] fusion devices.

Beyond the core plasma–neutral coupling, rarefied flows play a key role in determining tritium retention and material erosion. Under transitional flow conditions, the rate of particle re-deposition and molecular desorption from divertor surfaces depends sensitively on the local accommodation coefficients and surface temperature. These effects influence the lifetime of plasma-facing components and the overall tritium inventory, a major safety and regulatory concern for next-generation reactors. Understanding these interactions requires a comprehensive combination of kinetic simulations, experimental diagnostics, and material surface studies.

Within this context, as highlight of this paper is the numerical study on the neutral transport of fuel gas (H_2) along with seeding impurities (Ar, Ne) and helium in the W7-X sub-divertor is presented. This is accomplished using the DSMC solver within the DIVGAS workflow. Figure 1 shows the evolution of the helium partial pressure in the sub-divertor as a function of the incoming helium concentration at the inlet pumping gap. The results indicate a non-linear dependence of the sub-divertor helium partial pressure on the inlet helium concentration, whereas the molecular hydrogen pressure remains nearly independent of it. In addition, the comparison with experimental measurements shows reasonable agreement. The simulations aim to estimate key macroscopic parameters, such as partial pressure, temperature, and molar fraction for each gas species. The results provide valuable insights into neutral impurity transport in the W7-X sub-divertor and its implications for exhaust performance. These

findings offer practical guidelines for optimizing the current design along with the qualitative and quantitative agreement between numerical and experimental data [15, 16].

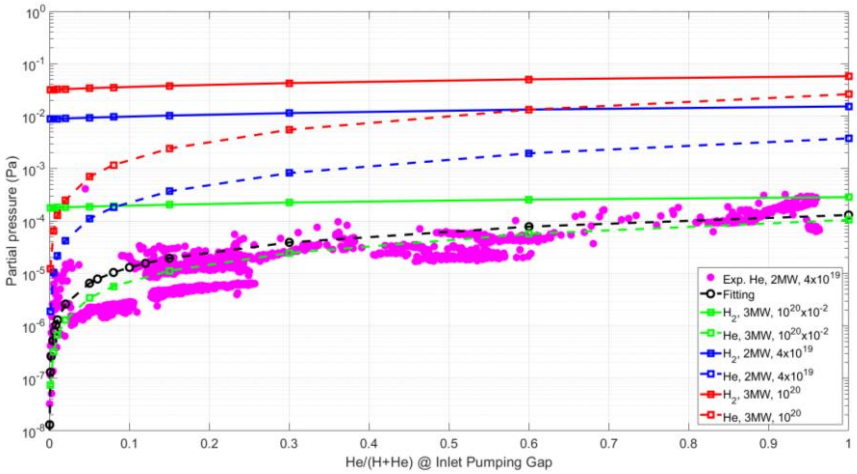

***Figure 1**: Evolution of helium partial pressure in the sub-divertor as a function of the incoming helium concentration at the inlet pumping gap.*

As fusion research advances toward reactor-scale devices capable of steady-state operation, the importance of rarefied gas dynamics will only increase. Future reactors such as SPARC, ITER and DEMO will demand even greater exhaust efficiency and tighter control of impurity sources, both of which depend on the detailed understanding of gas flow behavior in non-continuum regimes. The continued development of hybrid plasma–neutral modeling frameworks, improved algorithms with adaptive mesh refinement, and validated experimental diagnostics for rarefied regimes will be essential for meeting these challenges.

In summary, the study of rarefied gas flows in tokamaks and stellarators reactors, forms a critical foundation for achieving effective exhaust, stable detachment, and safe tritium management in magnetic confinement fusion. Integrating rarefied flow physics into reactor design and operational strategies—through advanced numerical simulations and targeted experiments—will play a decisive role in the realization of reliable, long-duration fusion power.

References

[1] Bird, G. A., *Molecular gas dynamics and the direct simulation of gas flows*. New York: Oxford Science Publications, Oxford University Press Inc., (1994).
[2] Pshenov, A. A., Bonnin, X., Pitts, R. A., SOLPS-ITER simulations of the ITER divertor with improved plasma-facing component geometry, Nuclear Materials and Energy, 42, 2025.
[3] Feng, Y., et al., Recent improvements in the EMC3-eirene code, Contributions to Plasma Physics 54.4-6, 426-431, 2014.
[4] Winters, V., et al, EMC3-EIRENE simulation of first wall recycling fluxes in W7-X with relation to H-alpha measurements, Plasma Phys. Control. Fusion, 63 045016, 2021.
[5] Boeyaert, D., et al., Analysis of the neutral fluxes in the divertor region of Wendelstein 7-X under attached and detached conditions using EMC3-EIRENE, Plasma Phys. Control. Fusion, 66, 015005, 2023.
[6] Reiter D., Baelmans M. and Börner P., The EIRENE and B2-EIRENE codes Fusion Sci. Technol. 47 172–86, 2005.
[7] Varoutis, S., Igitkhanov, Y., Day, C., Effect of neutral screening on pumping efficiency in the DEMO divertor, Fusion Engineering and Design, 146, 1741-1746, 2019.
[8] Varoutis, S., et al., Simulation of neutral gas flow in the JET sub-divertor, Fusion Engineering and Design, 121, 13-21, 2017.

[9] Valougeorgis, D., Naris, S., Acceleration Schemes of the Discrete Velocity Method: Gaseous Flows in Rectangular Microchannels, SIAM Journal on Scientific Computing, 25(2), 2003.
[10] Varoutis, S., et al., Numerical analysis of gas exhaust in Wendelstein 7-X using the Direct Simulation Monte Carlo method, Nuclear Fusion, 65(7), 2025.
[11] Varoutis, S., et al., Numerical simulation of neutral gas dynamics in the W7-X sub-divertor, Nuclear Fusion, 64(7), 2024.
[12] Gleason-Gonzalez, C., Varoutis, S., et al., Simulation of collisional effects on divertor pumping in JT-60SA, Fusion Engineering and Design, 109, 693-699, 2016.
[13] Varoutis, S., Igitkhanov, Y., Day, C., Assessment of the 3D geometrical effects on the DEMO divertor pumping efficiency, Nuclear Materials and Energy, 19, 120-123, 2019.
[14] Varoutis, S., Igitkhanov, Y., Day, C., Optimization of pumping efficiency and divertor operation in DEMO, Nuclear Materials and Energy, 12, 668-673, 2017.
[15] S Varoutis et al., Numerical assessment on the impurity transport in the W7-X particle exhaust, 31st IEEE Symposium on Fusion Engineering (SOFE) (2025).
[16] S Varoutis et al., Numerical assessment of He exhaust in the W7-X stellarator and comparisons to first, time-resolved experimental data, submitted to Nuclear Fusion (2025).

NEGF26-686055

THE USE OF THE THERMOPHORETIC FORCE FOR AEROSOL PARTICLE SEPARATION

Jobic Y.*[1], Topin F.[1], Romero-Deza A.[1,2], Rojas-Cardenas M.[2], Colin S.[2], Baldas L.[2], Magaud P.[2], Raimbault V.[3], Camps T.[3], Graur I.[1]

[1]Aix-Marseille Université, CNRS, IUSTI UMR 7343, Marseille, France
[2] Univ Toulouse, CNRS, IMT Mines Albi, INSA Toulouse, ISAE-SUPAERO, Institut Clément Ader (ICA), Toulouse, France
[3]LAAS, CNRS, Toulouse, France
*yann.jobic@univ-amu.fr

KEY WORDS

Aerosol particle, thermophoretic force, temperature gradient, gas flow at small scale

ABSTRACT

The conception of a micro-separator for aerosol particles based on the thermophoretic effect is proposed. The first step in designing of such a micro-device is the development of a mathematical model. A three-dimensional model of a mini-channel (millimetric size) is proposed, and several key parameters are tested, including the length and width of the mini-channel, the intensity of the temperature gradient, and the velocity of the carrier gas. The next steps will be the fabrication of a mini-prototype followed by experimental testing of its efficiency. Ultimately, the final micro-device will be manufactured and tested.

Introduction

Aerosols are defined as suspensions of solid particles or liquid droplets in a gas. They originate from both natural and anthropogenic sources and can be harmful to the environment and to human health. Separating particulate matter using a microfluidic device for concentration measurements and analysis is therefore of primary importance for both indoor and outdoor applications. Aerosol particle sizes range from the nanometric to the micrometric scale. Aerosols with diameters smaller than 2.5 μm (PM2.5) can reach deep into the lungs, causing oxidative stress and respiratory diseases.
This work aims to develop a microfluidic thermophoretic separator for aerosol particles in the 0.01-2.5 μm range. The thermophoretic separation principle [1] is especially attractive because particle trajectories can be deflected simply by locally heating the surrounding gas - without moving parts. A microfluidic separator can be a strong asset for measuring global and local aerosol concentrations. It is cost-effective

* Corresponding author

and can be deployed in large numbers at strategic locations. This will facilitate the creation of health- and environmental-related databases. A microscale device also reduces the required particle quantity and measurement time. The microfluidic device will be capable of separating different types of aerosols based on particle size, mass density and thermal conductivity. To our knowledge, most efforts toward developing lab-on-a-chip thermophoretic particle separator have focused on liquid flows [2], [3]. Very few attempts have been made to downscale gas flow separator to the millimetric or micrometric range. The only related work was carried out at the University of California, Berkeley, where a microfluidic air sensor for airborne particles (25mm x 21 mm x 2 mm footprint) was developed. The thermophoretic principle was used to deposit particles onto the surface of a mass-sensitive film bulk acoustic resonator, while the main particle separation relied on a virtual impactor [4, 5].

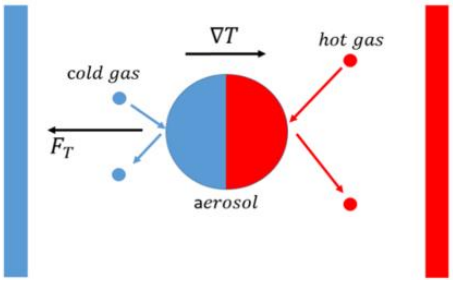

Figure 1: Thermophoretic effect on a particle

Numerical modelling

The entire mini-separator device, including the heated/cooled solid blocks, entrance section, the mini-channel and the exit section for separated particles, is modeled.
Three dimensional simulations of the carrier gas flow with aerosol particles inside a mini-channel are performed. Various geometrical configurations and dimensions are tested to determine the optimal design - a channel with a square cross-section of 1mm^2 and a length of 4mm. The channel walls are maintained at two different temperatures, T_{hot} and T_{ref}, (room temperature), thus creating the desired temperature gradient. The simulations are carried out using the commercial software Star-CCM+.
The flow is modeled with the unsteady Navier-Stokes equations, solved implicitly for stability reasons. The gas density is computed using the ideal gas law, relating it to the temperature and pressure. The heat conduction equation is solved in the solid parts coupled with the conjugate heat transfer with the gas phase.
The motion of aerosol particles in the air flow, injected uniformly at the device inlet, is simulated using a Lagrangian approach. In the low-concentration conditions considered here, the particle-particle interactions and the gas displacement due to particles are negligible. The thermophoretic and drag forces acting on the particles are taken computed using a user-defined function implementing the most widely used expressions in the literature [6], [7]. Gravity, oriented along the main flow direction, is also included, as it may impact particles trajectoires when residence times of the particles are sufficiently long.

Results and discussion

The temperature gradient normal to the flow direction induces a thermophoretic force that deflects aerosol particles towards the cold side, resulting in particles separation, see Fig. 1. Simulations of the gas flow with particles of different sizes show that particle diameter has the strongest influence on deviation, with

maximum displacement observed for particles with a radius of approximately 1 μm under the present conditions.
However, to improve separation efficiency, the initial particle position must also be controlled. This is accomplished by focusing the particles in the center of the channel starting from the inlet section. A new entrance section is therefore added, equipped with two side channels delivering additional carrier gas flow to concentrate the particle stream at the centerline (see Fig. 2). A series of tests is considered to find the optimal mass flow rate in focalisation channels to ensure centered particle entry into the mini-channel. After the focalization section, the second part of the channel applies the thermal gradient, which induces thermophoretic deviation. Different hot wall temperatures are tested to analyse the influence of the temperature gradient intensity on particle displacement. The exit section, containing two outlet channels, is positioned such that the most largely displaced particles reach the cold wall. This position depends on the gas mass flow rate, the temperature gradient, and the particle size. To enhance sorting performance, a slight pressure difference is applied between the two outlets. Our results show that particles between 1 μm to 10 μm are effectively separated, see top left of Fig. 2.

Conclusion

The first step in the development of the thermophoretic aerosol particle micro-separator has been carried out. The optimal dimensions of the mini-channel have been identified, and key flow parameters, such as the applied temperature gradient and carrier gas velocity, have been optimized. The next steps involve the fabrication of the prototype and testing its performance under laboratory conditions.

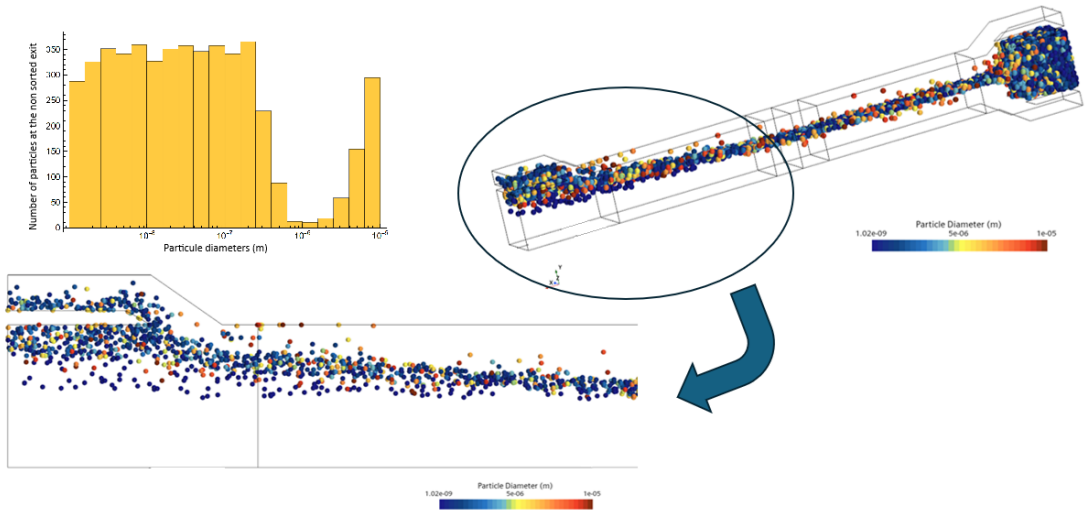

Figure 2: Mini-channel with focalisation part

Acknowledgements

The authors thank the ANR project AERATOR ANR-23-CE04-0002-02 for financial support of this research work.

References and citations

[1] R. Saxton, W. Ranz, Thermal force on an aerosol particle in a temperature gradient, Journal of Applied Physics 23 (8) (1952) 917–923.
[2] P. Greelhoed, R. Lindken, J. Westerweel, Thermophoretic separation in microfluidics, Chemical Engineering Research and Design 84 (5) (2006) 370–373.
[3] S. Choe, B. Kim, M. Kim, Progress of microfluidic continuous separation techniques for micro-/nanoscale bioparticles, Biosensors 11 (11) (2021) 464.
[4] I. Paprotny, F. Doering, P. Solomon, R. M. White, L. A. Gundel, Microfabricated air-microfluidic sensor for personal monitoring of airborne particulate matter: Design, fabrication, and experimental results, Sensors and Actuators A 201 (2013) 506–516.
[5] D. Fahimi, O. Mahdavipour, J. Sabino, R. White, I. Paprotny, Vertically-stacked MEMS $PM_{2.5}$ sensor for wearable applications, Sensors and Actuators A 299 (2019) 111569.
[6] J. R. Brock, On the theory of thermal forces acting on aerosol particles, Journal of colloid sciences 17 (1962) 768–780.
[7] R. A. Millikan, Coefficients of slip in gases and the law of reflection of molecules from the surface of solids and liquids, Phys. Rev. 21 (1923) 217–238.

NEGF26-684971

THERMAL AND GAS-SURFACE INTERACTION EFFECTS IN RAREFIED RAYLEIGH-BÉNARD CONVECTION

Sanjana Rao[1], Krishnansh B Chandarana[1], Shesh N Dhurandhar[1], A Sameen[1,2]
[1]Department of Aerospace Engineering, Indian Institute of Technology Madras, Chennai 600036, India
ae23d006@smail.iitm.ac.in
[2]Geophysical Flows lab, Indian Institute of Technology Madras, Chennai 600036, India
sameen@smail.iitm.ac.in

KEY WORDS

Gas-Surface Interaction, Heat Transfer, Non-Continuum, DSMC

ABSTRACT

Rayleigh-Bénard convection (RBC) is a buoyancy-driven flow that arises in a fluid domain between a heated and cooled region. It has been widely studied in heat transfer and finds applications in MEMS devices, spacecraft reentry, etc. These applications cover both continuum as well as non-continuum regimes. In the non-continuum regime, much of the research has focused on identifying the stability boundaries (neutral curve) that separate the pure conductive heat transfer state from the onset of convection. The onset of convection is usually governed by the Rayleigh number (Ra). However, in the rarefied regime, using the Chapman-Enskog approximation for low Knudsen numbers, it has been found that the Rayleigh number is a function of the Knudsen number (Kn), the Froude number (Fr) and the temperature ratio (r) [1, 2].

$$Ra = \frac{512}{75\pi}\frac{(1-r)}{r}\frac{1}{Fr\,Kn^2} \tag{1}$$

Here, $r = T_c/T_h$ is the temperature ratio, where T_h and T_c are the temperatures of the hot and cold walls respectively, $Kn = \lambda/H$, where λ is the mean free path and $Fr = V^2/gH$, where V is the velocity, g is gravitational acceleration and H is the distance between the hot and cold walls. Thus, the stability boundaries for a particular temperature ratio are determined on the Kn-Fr plane [2, 3, 4, 5]. While the critical Rayleigh number Ra_{cr}, which marks the transition from conductive to convective heat transfer is 1708 for no-slip flows with isothermal boundaries, it has been found to increase to 1770±15 for slip flows with diffuse boundaries. The instability region for each Kn is confined to a small range of Fr. It has been shown from linear stability analysis as well as physical reasoning that rarefaction has a dampening or stabilizing effect on convection [3]. Thus for a fixed temperature ratio, there is a maximum Knudsen number beyond which instabilities do not lead to convection. For a constant heat flux boundary, which provides a destabilizing effect, the Ra_{cr} has been found to reduce to 720 [3]. Ben-Ami & Manela [3] found that when implemented, the constant heat flux boundary condition has a wider instability region that extends to higher Kn and lower Fr numbers.

In the slip or transition flow regime, molecular interactions play an important role in defining heat exchange and dynamics. Molecular behavior at surfaces is modeled using various GSI models, which dictate how molecules reflect and exchange energy with surfaces. In this work, we investigate non-continuum Rayleigh-Benard Convection using the Direct Simulation Monte Carlo (DSMC) method [6]. Specifically, we study the effect of isothermal and heat flux boundary conditions along with various Gas Surface Interaction (GSI) kernels as listed in Table 1, the effect they have on the stability margins (neutral curves) and heat transfer characteristics of the system.

Numerical Methodology

DSMC is a stochastic approach in which a large number of particles move and collide just as physical molecules do. It obtains a solution to the Boltzmann equation. Here, a single particle can represent a large number of molecules based on a particle weighting (f). DSMC decouples molecular motion and collisions by using time steps smaller than the mean collision time. Molecules move first, then collisions between nearby particles are probabilistically computed based on collision models from kinetic theory.

Molecular interactions at surfaces are represented using GSI models such as specular, fully diffuse, partially diffuse (Maxwell model), and Cercignani–Lampis–Lord (CLL) [7], which define how molecules reflect and exchange energy with the surface. The accommodation coefficient α representing the degree of equilibration between the incident molecules and the wall is dependent on several factors such as gas species, wall material, temperature of gas and wall, lattice arrangement of the wall, Kn, bulk gas velocity, etc. Combinations of thermal boundary conditions and GSI are examined, as summarized in Table 1.

Thermal BC	**Gas–Surface Interaction (GSI) Kernels**				
Isothermal	Specular $\alpha = 0$	Fully Diffuse $\alpha = 1$	Partially Diffuse $\alpha = 0.8$	CLL1 (Rough Surface) $\alpha_T = 0.9, \alpha_n = 1$	CLL2 (Clean Surface) $\alpha_T = 0.2, \alpha_n = 0.4$
Const. Heat Flux					

Table 1: Thermal boundary conditions and Gas-Surface Interaction (GSI) kernels along with their specific accommodation coefficients used at the hot and cold walls.

The constant heat-flux boundary condition is implemented, as given by Ben-Ami & Manela [3]. The wall temperature is not known a priori. To impose a prescribed heat flux, mass and energy conservation between incident and reflected molecules is enforced every timestep. Reflected velocities are adjusted such that the net energy exchange matches the specified heat flux, allowing dynamic determination of the wall temperature at each time step. The formulation for the determination of wall temperature for fully diffuse GSI is shown in Equation 2

$$T = \frac{1}{2R}\left\{\frac{\mathcal{H}^*_{\text{in}} + q^*_w}{\mathcal{M}^*_{\text{in}}} - \frac{u^{*2}_{g,\text{in}}}{8}\right\}_{(t_i,x_j)}. \tag{2}$$

Here, $\mathcal{M}^*_{\text{in}}(t_i, x_j)$, $u^*_{g,\text{in}}(t_i, x_j)$, and $\mathcal{H}^*_{\text{in}}(t_i, x_j)$ denote the macroscopic incoming mass flux, gas velocity, and energy flux per unit mass, respectively. The same underlying principle is extended to develop the formulations for the determination of wall temperatures in the case of partially diffuse and Cercignani–Lampis–Lord (CLL) GSI models.
In this study, we use the 2D numerical setup of Stefanov *et al.* [2] with an aspect ratio $L/H = 2$, where L and H are the length and height of the domain, respectively. The top ($y = 1$) and bottom ($y = 0$) walls are the cold and hot walls, respectively as illustrated in Fig. 1a. The boundary conditions at the top and

bottom boundaries are as shown in Table 1. Periodic boundary conditions are applied at the side walls. A temperature ratio, $r = 0.1$ is used with hot wall temperature $T_h = 160K$. For the isothermal case, the temperatures are prescribed at the walls. For the constant heat-flux case, a constant heat flux obtained from the inversion of Equation (2) is imposed at the hot and cold walls, q_h and q_c. Argon is used as the working gas, and molecular collisions are modeled using the variable hard-sphere (VHS) model. A fixed Prandtl number $Pr = 2/3$ is used. An acceleration of (0,-g) is applied on the particles based on the Fr. The DSMC solver SPARTA [8] is used in this study. The computational domain is discretized such that $\Delta x < \lambda/3$ and the timestep $\Delta t < min(MCT, MTT)$ where MCT and MTT are the Mean Collision Time and the Mean Transition Time, respectively.

Results

Validation of the computational setup is done by comparing the present results with those of Stefanov *et al.* [2]. The line-averaged, non-dimensional density profiles along the height of the domain height are shown in Fig. 1 for three (Kn, Fr) pairs using isothermal, fully diffuse top and bottom boundaries.

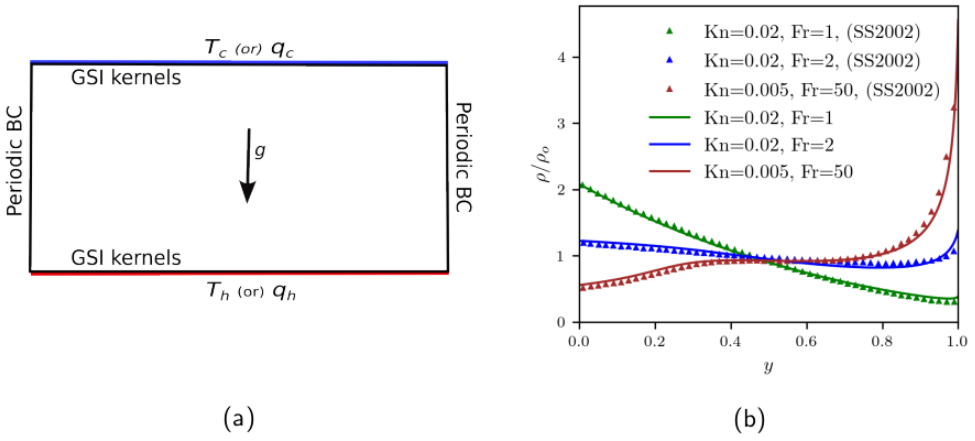

Figure 1: (a) Computational domain with hot and cold walls prescribed by temperatures T_h and T_c (isothermal setup) or by constant heat fluxes q_h and q_c (constant heat-flux setup). (b) Comparison of present results (solid lines) with those of Stefanov *et al.* [2] (SS2002) (symbols) for Kn = 0.02, Fr = 1 and 2, and Kn = 0.005, Fr = 50.

The influence of surface roughness on instability is first examined using isothermal wall conditions with varying GSI. It is observed that both the temperature jump and velocity slip increase as α decreases, indicating lesser equilibration of molecules with the wall. For instance, a transition from a fully diffuse GSI to a partially diffuse GSI with $\alpha = 0.8$ results in more pronounced slip and temperature jump effects. A lower α, corresponding to a cleaner or less accommodating surface, can enhance and promote the onset of flow instability. This behavior could be attributed to weaker momentum and thermal interaction between the gas and the wall, which reduces the stabilizing (damping) influence of the wall on the flow. Thus, a cleaner surface, such as the CLL2 GSI model, could enhance convection and change the onset of instability.
This behavior is illustrated in Fig. 2, where the flow at Kn = 0.02 and Fr = 10.5 is identified to remain in purely conductive state for isothermal fully diffuse boundaries based on a Nusselt number close to unity, the absence of bulk motion and circulation patterns, and nearly horizontal isotherms, while the isothermal CLL clean boundaries exhibit a transition to convection.

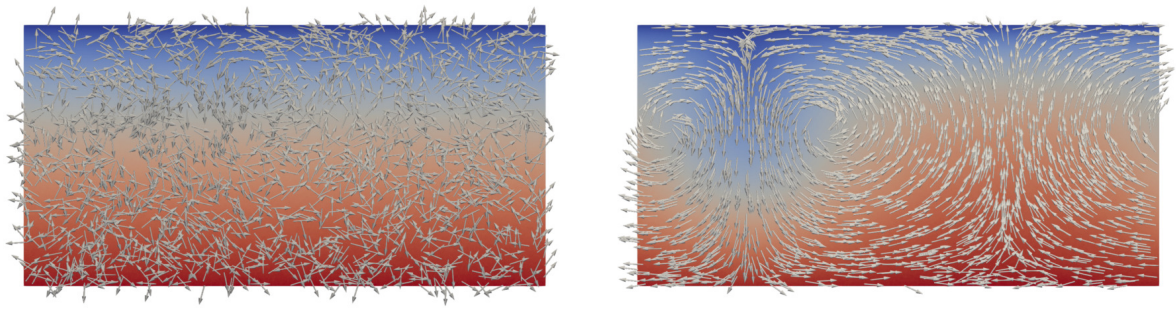

(a) (b)

Figure 2: Velocity vector fields overlaid on temperature contours for Kn = 0.02 and Fr = 10.5, comparing (a) fully diffuse and (b) CLL2 (clean) GSI models.

A similar trend is observed when the thermal boundary condition is changed from isothermal to constant heat flux, as reported. Constant heat-flux, fully diffuse boundaries are found to enhance convection compared to isothermal, fully diffuse boundaries. In Fig. 3, the neutral curve separating the conduction and convection regimes is shown. For each Knudsen number, the critical Froude number marking the transition between conduction and convection regimes is indicated.
First, when comparing GSI models under isothermal boundary conditions, the CLL2 GSI model widens the neutral curve to higher Fr values for each Kn. It also slightly increases the maximum Kn limit at which convection can develop for a given temperature ratio, r. Next, comparing isothermal and constant heat flux boundaries for the fully diffuse GSI, the neutral curve both widens as well as increases in height. There is no single neutral curve for non-continuum RBC. Previous studies have shown that the neutral curve depends on parameters such as the temperature ratio, collision model, Prandtl number, and thermal boundary condition [2, 5]. Here, we demonstrate that gas-surface interaction effects, combined with thermal boundary conditions, significantly influence the onset and sustenance of instability.

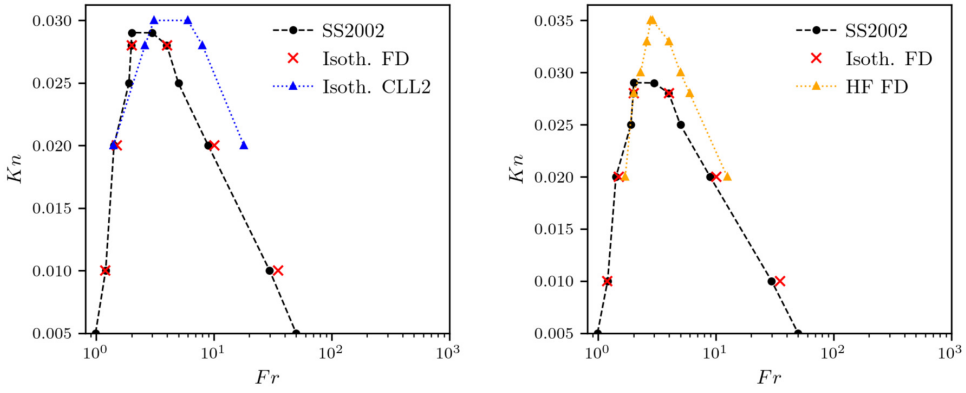

(a) (b)

Figure 3: Comparison of neutral curves for (a) fully diffuse and CLL2 GSI models under isothermal conditions and (b) different thermal boundary conditions (isothermal vs. constant heat-flux) for fully diffuse walls.

The heat transfer characteristics, particulary, the variation of bulk, hot and cold wall Nusselt number with GSI models, thermal boundary condition, Knudsen number and Froude number, as well as the complete

set of neutral curves for all combinations of thermal boundary conditions and GSI models, as summarized in Table 1, along with their respective effects across the low and high Kn regimes, will be discussed in detail during the conference.

Acknowledgements

We would like to thank the National Supercomputing Mission (NSM) for providing computing resources of 'PARAM RUDRA' at IIT Madras, implemented by C-DAC, supported by the Ministry of Electronics and Information Technology and Department of Science and Technology, Government of India.

References and citations

[1] Golshtein, E., and T. Elperin. (1996). Convective Instabilities in Rarefied Gases by Direct Simulation Monte Carlo Method. Journal of Thermophysics and Heat Transfer 10, no. 2, 250–256.
[2] Stefanov, S., V. Roussinov, and C. Cercignani. (2002). Rayleigh-Bénard Flow of a Rarefied Gas and Its Attractors. I. Convection Regime. Physics of Fluids 14, no. 7
[3] Ben-Ami,Y., & Manela, A. (2019). Effect of heat-flux boundary conditions on the Rayleigh-Bénard instability in a rarefied gas. Physical Review Fluids, 4, 3.
[4] Goshayeshi, B., G. Di Staso, F. Toschi, and H. J. H. Clercx. (2020). Numerical Study of Heat Transfer in Rayleigh–Bénard Convection under Rarefied Gas Conditions. Physical Review E 102, no. 1, 013102.
[5] Wu, C., L. Bi, J. Zhao, Z. Tang, X. Yuan, and D. Wen. (2024). Instability Onset of Rayleigh–Bénard Convection for Diatomic Rarefied Gases: Effects of Molecular Interaction Models and Flow Parameters. International Journal of Heat and Mass Transfer 220, 124923.
[6] Bird, G. A. (1998). Molecular Gas Dynamics and the Direct Simulation of Gas Flows. Oxford: Clarendon Press.
[7] Lord, R. G. (1991). Some Extensions to the Cercignani–Lampis Gas–Surface Scattering Kernel. Physics of Fluids 3, 706–710.
[8] Plimpton, S. J., & Gallis, M. A. (2015). SPARTA Direct Simulation Monte Carlo (DSMC) Simulator, http://sparta.sandia.gov.

NEGF26-691080

THERMALLY-INDUCED FLOWS IN MICROFLUIDIC SYSTEMS: FROM OPTOTHERMAL FLUIDIC EXPERIMENTS TO NON-EQUILIBRIUM GASEOUS MODELING

Tetsuro Tsuji*[1]
[1]Kyoto University, Kyoto, Japan
tsuji.tetsuro.7x@kyoto-u.ac.jp

KEY WORDS

Thermophoresis, Thermo-osmosis, Thermal slip, Photothermal effect, Kinetic model, Fluid-solid interaction, Optical trapping

ABSTRACT

In this talk, some recent experimental and theoretical studies on thermally-induced microflows will be introduced. In the experimental part, we focus on thermophoresis, namely, a microparticle motion along a temperature gradient in fluids. Using an optothermal microfluidic system in liquids combined with optical trapping, thermally-induced flows around microparticles are detected, and the connection between the thermally-induced flows and the thermophoresis is clarified. To measure such slow microflows, optically-trapped particle tracking velocimetry is also proposed. Optothermal microfluidic systems are found to be effective, feasible, and convenient experimental setup to investigate thermal microflows. As an instant computational tool for optothermal microfluidic systems, a semianalytical model has been developed. In the modeling part, a kinetic model on thermally-induced non-equilibrium gas flows will be introduced. The model incorporates the fluid–solid molecular interaction potential, and a thermal-slip boundary condition is derived using the generalized slip-flow theory. Although the model is extremely simple, we have shown that the model reproduces qualitatively the sign reversal of the thermal-slip coefficients depending on the strength of the fluid-solid interaction. These outcomes on thermally-induced microflows are expected to contribute to the development of novel microfluidic functions such as separation and concentration.

Introduction

Thermophoresis is the motion of nano- and microscale objects along the temperature gradient of a fluid. The characteristics of thermophoresis are sensitively dependent on the choices of the object and the fluid, and microfluidics applications have demonstrated that thermophoresis can be applied to the separation of colloidal mixtures [1,2]. Similarly, the temperature gradient of a solid (e.g., substrates, spheres) induces thermo-osmosis, which is a creeping fluid flow near the solid boundaries [3]. Thermo-osmosis is a fundamental nonequilibrium effect in fluid mechanics at the nanoscale, emerging in both for gases and liquids, exploring a novel application for conversion from heat to motion.

The driving mechanism of thermo-osmosis and thermophoresis is the temperature gradient, and thus, a key to these applications is the method of producing the temperature field. Optothermal fluidics,

i.e., optical-heating-mediated fluidics, is a promising experimental tool for this purpose because we can easily localize the heat in micro- and nanoscales using standard optical systems, generating a huge magnitude of temperature gradient of the order of 1 K/μm. Recently, we have developed a semianalytical model for optothermal fluidics [4]. Using an open-source code for the model, temperature and flow fields for optothermal fluidics, including thermo-osmosis near substrates, can be obtained instantly. Simultaneously, we have tried to develop a theoretical model to investigate thermo-osmosis, that is, a thermal-slip coefficient on boundaries, using the generalized slip-flow theory in the kinetic theory of gases [5]. The model reproduces qualitative trends that have been reported in molecular simulation, such as the flow reversal due to the change of fluid−solid interaction potential.

In this presentation, we will briefly introduce our researches on optothermal fluidics mentioned above. In particular, the results of Ref. [3], which investigated the connection between the thermophoresis of microparticles and the thermo-osmotic slip flows over the particle surface, will be mainly discussed. A key to evaluating thermo-osmotic slip flows was the optical trapping of tracers (a more generalized method has been proposed in [6]). That is, fluorescent flow tracers are optically confined in a region-of-interest near the surface of the microparticle placed in the optothermally-generated temperature field (Figure 1); the distribution of these trapped tracers is analyzed to obtain the characteristics of thermo-osmosis. It is shown that the surface properties of microparticles significantly affects thermo-osmosis near the microparticle surface.

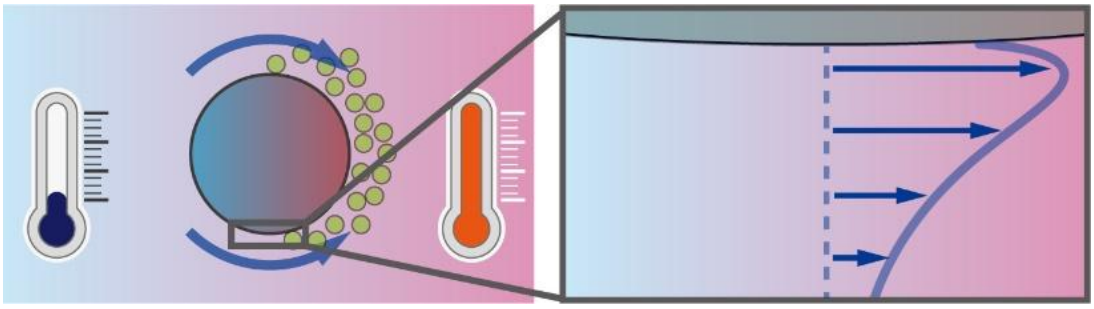

Figure 1: Schematic of the evaluation of thermo-osmosis around a thermophoretic microparticle in Ref. [3].

Acknowledgments

This work was supported by the Japan Society for the Promotion of Science KAKENHI Grants No. 24K00803 and No. 25K01156, and also by the Japan Science and Technology Agency PRESTO Grant No. JPMJPR22O7.

References and Citations

[1] Tsuji, T. & Saita, S. & Kawano, S. (2018). Dynamic pattern formation of microparticles in a uniform flow by an on-chip thermophoretic separation device. *Phys. Rev. Applied*, **9**, 024035.
[2] Tsuji, T. & Sasai, Y. & Kawano, S. (2018) Thermophoretic manipulation of micro-and nanoparticle flow through a sudden contraction in a microchannel with near-infrared laser irradiation. *Phys. Rev. Applied* **10**, 044005.
[3] Tsuji, T. & Mei, S. & Taguchi, S. (2023). Thermo-osmotic slip flows around a thermophoretic microparticle characterized by optical trapping of tracers. *Phys. Rev. Applied*, 20, 054061.
[4] Tsuji, T. & Saito, S. & Taguchi, S. (2024). Semianalytical model of optothermal fluidics in a confinement. *Phys. Rev. Fluids*, 9, 124202.
[5] Tsuji, T. & Takita, K. & Taguchi, S. (2025). Slip-flow theory for thermo-osmosis based on a kinetic model with near-wall potential. *Phys. Rev. Fluids*, 10, 114202.
[6] Tsuji, T. & Hashimoto, S. & Taguchi, S. (2025). Optically-trapped particle tracking velocimetry. arXiv:2509.03676.

NEGF26-686014

Thermodynamically Consistent Incorporation of the Langmuir Adsorption Model into Compressible Fluctuating Hydrodynamics

Changho Kim*[1], Hyun Tae Jung[2], Hyungjun Kim[2], Alejandro Garcia[3], Andrew Nonaka[4], John Bell[4], Ishan Srivastava[4]
[1]Department of Applied Mathematics, University of California, Merced, California 95343, USA
ckim103@ucmerced.edu
[2]Department of Chemistry, Korea Advanced Institute of Science and Technology, Daejeon 34141, South Korea
chemtae@kaist.ac.kr, linus16@kaist.ac.kr
[3]Department of Physics and Astronomy, San Jose State University, San Jose, California 95192, USA
alejandro.garcia@sjsu.edu
[4]Center for Computational Sciences and Engineering, Lawrence Berkeley National Laboratory, Berkeley, California 94720, USA
ajnonaka@lbl.gov, jbbell@lbl.gov, isriva@lbl.gov

KEY WORDS

Mesoscopic fluid simulation, stochastic continuum modeling, thermal fluctuations, gas-solid interface, stochastic chemistry, structure factor spectrum, ideal gas mixture

ABSTRACT

For a gas-solid interfacial system where chemical species undergo reversible adsorption, we develop a mesoscopic stochastic modeling method that simulates both gas-phase hydrodynamics and surface coverage dynamics by coupling the Langmuir adsorption model with compressible fluctuating hydrodynamics. To this end, we derive a thermodynamically consistent mass-energy update scheme that accounts for how the mass and energy variables in the gas and surface subsystems should be updated according to the changes in the number of molecules of each species in each subsystem due to adsorption and desorption events. By performing a stochastic analysis for the ideal Langmuir model and the full hydrodynamic system, we analytically confirm that our mass-energy update scheme captures thermodynamic equilibrium predicted by equilibrium statistical mechanics. We find that an internal energy correction term is needed, which is attributed to the difference in the mean kinetic energy of gas molecules colliding with the surface from that computed from the Maxwell-Boltzmann distribution. By performing an equilibrium simulation study for an ideal gas mixture of CO and Ar with CO undergoing reversible adsorption, we validate our overall simulation method and implementation.

* Corresponding author

Disclaimer

This extended abstract is based on the recent collaborative work among UC Merced, KAIST, and Berkeley Lab. A manuscript has been submitted for publication in a journal and the preprint is available on arXiv [1].

Motivation and Question to be Addressed

Computational modeling of **reactive gas-solid interfacial systems**, e.g., heterogeneous catalysts, plays an important role in various fields of science and engineering, including energy and environmental sciences. Due to its intrinsic multi-phase, multi-scale nature, an accurate and computationally efficient description of both the reactive dynamics on the catalytic surface and the transport dynamics in the gas phase is required. However, since these dynamics have disparate natures, the use of a single traditional simulation approach usually leads to inaccurate or computationally inefficient simulations.
As an alternative, several hybrid simulation approaches have been proposed for reactive gas-solid interfacial systems. In the CFD–KMC hybrid approach, computational fluid dynamics (CFD) is employed for gas-phase hydrodynamics, whereas kinetic Monte Carlo (KMC) is used for surface chemistry. Most existing CFD–KMC hybrid simulation methods are based on the macro-micro coupling structure or the heterogeneous multiscale method, where the KMC (micro solver) is *passively* coupled to CFD (macro solver) using one-way coupling under the assumption of complete scale separation. However, for a **mesoscale gas-solid interfacial system**, where the gas-phase hydrodynamics and surface reaction dynamics have comparable time and length scales (see the left panel of Fig. 1), this CFD–KMC hybrid approach based on the macro-micro coupling is not applicable and a new hybrid simulation approach based on *two-way, concurrent* coupling is needed.
In this mesoscale hybrid approach, it is assumed that the domain of the surface chemistry solver corresponds to a physical boundary of the continuum hydrodynamics solver and these solvers update the states of the corresponding subsystems concurrently while exchanging molecules due to adsorption and desorption. Since thermal fluctuations are significant at mesoscales, they need to be incorporated in the continuum CFD solver. The **fluctuating hydrodynamics (FHD) approach** provides a suitable mesoscopic simulation framework [2, 3, 4] and has been used to develop two-way, concurrent continuum–particle coupling methods for nonreactive hydrodynamic systems, e.g., direct simulation Monte Carlo [5]. In this work, we address one of the fundamentally important theoretical questions for the development of the FHD–KMC coupling, i.e., **how to correctly combine FHD and KMC**, by investigating **thermodynamic consistency**.

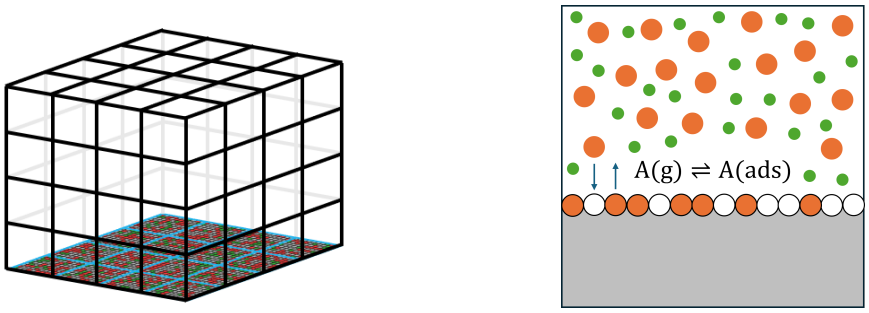

Figure 1: Schematic diagrams of an FHD-KMC coupling (left) and the Langmuir adsorption (right).

Main Results

We develop a novel mesoscopic stochastic modeling method that integrates the Langmuir adsorption model (see the right panel of Fig. 1) with compressible FHD. A primary theoretical achievement of this work is the derivation of a **thermodynamically consistent mass–energy update scheme** to handle the exchange of mass and energy variables between the gas and surface subsystems during adsorption and desorption events. Through a rigorous stochastic analysis applied to the ideal Langmuir model and the full hydrodynamic system, we analytically confirm that this update scheme successfully captures the thermodynamic equilibrium predicted by equilibrium statistical mechanics.
A crucial element identified during the derivation of the mass–energy update scheme is the requirement for an **internal energy correction term**, quantified as $\frac{1}{2}k_BT$ per molecule. This correction is necessary because the mean kinetic energy of a gas molecule colliding with the surface differs from the mean kinetic energy calculated from the bulk Maxwell–Boltzmann distribution. Specifically, the normal velocity component of a molecule colliding with the wall adheres to a Rayleigh distribution, resulting in an average kinetic energy of k_BT for that component, rather than $\frac{1}{2}k_BT$ associated with the other two velocity components; hence, the mean kinetic energy of the molecule ($2k_BT$) is larger by $\frac{1}{2}k_BT$ than the standard $\frac{3}{2}k_BT$ mean kinetic energy for the bulk gas. Furthermore, we develop a thermodynamically consistent reaction (TCR) model for Langmuir adsorption, which guaranties that the formulation and parameter selection are based on consistent chemical potential models, thus ensuring that the relationship between the equilibrium constant and the rate constants is preserved.
We perform extensive numerical validations using equilibrium simulations of an ideal gas mixture (CO and Ar, with CO undergoing reversible adsorption) to confirm the accuracy of our methodology beyond the weak-noise limit. The simulation results obtained using our update scheme faithfully reproduce the expected thermodynamic equilibrium properties. Specifically, cell variances and structure factor spectra for all state variables, including mass densities, velocity components, temperature, and surface coverage, agree with theoretical predictions based on equilibrium statistical mechanics within minimal statistical errors, e.g., cell variance profiles agreeing within 0.1% error (see Fig. 2). Conversely, thermodynamically inconsistent settings—such as replacing instantaneous partial pressure and temperature with mean values in the adsorption rate calculation (mimicking a passive macro-micro coupling)—lead to significant devi-

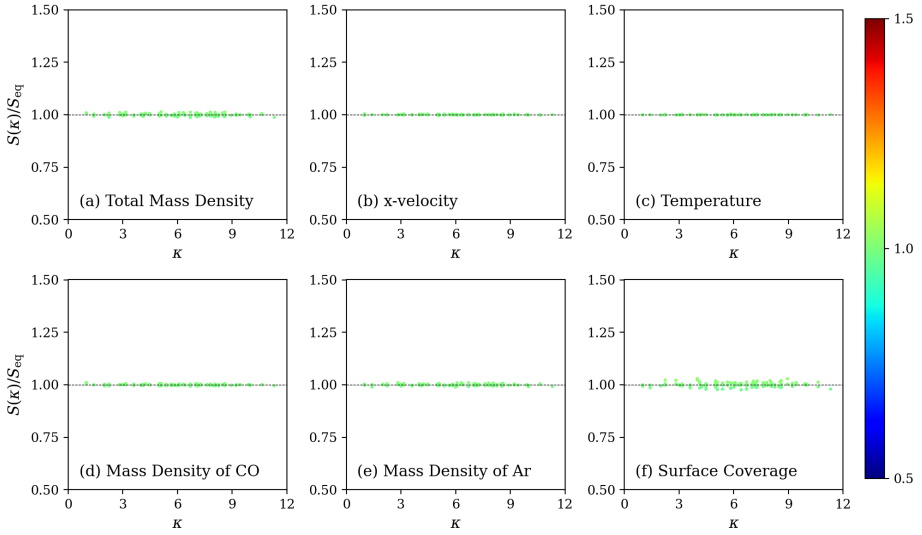

Figure 2: Correct structure factor spectra obtained using our thermodynamically consistent mass-energy update scheme.

ations, e.g., exceeding 10% error in cell variances and unphysical fluctuations for mass density variables near the adsorbent surface (see Fig. 3). Most importantly, our validation study demonstrates the critical role of the $\frac{1}{2}k_BT$ energy correction term. When this correction is omitted from the reversible adsorption update, the resulting simulation displayed statistically significant nonzero correlations between thermodynamic variables such as (ρ_{CO}, T), (θ, T), and $(\theta, \rho_{\mathrm{CO}})$ in the bottom layer contacting the adsorbent surface, which should be zero at equilibrium. These findings confirm that our methodology provides a foundational, thermodynamically consistent framework for modeling fluctuations at the gas-solid interface.

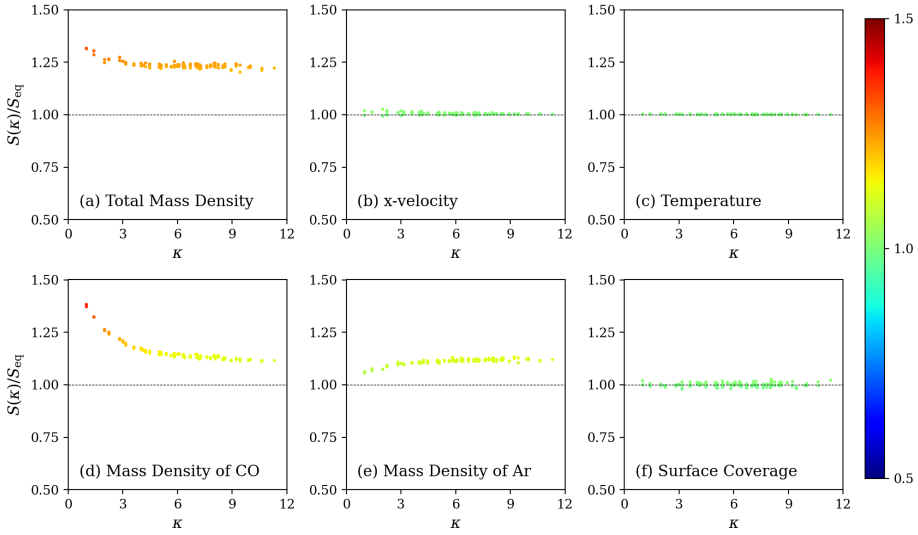

Figure 3: Structure factor spectra obtained using a thermodynamically inconsistent setting mimicking a passive macro-micro coupling.

Acknowledgements

This work was supported in part by the National Science Foundation of U.S. under Grant No. CHE-2213368, the U.S. Department of Energy, Office of Science, Office of Advanced Scientific Computing Research, Applied Mathematics Program under Contract No. DE-AC02-05CH11231, and the National Research Foundation of Korea under Grant Nos. RS-2024-00405261 and RS-2024-00450102.

References and citations

[1] Jung, H. T., Kim, H., Garcia, A. L., Nonaka, A. J., Bell, J. B., Srivastava, I., & Kim, C. (2025). Thermodynamically consistent incorporation of the Langmuir adsorption model into compressible fluctuating hydrodynamics. arXiv:2510.15329.

[2] Garcia, A. L., Bell, J. B., Nonaka, A. J., Srivastava, I., Ladiges, D. R., & Kim, C. (2025). An introduction to computational fluctuating hydrodynamics. arXiv:2406.12157.

[3] Srivastava, I., Ladiges, D. R., Nonaka, A. J., Garcia, A. L., & Bell, J. B. (2023). Staggered scheme for the compressible fluctuating hydrodynamics of multispecies fluid mixtures. Phys. Rev. E 107, 015305.

[4] Polimeno, M., Kim, C., Blanchette, F., Srivastava, I., Garcia, A. L., Nonaka, A. J., & Bell, J. B. (2025). Thermodynamic consistency and fluctuations in mesoscopic stochastic simulations of reactive gas mixtures. J. Chem. Phys. 162, 154107.

[5] Donev, A., Bell, J. B., Garcia, A. L., & Alder, B. J. (2010). A hybrid particle-continuum method for hydrodynamics of complex fluids. Multiscale Model. Simul. 8, 871.

Author Index